Evolution of Remnant Radio Galaxies

Submitted in partial fulfillment of the requirements
of the degree of

Doctor of Philosophy

by

Sushant Dutta
(Roll No. 17330035)

Supervisor:
Dr. Veeresh Singh

Department of Physics
INDIAN INSTITUTE OF TECHNOLOGY GANDHINAGAR
2022

I dedicate this thesis to my family, and to all those who are interested in science.

Abstract

Active Galactic Nuclei (AGN) are manifestations of accretion around the Super-Massive Black Holes (SMBHs) residing in the centres of galaxies. Radio galaxies, a subclass of AGN, emit copiously at radio wavelengths and exhibit a typical radio morphology comprising a core, a pair of highly collimated relativistic jets that eventually form radio lobes at their extremities. Understanding the evolution of radio galaxies is one of the important aspects of galaxy evolution, as AGN jet activity influences host galaxy and surrounding inter-galactic-medium (IGM) via feedback processes. In last few decades, multi-frequency radio observations probing radio emission at different spatial-scales have revealed that the AGN jet activity in galaxies is only a phase (active phase) lasting for several tens of Myr during which the radio size can grow up to a few hundred kpc and rarely, up to a few Mpc. After an active phase, AGN activity ceases or drops below a certain threshold level so that the outflowing jets are no longer supported and the radio lobes begin to fade away. During the fading period termed as the 'remnant phase' or 'dying phase', the radio core and jets disappear but the radio lobes can still be detected for a period of a few tens of million years before they disappear due to radiative and dynamical losses. The duration of remnant phase is arguably a small fraction of the duration of active phase, hence remnant sources are believed to represent a short-lived final phase of the radio galaxy's evolution. Remnant radio galaxies (hereafter 'remnants') are deemed to be less abundant owing to the relatively short duration of the remnant phase. Due to their relative paucity remnants are poorly understood. Specifically, AGN duty cycle and its dependence on various factors such as the jet kinetic power, host galaxy, and large-scale cluster environment are still a matter of investigation.

This thesis presents the search and characterization of remnants in the XMM-LSS deep field by using sensitive radio observations at 325 MHz from the Giant Metrewave Radio Telescope (GMRT), at 150 MHz from the LOw Frequency ARray (LOFAR), at

1.4 GHz from the Jansky Very Large Array (JVLA), and at 3 GHz from the VLA Sky Survey (VLASS). By using both morphological criteria *viz.*, undetected radio core as well as spectral criteria *viz.*, high spectral curvature, and ultra−steep spectrum, we identify a sample of 21 remnant candidates that are found to reside mostly in non−cluster environments, and exhibit diverse properties in terms of morphology, spectral index ($\alpha_{150\ \mathrm{MHz}}^{1.4\ \mathrm{GHz}}$ in the range of -1.71 to -0.75 with a median of -1.10), and linear radio size (ranging from 242 kpc to 1.3 Mpc with a median of 469 kpc). Our study attempts to identify remnant candidates down to the flux density limit of 6.0 mJy at 325 MHz, and yields a stringent upper limit on the remnant fraction (f_{rem}) to be 5%, a lower value than those reported previously. The observed f_{rem} seems consistent with the predictions of an evolutionary model assuming power law distributions of the duration of active phase and jet kinetic power with index -0.8 to -1.2.

This thesis also highlights the fact that most of the previous studies searched remnants using morphological criteria and they have preferentially identified large angular size sources resulting into a bias towards the remnants of powerful FR-II radio galaxies. This thesis presents the first attempt to perform a systematic search for remnants of small angular sizes (<30″) by exploiting spectral curvature criterion in the 150 MHz − 1.4 GHz spectral window. We identify a sample of 48 small-size remnant candidates that exhibit strong spectral curvature *i.e.*, $\alpha_{150\ \mathrm{MHz}}^{325\ \mathrm{MHz}}$ - $\alpha_{325\ \mathrm{MHz}}^{1.4\ \mathrm{GHz}} \geq 0.5$. Our study unveils a new population of small-size (<200 kpc) remnant candidates, and contradicts previous findings suggesting that the small-size remnants mostly reside in cluster environments wherein dense surrounding medium confines the growth of radio source. We find that most of our small-size remnants reside in less dense environments. We speculate that a relatively shorter active phase and/or the low jet kinetic power can be plausible reasons for the small size of remnant candidates.

We model the radio spectral energy distributions (SEDs) of a subsample of remnants using band-3 uGMRT and ancillary radio observations. The continuous injection off model ($\mathrm{CI_{OFF}}$), that assumes an active phase with continuous injection followed by a remnant phase, provides reasonably good fits to the SEDs. Our study finds the total source ages (t_{s}) in the range of 20 Myr to 42 Myr with $t_{\mathrm{OFF}}/t_{\mathrm{s}}$ ratio distributed in the range of 0.1 to 0.6, which in turn suggests them to belong to different evolutionary phases. We note that, in comparison to the remnants reported in the literature, our sample sources tend to show lower spectral ages that can be explained by the combined effects of more dominant inverse Compton losses for our sources present at the relatively higher redshifts, and possible rapid expansion of lobes in their less dense environments.

Contents

List of Tables

List of Figures

Declaration

I, Sushant Dutta, declare that this thesis represents the result of research work carried out by me at the Physical Research Laboratory, Ahmedabad India, under the supervision of Dr. Veeresh Singh. I also declare that I have adhered to all principles of academic honesty and integrity and have not misrepresented or fabricated or falsified any idea/data/fact/source. The work presented in this thesis has not been submitted for the award of any degree, diploma, associateship etc. to any university or institute.

Sushant Dutta

Date:

Sushant Dutta

Roll No. 17330035

Certificate

It is certified that the work contained in the thesis titled "Evolution of Remnant Radio Galaxies" has been carried out by Mr. Sushant Dutta (Roll No. 17330035) under my supervision at the Physical Research Laboratory, Ahmedabad, India. This work has not been submitted elsewhere for the award of any degree or diploma.

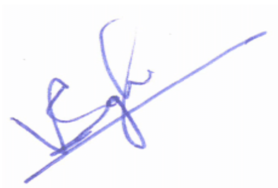

Date:

Dr. Veeresh Singh

(Thesis Supervisor)

Assistant Professor

Astronomy & Astrophysics Division

Physical Research Laboratory

Unit of Department of Space, Govt. of India

Ahmedabad-380009, Gujarat, India

Acknowledgements

I would like to express my deep gratitude for those who helped me to reach the juncture of writing the acknowledgment of my Ph.D. thesis. I am most obliged to my Ph.D. thesis supervisor Dr. Veeresh Singh for his guidance and constant support throughout my Ph.D. years and without his cooperation it would not have been possible to complete this thesis. I am grateful for his encouragement to interact and collaborate with experts. I express my gratefulness to our collaborators Prof. C. H. Ishwara Chandra and Dr. Yogesh Wadadekar for their extensive help. I am also thankful to my collaborator Dr. Ian Heywood who provided 1.5 GHz wide-band JVLA image and source catalog, and despite his busy schedule, he was always ready to address my all email queries.

I had opportunity to attend the Radio Astronomy School (RAS) at NCRA, Pune in 2019 where I learnt radio interferometry and observational techniques. I would like to thank the RAS organizers as well as the tutors who taught me how to reduce and analyse radio data, specifically from the GMRT. I thank to the staff of the GMRT who have made GMRT observations possible. GMRT is run by the National Centre for Radio Astrophysics of the Tata Institute of Fundamental Research. Furthermore, I acknowledge that for this research work I have made use of NASA's Astrophysics Data System and the NASA/IPAC Extragalactic Database (NED) which is operated by the Jet Propulsion Laboratory, California Institute of Technology, under contract with the National Aeronautics and Space Administration. This work has used the data obtained with the International LOFAR Telescope (ILT). The LOw Frequency ARray (LOFAR) is designed and constructed by the ASTRON. It has observing, data processing, and data storage facilities in several countries, which are owned by various parties (each with their own funding sources) and are collectively operated by the ILT foundation under a joint scientific policy. We also used data obtained with the Very Large Array (VLA). The VLA is operated by the National Radio Astronomy Observatory, a facility of the National Science

Foundation operated under cooperative agreement by Associated Universities, Inc.

I would like to thank my DSC members – Prof. Sachindra Naik, Dr. Shashikiran Ganesh and Dr. Kinsuk Acharyya for examining my progress during Ph.D. years and for their suggestions to improve my thesis work. In addition, I sincerely thank to the Academic Committee for rigorously reviewing and giving valuable comments/suggestions during the annual reviews at PRL. I would also like to thank all my Ph.D. course-work instructors who taught me the basics of Astronomy and Astrophysics, which was necessary before I could begin my research work in a specialized field of Astrophysics. I humbly would take this opportunity to thank the Director PRL Dr. Anil Bhardwaj and all the PRL staff members for the support and facilities which I received from the institute during my stay at PRL.

When it comes to acknowledge the friends, it is a long list. First and foremost, Neeraj Kumari, my best friend in PRL, with whom I cherished my Ph.D. life and used to spend most of the time discussing about various things. Well, she is also my teacher because she taught me some valuable lessons in life. I am grateful to all my friends-cum-batchmates over the years in Astronomy & Astrophysics division at PRL – Abhijit Kayal (fellow disciple), Vipin Kumar, Aravind K, Shanwlee Sow Mondal, Biswajit Mondal and Abhay Kumar; my seniors – Archita Rai, JNHS Aditya, Shivangi Gupta, Sandeep Rout, Parveen Kumar, Vineet Ojha; and my juniors – Naval, Akanksha, Namita, Arup, Birendra, Vineet, Sanjay, Narendra. Other names of my batchmates with whom I rejoiced Ph.D. days at hostel and campus include Ankit, Alka, Rituparna, Anshika, Sarika, Satyajeet, Kamlesh, Suraj, Ramanuj, Subith, Madhusudhan, Partha, Himanshu, Shivani, Sana, Atif, Milan, Amit, Sovan, Hrushikesh, Tanmay, Sudipta, Vishal, Deepak, Hirdesh. Over all these years I enjoyed playing Table Tennis, Badminton, Volleyball, Cricket and would like to thank all those friends who have been enthusiastically participating.

The pages would never be sufficient to appreciate the contribution and cooperation of all of my teachers and friends outside PRL, nonetheless, I must remember my Mathematics and Physics teachers Ved Pal Verma and Dr. S. C. Tiwari. I am indebted to my parents, my elder brother and all the family members for their encouragement, blessings and everlasting heartily support, which is beyond the words.

Sushant Dutta

List of Abbreviations

AGN	Active Galactic Nucleus
ASKAP	Australian SKA Pathfinder
ALMA	Atacama Large Millimeter Array
CSO	Compact Symmetric Object
CSS	Compact Steep Spectrum
CMB	Cosmic Microwave Background
DDRG	Double-Double Radio Galaxy
DB	Dirty Beam
EMU	Evolutionary Map of the Universe
FR	Fanaroff−Riley
FSRQ	Flat-Spectrum Radio Quasar
FWHM	Full Width Half Maximum
FIRST	Faint Images of the Radio Sky at Twenty-Centimeters
FoV	Field of View
GMRT	Giant Meterwave Radio Telescope
GPS	Gigahertz Peaked-Spectrum
GLEAM	Galactic and Extragalactic All-sky Murchison Widefield Array
HSC−SSP	Hyper Suprime−Cam Subaru Strategy Program
HFP	High-Frequency Peaker
Herschel-ATLAS	Herschel Astrophysical Terahertz Large Area Survey
HBA	High Band Antenna

IGM	Inter-Galactic Medium
ICM	Intra-Cluster Medium
ISM	Inter-Stellar Medium
IR	Infrared
IC	Inverse-Comptonization
JVLA	Jansky Very Large Array
LOFAR	LOw Frequency ARray
LoTSS	LOFAR Two-metre Sky Survey
LBA	Low Band Antenna
LAT	Large Area Telescope
MWA	Murchison Widefield Array
NRAO	National Radio Astronomical Observatory
NVSS	NRAO VLA Sky Survey
PAF	Phased Array Feed
PSF	Point Spread Function
RRG	Remnant Radio Galaxy
RL	Radio-Loud
RQ	Radio-Quiet
RACS	Rapid ASKAP Continuum Survey
RFI	Radio Frequency Interference
SCP	Spectral Curvature Parameter
SMBH	Super-Massive Black Hole
SSC	Synchrotron Self-Compton
SSA	Synchrotron Self-Absorption
SKA	Square Kilometer Array
SFG	Star-Forming Galaxy

SED	Spectral Energy Distribution
TGSS	TIFR-GMRT Sky Survey
UV	Ultraviolet
USS	Ultra-Steep Spectrum
uGMRT	upgraded Giant Meterwave Radio Telescope
VLASS	Very Large Array Sky Survey
VLSSr	VLA Low-frequency Sky Survey Redux
VLBI	Very Long Baseline Interferometery
XMM−LSS	XMM-*Newton* Large−Scale Structure

List of Publications

Peer − Reviewed Journals

1. **Sushant Dutta**, Veeresh Singh, C.H. Ishwara Chandra, Yogesh Wadadekar, Abhijit Kayal and Ian Heywood, "Search and Characterization of Remnant Radio Galaxies in the XMM−LSS Deep Field", 2022, The Astrophysical Journal, arXiv:2212.10133.

2. **Sushant Dutta**, Veeresh Singh, C. H. Ishwara Chandra, Yogesh Wadadekar and Abhijit Kayal, "Characteristics of Remnant Radio Galaxies Detected in the Deep Radio Continuum Observations from the SKA Pathfinders", 2022, Journal of Astrophysics and Astronomy, 43, 96, doi: 10.1007/s12036-022-09883-y.

3. Veeresh Singh, **Sushant Dutta**, Yogesh Wadadekar and C. H. Ishwara-Chandra, "Remnant Radio Galaxy Candidates of Small Angular Sizes", 2021, Galaxies, 9, 121, doi: 10.3390/galaxies9040121.

Contributory

1. Abhijit Kayal, Veeresh Singh, C.H. Ishwara Chandra, Yogesh Wadadekar and **Sushant Dutta**, "Detection of Radio-AGN in Dust-Obscured Galaxies using Deep uGMRT Radio Continuum Observations", 2022, Journal of Astrophysics and Astronomy, 43, 84, doi: 10.1007/s12036-022-09873-0.

Chapter 1

Introduction

1.1 Active Galactic Nuclei

Most of galaxies host supermassive black holes (SMBH; $\sim 10^6 - 10^9$ $M_\odot$) in their centres. Due to their high gravitational potential SMBHs accrete matter whenever available in their vicinity. The accreting material around SMBH radiates at a wide range of frequencies and such systems are known as the active galactic nuclei (AGN). Observations have shown that AGN can be identified by their peculiar characteristics such as (i) presence of strong emission lines of a wide range of ionization in their IR, optical and UV nuclear spectra; (ii) continuum emission arising from the non-thermal processes; (iii) emission observed across nearly entire electromagnetic spectrum ranging from the radio to X-rays or even gamma-rays; (iv) variable nuclear emission over different timescales ranging from hours to years; (vi) high bolometric luminosity in the range of 10^{42} ergs s^{-1} to 10^{48} ergs s^{-1} (see Peterson, 1997; Padovani et al., 2017). Hence, AGN can be studied in all bands of the electromagnetic spectrum and they can be detected upto high-redshifts due to their high luminosities. Based on their observational properties AGN can be divided into different subclasses namely Seyfert galaxies, quasars, radio galaxies and blazars. The observational properties of different subclasses are briefly outlined in the following subsection.

1.1.1 AGN Classification

Based on the observational properties, AGN can be classified into different subclasses named as Seyfert galaxies, quasars, radio galaxies and blazars. In this section, we describe basic properties of different types of AGN. According to the unification model, most of the observed differences between different subclasses of AGN can be explained by the orientation and relativistic beaming effects (*e.g.*, Urry & Padovani, 1995; Padovani et al., 2017). In Figure 1.1 we show a cartoon image depicting different subclasses as per the unification model.

1.1.1.1 Seyfert Galaxies

In 1943 Carl Seyfert discovered six spiral galaxies showing cores of high surface brightness, and optical spectra of their central regions dominated by broad emission lines of high excitation (Seyfert, 1943). The high excitation suggested the presence of gas excited by photons with energies much higher than the photons arising from young stars causing ionization of H II regions. Later on, Seyfert galaxies were recognised as a subclass of AGN due to the similarity of their optical spectra with quasars. In the current classification scheme of AGN, Seyfert galaxies are identified as low-luminosity AGN hosted in nearby spiral galaxies. Seyfert galaxies are further subdivided into Seyfert type 1 and Seyfert type 2 subclasses based on the presence and absence of broad permitted emission lines (full width half maxima (FWHM) of lines $\geq$1000 km s^{-1}) in their optical spectra, respectively (Antonucci, 1993).

1.1.1.2 Quasars

The discovery of quasars began with the identification of a point-like optical counterpart of a strong radio source 3C 273 (Schmidt, 1963). The strong radio sources with point-like optical counterparts were termed as quasi-stellar radio sources, in short quasars. However, later studies identified a large population of radio-quiet quasars with optical spectra similar to radio-loud quasars. The optical spectra of quasars were found to be dominated by strong emission lines with their widths in the range of a few thousands km s^{-1} to 10^4 km s^{-1} (Osmer & Smith, 1976; Barthel et al., 1990). Unlike Seyfert galaxies, quasars are more luminous and are found at higher redshifts. The difference between Seyfert galaxies and quasars is mainly luminosity *i.e.*, quasars have optical B band absolute magnitude (M$_B$) $\leq$-22.25 (Véron-Cetty & Véron, 2010). Quasars often outshine their host galaxies, and hence making it difficult to study the properties of their host galaxies. However, deep optical imaging observations suggest that quasars are likely to be hosted in elliptical galaxies (Dunlop et al., 2003).

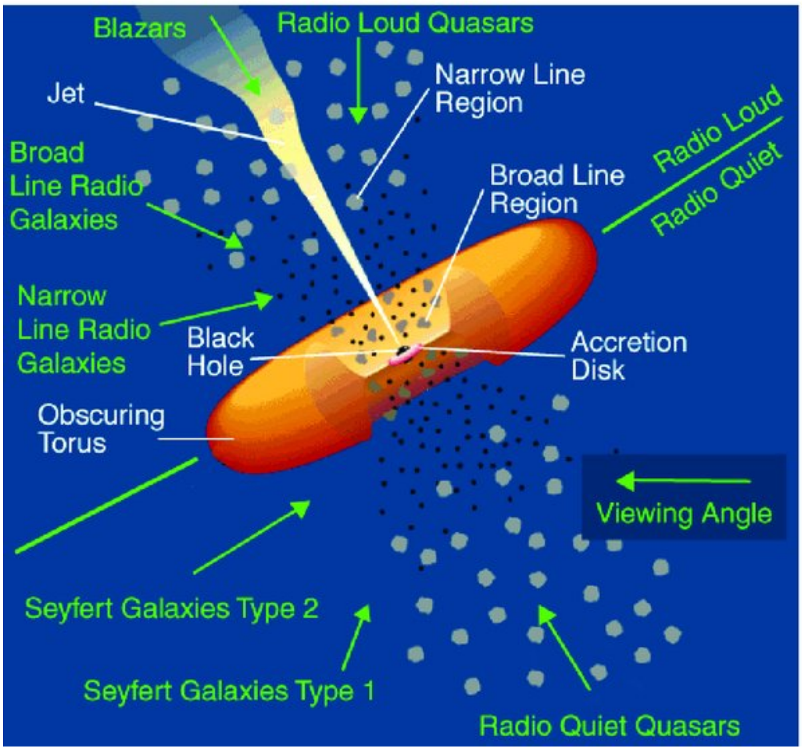

Figure 1.1: A cartoon image depicting AGN components *i.e.*, supermassive black hole, accretion disk, obscuring torus, broad-line region, narrow-line region and radio jet lobe. The different subclasses namely Seyfert galaxies, quasars, radio galaxies and blazars are also shown as per the unification model. Credit: (Urry & Padovani, 1995).

1.1.1.3 Radio Galaxies

Radio galaxies emit strongly at radio wavelengths, and exhibit a well defined radio morphology consists of a radio core coinciding with the centres of optical host, a pair of highly collimated outflowing jets traversing well beyond the host galaxy, and lobes at their ends (see Figure 1.2). The confirmation of AGN in radio galaxies comes from a variety of other characteristics such strong emission lines in the nuclear spectra, emission across a wide range of frequencies from radio to X-ray (Schmidt, 1965; Worrall & Birkinshaw, 1994). In 1974, Fanaroff & Riley (1974) classified radio galaxies into two subclasses (Fanaroff-Riley type I (FR I) and Fanaroff-Riley type II (FR II)) based on their radio morphologies. The FR II radio galaxies show highly collimated jets and bright hotspots at the edges of their lobes. While, FR I radio galaxies exhibit turbulent decelerating jets and diffuse wind-like lobes with no edge-brightening. In general, FR IIs with radio luminosity $P_{178\ \mathrm{MHz}} \geq 5 \times 10^{25}$ W Hz^{-1} sr^{-1} are more powerful than FR Is. Although, FR I $-$ FR II dividing luminosity is found to be a function of host galaxy optical luminosity (Ghisellini & Celotti, 2001). More recently, using LOFAR Two-Metre Sky Survey (LoTSS) Mingo et al. (2019) demonstrated that the radio luminosity does not reliably predict FR I $-$ FR II division. They found a large population of low-luminosity FR IIs residing in host galaxies of low optical luminosities, which in turn infers that FR I $-$ FR II division can be attributed to the jet power and environment. The FR IIs with low-power jets, hosted in lower mass galaxies, may remain undisrupted to form edge-brightened lobes. While, FR Is residing in denser environments can suffer jet disruption leading to the formation of core-brightened lobes (Gendre et al., 2013). Recent studies also suggest a third subclass of radio galaxies namely FR 0s which exhibit radio morphology similar to FR Is but lack extended emission from lobes and appear more core-dominated (Baldi et al., 2015). Some radio galaxies also show highly bent appearances and are called wide-angle tail, narrow-angle tail based on the degree of bending of jets from their initial directions (Blanton, 2000).

1.1.1.4 Blazars

Blazars are radio-loud AGN with relativistic jets pointed close to the observer's line-of-sight, and show strongly as well as rapidly variable non-thermal emission, flat radio spectra, high polarization, high luminosities and super-luminal motion (Urry & Padovani, 1995; Giommi et al., 2013). Blazars are classified into BL-Lac sources and flat-spectrum radio quasars (FSRQs) based on the angle between jet axis and line-of-sight. The BL-Lac sources with nearly pole-on view (jet axis aligned with the line-of-sight within a few degrees) show featureless optical spectra or weak emission lines with the rest-frame equivalent width (EW) < 5Å (Stocke & Rector, 1997). While FSRQs making 5° to 15° angle between the jet axis and line-of-sight, show strong quasar emission lines and higher radio polarization (Laurent-Muehleisen et al., 1999). The broad-band spectral energy distributions (SEDs) of blazars generally exhibit two peaks, one lying in the infrared-to-soft X-ray regime and second peak in the hard X-ray to gamma ray regime. The high energy peak is produced by inverse Compton upscattering of seed photons within the jet by the relativistic electrons present in the jet (synchrotron self-Compton, SSC) (Inoue & Takahara, 1996). Blazars are one of dominant source populations in the γ-ray surveys performed with the Fermi Large Area Telescope (LAT) due to their strong emission in the high energy bands (Abdo et al., 2009).

1.1.2 Radio-Loud and Radio-Quiet AGN

In addition to the aforementioned four subclasses, AGN can be divided into radio-loud (RL) and radio-quiet (RQ) categories based on their flux ratio of radio to optical or radio luminosity (Kellermann et al., 1989). Conventionally, radio loudness parameter $R = \frac{\nu_{5\mathrm{GHz}} S_{5\mathrm{GHz}}}{\nu_{4400} S_{4400}}$ is used to classify AGN as either RL ($R > 10$) or RQ ($R < 10$). Early studies suggested the existence of RL−RQ dichotomy with an apparent dearth of radio-intermediate sources (Visnovsky et al., 1992; Kellermann et al., 1994). However, some of the studies finding a sizable population of radio-intermediate sources inferred a continuous distribution of radio loudness parameter rather than being bimodal (see Falcke et al., 1996; Singh et al., 2015; Järvelä et al., 2022). To address the RL−RQ dichotomy, there have been a large number of studies suggesting the crucial role of various fundamental parameters of the AGN−galaxy system, *e.g.*, mass and spin of black hole, accretion rate and Hubble type of host galaxy that can influence the radio nature of AGN (*e.g.*, Laor, 2000; McLure & Jarvis, 2004; Sikora et al., 2007; Rafter et al., 2011; Retana-Montenegro & Röttgering, 2017). In general, RL-AGN constitute radio-galaxies and blazars, while Seyfert galaxies are mostly RQ-AGN (see Figure 1.1). As mention in the previous section quasars fall into both categories with majority of them being RQ. In recent literature, classical RL−RQ classification is being substituted with a more generic terminology of jetted and non-jetted AGN (see Padovani et al., 2017). The jetted-AGN include all sources showing radio jets at different scales and of varying radio powers irrespective of their AGN subclass. Radio galaxies with large-scale jets are the prime examples of jetted-AGN. A brief description of our current understanding about the formation and evolution (life-cycle) of radio galaxies is given in the following section.

1.2 Radio Galaxies and Their Life-Cycle

1.2.1 Morphological Components of Radio Galaxies

Radio galaxies are characterized with a distinct radio morphology consist of a core, a pair of outflowing collimated jets that form lobes at the their ends (see Figure 1.2). Here, we provide a brief description of the properties of different morphological components.

1.2.1.1 Core

Conventionally, radio core is defined as an unresolved point-like component in the radio images of arcsecond resolution. The VLBI observations of parsec-scale resolution too show radio core as an unresolved component suggesting core to be optically thick base of the jet (Horiuchi et al., 2006; Doeleman et al., 2012). For instance, 1.4 mm VLBI observations of Centaurus A showed an unresolved core component with size $\leq$120 Schwarzschild radii and brightness temperature of 1.4×10^{11} K (Kim et al., 2018). The core radio emission is believed to be self-absorbed non-thermal synchrotron emission giving a flat radio spectrum (Verdoes Kleijn et al., 2002; Kharb & Shastri, 2004).

1.2.1.2 Jets

Radio galaxies exhibit highly collimated outflowing jets emanating from the close vicinity of accreting SMBH and traversing upto several hundreds of kpc. Several jetted-AGN showing super-luminal motion confirm the relativistic speed of outflowing material in the jet (Lister et al., 2013). The jet acceleration and collimation is believed to occur simultaneously at a distance of 10^4 to 10^6 gravitational radii (Vlahakis & Königl, 2004; Marscher et al., 2008). M87 being the nearest radio galaxy has been an ideal target for observations attempting to understand acceleration and collimation at various spatial scales. The VLBI monitoring observations of the M87 jet have revealed that the jet achieves relativistic speed at a distance of 1000 gravitational radius itself (Mertens et al., 2016; Park et al., 2019). The theoretical models assume magneto-centrifugal launching either from a rotating accretion disk or from the SMBH ergosphere, and subsequent collimation of the material due to confinement of the plasma in a helical magnetic field (Blandford & Znajek, 1977; Blandford & Payne, 1982). The VLBI observations of several AGN have provided the evidence of helical magnetic fields present within the first few parsecs (Hovatta et al., 2012; Gabuzda et al., 2015, 2017). More recently, using JVLA broad-band full-polarization radio observations Pasetto et al. (2021) confirmed a double-helix morphology of the jet material on the scales of 1 kpc. The JVLA polarization observations provide a direct evidence for the presence of a helical magnetic field in the jet.

1.2.1.3 Hotspots

Hotspots are compact and bright regions detected at the edge of lobes in FR II radio galaxies (see Figure 1.2). Hotspot can be considered as a surface where relativistic jet impinged upon and create shock responsible for acceleration of the particles that radiate intensely. In general, hotspots emit mostly at radio wavelengths, however, observations of nearby radio galaxies have revealed the detection of hotspots in various wavelengths ranging from infrared, optical to X-rays (Mack et al., 2009; Werner et al., 2012; Isobe et al., 2017). Using full-polarization Atacama Large Millimeter Array (ALMA) observations of the hotspots in 3C 445 radio galaxy Orienti et al. (2017) reported the bright and highly polarized components enshrouded by diffuse unpolarized emission. These results suggest that the hotspots can be a combination of multiple and intermittent compact acceleration sites producing enhanced emission.

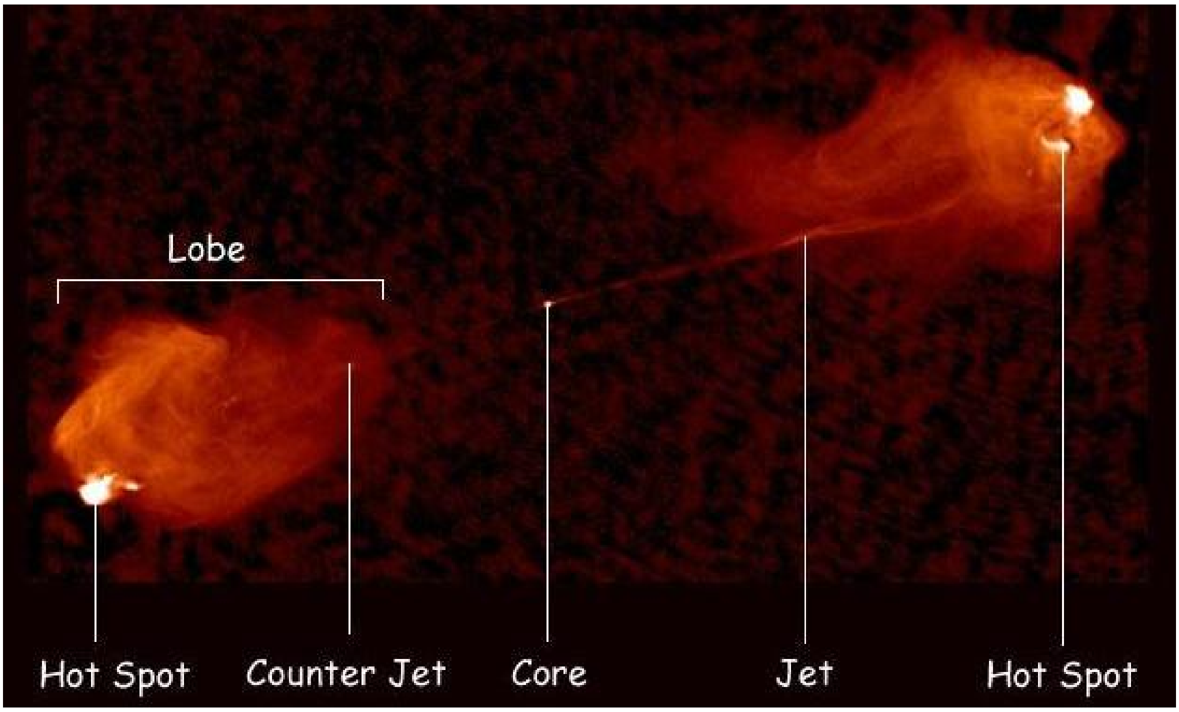

Figure 1.2: Cygnus A radio galaxy imaged at 5 GHz with the Very Large Array. Image credit : NRAO.

1.2.1.4 Lobes

Lobes in radio galaxies are cocoons of plasma fuelled by the outflowing jets (see Figure 1.2). The typical size of lobes in the range of 50 kpc to 100 kpc implies a timescale for their growth spanning from tens to hundreds of millions of years (Blundell & Rawlings, 2000; Mullin et al., 2008). The radio emission from lobes is interpreted as the synchrotron emission produced via relativistic electrons gyrating in the magnetic field. The synchrotron emission resulting a power-law radio spectrum across a wide range of frequencies (nearly 10 MHz to 100 GHz) is the result of power-law energy distribution of energetic electrons (Hardcastle & Looney, 2008). Notably, X-ray emission is also observed from the lobes of radio galaxies and the high energy emission is attributed to the inverse Comptonization (IC) of low energy photons mainly from the cosmic microwave background (CMB) (Kataoka et al., 2003; Isobe et al., 2002, 2005). The total power emitted via synchrotron and IC/CMB can be given by the following equation.

$$P_{rad} = 1.05\times10^{-15}\gamma^2(B^2 + B^2_{\rm CMB})\ \text{erg s}^{-1} \tag{1.1}$$

where $\gamma = (1-(v/c)^2)^{1/2}$ is the Lorentz factor of electrons, B denotes magnetic field in the lobes and $B_{\rm CMB} = 3.25\ (1+z)^2\ \mu$G is the magnetic field equivalent to the energy density of CMB at redshift z (Murgia et al., 1999). The ratio $B/B_{\rm CMB}$ determines the more relevant emission process, *i.e.*, synchrotron or IC/CMB. In nearby sources ($z < 0.5$) with large lobes, $B/B_{\rm CMB}$ ratio is of the order of a few suggesting that radiative losses from both synchrotron as well as IC/CMB processes are important (Massaro & Ajello, 2011). In addition to the radiative cooling, energy losses would also occur if lobes are overpressured *w.r.t.* their ambient medium, and go through adiabatic expansion (Longair et al., 1973). According to the self-similar expansion scenario (Matthews & Scheuer, 1990; Kaiser & Alexander, 1997) adiabatic losses can be more dominant in the initial phase of the lobe evolution.

1.2.2 Life-Cycle of Radio Galaxies

1.2.2.1 From Compact Symmetric Objects to Large Double-Lobed Radio Galaxies

The VLBI observations offering milli-arcsec angular resolution have revealed compact symmetric objects (CSOs) showing two lobes with total end-to-end span of less than a few hundreds of parsecs. The multi-epoch VLBI observations providing measurements of the advancement of hotspots suggest these sources to be young with typical kinematic ages of only a few thousands of years (see Wilkinson et al., 1994; Owsianik & Conway, 1998; Peck & Taylor, 2000). One of the defining characteristic features of compact double-lobes sources is peaked radio spectrum. Based on the frequency at which spectrum peaks ($\nu_{\rm p}$), sources are called high-frequency peakers (HFP) ($\nu_{\rm p}$ > 5 GHz), and giga-hertz peaked spectrum (GPS) sources (0.5 GHz < $\nu_{\rm p}$ < 5 GHz) with their total sizes less than a kpc. The compact steep spectrum (CSS) sources with $\nu_{\rm p}$ < 0.5 GHz have larger radio sizes in range of 1 kpc to 20 kpc. The compact double-lobed radio sources *i.e.*, HFP sources, GPS sources, and CSS are believed to represent the early phase of radio-AGN (O'Dea, 1998; O'Dea & Saikia, 2021). Despite their relatively small radio sizes these sources are powerful radio-loud AGN ($\rm L_{1.4\ GHz} > 10^{25}$ W Hz^{-1}) (Orienti, 2016). However, deep radio observations have also identified a fainter population of compact young radio sources that are believed to possess low-power small-scale jets (Baldi et al., 2015; Hardcastle et al., 2019). Notably, these compact and young radio sources are different than the powerful compact radio sources (FSRQs and blazars) with dominant relativistic beaming from jets closely aligned with the line-of-sight (Readhead et al., 2021). The peaked radio spectra in young radio sources are interpreted in terms of synchrotron self absorption or free-free absorption occurring below $\nu_{\rm p}$, while emission is optically thin with steep spectrum at frequencies above $\nu_{\rm p}$. It is suggested that $\nu_{\rm p}$ is inversely correlated with the total radio size wherein HFP sources evolves into GPS sources and then CSS sources (O'Dea, 1998). The CSS sources eventually evolve into classical radio galaxies as jet-lobe system pierces through the interstellar medium and comes out of the host galaxy (see Figure 1.3). However, a much larger fraction of compact young radio sources than the large-size radio galaxies in a flux-limited sample infers that all compact double-lobed sources do not evolve into radio galaxies possibly due to the confinement of growth of jets in a dense environment of host galaxy or a short-lived radio-AGN activity (see van Breugel et al., 1984; Orienti & Dallacasa, 2021). In a recent study, Nyland et al. (2020) discovered 14 compact (<1 kpc) peaked radio-spectrum sources with strong intrinsic radio variability over decadal timescales. The properties of these sources suggest frequent episodes of short-lived AGN jets that do not grow to large scales. Radio sources with intermittent but powerful jets on subgalactic scales can drive significant feedback which can influence galaxy evolution.

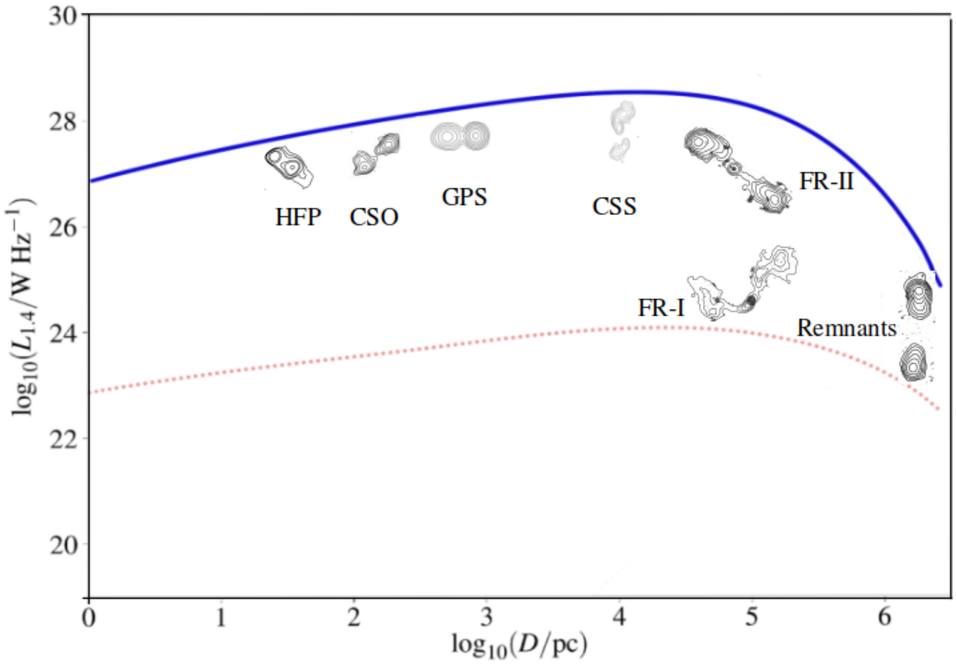

Figure 1.3: A cartoon picture depicting different evolutionary phases of a radio galaxy in the radio luminosity versus radio size plot. The theoretical evolutionary tracks shown by the dotted and solid curves are from Hardcastle et al. (2019) and represent the evolution of sources with low (10^{35} W) and high (10^{39} W) jet kinetic power, respectively. The radio images of different phases (HFP, CSO, CSS, FR I, FR II and remnant) are only for the representative purpose and are not scaled to their relative sizes.

Figure 1.3 shows different evolutionary phases of a radio galaxy in the radio luminosity versus radio size plot. In the early phase of evolution, radio size as well as luminosity keep increasing as source grow, while in the late phase of evolution, radio size continue to increase but radio luminosity begins to decline due to increasing energy losses (radiative cooling occurs over a much larger volume). According to the evolutionary models, young peaked-spectrum radio sources evolve into CSS sources which eventually turn into large-size radio galaxies with sizes of a few hundred kpc (An & Baan, 2012). A small fraction radio galaxies commonly known as giant radio galaxies (GRGs) grow upto the total size of 1 Mpc or even larger (Schoenmakers et al., 2000; Kuźmicz et al., 2018; Dabhade et al., 2020). It is believed that the jet kinetic power, duration of jet flow and the interaction with the ambient medium decide whether a compact radio source will evolve into a large-size radio galaxy. The FR I − FR II morphological division is also linked to jet dynamics such that the jets traversing with relativistic speed upto their termination point lead to the formation of FR II morphology with edge-brightened lobes, while relativistic jets that decelerate on kpc scales give rise FR I morphology (Laing & Bridle, 2002; Tchekhovskoy & Bromberg, 2016).

The study of radio galaxies population is also important due to the feedback mechanisms via which they influence the evolution of galaxies and large-scale structure (see McNamara & Nulsen, 2007, 2012; Fabian, 2012). In the literature, AGN driven outflows (jets and winds) have been routinely incorporated into the galaxy evolution models to explain various observational facts such as the correlations between black hole mass and host galaxy properties (Silk & Rees, 1998; Di Matteo et al., 2005), the relative dearth of high mass galaxies (Benson et al., 2003; Bower et al., 2012), the strong colour bimodality of galaxies (Strateva et al., 2001; Baldry et al., 2004), and the lack of cooling flows in galaxy clusters (Peterson et al., 2003). There are many observational evidence suggesting the energy transfer from jets to their environments via shocks on scales ranging from the parsec to hundreds of kpc. The expanding lobes causing shock fronts on galaxy scales and excavating cavities in galaxy groups, and clusters have been observed in the X-ray observations (*e.g.*, Kraft et al., 2003; Croston et al., 2007; Randall et al., 2015; Irwin et al., 2019). In this thesis, we shall discuss the large-scale environments of remnant radio galaxy candidates which can influence their evolution.

1.2.2.2 Remnant Phase of Radio Galaxies

Remnant phase represents the final stage of the radio galaxy evolution after the cessation of AGN activity. When AGN activity switches off or drops drastically to such a low level that jets are no longer sustained but radio lobes can be detected for a period of time before they completely fade away. Radio galaxies with no active core and jets are called remnant radio galaxies (hereafter remnants). In Figure 1.4 we show two examples of remnants J021659-044920 (Tamhane et al., 2015) and NGC 1534 (Duchesne & Johnston-Hollitt, 2019). In both the sources, only remnant lobes are detected with no apparent emission from the core. Early studies in the literature also used different names such as fading radio sources, dying radio galaxies or relic sources (Parma et al., 2007; Dwarakanath & Kale, 2009). In the remnant phase, radio lobes loose their energy via radiative cooling of relativistic electron with no supply of fresh plasma. The radio spectrum of a remnant source begins to show strong curvature with exponential fall at high frequencies as high energy electrons emitting high-frequency radio emission radiate faster than the low energy electrons emitting at low-frequencies (Murgia et al., 2011). Therefore, low-frequency radio observations are advantageous to detect remnants. In the following section, we discuss previous studies on remnant radio galaxies and their limitations that form the motivation of this thesis.

We note that 'remnant' word is also often used for radio relics and halo associated with cluster of galaxies. To bring clarity and avoid any confusion we show an example of radio relic in Figure 1.5 and radio halo in Figure 1.6. Radio relics are Mpc-scale extended radio sources located in the cluster periphery and show high levels of polarization ($\geq$10 per cent at GHz frequencies), while radio halos are centrally located diffuse radio emitting sources in merging clusters. In both relics as well as halos, radio emission do not belong to any optical counterparts but originate from the acceleration of cosmic rays in the cluster medium (see van Weeren et al., 2019). The sizes of radio relics and halo can range from few hundreds of kpc to a few Mpc. As evident from their example figures, remnant radio galaxies showing old lobes can be easily distinguished from the radio halo and relics based of their radio morphologies.

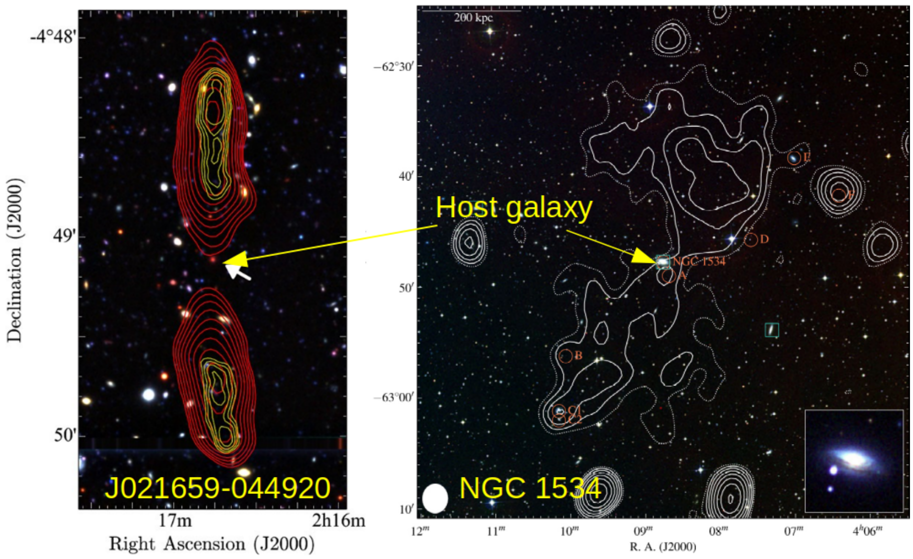

Figure 1.4: Two examples of remnant radio galaxies. *Left panel*: J021659-044920 for which 325 MHz GMRT (in red) and 1.4 GHz VLA (in yellow) radio contours are overlaid on the Subaru optical RGB image. Image credit: Tamhane et al. (2015). *Right panel*: NGC 1534 for which 200 MHz MWA radio contours are overlaid on the Digitized Sky Survey (DSS) optical image. Image credit: Duchesne & Johnston-Hollitt (2019).

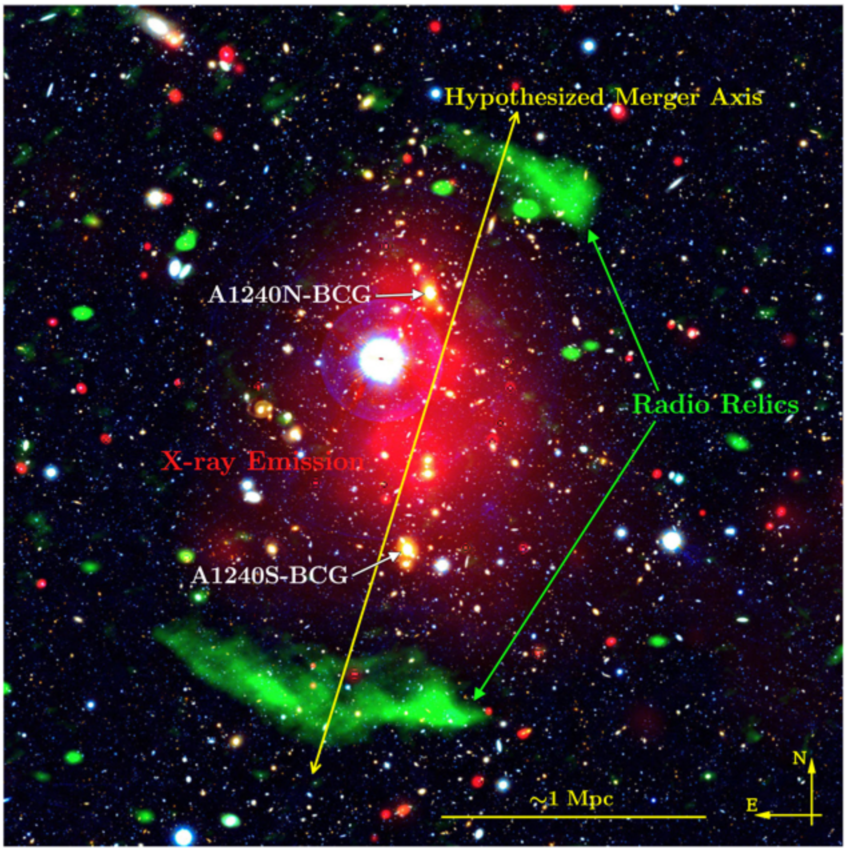

Figure 1.5: Radio (green), optical (RGB), and X-ray (red) composite image of merging cluster A1240. Radio, optical and X-ray observations are from LOFAR, Subaru, and *Chandra*. Radio relics located in the peripheral region are marked. Image credit: Cho et al. (2022).

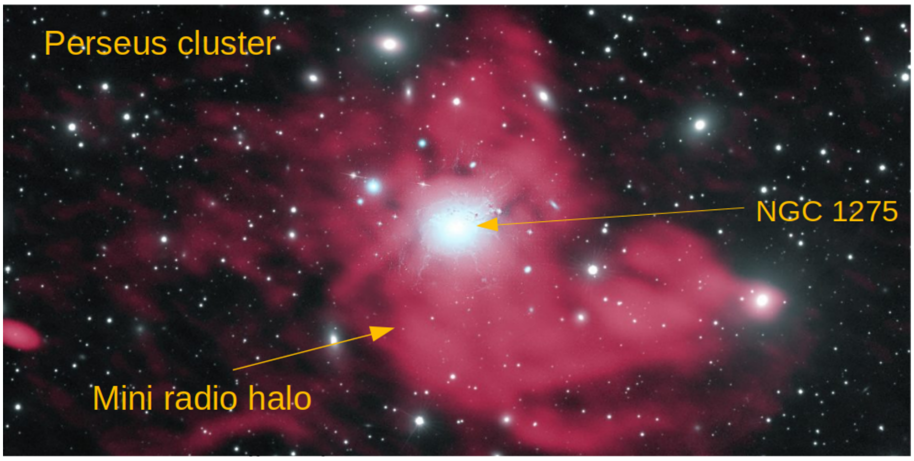

Figure 1.6: The 230−470 MHz JVLA radio image of mini radio halo in the Perseus cluster. The radio emission (in red) in overlaid on the SDSS optical (in white) image. Image credit: Gendron-Marsolais et al. (2017).

1.3 Motivation of the Thesis

The serendipitous discovery of individual remnant radio galaxies, ***e.g.***, B2 0924+30 (Cordey, 1987; Shulevski et al., 2017), J021659-044920 (Tamhane et al., 2015), blob1 (Brienza et al., 2016) and NGC 1534 (Duchesne & Johnston-Hollitt, 2019), WISEA J152228.01+274141.3 (Lal, 2021) etc. and the small samples of remnants derived in deep field surveys (Mahatma et al., 2018; Jurlin et al., 2021), led to the notion of remnants being rare sources. Notably, remnants seem to be even rarer than the double-double radio galaxies (DDRGs) which exhibit two pairs of lobes resulting from the two different episodes of AGN-jet activity (Saikia & Jamrozy, 2009; Nandi & Saikia, 2012; Morganti, 2017). DDRGs show outer pair of lobes from the previous episode of AGN activity (Mahatma et al., 2019; Nandi et al., 2019; Marecki et al., 2021), and can be regarded as a subset of remnants. However, here we consider remnant sources with no apparent episodic AGN-jet activity. The rarity of remnants has conventionally been attributed to the rapid energy losses at work in relic lobes. Albeit, the timescale over which a remnant can be detected varies from source to source and depends on various factors such as the source size, magnetic field in the lobes and the large-scale environment (Turner, 2018). The evolution of radio galaxies in their remnant phase is not well understood due to their paucity.

In recent years, there have been attempts to perform systematic searches for remnants (see Godfrey et al., 2017; Brienza et al., 2017; Mahatma et al., 2018). However, such studies often face limitations imposed by the selection criteria and the flux density limits of radio observations. For instance, using Ultra-Steep Spectrum (USS; $\alpha_{74\ \mathrm{MHz}}^{1.4\ \mathrm{GHz}} <$ -1.2, where S$\nu \propto \nu^{\alpha}$) selection criterion Godfrey et al. (2017) found that only $\leq$2% of their sample sources are remnant candidates. Brienza et al. (2017) argued that the use of a single criterion is likely to miss a fraction of remnants, and both morphological as well as spectral criteria ought to be used for the identification of full remnant population. Mahatma et al. (2018) emphasized that the absence of radio core in deep radio observations can be considered as a reliable selection criterion for remnants, irrespective of their radio morphology and spectral behaviour. The key points on the need for search and characterization of remnant sources using deep radio surveys are listed as below.

- Despite concerted efforts, studies based on the sensitive low-frequency radio observations in deep fields have yielded only small samples limited to a few dozens (see Mahatma et al., 2018; Quici et al., 2021; Jurlin et al., 2021). The remnant searched in the deep fields are also limited to relatively bright sources. For instance, Mahatma et al. (2018) searched remnants in the Herschel−ATLAS field only above 80 mJy at 150 MHz. Considering the importance of statistical studies we aim to search for a new population of remnants, in particular down to the faint flux densities.

- We emphasize that the morphologically identified remnants are inherently biased towards the remnants of more powerful large-size radio galaxies, and are found to be less in number. Hitherto, there has not been any systematic study to search and characterize remnants of small angular sizes ($< 30''$). Albeit, evolutionary models assuming a power-law distribution of jet kinetic powers and source ages predict a much higher fraction of small-size remnants (Shabala et al., 2020). Therefore, it becomes important to perform a systematic search for remnants of small sizes and understand their nature.

- Determining the fraction of remnants ($f_{\rm rem}$) among the population of radio galaxies can help us to constrain the AGN duty cycle and evolutionary models. The remnant fraction depends on the flux density regime at which remnants are probed, and a high flux cutoff limit would be hindrance in unveiling the full population of remnants. Therefore, we aim to constrain $f_{\rm rem}$ in a sample of radio galaxies detected at lower flux densities and higher redshift.

- It has been suggested that the remnants residing in cluster environments can be detected over a much longer timescales due to slow or even arrested expansion of lobes in dense intra−cluster medium (ICM), and hence, one can expect a higher tendency of remnants to reside in cluster environments (see Murgia et al., 2011). Therefore, we aim to investigate the large−scale environments of our remnant candidates.

- The timescale over which a remnant can be detected can vary from source to source, and it can depend on various factors such as the source size, magnetic field in the lobes and the large-scale environment. We estimate active and remnant phase timescales and investigate their dependence on various source parameters and the large-scale environment.

1.4 Thesis Outline

Here, we give a brief mention of the work presented in the next chapters.

- Chapter 2 provides a brief overview of the basic principles of radio interferometric techniques, data reduction and analysis. The radio data reduction section discusses various steps that include data editing, calibration, and imaging algorithms. This thesis work is based on observations carried out with the GMRT, upgraded GMRT, LOFAR and VLA, hence, we provide a brief details of the system parameters of these telescopes. We attempt to highlight the advantages of multi-frequency radio surveys in deep fields.

- Chapter 3 presents our work on the search and characterization of remnant radio galaxy candidates in the XMM−LSS deep field using radio observations at 150 MHz LOFAR, 325 MHz GMRT, 1.4 GHz JVLA and 3 GHz VLASS. We discuss morphological as well as spectral criteria that are used to identify remnants. The characterization of our remnant candidates in terms of physical properties such as surface brightness, core prominence, redshifts, radio power and their large-scale environments is also presented. At the end, we discuss the importance and implication of remnant fraction.

- Chapter 4 is devoted to search and characterise of remnant candidates of small angular sizes ($< 30''$). This chapter highlights the prevalent bias towards large-size remnants and emphasizes the need for a systematic search for small-size remnants. Our study presents the first systematic search of small-size remnants and identify, hitherto, the largest sample of 48 remnant candidates. This chapter also presents the analysis of characteristics properties such as spectral index, redshifts, large-scale environments of our remnant candidates.

- Chapter 5 presents the spectral ageing analysis of a sub-sample of our five remnant candidates. The spectral ageing analysis is limited to those sources that have band-3 uGMRT observations and measurements of redshift and size. Using 150 MHz LOFAR, 325 MHz GMRT, 400 MHz uGMRT and 1.5 GHz JVLA radio observations we model the radio SEDs with the continuous injection off (CI_{OFF}) model and obtain source ages, timescales of active and remnant phases. Further, we present a comparison of spectral ages of our sample sources and the remnant sources already studied in the literature. This chapter also presents a discussion the role of various factors such as redshift, magnetic field and large-scale environment that can influence the evolution of remnants.

- Chapter 6 summarizes the work presented in this thesis. we attempt to highlight the importance of discovering a new remnant population including a large sample of small-size sources. The importance and implication of our thesis work in the context of our current understanding on remnant sources is also mentioned. At the end, we propose a future research work that has emerged from the thesis work.

Chapter 2

Radio Observations and Data Reduction

2.1 Introduction

Sensitive multi-frequency radio observations are key to identify remnant radio sources. Deep low-frequency (<1 GHz) radio observations are crucial to detect diffuse low-surface-brightness emission from relic lobes. In this thesis, we used radio observations taken at various frequencies, ***e.g.***, 150 MHz, 325 MHz and 1.4 GHz. Hence, we describe basic observational techniques and data reduction methods that are employed to obtain radio continuum images. Further, we provide the details of radio interferometric arrays from which observations are acquired.

2.2 Radio Interferometric Techniques

Radio interferometry is a powerful technique which provides a high resolution (∼a few arcsec to even micro-arcsec) imaging. We discuss the basic principles of radio interferometric synthesis imaging in the following section. These details can be found in a standard text book of radio interferometry (***e.g.***, Thompson et al., 2017). Although, for sake of completeness we give a brief overview of the synthesis imaging and data reduction procedure.

2.2.1 Aperture Synthesis

The Rayleigh criterion describes the angular resolution of a telescope, ***i.e.***, $\theta = \lambda/\mathrm{D}$, where θ is the angular resolution, λ is the observing wavelength and D is the measure of aperture size. To achieve an angular resolution of around $1''$ at radio wavelengths, similar to the optical telescopes, we require $\sim 10^4 - 10^7$ times larger radio telescope than an optical telescope. This is simply due to the fact that radio wavelength is $\sim 10^4 - 10^7$ larger than optical wavelengths. For instance, a 60 km diameter radio telescope is needed to achieve $1''$ resolution at 1 GHz, and building such a large telescope is impossible due to structural limits in constructing large dish antennas. However, a large aperture can be synthesized from individual smaller telescopes using radio interferometric technique. In this case, a radio source is observed using several radio antennas simultaneously and signal from one antenna is combined with other antennas to provide the estimate of the intensity.

The simplest radio interferometer is a pair of radio telescopes *i.e.*, two-element interferometer where an antenna is called an element of interferometer. Figure 2.1 shows a schematic diagram of a two-element interferometer in which each antenna receives incoming plane parallel electromagnetic waves from a distant source. The receiver system placed at the focus of each parabolic dish detects only a very narrow radio frequency range centered on $\nu = \omega/(2pi)$ and voltage outputs from two receivers are correlated (multiplied and averaged). The output voltage V1 of antenna 1 is the same as the output voltage V2 of antenna 2, but signal at antenna 1 is delayed by $\tau_{\mathrm{g}} = \overrightarrow{b}.\hat{s}/c$, where $\overrightarrow{b}$ is the baseline vector pointing from antenna 1 to antenna 2, $\hat{s}$ is the unit vector along the source direction and c is the speed of light. Since radio electromagnetic wave travels an extra path length to reach to antenna 1, voltage is corrected for the corresponding time delay. The voltages from both the antennas are amplified, multiplied, and time averaged by the correlator. Therefore, correlator output (measured in terms visibilities) is a response such that its amplitude is proportional to the flux density of radio source and phase $\omega\tau_{\mathrm{g}}$ depends on the delay and the frequency. The quasi-sinusoidal fringe shown in Figure 2.1 represents the output of correlator when the source direction is changing at a constant rate.

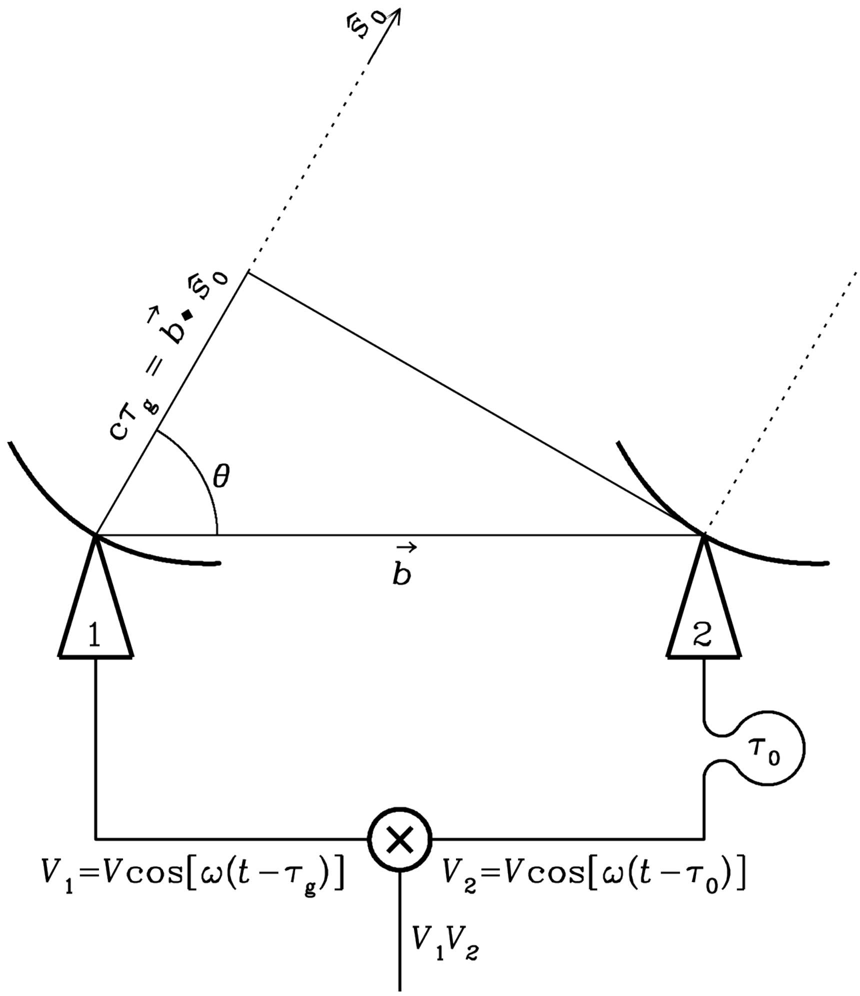

Figure 2.1: A schematic diagram of two-element interferometer. Credit: NRAO.

2.2.2 Principle of Radio Interferometry

The fundamental relationship between source intensity distribution and spatial coherence function is given by van Cittert−Zernike theorem which states that the spatial coherence function is the Fourier transform of the source intensity distribution. Considering $I_\nu(l,m)$ represents the distribution of source intensity, where l and m are the direction cosines with respect to the phase tracking center and ν is the observing frequency, the spatial coherence function can be given as

$$V_\nu(u,v) = \int_{-\infty}^{+\infty}\int_{-\infty}^{+\infty} I_\nu(l,m)e^{-2\pi i(ul+vm)}dldm \tag{2.1}$$

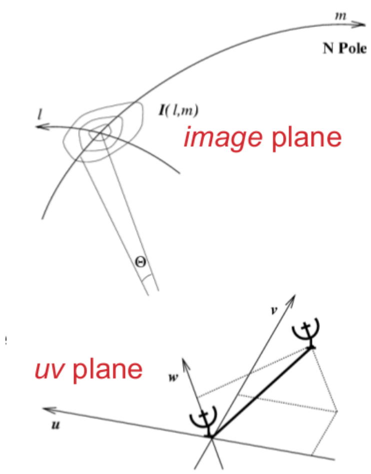

Figure 2.2: Schematic diagram of two-element interferometry where source is shown in the image plane (Fourier plane of uv plane). The direction cosines (l and m) are shown in the diagram.

The intensity distribution of the source, $I_\nu(l,m)$, can be estimated by inverse Fourier transform of the spatial coherence function. One can measure a single (u,v) component of the Fourier plane of $I_\nu(l,m)$ using a two-element radio interferometer. To sample entire Fourier plane (or uv plane), many such two-element interferometers are used in a radio interferometric array.

$$I_\nu(l,m) = \int_{-\infty}^{+\infty}\int_{-\infty}^{+\infty} V_\nu(u,v)e^{2\pi i(ul+vm)}dudv \tag{2.2}$$

The spatial coherence function is also referred as visibility function, denoted by $V_{\rm ij}$, where i and j represents the $i^{\rm th}$ and $j^{\rm th}$ antenna of an array. $V_{\rm ij}$ is the value of spatial coherence function at a location given by the separation between $i^{\rm th}$ and $j^{\rm th}$ antennas (also called baseline). In a radio interferometric array, signal from one antenna is cross-correlated with the signal from another antennas and one antenna pair gives one value of visibility function. An ensemble of complex visibilities obtained from antenna pairs ($e.g.$, N-element array forms $N(N$-1$)/2$ antenna pairs) sample the visibility function. Since the visibilities are sampled at discrete times for each antenna pair, one can write equation 2.1 as

$$V_{ij}(t) = \int_{-\infty}^{+\infty} \int_{-\infty}^{+\infty} I_\nu(l,m) e^{-2\pi i (u_{ij}(t) l + v_{ij}(t) m)} dl dm \qquad (2.3)$$

Therefore, visibility is a function of a baseline at a given frequency and time.

2.3 Radio Data Reduction

Here, we provide a theoretical formalism of various steps (*i.e.*, flux and phase calibration, deconvolution and self-calibration) of radio data reduction.

2.3.1 Calibration

In general, the observed visibilities deviate from the true visibilities due to various reasons. For example, phase distortion during the signal processing and phase irregularities in the incoming radio wavefront caused by density fluctuations in the ionosphere. In principle, relationship between true visibility (V_{true}) and observed visibility (V_{obs}) can be arbitrary, although within good approximation (*e.g.*, output of electronic devices is almost a linear function of input, response of one antenna pair is independent of other antenna pair) observed visibilities can be considered as a linear function of true visibilities. To get the true visibilities, correction coefficients are required and this process is known as calibration. The basic calibration formula can be expressed as

$$V_{ij}^{obs}(t) = G_{ij}(t) V_{ij}^{true}(t) + \varepsilon_{ij}(t) + \eta_{ij}(t) \qquad (2.4)$$

where, G_{ij} is baseline-based complex gain, $\varepsilon_{\mathrm{ij}}$ is baseline-based complex offset, η_{ij} is a stochastic complex noise and t is the time of the observation. In most of the cases, data corruption occurs before signals from two antennas are cross-correlated so the baseline-based complex gain G_{ij} can be approximated as the product of the antenna-based complex gains g_{i}(t) and g_{j}(t) and one can write

$$G_{ij}(t) = g_i(t)g_j^*(t) = a_i(t)a_j(t)e^{i(\phi_i(t)-\phi_j(t))} \tag{2.5}$$

where, a_{i} is antenna-based amplitude correction and ϕ_{i} is antenna-based phase correction. Antenna-based calibration values are preferred over baseline-based ones since most variations in the instrument are related to particular antennas, either arising from the medium above the antenna or in the electronic components. The errors, in this case, are usually smaller due to a well-designed correlator. The details of the calibration methods can be found in Fomalont & Perley (1999). As indicated from Equation 2.5, calibration procedure includes amplitude (flux) and phase corrections, described below.

2.3.1.1 Flux Calibration

Flux calibration is performed by observing a standard point radio source with known non-variable flux density. The flux calibrators must be a point radio source (angular size less than the resolution element) with accurately known position and spectrum. The flux calibrators are chosen to be strong unresolved radio sources so that they allow calibration in short time-scale. For the flux calibrator, the true visibilities are well known and the observed visibilities can be obtained by observing it at the beginning and end of the observing session. In this way, we determine calibration gain terms given in Equation 2.4. If flux density of the calibrator source is S then the amplitude of true visibility would be S, and the complex gains can be expressed as

$$G_{ij}(t) = V_{ij}^{obs}(t)/S \tag{2.6}$$

The baseline-based offset term, ε_{ij} in Equation 2.4, is usually insignificant unless noticeable cross-talk occurs between different antenna channels or correlator malfunctions. After proper averaging of the data in a scan, stochastic noise term, η_{ij}, is also assumed to be insignificant.

2.3.1.2 Phase Calibration

Along with flux calibration, phase calibration is also necessary to determine complex gains. The phase calibrator should be close to the target (within ∼10 degrees) and is usually observed more often in a scan. In general, a phase calibrator is observed within every 5−30 minutes depending upon the band, configuration and atmospheric attenuations. The fluctuations in phase are caused by the ionosphere as well as troposphere. The troposphere effects are more prominent at frequencies $\geq$ 20 GHz, where oxygen and water vapor absorb or emit. Moreover, the ionosphere introduces a dispersive phase variation, directly proportional to λ^2 and hence ionospheric effects are more dominant at longer wavelengths. In addition, ionosphere becomes more variable and active at sunrise and sunset, and during solar cycle maxima.

2.3.1.3 Bandpass Calibration

In case of spectral and continuum mode observations, bandpass calibration is also performed along with flux and phase calibrations. The objective of bandpass calibration is to correct for complex gain fluctuations as a function of frequency across the bandwidth of receiver. The relative frequency response can be estimated in all the channels by observing a strong calibrator source having a flat spectrum across the frequency bandwidth. Considering $G_{\mathrm{ij}}(\nu)$ as the baseline-based complex gain, we can estimate the variations in antenna gain with frequency. The frequency and baseline dependent bandpass gain can be expressed as the product of antenna-based gains and can be converted into antenna-based bandpass amplitude and phase calibrations.

2.3.2 Data Editing

In radio observations, signal from an astrophysical source can be corrupted by radio frequency interference (RFI) from a variety of terrestrial sources emitting at radio frequencies such as broadcasting radio and TV signals, cell phones, communication and navigation satellites, and wireless control and monitoring systems. Therefore, it is essential to discard the corrupted data. The procedure of identifying and discarding the discrepant data is called 'flagging' or data editing. Calibration and editing of the data are performed iteratively in the reduction process.

2.3.3 Self-Calibration

As discussed earlier, initial calibration solves for the complex gains by observing a standard calibrator, however, it is constrained by some factors because complex gains are derived for different directions and time (*i.e.*, troposphere and ionosphere are non-uniform and vary). In the process of self-calibration, the target source itself is used as a calibrator source to calibrate the antenna-based complex gains as a function of time. If all the baselines are correlated in an N-element interferometric array, N complex gain errors occur which corrupt $\frac{1}{2}N(N-1)$ visibilities at a given time. Therefore, $\frac{1}{2}N(N-1)-N$ complex numbers are available and can be used to constrain the true source brightness distribution. Self-calibration uses the phase closure of three antennas, *i.e.*, triangle of the baselines, and the errors for individual antenna vanish in summing the visibility phases around the triangle. Similarly, the closure amplitude around four antennas *i.e.*, rectangle of the baselines, is used to mitigate errors in theoretical flux calibration. Therefore, there are $\frac{1}{2}N(N-1)-N$ constraints on the amplitude and $\frac{1}{2}N(N-1)-(N-1)$ constraints on the phase in an N-element interferometric array. For large N, self-calibration involves following iterative procedure : (i) first, a source brightness distribution model is assumed, where the model is usually derived from the initial image or a point radio source; (ii) antenna gains are then solved using above approximated model and closure constraints; and (iii) finally, the corrected complex gains are applied to the visibility data and the corrected data are used as new source model in the next iteration of self-calibration. To obtain components providing a new source model for the next iteration, `CLEAN` (iterative deconvolution) algorithm (Högbom, 1974) is applied.

2.3.4 Deconvolution and Imaging

As discussed in Section 2.2.2, source brightness distribution is simply the inverse Fourier transform of the complex visibility function (see Eqn 2.1). However, in a realistic scenario, the visibility function, $V_\nu(u,v)$, is sampled at discrete places in the u−v plane. The sampling function, $S_\nu(u,v)$, is chosen such that it has a value '1' wherever data is present and '0' elsewhere. Thus, an observer gets a dirty image which can expressed with the following equation.

$$I_\nu^D(l,m) = \int_{-\infty}^{+\infty}\int_{-\infty}^{+\infty} V_\nu(u,v)S_\nu(u,v)e^{2\pi i(ul+vm)}dudv \tag{2.7}$$

where $I_\nu^D(l,m)$ is called dirty map or dirty image. It is related to the true source brightness distribution by

$$I_\nu^D = I_\nu \star DB \tag{2.8}$$

where star ($\star$) represents the convolution and dirty beam (DB) is the inverse Fourier transform of the sampling function $S_\nu(u,v)$. The dirty beam is point spread function (PSF) of the synthesized array associated with sampling function.

The convolution of dirty beam and true brightness distribution gives the source brightness distribution which is estimated by taking inverse Fourier transform of the sampled spatial coherence function. Therefore, deconvolution of dirty beam with the observed brightness distribution is required to obtain the true brightness distribution. There are two deconvolution algorithms namely `CLEAN` (Högbom, 1974)) and Maximum Entropy Method (`MEM`; Cornwell & Evans, 1985; Narayan & Nityananda, 1986) that are often used in the aperture synthesis imaging. The `CLEAN` algorithm iteratively deconvolves the dirty beam from the dirty map (observed brightness distribution). While, `MEM` uses dirty image and minimizes its entropy (a smoothness function).

2.4 Radio Interferometric Arrays

In this section, we provide a brief overview of some of the radio interferometric arrays allowing us to image radio sky using aperture synthesis principles. We cover the details of those radio telescopes from which data are used for this thesis.

2.4.1 Giant Metrewave Radio Telescope and its Upgraded Version

The Giant Metrewave Radio Telescope (GMRT; Swarup, 1991) is an interferometric array consists of 30 fully steerable parabolic dishes each of 45m diameter. This telescope is located at a site about 80 km north of Pune, India. Fourteen of the thirty dishes are placed in a region of about one square kilometer called central square array. While, remaining sixteen dishes are spread out along the three arms of an approximately 'Y'-shaped configuration over a much larger region, with the longest baseline of about 25 km. The GMRT has been operating mainly in five frequency bands centred at 150 MHz, 235 MHz, 325 MHz, 610 MHz and 1420 MHz. All these feeds provide dual polarization outputs. More details can be found at the GMRT website[1]. Some of the key system parameters of GMRT are given in Table 2.1.

Recently, GMRT has gone through a major upgrade which has increased its sensitivity by upto three times and has made it a more powerful telescope. Unlike legacy GMRT, the upgraded GMRT (uGMRT; Gupta et al., 2017) provides nearly a seamless frequency coverage from 125 MHz to 1460 MHz. The uGMRT offers a maximum instantaneous bandwidth of 400 MHz, instead of 32 MHz bandwidth of the original GMRT design. The feeds and front-end electronics were also improved to realise the wide bandwidths of uGMRT. The resultant wide bands are 50−80 MHz (band-1), 120−250 MHz (band-2), 250−500 MHz (band-3), 550−850 MHz (band-4), and 1050−1450 MHz (band-5). The system parameters of uGMRT are given in Table 2.1.

[1]http://www.ncra.tifr.res.in/ncra/gmrt

Table 2.1: The GMRT and uGMRT system parameters.

Band	Bandwidth (MHz)	RMS-Noise† (μJy/beam)	Primary Beam‡ ($'$)	Synthesized Beam‡ ($''$)
GMRT				
150 MHz	150−156	700	186	20
235 MHz	236−244	250	114	13
325 MHz	305−345	40	81	9
610 MHz	580−640	20	43	5
1400 MHz	1000−1450	10	24	2
uGMRT				
Band-2	125−250	500	120	17.3
Band-3	250−500	15	75	8.3
Band-4	550−850	6	38	4.3
Band-5	1000−1460	2.5	23	2.3

Notes - The quoted system parameters are taken from the GMRT user manual[2].

†: The RMS noise values are the best values known to us in the continuum mode.

‡: The values for primary and synthesised beams are at the centre frequency of the band.

2.4.2 Low-Frequency Array

The LOw-Frequency ARray (LOFAR; van Haarlem et al., 2013) is a radio interferometer operating in the frequency range of 30 MHz to 240 MHz. The LOFAR consists of dipole antenna stations with 24 core stations located in north Netherlands, 14 remote stations distributed across the Netherlands and 14 international stations distributed across central to north-western Europe. The LOFAR utilises two types of antennas *viz.*, Low Band Antennas (LBAs) designed to operate in 30−80 MHz band, and High Band Antenna (HBA) working in 110-240 MHz frequency range. Both LBA and HBA are phased array dipole antennas coupled with the digital beam-forming techniques. With baselines ranging from a few tens of meters to over one thousand kilometers, LOFAR provides a wide range of angular resolutions from 0.5° to sub-arcsecond scales. Also, owing to its large collecting area (*e.g.*, a phased array of around 20,000 HBA dipole antennas offers a collecting area of $\sim$1 km^2) LOFAR allows us to achieve the noise-rms of nearly 100 μJy in the 110-240 MHz frequency band for a typical eight-hour observation (Williams et al., 2016). The high sensitivity and sub-arcsec resolution make LOFAR the best telescope currently operating at low-frequencies ($<$ 240 MHz). More details about the LOFAR can be found at its website[3].

2.4.3 Very Large Array

The Very Large Array (VLA) is a radio interferometer, located in New Mexico USA, consisting of 27 antennas each with 25m diameter (Thompson et al., 1980). The 27 antennas are positioned in a configuration forming three equiangular arms with nine antennas per arm. The VLA is used in four different standard configurations namely 'A', 'B', 'C' and 'D' with maximum baseline lengths of 36 km, 11 km, 3.4 km and 1 km, respectively, by changing the positions of antennas placed on a railway track. The different array configurations allow observers to obtain a wide range angular resolutions and image surface brightness sensitivities. For instance, most compact 'D' array offers a low angular resolu-

[3] https://www.astron.nl/telescopes/lofar/

tion of 45$''$ at 1.4 GHz, while 'A' configuration with the longest baselines gives an angular resolution of $1''.3$ at the same frequency. During 2001 to 2012, VLA went through a major upgrade by changing conventional narrow-band receivers to the high-speed wide-band receivers. The upgraded VLA, also called as Jansky VLA or JVLA, offers a seamless frequency coverage from 1.0 GHz to 50 GHz divided into eight bands ***i.e.***, 1.0 GHz−2.0 GHz (L band), 2.0 GHz−4.0 GHz (S band), 4.0 GHz−8.0 GHz (C band), 8.0 GHz−12 GHz (X band), 12 GHz−18 GHz (Ku band), 18 GHz−26.5 GHz (K band), 26.5 GHz−40 GHz (Ka band), and 40 GHz−50 GHz (Q band) (see Perley et al., 2011). The JVLA provides sensitive radio continuum images with a typical noise-rms of a few μJy using just one hour observing time. More details about the JVLA can be found in the National Radio Astronomical Observatory (NRAO) website[4].

In addition to the aforementioned three radio interferometers it would be worth mentioning more recently commissioned MeerKAT and Australian SKA Pathfinder (ASKAP) radio telescopes. The MeerKAT, a radio interferometric array located in South Africa, consists of 64 dish antenna each with 13.5m diameter. Notably, dish antennas in the MeerKAT are designed with offset Gregorian optics providing an unblocked aperture. To detect the radio emission at various angular scales specially large-scale diffuse radio emission, MeerKAT antennas are placed in a configuration having 75 per cent antennas within a core region of 1 km diameter, and the remaining antennas sparsely distributed around the core giving a maximum baseline of 8 km (Jonas & MeerKAT Team, 2016). This telescope can operate in the 544 MHz − 1088 MHz (UHF), 856 MHz − 1712 MHz (L band), and 1750 MHz − 3500 MHz (S band) frequency regimes.
The ASKAP, a radio interferometer consisting of 36 dish antennas each with 12m diameter, is located in the Murchison Radio-astronomy Observatory in Western Australia. The antenna are distributed in an area providing maximum baseline of 6.0 km (Hotan et al., 2021). Each antenna is equipped with a phased array feed (PAF) wherein Each PAF comprises 188 individual receiving elements enabling a large field-of-view (FoV) of nearly 30 degrees. The large FoV of ASKAP makes it a very useful telescope to perform rapid large-area surveys in the frequency band of 700 and 1800 MHz.

[4]https://public.nrao.edu/telescopes/vla/

2.5 Low-Frequency Radio Surveys in Deep Fields

Radio observations trace the synchrotron radio emission from star-forming galaxies (SFGs) and AGN across a wide range of frequency ***i.e.***, 30 MHz to 10 GHz (Condon, 1992). Radio-loud AGN are the most dominant population at higher flux densities, while radio-quiet AGN and SFGs begin to dominate the source population at the faint flux densities below 1.0 mJy (Ibar et al., 2009; Bonzini et al., 2013). Sky surveys at various wavelengths including radio wavelength are often performed in the Tiered fashion (smaller area with higher depths) considering the limited telescope time allocated for the survey and desire to obtain sensitive as well as large-area observations. In other words, there is a trade-off between sky-area coverage and depth. In general, large-area surveys are shallower due to less time spent on per pointing than the small-area surveys. Both large-area shallow survey and small-area deep survey complement each other. For instance, bright radio sources with low surface density (let say giant radio galaxies) require a large area to be observed, while studies aiming to understand the cosmological evolution of SFGs and various sub-populations of AGN require deep surveys enabling us to detect sources upto higher redshifts.

In recent times, there have been attempts to perform large-area radio surveys at various frequencies using different telescopes, for instance, 150 MHz TIFR-GMRT Sky Survey (TGSS; Intema et al., 2017) with the GMRT, Galactic and Extragalactic All-sky Murchison Widefield Array survey (GLEAM; Hurley-Walker et al., 2017) in 72 MHz − 231 MHz band with the MWA; 150 MHz LOFAR Two-metre Sky Survey (LoTSS; Shimwell et al., 2017) with the LOFAR, Evolutionary Map of the Universe (EMU; Norris et al., 2021) survey at 944 MHz as well as Rapid ASKAP Continuum Survey (RACS; McConnell et al., 2020; Hale et al., 2021) at 887.5 MHz with the ASKAP, and 3.0 Very Large Array Sky Survey (VLASS; Lacy et al., 2020) with the VLA. All these large-area surveys essentially cover (nearly a few 10000 deg^2) the entire sky visible to their respective telescopes. To achieve higher depths, there have also been deeper radio surveys of carefully chosen well defined sky regions called deep fields. These fields, ***e.g.***, *XMM-Newton* Large Scale Structure field (XMM-LSS), European Large Area ISO Survey north and south (ELAIS S1 and ELAIS N1); *Chandra* Deep Field South (CDFS), Hubble Deep

Field (HDF), Lockman Hole and COSMOS deep field, cover a sky-area in the range of a few square degrees to a few tens of square degrees, and are surveyed at multiwavelengths ranging from radio to X-rays (*e.g.*, Hughes et al., 1998; Alexander et al., 2003; Ishwara-Chandra et al., 2020; Heywood et al., 2022). One of the key science drivers of deep field surveys is to understand the evolution of AGN and SFGs across cosmic epochs. To search and characterize remnant source population we choose the XMM-LSS field owing to the availability of deep multi-frequency radio surveys ranging from 150 MHz to 3.0 GHz as well as deep multiwavelength ancillary data. The deep low-frequency radio observations are advantageous to detect remnant sources often showing steep radio spectra. The details of radio observations available in the XMM-LSS are given in the relevant sections of chapter 3, chapter 4 and chapter 5.

Chapter 3

Search and Characterization of Remnant Radio Galaxies in the XMM-LSS Deep Field

3.1 Introduction

It is well known that the AGN jet activity in galaxies is only a phase (active phase) lasting for several tens of Myr during which the radio size can grow upto a few hundred kpc and rarely, upto even a few Mpc (Parma et al., 2007; Machalski et al., 2008). After an active phase, AGN activity ceases or drops below a certain threshold level so that the outflowing jets are no longer supported and the radio lobes begin to fade away (Parma et al., 1999). During the fading period termed as the 'remnant phase' or 'dying phase', the radio core and jets supposedly disappear but the radio lobes can still be detected for a period of a few tens of million years before they disappear due to radiative and dynamical losses (Slee et al., 2001; Murgia et al., 2011). The duration of remnant phase is arguably a small fraction of the duration of active phase, hence remnant sources are believed to represent a short−lived final phase of the radio galaxy's evolution (Morganti, 2017). Remnant radio galaxies (hereafter 'remnants') are deemed to be less abundant owing to the relatively short duration of the remnant phase. Due to their relative paucity remnants are poorly understood. Specifically, AGN duty cycle and its dependence on various factors such as the jet kinetic power, host galaxy, and large−scale cluster environment are still a matter of investigation.

To understand the characteristics of remnants there have been attempts to carry out systematic searches for them by exploiting mainly low−frequency (<1.4 GHz) radio surveys (*e.g.*, Parma et al., 2007; Murgia et al., 2011; Godfrey et al., 2017; Brienza et al., 2017; Mahatma et al., 2018; Quici et al., 2021). Low−frequency radio surveys are advantageous to search for remnants owing to the steepening of radio spectrum of relic plasma in radio lobes. In fact, samples of USS radio sources have been used to identify potential remnant candidates. For instance, Godfrey et al. (2017) utilised shallow but wide−area 74 MHz VLA Low−frequency Sky Survey Redux (VLSSr, Lane et al. (2014)) in combination with the 1.4 GHz Faint Images of the Radio Sky at Twenty−Centimeters survey (FIRST; Becker et al. (1995)) and the NRAO VLA Sky Survey (NVSS; Condon et al. (1998)) survey, and reported that fewer than 2% of Fanaroff−Riley type II (FR II) radio galaxies with $S_{74\ \mathrm{MHz}}$ >1.5 Jy are candidate USS remnants ($\alpha_{74\ \mathrm{MHz}}^{1400\ \mathrm{MHz}}$ < -1.2, $S_{\nu} \propto \nu^{\alpha}$). The lobes of low-surface-brightness emission detected in the serendipitously discovered individual remnants *e.g.*, B2 0924+30 (Cordey, 1987; Jamrozy et al., 2004; Shulevski et al., 2017), J1324-3138 (Venturi et al., 1998), blob1 (Brienza et al., 2016), NGC 1534 (Duchesne & Johnston-Hollitt, 2019), emphasizes the need of deep low-frequency observations. The shallow radio surveys of previous generations are likely to miss a significant population of remnants possessing diffuse low−surface−brightness emission. Keeping this in view, sensitive low−frequency radio surveys have been carried out in deep extragalactic fields to search for and obtain large samples of remnants.

For instance, using 150 MHz LOw Frequency ARray (LOFAR; van Haarlem et al. (2013)) observations in the Lockman Hole field Brienza et al. (2017) identified 23 remnant candidates in a sample of 158 sources detected above a flux density cutoff limit of 40 mJy and radio size $\geq$40$''$ at 150 MHz. In a follow up study Jurlin et al. (2021) performed deep (noise−rms $\sim$ 9−10 μJy beam^{-1}) JVLA A−configuration observations of the remnant candidates reported in the Lockman Hole field, and identified only 13/23 candidates as genuine remnants. In a similar study Mahatma et al. (2018) reported remnants in the Herschel−ATLAS field using 150 MHz LOFAR and 6.0 GHz JVLA observations and found only 11 remnants in a sample of 127 sources with a flux density cutoff limit ($S_{150\ \mathrm{MHz}}$) $\geq$80 mJy and radio size $\geq$40$''$. The cutoff limits on the flux density and radio size were placed to examine morphological structures, attain completeness above a flux limit, and to find USS sources using the 1.4 GHz NVSS, a relatively shallow survey.

It is important to note that the aforementioned studies have demonstrated the potential of the combination of deep low−frequency and deep high−frequency observations to identify remnants. However, a high flux density cutoff limit hinders the identification of remnants and their nature at lower flux densities. Also, a high flux density cutoff limit is likely to result in a smaller sample that can be biased towards the remnants of powerful radio galaxies. Considering the limitations introduced by the high flux density cutoff limit we attempt to search and characterize remnants down to a fainter flux density limit *i.e.*, 6.0 mJy at 325 MHz that corresponds to 10.3 mJy at 150 MHz, assuming a typical spectral index of -0.7. The expectation is that a search for remnants over a wide range of flux densities reaching down to faint levels would allow us to obtain a larger sample, a more robust determination of remnant fraction, and its dependence on the flux density and luminosity. Also, a larger sample would enable us to use a more robust statistical approach in constraining the evolutionary models of remnant phase. In this work, we attempt to carry out a systematic search for remnants in the *XMM−Newton* Large−Scale Structure (XMM−LSS) field by using sensitive 325 MHz Giant Meterwave Radio Telescope (GMRT) radio observations ($5\sigma \sim 0.75$ mJy beam^{-1}) and existing ancillary multi−frequency radio data. We note that our study deals with only remnants and excludes active sources with any apparent episodic or intermittent AGN activity.

This chapter is organized as follows. In Section 3.2, we provide the details of multi−frequency radio data and optical data available in the XMM−LSS field. Section 3.3 describes the selection criteria adopted to identify remnant candidates. In Section 3.4, we discuss various characteristic properties of remnant candidates and their comparison to active sources. In Section 3.5, we determine remnant fraction and discuss its dependence on the flux density. In Section 3.6, we list the conclusions.
In this study we use the cosmological parameters $H_0 = 70$ km s^{-1} Mpc^{-1}, $\Omega_m = 0.3$, and $\Omega_\Lambda = 0.7$.

3.2 Radio Observations and Auxiliary Surveys in the XMM-LSS

The XMM−LSS field has been observed across nearly the entire electromagnetic spectrum spanning over radio (Tasse et al., 2007; Hale et al., 2019; Heywood et al., 2020), near−IR (Jarvis et al., 2013), mid−IR (Lonsdale et al., 2003; Mauduit et al., 2012), far−IR (Oliver et al., 2012), optical (Erben et al., 2013; Aihara et al., 2018), to X−ray (Pierre et al., 2004; Chen et al., 2018), including optical spectroscopic data (Le Fèvre et al., 2013, 2015; Davies et al., 2018; Scodeggio et al., 2018). To search for remnants, we exploit deep low−frequency 325 MHz GMRT observations in combination with mainly 150 MHz LOFAR and 1.4 GHz JVLA observations. Table 3.1 lists the basic parameters of these deep field radio observations. Figure 3.1 shows the footprints of 325 MHz GMRT, 150 MHz LOFAR and 1.4 GHz JVLA observations. We note that the coverage of 1.4 GHz JVLA observations (5.0 deg^2) is much smaller than that of 325 MHz GMRT observations (12.5 deg^2) (see Figure 3.1). Hence, outside the JVLA region, we use relatively less sensitive 3.0 GHz Very Large Array Sky Survey (VLASS; Lacy et al. (2020)) data, whenever high resolution images are required. To account for the impact of differing sensitivities of high−frequency (≥1.4 GHz) observations we divide 12.5 deg^2 area of 325 MHz GMRT into two sub−regions : (i) 5.0 deg^2 area covered by the JVLA observations named as the XMM−LSS−JVLA, and (ii) 7.5 deg^2 area outside the JVLA observations named as the XMM−LSS−Out. In the following sub−sections, we provide a brief description of the radio and optical data used in our study.

3.2.1 Multi-frequency Radio Observations

3.2.1.1 325 MHz GMRT Radio Observations

The 325 MHz GMRT observations centered at RA = 02^h 21^m 00^s (J2000) and DEC = -04° 30′ 00″ (J2000) covers an area of 12.5 deg^2 with 16 pointings in the XMM−LSS field. These observations were carried out with the legacy GMRT equipped with the software correlator and instantaneous bandwidth of 32 MHz. To optimize the uv coverage, observations were performed in semi−snapshot mode with each scan of 6−17 minutes duration. With an average exposure time of 2.5 hours per pointing the final 325 MHz GMRT mosaiced image has nearly uniform sensitivity with an average noise−rms of 150 μJy beam^{-1}. The final map with a synthesized beam−size of 10″.2 × 7″.9 yields the detection of 3739 individual radio sources above the flux limit of 5σ in the deeper regions (noise−rms <200 μJy beam^{-1}) and 6σ in the relatively shallower regions (noise−rms >200 μJy beam^{-1}). More details on these observations can be found in Singh et al. (2014) who used it to study the population of USS radio sources. These observations have also been used to study the radio−FIR correlation in blue−cloud galaxies (Basu et al., 2015), a giant remnant radio galaxy J021659-044920 (Tamhane et al., 2015), the population of infrared−faint radio sources (Singh et al., 2017) and remnant candidates of small angular sizes (Singh et al., 2021).

Table 3.1: Summary of deep multi−frequency radio observations.

Frequency	Telescope	Area (deg^2)	5σ limit (mJy beam^{-1})	Beam−size ($'' \times ''$)	PA (deg)	No. of total Sources	Reference
150 MHz	LOFAR	27.0	1.4−1.97	7.5 × 8.5	106	3044	Hale et al. (2019)
325 MHz	GMRT	12.5	0.75	10.2 × 7.9	74.6	3739	Singh et al. (2014)
1.4 GHz	JVLA	5.0	0.08	4.5	0.0	5760	Heywood et al. (2020)

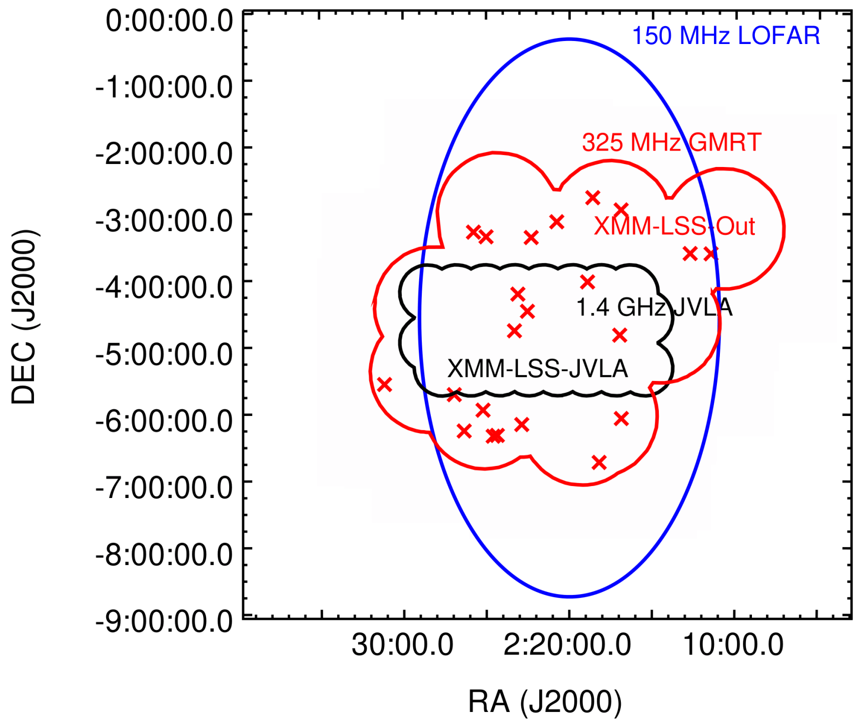

Figure 3.1: The footprints of 325 MHz GMRT observations (in Red), 150 MHz LOFAR observations (in Blue) and 1.4 GHz JVLA observations (in Black) in the XMM-LSS field. The HSC−SSP wide component covers full region of the XMM−LSS. The 5.0 deg^2 XMM−LSS−JVLA region covered with deep 1.4 GHz JVLA observations and the XMM−LSS−Out region outside to JVLA region, are marked. The positions of our remnant candidates are marked by red cross symbols.

3.2.1.2 150 MHz LOFAR Radio Observations

The XMM−LSS field has been observed with the LOFAR using the High Band Antenna (HBA; 110−240 MHz) having central frequency at 150 MHz (Hale et al., 2019). With three four−hour pointings LOFAR observations cover 27 deg^2 sky area, centered at RA

= $02^h\ 20^m\ 00^s$ (J2000) and DEC = -04° 30′ 00″ (J2000), with elliptical footprints aligned in the north−south direction (see Figure 3.1). The final mosaiced map has a median noise−rms of 0.40 mJy beam^{-1}, while noise−rms reaches down to 0.28 mJy beam^{-1} in the central region. With the synthesized beam−size of $7''.5 \times 8''.5$ these observations detect a total of 3044 individual radio sources. We note that the angular resolution and sensitivity of 150 MHz LOFAR observations are comparable to that of 325 MHz GMRT observations. Average 5σ depth of 1.97 mJy beam^{-1} in the 150 MHz LOFAR observations scales to $\sim$ 1.15 mJy beam^{-1} at 325 MHz, assuming a typical spectral index value of -0.7. Hence, combination of sensitive 150 MHz LOFAR observations and 325 MHz GMRT observations will enhance the chance of remnant detection.

3.2.1.3 1.4 GHz JVLA Radio Observations

Recently, Heywood et al. (2020) carried out 1.4 GHz wide-band (0.994−2.018 GHz) JVLA (B-configuration) radio observations of 5.0 deg^2 sky area over the near-IR VIDEO region (Jarvis et al., 2013) in the XMM−LSS field. With 32 pointings the final mosaiced map has a median noise−rms of 16 μJy beam^{-1} and angular resolution of $4''.5$. These are one of the deepest 1.4 GHz observations over the largest area (5.0 deg^2) in the XMM−LSS field, and detect a total of 5760 radio sources above 5σ flux limit. The JVLA observations performed with the B−configuration in the wide-band continuum mode allow sub−band imaging, and provide in-band spectral indices for 3458 radio sources.

3.2.1.4 3 GHz Very Large Array Sky Survey (VLASS)

In our work, we also use data from the 3 GHz VLASS which covers the entire sky north of -40° declination. The VLASS is being carried out with 2−4 GHz wide−band of JVLA in B/BnA−configuration offering angular resolution of $2''.5$ and noise−rms of 0.12 mJy beam^{-1} in one epoch observations (Lacy et al., 2020). The VLASS is designed to observe each field over three epochs with the separation of 32 months, allowing it to study variable radio sources. The coadded images of three epochs are expected to achieve noise−rms of 0.07 mJy beam^{-1}. We use the VLASS Epoch 1 Quick Look images and source catalog available at the Canadian Initiative for Radio Astronomy Data Analysis (CIRADA) website[1]. The high resolution deep VLASS images are useful in detecting the presence of a radio core.

We note that, in addition to the aforementioned radio observations, the XMM−LSS field is covered with shallow 74 MHz VLA observations having noise−rms 32 mJy beam^{-1} (Tasse et al., 2006). Due to lack of sensitivity similar to the 325 MHz GMRT observations these data are not very useful to perform a systematic search for remnants. We used 74 MHz flux densities, whenever available, for the SED fitting of our selected remnant candidates. Further, the XMM−LSS field is also surveyed at 240 MHz and 610 MHz with the GMRT. The 240 MHz GMRT observations achieved noise-rms of 2.5 mJy beam^{-1} and detected 466 sources in 18.0 deg^2 area, while relatively deeper (noise-rms $\sim$ 0.3 mJy beam^{-1}) 610 MHz observations detected 769 sources in 12.7 deg^2 area (Tasse et al., 2007). The 610 MHz GMRT observations were reprocessed by Smolčić et al. (2018) with an aim to achieve deep radio image of XXL−N field encompassing the XMM−LSS field as well. The final 610 MHz mosaic image covering an area of 30.4 deg^2 with a non-uniform noise-rms (200 μJy beam^{-1} in the inner area of 11.9 deg^2, and 45 μJy beam^{-1} in the outer area of 18.5 deg^2) and the resolution of $6''.5$ yields a catalog of 5434 radio sources at $\geq 7\sigma$ level. In principle, deep 610 MHz observations can be utilised to search for remnants but we find that, both 240 MHz and 610 MHz observations suffer from underestimated or missing flux density issue. The 610 MHz observations are also not ideal for the core detection due to moderate angular resolution and sensitivity. Therefore, we choose not to use 240 MHz and 610 MHz GMRT observations for our study.

3.2.2 Optical Survey

Deep optical data in the XMM−LSS field are available from the Hyper Suprime−Cam Subaru Strategic Program (HSC−SSP[2]) which is a three−tiered (wide, deep and ultra−deep), multi−band (g, r, i, z, y and four narrow−band filters) imaging survey carried out with a wide−field camera named Hyper Suprime−Cam installed at the 8.2−m Subaru tele-

[1] http://cutouts.cirada.ca/

[2] https://hsc-release.mtk.nao.ac.jp/doc/

scope (Aihara et al., 2018). The HSC−SSP survey's wide component reaches to a depth of $26.2^{+0.2}_{-0.3}$ mag at 5σ level for point sources in the i band and covers nearly 1200 deg^2 sky area mostly around the celestial equator. Deep component is nearly one magnitude deeper with 5σ detection limit of $26.9^{+0.2}_{-0.3}$ mag in i band and covers 7.0 deg^2 in each of the four separate fields (XMM−LSS, E−COSMOS, ELAIS−N1, DEEP2−F3). The ultra−deep survey is nearly 0.8 magnitude deeper than the deep component but it covers only 1.7 deg^2 sky area in each of the two sub−fields centered at the COSMOS and Subaru XMM−Newton Deep field Survey (SXDS). The 5σ limiting magnitudes are AB magnitudes (Oke & Gunn, 1983) measured within $2''.0$ diameter apertures and include effects of source confusion. We note that the 325 MHz GMRT observed region in the XMM−LSS field is completely covered with the HSC−SSP wide survey and 7.0 deg^2 area is covered with the deep component. We obtain optical data from the HSC−SSP third public data release (PDR3) that provides source catalogues and images with the median seeing of $0''.6$ in i band. We note that the HSC−SSP photometric data are more than one magnitude deeper than the previously available optical photometric data from the Canada−France−Hawaii Telescope Legacy Survey (CFHTLS) that reached down only to $i' = 24.5$ mag limiting magnitude at 5σ level (Ilbert et al., 2006). Hence, we prefer to use the HSC−SSP instead of the CFHTLS.

In addition to photometric data, HSC−SSP PDR3 also provides a collection of publicly available spectroscopic redshifts (spec-z table in the data access website[3]). The spectroscopic redshifts are gleaned from the existing spectroscopic surveys in the field such as Sloan Digital Sky Survey (SDSS) DR16 (Ahumada et al., 2020), SDSS IV QSO catalog (Pâris et al., 2018), VIMOS−VLT Deep Survey (VVDS; Le Fèvre et al. (2013)), PRIsm MUlti−object Survey (PRIMUS) DR1 (Cool et al., 2013), VIMOS Public Extragalactic Redshift Survey (VIPERS) PDR1 (Garilli et al., 2014)) in the XMM−LSS field. The spectroscopic objects are matched by the position within $1''.0$ to the HSC−SSP objects and the closest match is considered. In case, a HSC−SSP source is found to have more than one spectroscopic redshifts the secure redshift value with the smallest error is considered. We note that the VIPER survey pre−selected redshift range of $0.5 < z <$ 1.0 based on the optical and IR color−color plots, and spec−z measurements are limited to relatively bright optical sources ($i'_{\rm AB} < 22.5$). The PRIMUS also measured spec−z

[3]https://hsc-release.mtk.nao.ac.jp/doc/index.php/available-data_pdr3/

of galaxies only upto $z = 1.0$. In case of unavailability of spectroscopic redshift we use photometric redshifts available from the HSC−SSP PDR2 (Aihara et al., 2019). We opted for photo−z estimates derived by using a convolutional neural network (CNN) method that uses galaxy images in contrast to the earlier methods that used only integrated photometry of galaxies (see Schuldt et al., 2021). The CNN based photo−z estimates gives a precision of $\sigma = 0.12$ (68% confidence interval) for $|z_{pred}$ - $z_{ref}|$ in the redshift range of 0 to 4.0 for the full HSC−SSP photometric sample.

3.3 Selection Criteria and Identification of Remnants

In the literature, remnant sources have been identified by using both morphological as well as spectral criteria. For instance Mahatma et al. (2018) selected remnant sources based on the morphological criterion ***i.e.***, lack of radio core in sensitive high−frequency radio observations, while Godfrey et al. (2017) selected remnant sources using the steepness of the radio spectrum. We note that the non− detection of radio core, a seemingly robust criterion, is limited by the sensitivity of observations performed to examine the existence of core. Using both morphological and spectral criteria in their search of remnants Jurlin et al. (2021) argued that a weak core representing a dying or rejuvenated AGN activity may still be present in a remnant source. However, it is difficult to distinguish a dying radio core from a rejuvenated radio core. Also, there are suggestions that the AGN activity particularly in massive galaxies may always be present at some level, irrespective of their evolutionary stage (Sabater et al., 2019). Hence, in addition to absent core criterion, we also consider spectral criteria to obtain an unbiased sample of remnants. In the following subsections we provide the details of our selection criteria for remnants, and resultant remnant sub−samples.

3.3.1 Morphological Criterion

A typical remnant is expected to show relaxed radio morphology without compact components like core, hotspots, or jets (Saripalli, 2012). Although, a young remnant with recently switched off jets can still show hotspots in the lobes. As time elapses, radio lobes can become amorphous due to expansion, if lobes are over−pressured at the end of its life (Wang & Kaiser, 2008). More importantly, absence of radio core in deep high−resolution observations can be considered a manifestation of switched−off AGN activity. Hence, in principle, a remnant is expected to lack the radio core at all frequencies even in the deepest possible radio images (see Mahatma et al., 2018; Quici et al., 2021). Therefore, we use the absence of radio core in deep radio images as a criterion to identify remnants.

To search for remnants we began with a sample of 268 extended radio sources detected in the 325 MHz GMRT observations. Our initial sample is gleaned from the catalogue of 3739 sources detected in the 325 MHz GMRT radio observations by applying two conditions : (i) sources are detected with the signal−to−noise ratio (SNR) $\geq$10 to avoid contamination from spurious sources, and (ii) radio sources are extended with linear angular size (LAS) $\geq 30''$, nearly three times of the synthesized beam of GMRT at 325 MHz, to enable us to perform visual inspection of radio morphology. With LAS $\geq 30''$ we ensure a minimum of six 1.4 GHz JVLA/FIRST synthesized beams and twelve 3.0 GHz VLASS synthesized beams spread out across the source. This cut-off limit on the size allows us to minimize the blending of radio core with radio lobes, and is required for a clear interpretation of radio morphology. The LAS is measured as the end-to-end distance along the direction of maximum elongation in the 325 MHz image where minimum 3σ level emission is considered to account for the presence of diffuse extended emission.

To identify radio galaxies with absent radio core we visually inspected 3 GHz VLASS and 1.4 GHz FIRST cutouts for our all 268 sample sources. We attempted to identify the core component down to 3σ level by overlaying 3 GHz VLASS and 1.4 GHz FIRST radio contours onto the 325 MHz grey−scale images. We note that 3 GHz VLASS images with the resolution of $2''.5$ can identify radio core at 3σ limit of 0.36 mJy beam^{-1} flux density level. While, 1.4 GHz FIRST survey with the resolution of $5''.0$ can detect core component only upto 3σ = 0.6 mJy beam^{-1}. The FIRST 3σ flux density limit of 0.6 mJy at 1.4 GHz corresponds to 0.35 mJy at 3 GHz, if a typical spectral index of -0.7 is assumed. Thus, the VLASS is more effective in detecting a flat spectrum ($\alpha \geq$ -0.7) radio core, while the FIRST can be useful, if core exhibits steeper spectral index ($\alpha <$ -0.7). Hence, the FIRST and VLASS can be used in a complementary fashion to detect the core component. Using both 3 GHz VLASS and 1.4 GHz FIRST image cutouts we find only 20/268 sources with no detected radio core, but distinctly detected radio lobes in our 325 MHz image.

We note that 1.4 GHz JVLA observations available in 5.0 deg^2 XMM−LSS−JVLA region can confirm the presence or absence of radio core at a much fainter level ($3\sigma = 0.06$ mJy beam^{-1}). There are 10/20 sources falling within the XMM−LSS−JVLA region. The inspection of 1.4 GHz JVLA images reveals the presence of a radio core in 05/10 sources, and confirms them to be active. Hence, we find only five sources with no detected radio core in the XMM−LSS−JVLA region, and 10 sources with no detected radio core in the XMM−LSS−Out region. Thus, using absent−core criterion we identify a total of 15/268 ($\sim$ 5.6%) sources as the remnant candidates.

It is important to note that our criterion based on the non−detection of radio core selects only candidate remnants, and we cannot rule out the possibility of existence of a faint but undetected radio core. This is vindicated by the fact that, within the XMM−LSS−JVLA region, five out of ten sources with no detected core in the VLASS and FIRST images showed a faint core in deep 1.4 GHz JVLA images. We also point out that several of our sample sources, in particular those of smaller angular sizes ($\leq$60$''$), tend to pose difficulty in clearly separating out core from radio lobes. Thus, our remnant candidates selected by using morphological criteria are biased towards the sources of larger angular sizes. We note that all but two of our remnant candidates identified by using absent−core criterion show LAS $\geq$ 59$''$. Therefore, we use spectral criteria to identify remnant candidates that may have been missed by the morphological criterion owing to the limited sensitivity and angular resolution of the images used.

3.3.2 Spectral Curvature Criterion

According to the spectral ageing models integrated radio spectrum of an active radio source can be characterized with a broken power law, with a typical spectral index in the range of -0.5 to -0.7 below a break frequency $\nu_{\rm break}$, and a steeper spectral index α = $\alpha_{\rm inj}$ - 0.5 above $\nu_{\rm break}$ (Jaffe & Perola, 1973; Carilli et al., 1991). The appearance of spectral break can be explained by the fact that the high energy relativistic electrons in the lobes lose their energy faster with shorter radiative lifetimes than that for the low energy electrons, and it results in the steeping of spectrum at the high−frequency regime beyond a break frequency $\nu_{\rm break}$ (Komissarov & Gubanov, 1994). In remnant sources, with no supply of relativistic electrons, a new break appears at higher frequencies ($\nu_{\rm break,\ high}$) beyond which spectrum drops exponentially. As the remnant phase progresses, $\nu_{\rm break,\ high}$ shifts towards the lower frequencies. The ratio of $\nu_{\rm break,\ low}$ and $\nu_{\rm break,\ high}$, depends on the duration of remnant phase *w.r.t.*the total source age (Komissarov & Gubanov, 1994). Thus, for old remnants $\nu_{\rm break,\ low}$ and $\nu_{\rm break,\ high}$ can be sufficiently close, while for young remnants $\nu_{\rm break,\ high}$ is likely to be much higher than $\nu_{\rm break,\ low}$. Considering an exponentially fall above $\nu_{\rm break,\ high}$, the radio spectrum of a remnant source can be characterised with a steeper spectral index $\alpha \sim \alpha_{\rm inj}$ - 0.5 above $\nu_{\rm break,\ low}$, and a flatter spectral index similar to the injection spectral index $\alpha_{\rm inj} \sim$ -0.5 − -0.7 below $\nu_{\rm break,low}$ (Blandford & Ostriker, 1978; Murgia et al., 2011). To search for remnants we exploit the spectral curvature characteristic of remnant sources. We define spectral curvature as (SPC) = $\alpha_{\rm high}$ - $\alpha_{\rm low}$ in the frequency range of 150 MHz to 1.4 GHz; where $\alpha_{\rm high}$ = $\alpha_{\rm 325\ MHz}^{\rm 1.4\ GHz}$ and $\alpha_{\rm low}$ = $\alpha_{\rm 150\ MHz}^{\rm 325\ MHz}$. We use SPC $\leq$-0.5 to identify remnant sources in our sample, although its value depends on the evolutionary stage of the sources (see Murgia et al., 2011). The error on the spectral index ($\alpha_{\rm err}$) is estimated as per the following expression.

$$\alpha_{\rm err} = \frac{1}{ln(\nu_1/\nu_2)}\sqrt{\left(\frac{S_{1,\rm err}}{S_1}\right)^2 + \left(\frac{S_{2,\rm err}}{S_2}\right)^2} \tag{3.1}$$

Where $S_{1,\rm err}$ and $S_{2,\rm err}$ are errors in the flux densities S_1 and S_2, measured at the frequencies ν_1 and ν_2, respectively.

We estimate the two point spectral index between 325 MHz and 1.4 GHz ($\alpha_{\rm 325\ MHz}^{\rm 1.4\ GHz}$) using the total flux densities at the respective frequencies. The 1.4 GHz flux densities are mainly taken from the NVSS considering the fact that larger NVSS synthesized beam (45″) would be advantageous in capturing faint diffuse emission, while radio observations of higher resolution *i.e.*, FIRST and JVLA are likely to miss the detection of diffuse extended emission. In our sample of 268 sources we find 1.4 GHz NVSS counterparts for 245 sources. Out of remaining 23 sources, nine sources fall within the XMM−LSS−JVLA region and we obtain 1.4 GHz flux density from the JVLA observations as these sources show complete detection of extended emission, and flux densities are derived from the JVLA image convolved with 45″ Gaussian beam equivalent to the NVSS beam−size. Thus, we estimate two point spectral index $\alpha_{\rm 325MHz}^{\rm 1.4GHz}$ for 254/268 sources and place an upper limit on $\alpha_{\rm 325MHz}^{\rm 1.4GHz}$ for remaining 14 sources by using the NVSS flux density upper limit of 2.5 mJy.

To obtain spectral index between 150 MHz and 325 MHz ($\alpha_{\rm 150\ MHz}^{\rm 325\ MHz}$) we search for 150 MHz counterparts of our sample sources mainly using 150 MHz LOFAR catalogue. Due to high sensitivity of the LOFAR observations ($5\sigma \sim 1.4$ mJy) all 231/268 sources falling within the LOFAR region are detected at 150 MHz. We ensure that all source components are consistently matched at both the frequencies by overlaying 150 MHz catalogue source positions onto the 325 MHz GMRT images. We note that the similar resolution and depth of 150 MHz LOFAR and 325 MHz GMRT enable us to detect the extended emission at both the frequencies. For remaining 37 sources we check their detection in the 150 MHz TGSS survey. 22/37 sources show their detection in the TGSS catalog with 7σ flux limit cutoff ($S_{\rm 150\ MHz}$ <24.5 mJy). For remaining 15 sources we place an upper limit on their 150 MHz flux density ($S_{\rm 150\ MHz}$ <24.5 mJy) based on their non−detection in the TGSS. Thus, we estimate two point spectral index $\alpha_{\rm 150\ MHz}^{\rm 325\ MHz}$ for 253/268 sources and place an upper limit for remaining 15 sources. There is only one source that lacks the detection at both 150 MHz and 1.4 GHz frequencies and is excluded from our spectral analysis as both $\alpha_{\rm low}$ and $\alpha_{\rm high}$ remain unconstrained.

Figure 3.2 shows the diagnostic plot of $\alpha_{\rm 150\ MHz}^{\rm 325\ MHz}$ versus $\alpha_{\rm 325MHz}^{\rm 1.4GHz}$ that allows us to identify sources with strong spectral curvature (SPC ≤-0.5) in the frequency range of 150 MHz to 1.4 GHz. We note that while identifying remnant sources using spectral curvature diagnostic plot we avoid sources with $\alpha_{\rm 150\ MHz}^{\rm 325\ MHz} \geq$-0.5 *i.e.*, sources exhibiting flat or turnover spectrum in the low−frequency regime (below 325 MHz). Radio sources with peak frequency at ≤325 MHz can represent mega-hertz (MHz) peaked spectrum radio sources comprising mainly active young radio galaxies (see Callingham et al., 2017). Further, sources showing upturn spectrum *i.e.*, $\alpha_{\rm 150\ MHz}^{\rm 325\ MHz}$ steeper than $\alpha_{\rm 325\ MHz}^{\rm 1.4\ GHz}$ are also avoided. Sources showing upturn spectrum can possibly indicate episodic AGN activity wherein both remnant as well as young radio plasma co−exist, and a source appears much brighter at low−frequency due to substantial contribution from the remnant plasma (see Parma et al., 2007). However, we caution that the sources suffering with missing flux density at 325 MHz but not at 150 MHz can also give rise an artificially inverted spectrum in 150 MHz to 1.4 GHz regime. In fact, by using morphological criteria we found three remnant candidates showing inverted spectrum (see Table 3.3). In the spectral diagnostic plot, we identify sources with spectral curvature ≤-0.5 that are found in a region bounded by the lines $\alpha_{\rm high}$ = $\alpha_{\rm low}$ - 0.5 and $\alpha_{\rm 150\ MHz}^{\rm 325\ MHz}$ = -0.5 (see Figure 3.2). We find only nine sources with SPC ≤-0.5 that are selected as remnant candidates. Of these, there are 03/09 remnant candidates that have already been identified by using the morphological criterion. In principle, remaining six remnant candidates can also be identified by the absent−core criterion, but were deemed to be uncertain due to core−lobe deblending issue owing to their relatively smaller angular size. Therefore, the morphological and spectral selection criteria complement each other.

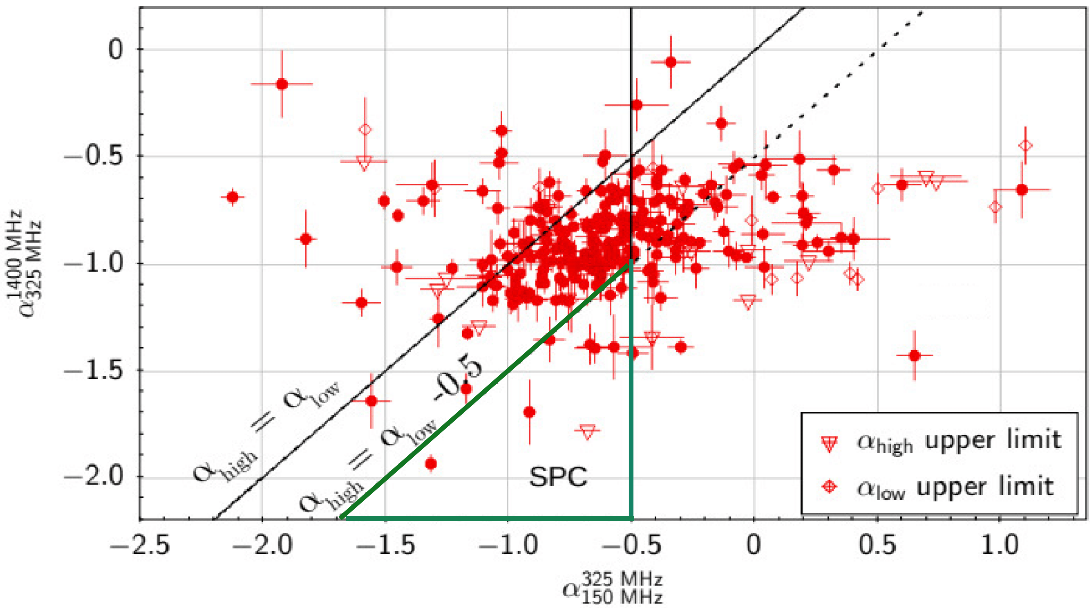

Figure 3.2: Low frequency spectral index ($\alpha_{\rm 150\ MHz}^{\rm 325\ MHz}$) versus high frequency spectral index ($\alpha_{\rm 325\ MHz}^{\rm 1.4\ GHz}$) plot. Sources showing strong spectral curvature ($\Delta\alpha$ ≤-0.5) fall within the green triangle which is bounded by the slanting line $\alpha_{\rm 325\ MHz}^{\rm 1.4\ GHz}$ = $\alpha_{\rm 150\ MHz}^{\rm 325\ MHz}$ - 0.5 and the vertical line $\alpha_{\rm 150\ MHz}^{\rm 325\ MHz}$ = -0.5.

3.3.3 Ultra−Steep Spectral (USS) Index Criterion

We note that, with our limited frequency coverage, the spectral curvature criterion (SPC = $\alpha_{\rm high}$ - $\alpha_{\rm low}$ $\leq$-0.5) would miss remnant sources in which spectral break falls below 325 MHz. According to the evolutionary models break frequency ($\nu_{\rm b}$) progressively shifts towards lower frequencies as source ages. The relation between total source age ($t_{\rm s}$) and $\nu_{\rm b}$ can be expressed with the following equation (see Komissarov & Gubanov, 1994; Slee et al., 2001).

$$t_{\rm s} = 1590 \left[\frac{B_{\rm eq}^{0.5}}{(B_{\rm eq}^2 + B_{\rm CMB}^2)\sqrt{\nu_{\rm b}(1+z)}} \right] \text{Myr} \tag{3.2}$$

Where $B_{\rm eq}$ and $B_{\rm CMB}$ = 3.25(1+z)^2 are equipartition magnetic field and inverse Compton equivalent magnetic field, respectively, in the unit of μG, and $\nu_{\rm b}$ is break frequency in GHz. For a remnant source with $\nu_{\rm b}$ = 325 MHz, we find $t_{\rm s}$ = 41 Myr by assuming a typical value for equipartition magnetic field ($B_{\rm eq}$) 3.0 μG and redshift (z) 0.67, the median redshift of our sample. Considering the same parameters but $\nu_{\rm b}$ = 150 MHz would result $t_{\rm s}$ = 60 Myr. We note that our estimates for the total source ages are similar to the remnants reported in the literature (see Parma et al., 2007; Brienza et al., 2016; Shulevski et al., 2017). Although, we mention that the source ages estimated here are based on various assumptions, and hence, these need to be considered as only characteristic timescales.

In our sample, remnant sources with $\nu_{\rm b}$ < 325 MHz would appear as the USS sources. Hence, USS radio sources can be regarded as the potential remnant candidates. Although, USS criterion selects only a fraction of remnant population consisting of mainly old remnants (see Godfrey et al., 2017). We search for USS sources ($\alpha_{\rm 150\ MHz}^{\rm 1.4\ GHz}$ $\leq$-1.2) based on the spectral index measured between 150 MHz and 1.4 GHz *viz.*, the widest spectral window available. We caution that the limit placed on the spectral index for defining an USS source is somewhat arbitrary, and is based on the fact that many remnant sources show steep spectral index (α) <-1.2 at low frequencies (Godfrey et al., 2017).

In our sample, 242/268 sources have estimates of 150 MHz − 1.4 GHz spectral index ($\alpha_{\rm 150\ MHz}^{\rm 1.4\ GHz}$) from their detection at both 150 MHz and 1.4 GHz frequencies, while 11 sources have only upper limits on $\alpha_{150\ \mathrm{MHz}}^{1.4\ \mathrm{GHz}}$ due to their non−detection at 1.4 GHz. The 1.4 GHz flux densities are mainly from the NVSS and the upper limits on $\alpha_{150\ \mathrm{MHz}}^{1.4\ \mathrm{GHz}}$ are derived by using the NVSS flux density limit of 2.5 mJy (see Section 3.3.2). Remaining 15 sources without 150 MHz flux density estimates have a lower limit on $\alpha_{150\ \mathrm{MHz}}^{1.4\ \mathrm{GHz}}$, and are likely to be sources with flatter index. These 15 sources are excluded from our analysis considering the fact that we are searching for USS sources. Figure 3.3 shows the distribution of $\alpha_{150\ \mathrm{MHz}}^{1.4\ \mathrm{GHz}}$ ranging from -1.72 to -0.05 with a median value of -0.81±0.02. We find that only 10/253 (∼3.9%) sources can be identified as USS sources. There are 02/10 USS sources with an upper limit on $\alpha_{150\ \mathrm{MHz}}^{1.4\ \mathrm{GHz}}$. Accounting for the errors on spectral indices the fraction of USS sources can be in the range of 2.6%−5.2%. We note that the fraction of USS sources found in our sample is similar to that reported in some previous studies (*e.g.*, Brienza et al., 2017).

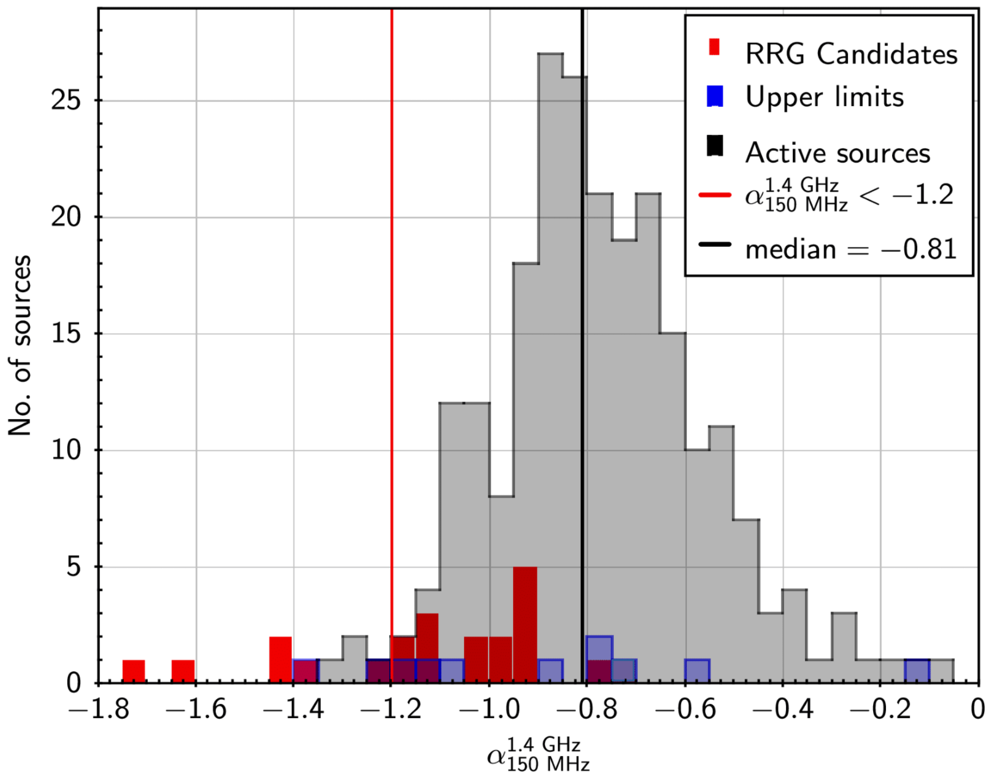

Figure 3.3: The histogram of spectral index $\alpha_{150\ \mathrm{MHz}}^{1.4\ \mathrm{GHz}}$. The vertical black line marks a median value of -0.81 and the vertical red line segregates USS sources having $\alpha_{150\ \mathrm{MHz}}^{1.4\ \mathrm{GHz}}$ ≤-1.2. Our remnant candidates are shown with the filled red bins.

We caution that our USS sample can be contaminated by other types of radio sources with same spectral characteristic such as high−z radio galaxies (HzRGs, Singh et al.

(2014)), some active FR II radio galaxies (Harwood et al., 2015) and cluster relics and halos (van Weeren et al., 2009). Radio relics and halos can be identified from their radio morphologies showing elongated filamentary structure and circular halo−like emission in contrast to double−lobe radio galaxies (van Weeren et al., 2011). We find that none among our ten USS sources shows morphology similar to a relic or a radio halo. We note that 02/10 of our USS sources are identified as active radio galaxies with core detected in the 1.4 GHz JVLA images. While, another 02/10 USS sources are identified as potential HzRGs due to their high surface−brightness and the non−detection of optical host. Thus, after discarding potential contaminants the USS criterion yields a sample of only six remnant candidates. Unsurprisingly, all but one of our USS remnant candidates are already identified by the morphological criterion, while remaining one USS remnant candidate is selected by the SPC criterion. Therefore, again we find that the morphological criterion *i.e.*, absent−core is effective in identifying majority of our remnant candidates, except sources with small angular sizes where deblending of core from lobes is difficult in the images having $2''.5-5''.0$ resolution. Further, identification of remnant candidates from both spectral as well as morphological criteria strengthens their remnant status.

3.3.4 Sample of Remnant Candidates

The remnant candidates, obtained in our study using various selection criteria, are shown in Table 3.2. The steps performed to down-size the sample size and resulting remnant fraction in different criteria shows that morphological selection criterion allows us to obtain the largest number of remnant candidates.

Table 3.2: Selection criteria and number of remnant candidates.

Sample	Criteria	Sample Size	Fraction
Extended sources with AGN activity	SNR $\geq$10, size $>30''$	268	
Sources above flux density cutoff limit	$S_{325\ \mathrm{MHz}}$ $\geq$6.0 mJy	263	
Remnant candidates	Morphology	15 (6 SPC or USS)	5.7%
Remnant candidates	SPC	9 (4 USS or Morph)	3.4%
Remnant candidates	USS	6 (6 SPC or Morph)	2.3%
Total no. of remnant candidates	Morphology or SPC or USS	21/263	8.0%

3.4 Characteristics of Remnant Candidates

With an aim to decipher the nature of our remnant candidates, we discuss their characteristic properties *i.e.*, radio spectra, surface−brightness, core−prominence upper limits, redshifts and luminosities, and compare them with the remnants reported in the literature.

3.4.1 Spectral Properties

3.4.1.1 Spectral Index Distribution

Figure 3.3 shows the distributions of two−point spectral index between 150 MHz and 1.4 GHz ($\alpha_{150\ \mathrm{MHz}}^{1.4\ \mathrm{GHz}}$) for our remnant candidates and active sources. We find that our 21 remnant candidates have $\alpha_{150\ \mathrm{MHz}}^{1.4\ \mathrm{GHz}}$ in the range of -1.72 to -0.74 with a median value of -1.02±0.06. While, active sources have $\alpha_{150\ \mathrm{MHz}}^{1.4\ \mathrm{GHz}}$ distributed in the range of -1.32 to -0.05 with a median value of -0.79±0.02. Therefore, in comparison to active sources, our remnant candidates show systematically steeper spectral indices even when majority (15/21) of them can be identified by using only morphological criterion. The two sample Kolmogorov−Smirnov (KS) test suggests that the spectral index distributions of active and remnant candidates are not similar *i.e.*, probability that the two samples come from the same distribution is only 0.54 (see Table 3.5). We caution that the small number of remnant candidates can affect the statistical result. The steep spectral indices ($\alpha_{150\ \mathrm{MHz}}^{1.4\ \mathrm{GHz}}$ <-1.0) of our remnant candidates can be understood as the spectral evolution of radio lobes suffering energy losses during the remnant phase. However, the remnant candidates with less steep spectral indices ($\alpha_{150\ \mathrm{MHz}}^{1.4\ \mathrm{GHz}}$ >-1.0) need to be examined more critically. We note that our remnant candidates with $\alpha_{150\ \mathrm{MHz}}^{1.4\ \mathrm{GHz}}$ >-1.0 tend to exhibit spectral curvature and the spectral indices between 325 MHz and 1.4 GHz ($\alpha_{325\ \mathrm{MHz}}^{1.4\ \mathrm{GHz}}$) are steeper than -1.0.

From Figure 3.3 it is evident that there is no sharp cutoff limit on the spectral index distribution that can enable us to differentiate between active sources and remnant candidates. In fact, active sources continue to remain present even if only USS sources are considered (see Section 3.3.3). Also, we note that only 12/21 (57%) of our remnant candidates are identified by using spectral criteria *i.e.*, spectral curvature as well as USS criterion, implying that a substantial fraction of remnants would be missed if search is limited only to the spectral criteria. Hence, we conclude that the morphological criteria are important for identifying the full population of remnant sources. This conclusion is similar to that found in some recent studies (*e.g.*, Mahatma et al., 2018; Jurlin et al., 2021).

3.4.1.2 Radio SEDs

To understand the spectral characteristics of our remnant candidates we model their radio spectral energy distributions (SEDs) over the widest possible range between 74 MHz to 1.4 GHz, subject to the availability of flux densities. In principle, flux densities measured at different frequencies should be matched in resolution and uv−coverage. However, we point out that the beam−sizes at 150 MHz ($7''.5\times8''.5$) and 325 MHz ($10''.2\times7''.9$) are comparable, and much larger beam−sizes at 74 MHz ($30''$ in the VLA) and at 1.4 GHz ($45''$ in the NVSS) would ensure the detection of low−surface−brightness emission. Although, unlike low-frequency observations, 1.4 GHz VLA observations have sparse uv-coverage that can possibly miss diffuse emission of very low-surface-brightness, which in turn would result flux density lower than the actual. Hence, we caution that the missing flux issue, if significant, would make spectral curvature artificially more stronger. We mention that 15/21 (71.4 per cent) of our remnant candidates have been identified by using the morphological criteria. While, remaining six remnant candidates identified with spectral curvature criterion would mostly continue to exhibit strong curvature ($\Delta\alpha$ <-0.5), even if 1.4 GHz flux density increases by a margin of 10 percent or so. Thus, a marginal missing flux density upto 10 per cent at 1.4 GHz is unlikely impact our results.

Since remnant sources can show power law or curved spectra we attempt to fit the radio SED of each remnant candidate with a power law model as well as with a curved power law model. The best fit is determined on the basis of goodness−of−fit defined by the reduced χ^2. The standard power law model is described as $\mathrm{S}_\nu = \mathrm{S}_0\ (\nu/\nu_0)^\alpha$, where spectral index α and flux normalization S_0 are constrained by the fitting, and ν_0 is the frequency at which S_0 is evaluated. Curved power law is defined as $\mathrm{S}_\nu = \mathrm{S}_0\ (\nu/\nu_0)^\alpha\ \mathrm{e}^{\mathrm{q}(\ln\nu)^2}$, where q parameterises the curvature of spectrum such that $q\ < 0$ represents a

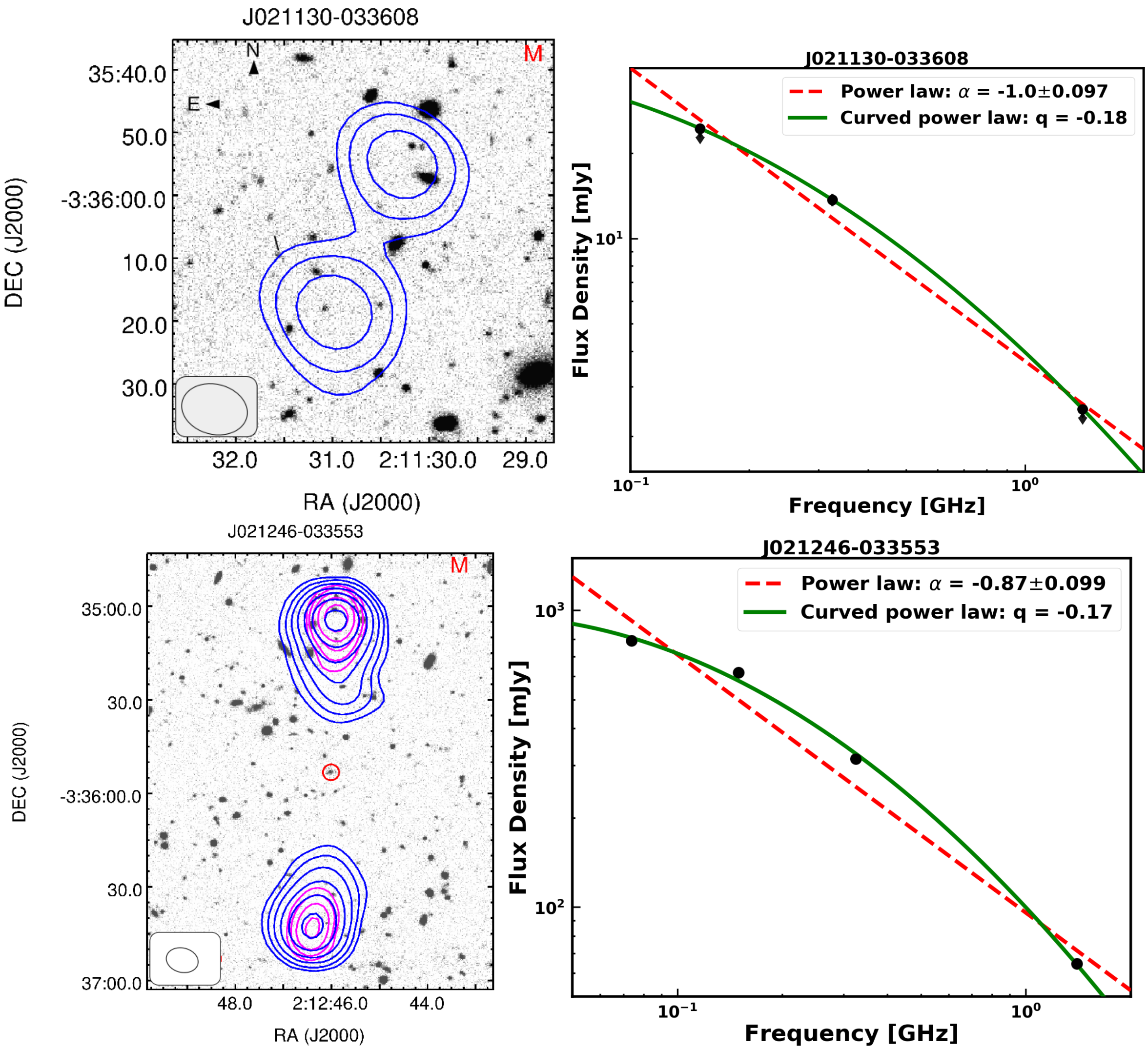

Figure 3.4: The images of our remnant candidates showing the radio contours from 325 MHz GMRT (in Blue), 1.4 GHz JVLA/FIRST (in Magenta) and 3.0 GHz VLASS (in Cyan) overlaid onto the corresponding HSC−SSP i band optical image. The radio contour levels are at $3\sigma \times$ (1, 2, 4, 8, 16, ...) and the corresponding optical image is logarithmically scaled. Potential host galaxy is marked with a red circle on it. Other probable host candidates are marked by red boxes. The GMRT 325 MHz synthesized beam of $10''.2 \times 7''.9$ is shown in the bottom left corner. Radio SED fitted by a power law and a curved power law is shown adjacent to the corresponding image of each source.

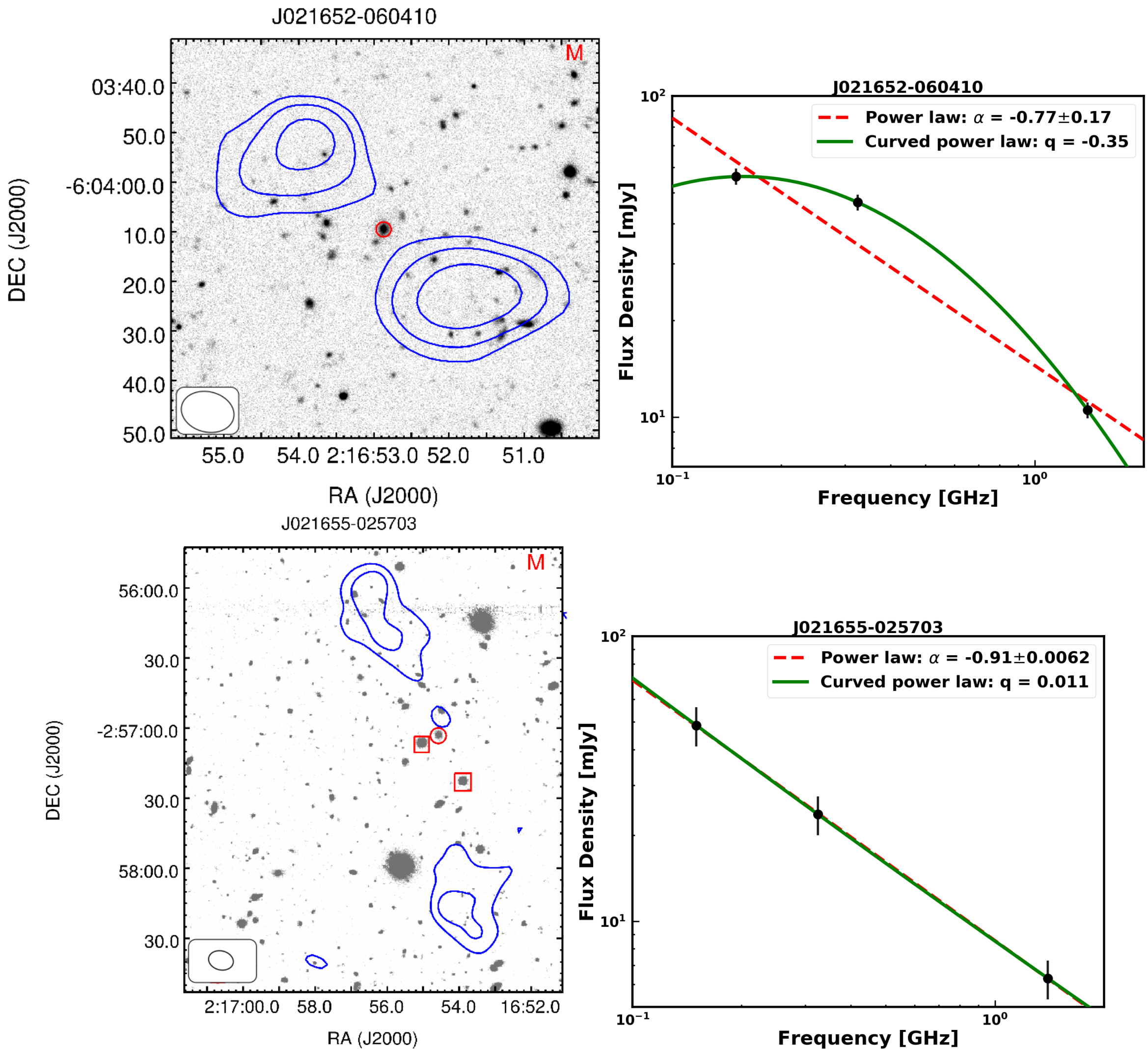

Figure 3.4: *Continue*

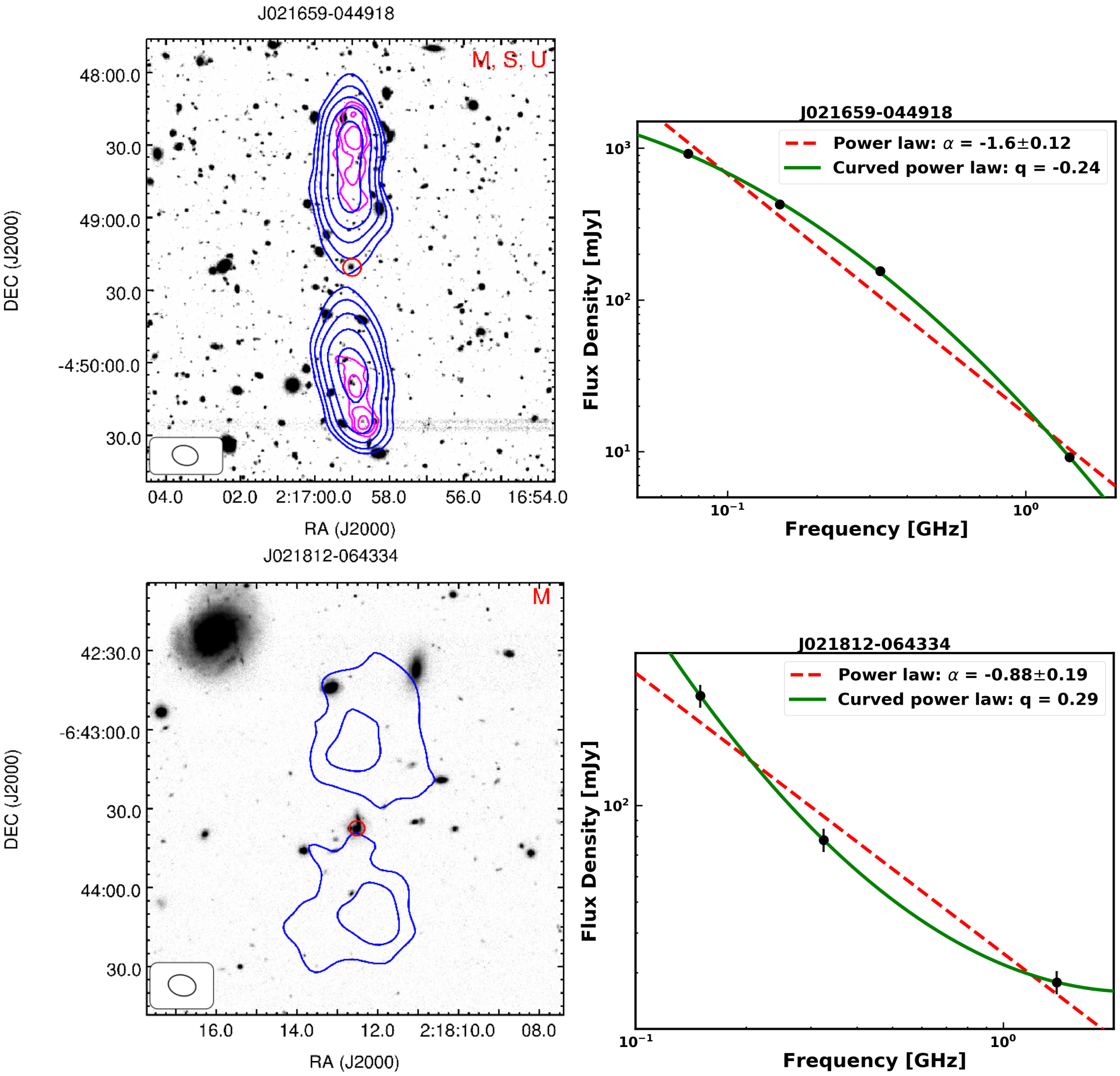

Figure 3.4: *Continue*

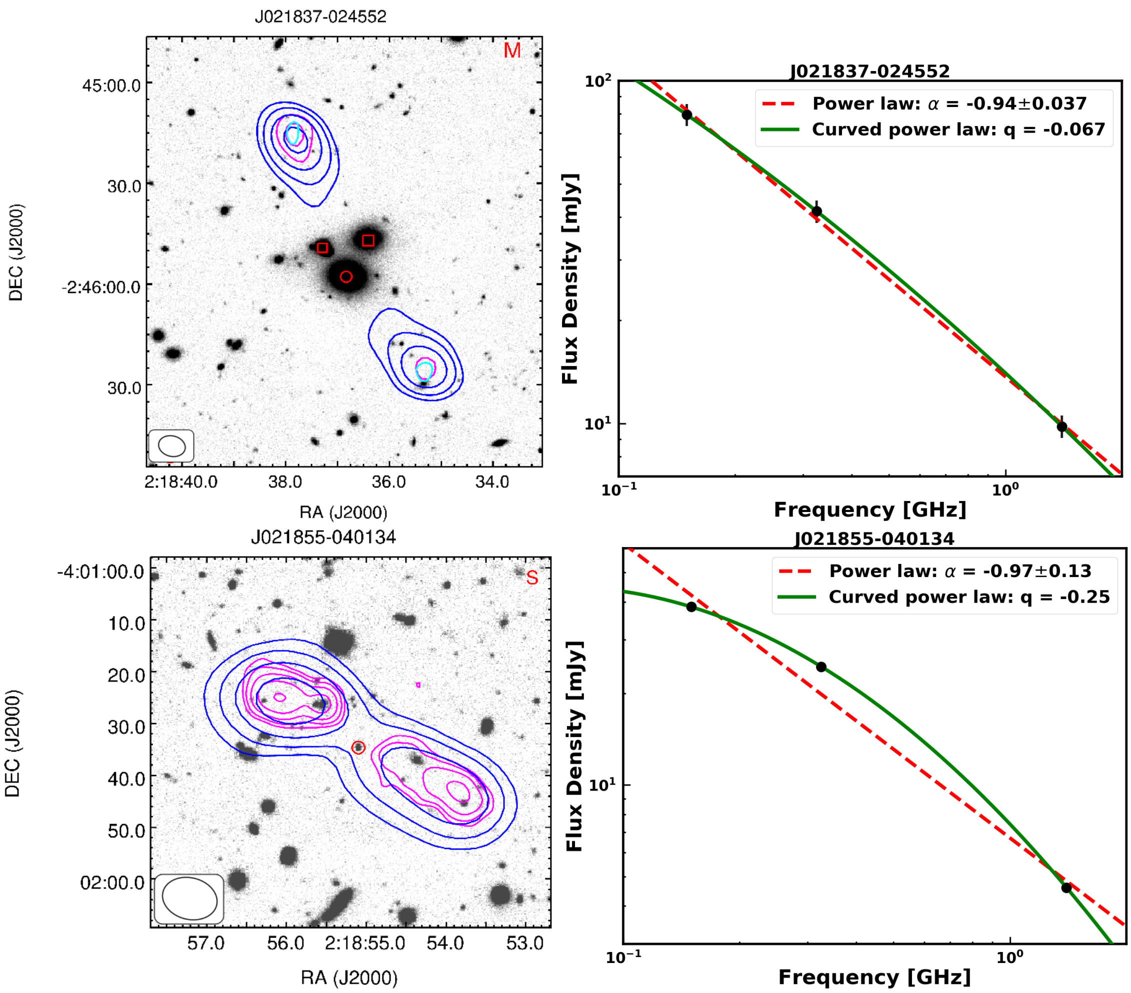

Figure 3.4: *Continue*

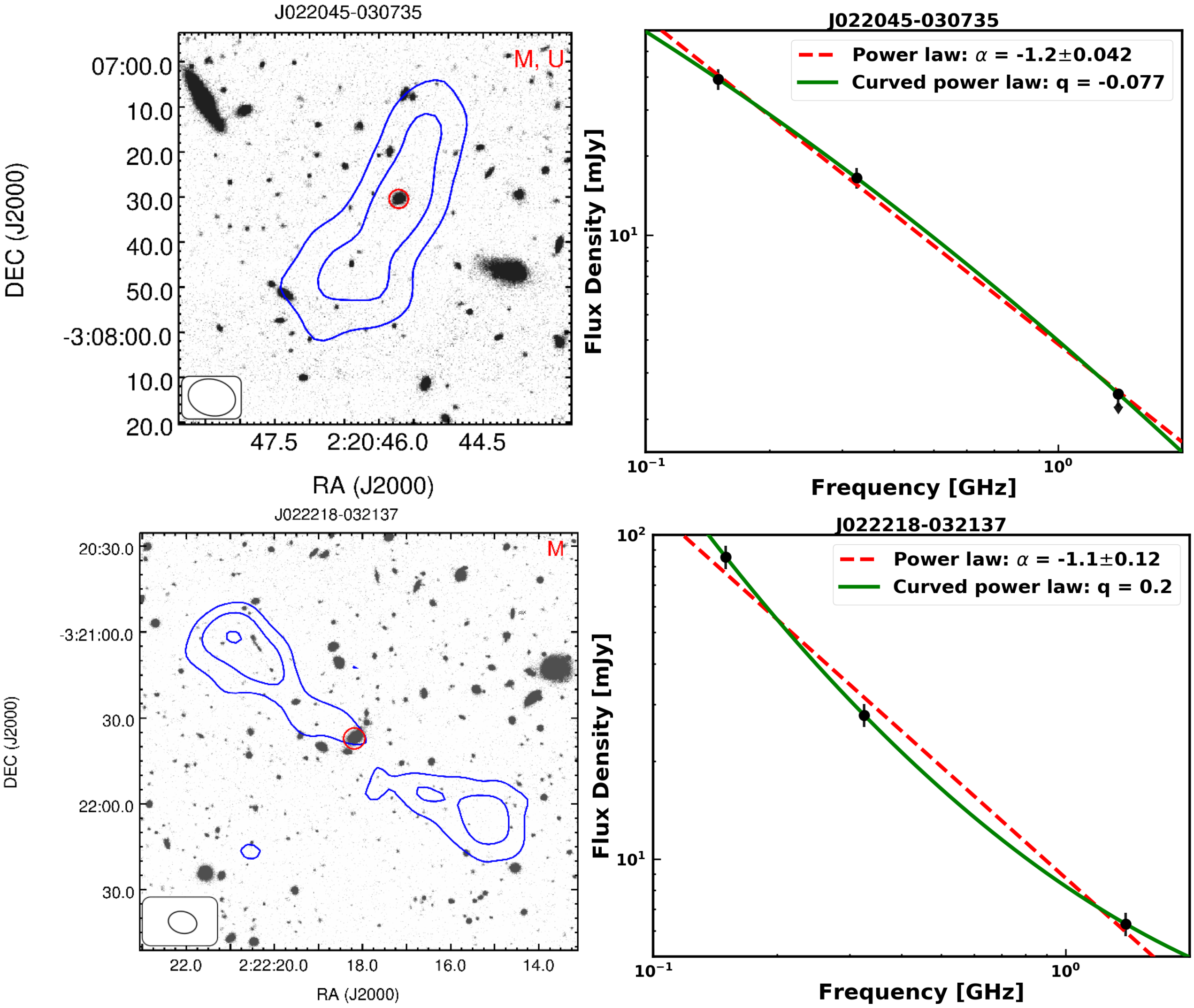

Figure 3.4: *Continue*

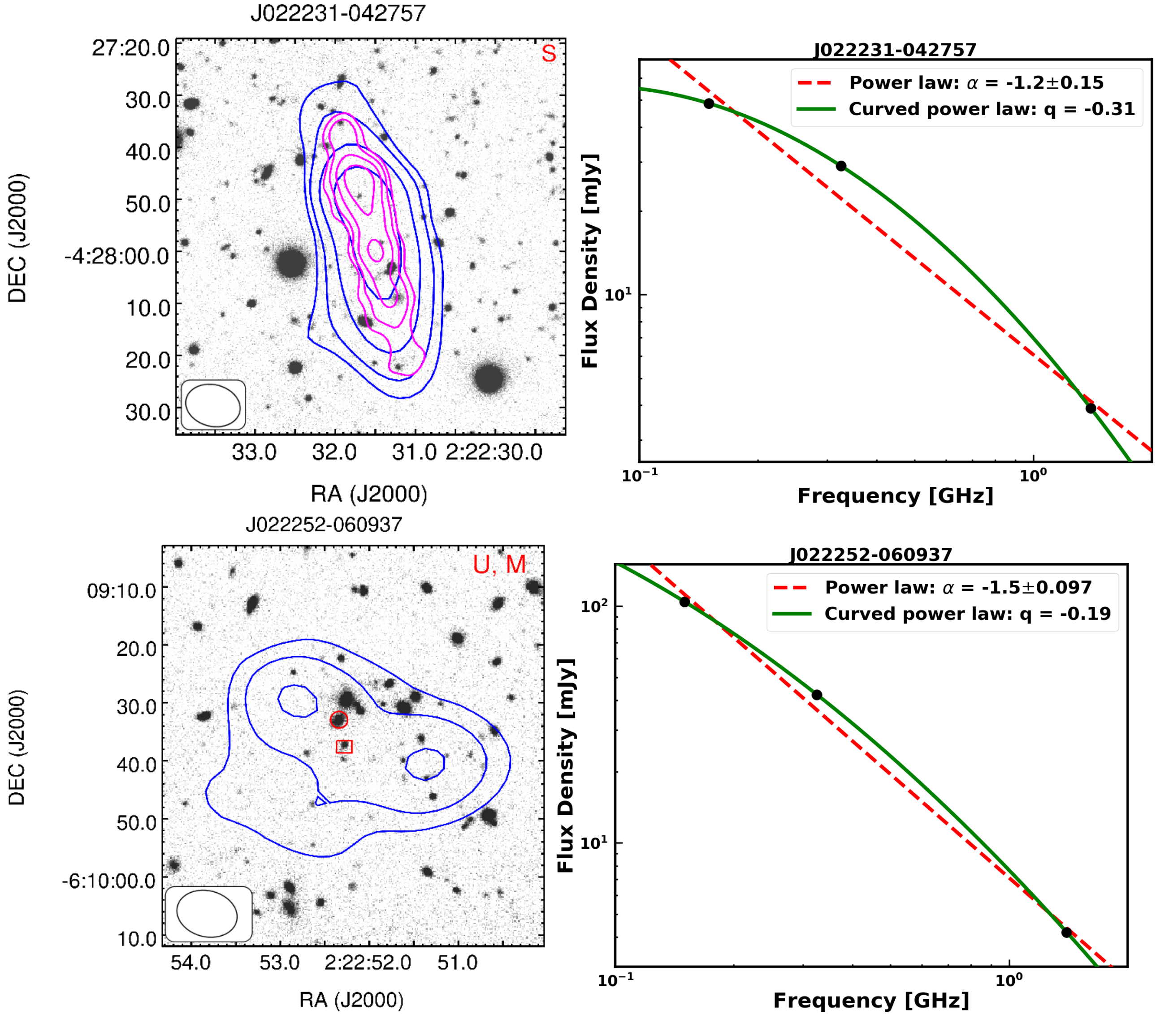

Figure 3.4: *Continue*

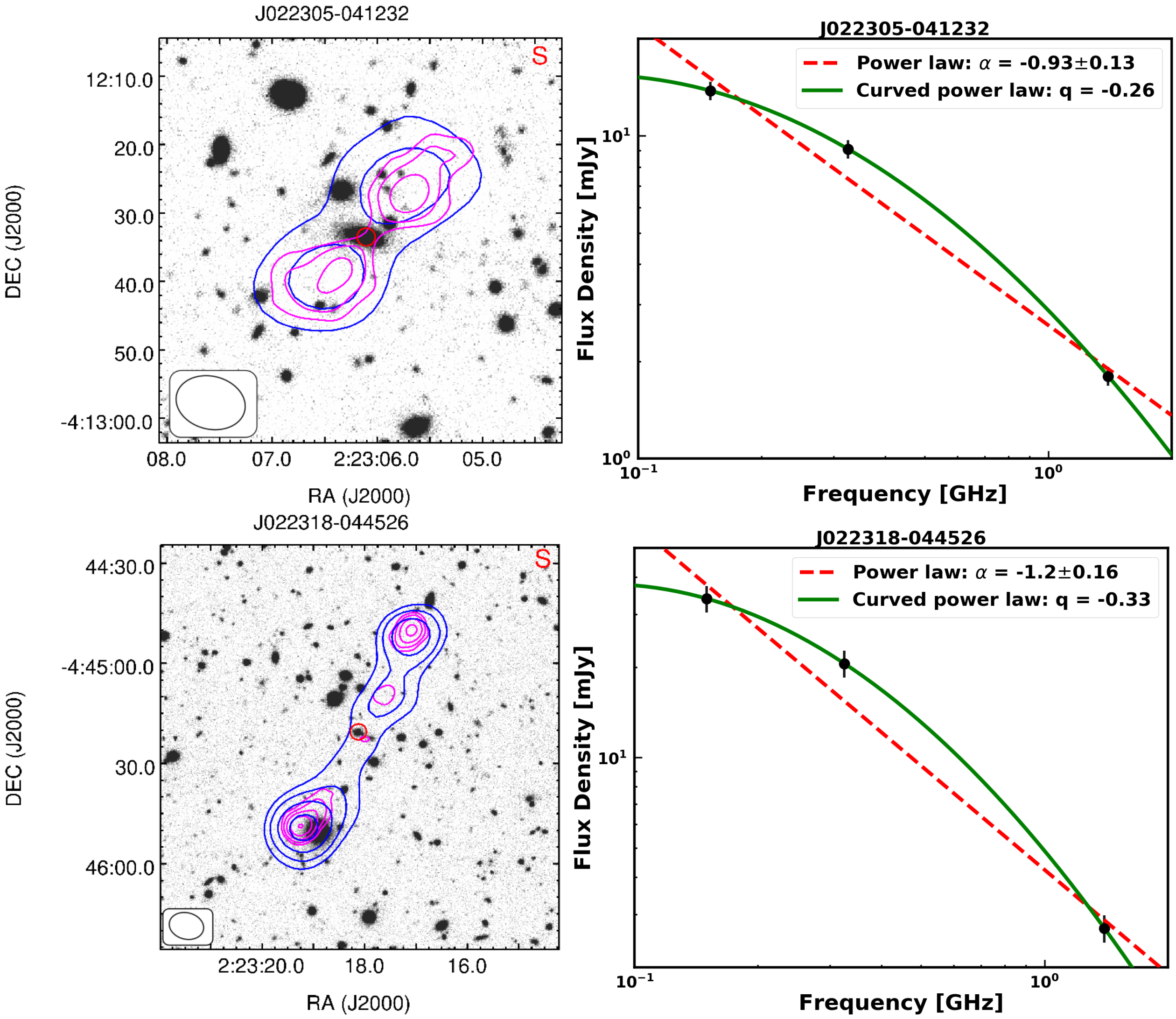

Figure 3.4: *Continue*

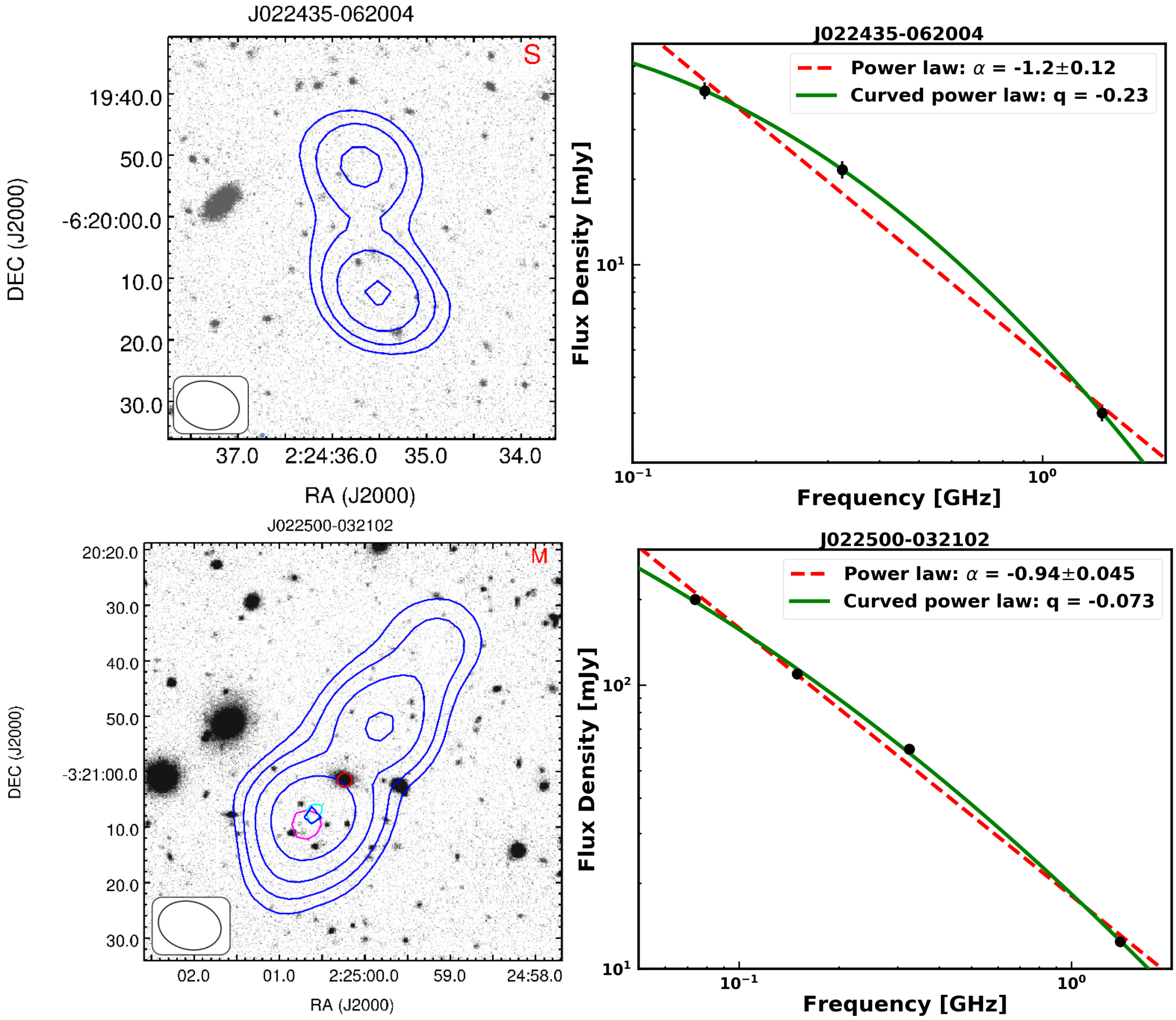

Figure 3.4: *Continue*

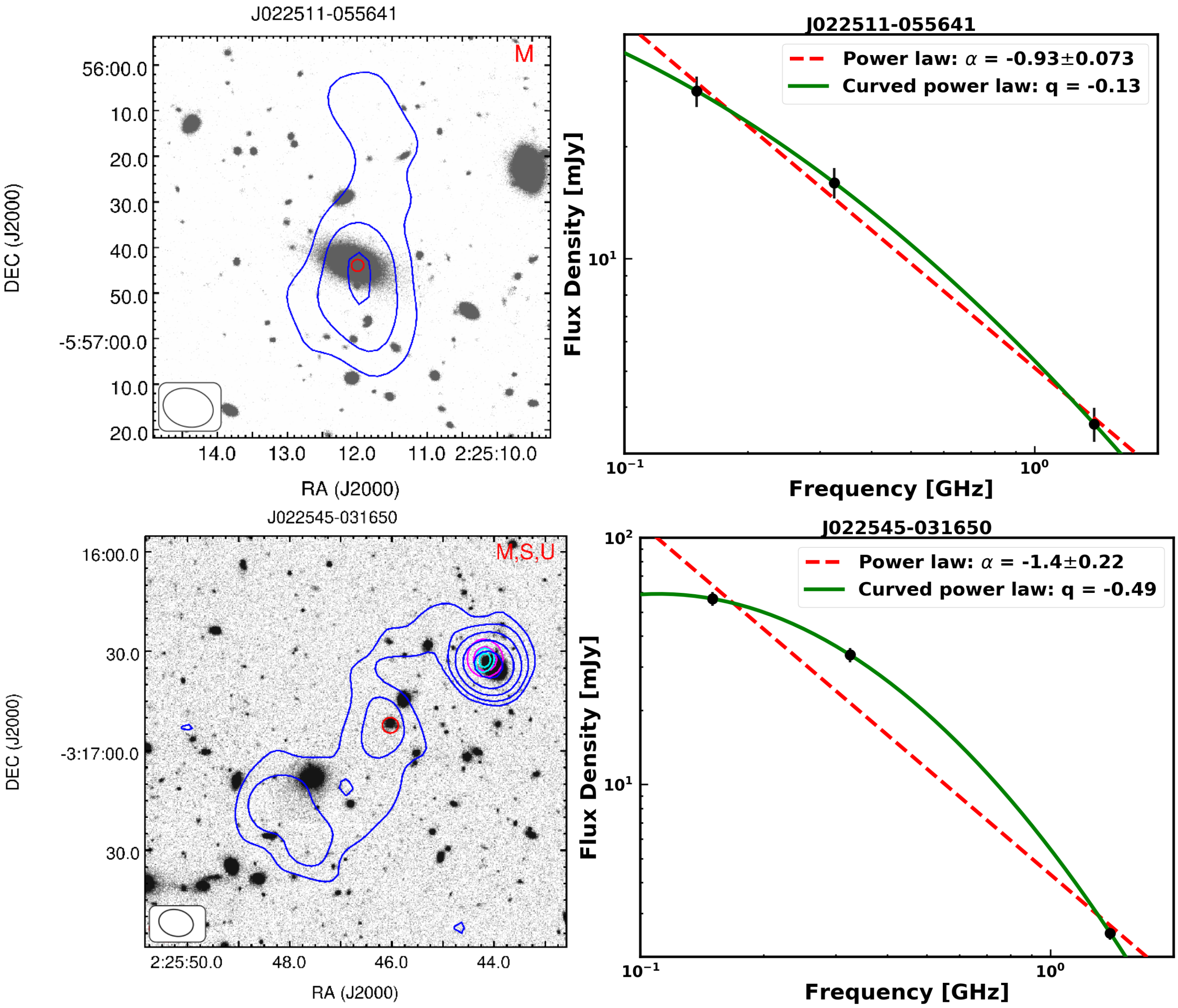

Figure 3.4: *Continue*

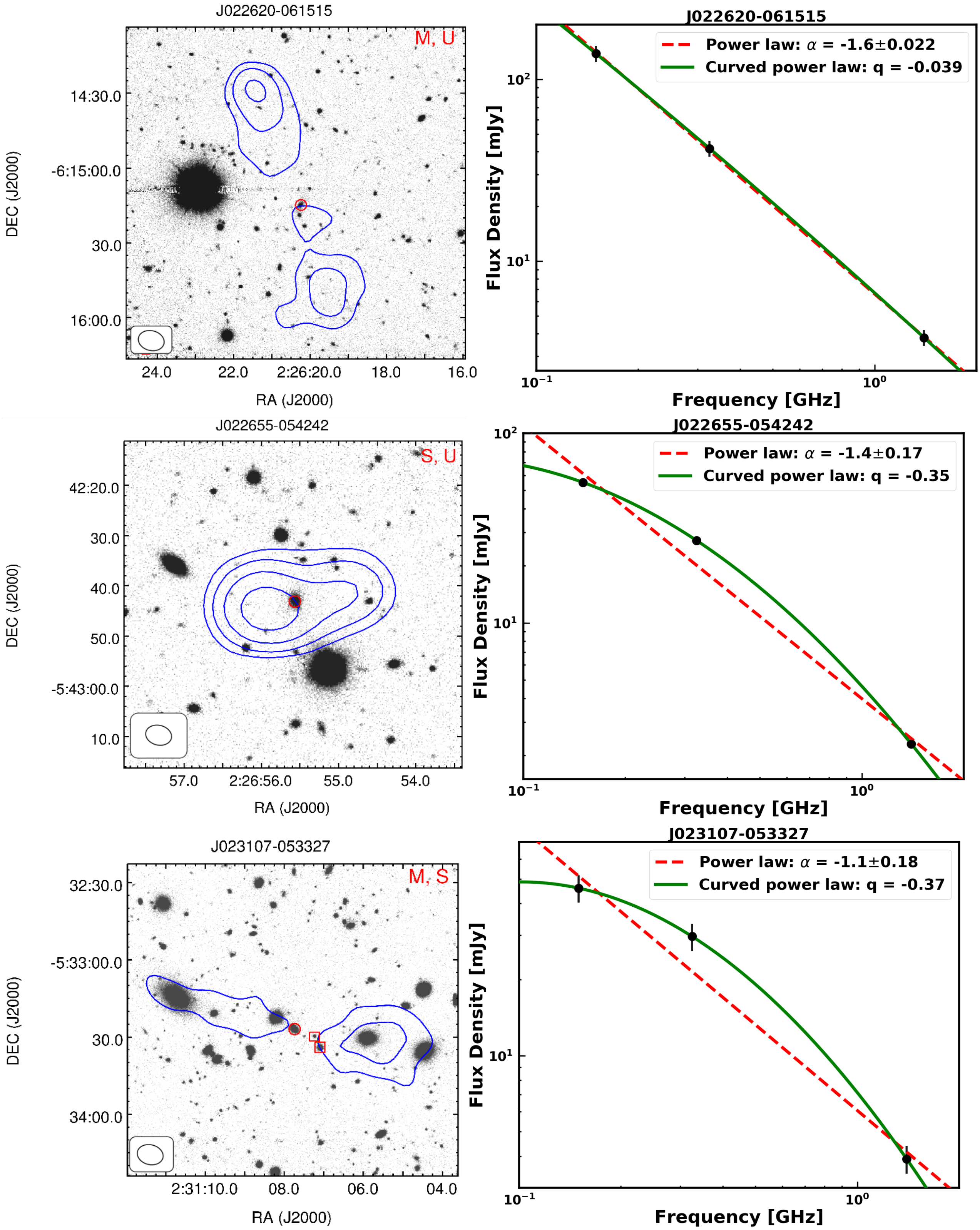

Figure 3.4: *Continue*

Table 3.3: The sample of remnant candidates.

Source Name	$S_{74\ \mathrm{MHz}}$ (mJy)	$S_{150\ \mathrm{MHz}}$ (mJy)	$S_{325\ \mathrm{MHz}}$ (mJy)	$S_{1.4\ \mathrm{GHz}}$ (mJy)	$\alpha_{150\ \mathrm{MHz}}^{1.4\ \mathrm{GHz}}$	$\alpha_{150\ \mathrm{MHz}}^{325\ \mathrm{MHz}}$	$\alpha_{325\ \mathrm{MHz}}^{1.4\ \mathrm{GHz}}$	$CP_{150\ \mathrm{MHz}}$ ($\times 10^{-3}$)	$SB_{325\ \mathrm{MHz}}$	Selection Criteria
(1)	(2)	(3)	(4)	(5)	(6)	(7)	(8)	(9)	(10)	(11)
J021130-033608		< 24.5	13.7±0.7	<2.5		>-0.76	<-1.16		47	M
J021246-033553	790±78	617.3±2.6	316.2±3.7	64.6±1.4	-1.01±0.01	-0.87±0.01	-1.09±0.02	<0.58	264	M
J021652-060410		56.1±1.5	46.6±2.7	10.5±1.3	-0.75±0.06	-0.24±0.05	-1.02±0.09	<6.4	65	M
J021655-025703		48.7±0.8	23.7±3.7	6.3±0.5	-0.92±0.04	-0.93±0.12	-0.91±0.12	<7.4	22	M
J021659-044918^{J}	920±120	428.2±1.8	155.3±2.5	9.2±0.5	-1.72±0.02	-1.31±0.01	-1.94±0.04	<0.14	105	M, S, U
J021812-064334		220.5±0.8	78.0±6.5	28.0±1.3	-0.92±0.02	-1.34±0.06	-0.70±0.07	<1.6	39	M
J021837-024552		79.6±1.3	41.6±3.1	9.8±0.5	-0.94±0.02	-0.84±0.06	-0.99±0.06	<4.5	68	M
J021855-040134^{J}		38.5±0.8	24.5±0.8	4.6±0.6	-0.95±0.06	-0.58±0.03	-1.15±0.09	<1.5	29	S
J022045-030735		39.2±0.6	16.5±1.5	<2.5	<-1.23	-1.12±0.07	<-1.29	<9.1	64	M, U
J022218-032137		85.5±0.9	27.8±2.3	6.3±0.5	-1.17±0.04	-1.45±0.06	-1.02±0.08	<4.2	28	M

J022231-042757[J]		48.7±0.6	29.0±0.9	3.9±0.5	-1.13±0.06	-0.67±0.03	-1.37±0.09	<1.2	160	S
J022252-060937		104.3±0.9	42.3±1.2	4.2±0.4	-1.44±0.04	-1.17±0.02	-1.58±0.07	<3.5	170	U, M
J022305-041232[J]		13.8±0.6	9.1±0.6	1.8±0.1	-0.91±0.02	-0.54±0.06	-1.11±0.05	<4.4	50	S
J022318-044526[J]		33.9±1.0	20.6±2.1	2.7±0.1	-1.13±0.01	-0.65±0.08	-1.39±0.07	<1.8	63	S
J022435-062004		41.0±1.4	21.6±1.5	3.0±0.4	-1.17±0.06	-0.83±0.06	-1.35±0.10	<8.8	132	S
J022500-032102	200±50	109.5±1.1	59.5±1.2	12.5±1.0	-0.97±0.04	-0.79±0.02	-1.07±0.06	<3.3	197	M
J022511-055641		28.2±0.3	16.0±1.5	3.6±0.6	-0.92±0.07	-0.73±0.07	-1.02±0.13	<12.8	63	M
J022545-031650		56.6±0.5	33.5±2.2	<2.5	<-1.39	-0.68±0.05	<-1.78	<6.4	37	M, S, U
J022620-061515		138.6±1.6	41.7±4.2	3.8±0.6	-1.61±0.07	-1.56±0.08	-1.64±0.13	<2.6	56	M, U
J022655-054242		55.1±1.1	27.2±0.8	2.3±0.5	-1.42±0.10	-0.91±0.03	-1.69±0.15	<6.5	198	S, U
J023107-053327		46.0±6.7	29.6±3.7	3.9±0.7	-1.10±0.10	-0.57±0.15	-1.39±0.15	<7.8	55	M, S

Notes – Column 1: Source name in J2000 coordinates; Column 2: 74 MHz flux density from the VLA observations; Column 3: 150 MHz flux density from the LOFAR observations; Column 4: 325 MHz flux density from the GMRT observations; Column 5: 1.4 GHz flux density from the NVSS, whenever available, otherwise from the JVLA observations; Column 6: global spectral index between 150 MHz and 1.4 GHz; Column 7: spectral index between 150 MHz and 325 MHz; Column 8: spectral index between 325 MHz and 1.4 GHz; Column 9: Upper limit on the core prominence (CP) where 3σ upper limit on the non−detected core is taken from 3.0 GHz VLASS or 1.4 GHz JVLA observations and total flux density is from 150 MHz LOFAR observations; Column 10: surface brightness (SB) in units of mJy arcsec^{-2} based on the 325 MHz GMRT observations; Column 11: selection criteria used to identify remnant candidate (M = morphology, S = spectral curvature, U = USS). Source falling within the JVLA observations region are marked with 'J' in Column 1.

Table 3.4: Redshifts, radio luminosities and sizes of remnant candidates.

Source Name	z	Reference	$\log L_{150\ \mathrm{MHz}}$ (W Hz^{-1})	$\log L_{325\ \mathrm{MHz}}$ (W Hz^{-1})	LAS ($''$)	Size (kpc)	Power law $\alpha_{\mathrm{fit}}^{\mathrm{PL}}$	Curved power law $\alpha_{\mathrm{fit}}^{\mathrm{CPL}}$	Curved power law q	SED
J021130-033608	>1.0		>26.11	>25.86	35.5	>284.3	<-1.00±0.10	-1.30±0.17	<-0.18	CPL
J021246-033553	1.16±0.11	HSS−SSP (p)	27.68	27.38	121.0	998.8	-0.87±0.10	-1.28±0.09	-0.17	CPL
J021652-060410	0.98±0.10	HSS−SSP (p)	26.37	26.29	63.0	502.1	-0.77±0.17	-1.30±0.30	-0.35	CPL
J021655-025703	0.65±0.04	HSS−SSP (p)	25.92	25.61	166.0	1149.1	-0.91±0.01	-0.90±0.06	0.01	PL
J021659-044918	1.3247±0.0011	SXDF (s)	27.92	27.47	155.0	1301.0	-1.60±0.12	-1.40±0.07	-0.24	CPL
J021812-064334	0.26±0.05	HSS−SSP (p)	25.65	25.19	117.0	469.1	-0.88±0.19	-0.50±0.05	0.29	CPL
J021837-024552	0.14±0.01	HSS−SSP (p)	24.61	24.33	98.5	241.6	-0.94±0.04	-1.00±0.08	-0.07	PL
J021855-040134	0.63±0.19	HSS−SSP (p)	25.79	25.59	60.7	413.8	-0.91±0.01	-0.90±0.06	-0.25	CPL
J022045-030735	0.76±0.07	HSS−SSP (p)	26.07	25.69	59.3	437.1	-1.20±0.05	-1.40±0.09	-0.08	PL
J022218-032137	0.58±0.05	HSS−SSP (p)	26.11	25.62	128.0	845.1	-1.10±0.12	-0.86±0.03	0.20	CPL

J022231-042757	>1.0		>26.45	>26.22	50.1	>401.2	-1.20±0.15	-1.60±0.07	-0.31	CPL
J022252-060937	0.73±0.23	HSS−SSP (p)	26.49	26.11	44.3	321.2	-1.50±0.10	-1.70±0.08	-0.19	CPL
J022305-041232	0.6314±0.0001	PRIMUS (s)	25.35	25.17	36.5	249.7	-0.93±0.13	-1.30±0.04	-0.26	CPL
J022318-044526	1.15±0.17	HSS−SSP (p)	26.44	26.22	78.0	642.1	-1.20±0.16	-1.70±0.05	-0.33	CPL
J022435-062004	1.89±0.16	HSS−SSP (p)	27.09	26.82	40.0	336.6	-1.20±0.12	-1.50±0.06	-0.23	CPL
J022500-032102	0.61±0.06	HSS−SSP (p)	26.22	25.95	64.0	429.5	-0.94±0.05	-1.10±0.07	-0.07	CPL
J022511-055641	0.3193±0.0001	SDSS (s)	24.96	24.72	65.0	302.1	-0.93±0.07	-1.10±0.04	-0.13	CPL
J022545-031650	0.36±0.07	HSS−SSP (p)	25.46	25.24	94.3	478.3	-1.40±0.22	-1.20±0.08	-0.49	CPL
J022620-061515	0.94±0.09	HSS−SSP (p)	26.97	26.45	107.0	844.2	-1.60±0.02	-1.70±0.13	-0.04	PL
J022655-054242	1.0255±0.0002	VIPER (s)	26.62	26.31	37.8	304.5	-1.40±0.17	-1.30±0.07	-0.35	CPL
J023107-053327	0.65±0.09	HSS−SSP (p)	25.95	25.76	110.0	764.2	-1.10±0.18	-1.30±0.11	-0.37	CPL

Notes – Spectroscopic and photometric redshifts are indicated by ‘s’ and ‘p’ within brackets in column 3. The linear angular size is measured from the 325 MHz GMRT image and represents end-to-end linear distance along the direction of maximum elongation. The $\alpha_{\rm fit}^{\rm PL}$ and $\alpha_{\rm fit}^{\rm CPL}$ represent spectral indices in power law and curved power law fits, respectively. The q value defines curvature parameter obtained from the curved power law model fit.

convex spectrum (see Quici et al., 2021). For optically−thin synchrotron emission arising from radio lobes, typical value of q ranges over -0.2≤ q ≤0. We note that the q parameter is not physically motivated and describes curvature only mathematically, although Duffy & Blundell (2012) suggested that q can be related to the physical quantities such as energy and magnetic field strength in radio lobes.

We note that the radio SEDs of all but three of our remnant candidates are limited within 150 MHz to 1.4 GHz spectral window, and only three sources have 74 MHz flux density measurements available. The best fit spectral parameters obtained with the power law as well as with the curved power law models are listed in Table 3.4. We find that the majority (17/21) of our remnant candidates are better fitted with a curved power law. For our remnant candidates, q parameter varies between -0.49 to 0.29 with a median value of -0.19±0.05. As expected (09/21) remnant candidates selected from the SPC criterion show systematically higher curvature with the q value ranging between -0.49 to -0.23 with a median value of -0.32±0.03. Two remnant candidates (J021812-064334 and J022218-032137) appear to show concave spectra (q >0) with 150 MHz flux density much higher than the value extrapolated from 325 MHz flux density and 325 MHz − 1.4 GHz spectral index ($\alpha_{325\ \mathrm{MHz}}^{1.4\ \mathrm{GHz}}$). Notably, both these sources have very low surface−brightness ($\mathrm{SB}_{325\ \mathrm{MHz}}$ = 39 mJy arcmin^{-2} and 28 mJy arcmin^{-2}, respectively), and hence, these sources can possibly contain more diffuse low−surface−brightness emission which is better detected at 150 MHz. We find that 04/21 of our remnant candidates are better fitted with a standard power law, and all but one of these sources are selected from the USS criterion. The USS remnant candidates are likely to be old with the break frequency shifted to the low−frequency regime (ν_b <325 MHz). To obtain physical parameters such as break frequency, remnant age, AGN duty cycle we require to fit the SED with the physical models that include active phase followed by a remnant phase after switching off the AGN activity. The continuous injection off model ($\mathrm{CI_{OFF}}$ model; (Komissarov & Gubanov, 1994)) is one of the commonly used models that considers a continuously injection phase (active phase) for a period of t_{ON} followed by a remnant phase for the duration of t_{OFF} with the total source age $t_s = t_{\mathrm{ON}} + t_{\mathrm{OFF}}$. We defer this exercise to chapter 5 where more flux density points are added to the radio SEDs from our uGMRT observations.

Table 3.5: Comparison between remnant candidates and active sources.

Parameter	Remnant Candidates			Active Sources			KS Test	
	N_{source}	Range	Median	N_{source}	Range	Median	D	p-value
$S_{150\ MHz}$ (mJy)	20	13.8−617.3	56.1±32.8	232	3.5−3053.7	67.8±39.2	0.18	0.48
$S_{325\ MHz}$ (mJy)	21	9.1−316.2	29.0±14.2	246	3.4−1800.9	41.0±19.3	0.26	0.11
$\alpha_{150\ MHz}^{1.4\ GHz}$	20	-1.72−-0.75	-1.10±0.05	223	-1.32−0.05	-0.79±0.02	0.17	0.54
z	19	0.14−1.89	0.65±0.09	159	0.059−2.66	0.84±0.05	0.22	0.27
Size (kpc)	19	241.6−1301	469.1±70.6	159	75.2−1651.1	314.3±22.8	0.44	1×10^{-3}
$\log L_{1.4\ GHz}$ (W Hz^{-1})	17	23.70−26.69	25.10±0.17	154	23.41−27.39	25.45	0.28	0.12
$\log L_{150\ MHz}$ (W Hz^{-1})	19	24.61−27.92	26.11±0.19	152	24.34−28.76	26.19±0.10	0.15	0.77
CP	20	>0.00014− >0.013	>0.0044	38	0.0017−0.305	0.025±0.011		
$SB_{325\ MHz}$ (mJy arcmin^{-2})	21	22.2−264	63.4±14.5					
q	20	-0.49−0.29	-0.19±0.04					

Notes − The two sample Kolmogorov−Smirnov (KS) test is a non−parametric statistical test that examines the hypothesis that two samples come from same distribution. D represents the maximum difference between the cumulative distributions of two samples and p−value is the probability that the null hypothesis, i.e., two samples comes from same distribution, is true. The error on the median value is taken as $\sigma_{SD}/\sqrt{N_{sample}}$ assuming normal distribution for the sample, where σ_{SD} is the standard deviation and N_{sample} is the sample size. Occasionally large errors found on the median values are due to the skewed non−Gaussian distributions.

3.4.2 Surface−Brightness

Remnants are expected to show low−surface−brightness emission as the radio emitting plasma in lobes radiates continuously with no supply of fresh energy. Low−surface−brightness may also arise due to the expansion of radio lobes if they are over−pressured at the end of active phase. For our remnant candidates, we estimate surface−brightness measured at 325 MHz (see Table 3.3). The surface−brightness of our remnant candidates is defined as the ratio of 325 MHz total flux density to the area over which radio emission is detected at $\geq 3\sigma$ level in the 325 MHz GMRT image. We note that the surface−brightness of remnant candidates should be estimated at the lowest frequency owing to the fact that remnants appear brighter at lower frequencies. However, due to unavailability of 150 MHz LOFAR images we estimate surface−brightness at 325 MHz. We find that the 325 MHz surface−brightness of our 21 remnant candidates are distributed in the range of 22.2 mJy arcmin^{-2} to 264 mJy arcmin^{-2} with a median value of 63.4$\pm$14.5 mJy arcmin^{-2} (see Table 3.3). The 15/21 remnant candidates identified with the morphological criterion have surface−brightness in the same range. While, 12/21 remnant candidates identified with the spectral criteria have surface−brightness in the range of 29 mJy arcmin^{-2} to 198.6 mJy arcmin^{-2} with a median of 64$\pm$20 mJy arcmin^{-2}. We find that irrespective of selection criteria remnant candidates tend to show low−surface−brightness. It is worth pointing out that Brienza et al. (2017) found 150 MHz surface−brightness in the range of 10−30 mJy arcmin^{-2} for their morphologically selected remnant candidates. In general, remnants of very low−surface−brightness are likely to be old in which energy loss has occurred over a much longer period, while the remnants of relatively higher surface−brightness can be relatively young. However, we note that the surface−brightness parameter is a frequency and resolution dependent parameter, and hence, surface−brightness measured with different observations may not be directly comparable.

3.4.3 Core Prominence

In the literature, core prominence (CP) defined as the ratio of core flux density to total flux density has been used as an indicator of the activity status (*e.g.*, Brienza et al., 2017). Remnant sources with no detected core can have only upper limits on CP that are expected to be systematically lower than the CP values for active sources of similar brightness. We determine the CP limits for our remnant candidates and compare their distribution *w.r.t.* active sources in our sample. Since, compact core is better detected in deep high resolution high−frequency observations, while extended radio emission from lobes is better detected in deep low−frequency observations, we define CP = $S_{\rm core}^{3.0\ \rm GHz}/S_{\rm total}^{150\ \rm MHz}$. The exact frequency at which core flux density is measured may not be very important owing to the fact that radio cores are generally expected to have flat spectrum upto higher frequencies (Hardcastle & Looney, 2008). We check the detection of core component in our sample sources by using 3.0 GHz VLASS, 1.4 GHz FIRST and 1.4 GHz JVLA image cutouts. The VLASS images with 3σ sensitivity of 0.36 mJy beam^{-1} and angular resolution of 2$''$.5 are better suited to detect and disentangle core component. However, deep JVLA observations with sensitivity (3σ = 0.048 mJy beam^{-1}) better than that for the VLASS and FIRST, are preferred, whenever available. We consider the detection of core above 3σ level, and task 'JMFIT' in the Astronomical Image Processing System (AIPS[4]) that fits an elliptical Gaussian to the core component, is used whenever core flux density is not listed in the catalogues.

For remnant candidates with undetected cores, we place an upper limit on CP by using 3σ limit on flux density. We note that the VLASS, JVLA and FIRST images of moderate resolutions (2$''$.5−5$''$.0) have limitations in detecting the core component in many of our sources, particularly in sources with relatively small sizes (<60$''$). Deep high−frequency radio observations yielding sub−arcsec resolution would be ideal to detect the core components in such sources. In our sample we obtain CP estimates for only 59 sources including upper limits placed on our 21 remnant candidates.

Figure 3.5 shows the distributions of CP parameter for the remnant candidates and active sources in our sample. 38 active sources have CP values distributed in the range

[4]http://www.aips.nrao.edu/index.shtml

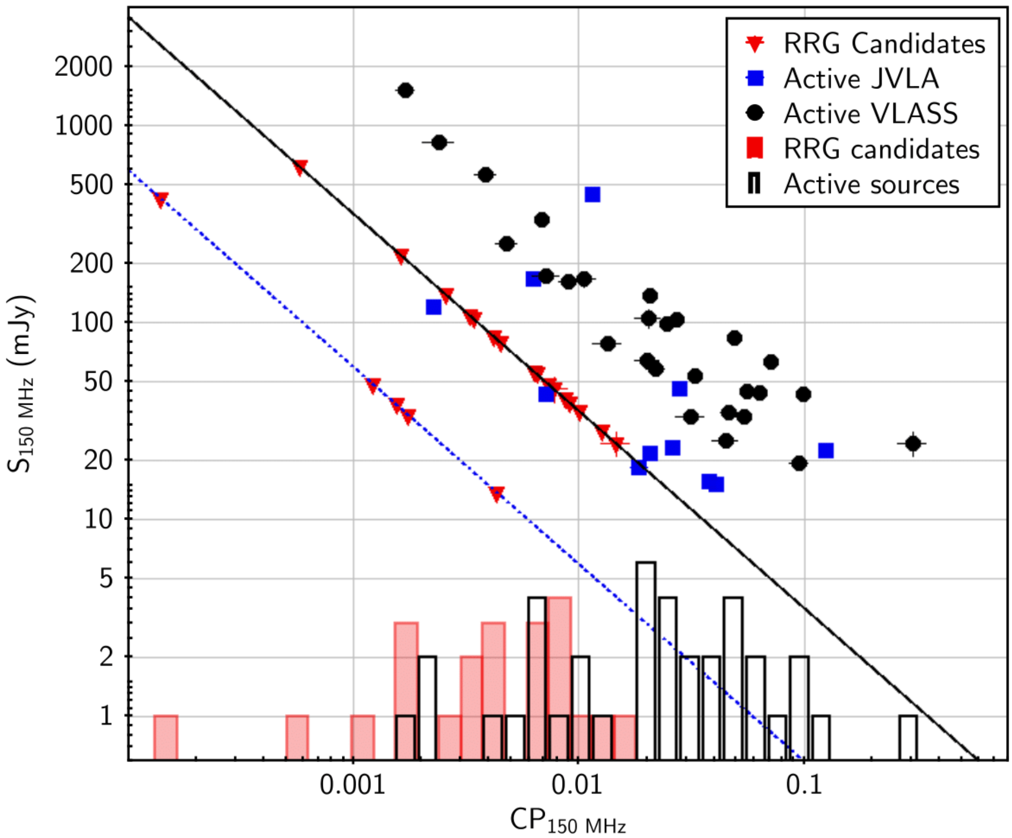

Figure 3.5: 150 MHz flux density versus core prominence (CP) parameter. For remnant candidates upper limits on CP are placed by using 3σ flux density limits from 3.0 GHz VLASS or 1.4 GHz JVLA observations. The upper limits on CP based on the 3σ sensitivity limits of 3.0 GHz VLASS and 1.4 GHz JVLA observations are shown in solid black line and dotted blue line, respectively. The histogram of CP is shown in the bottom where filled and empty bars represent the distributions of remnant candidates and active sources, respectively.

of 1.7×10^{-3} to 3.05×10^{-1} with a median value of $2.5 \pm 1.1 \times 10^{-2}$. While, 21 remnant candidates have upper limits on CP spanning over 1.4×10^{-4} to 1.3×10^{-2} with a median value of 4.4×10^{-3}. As expected remnant candidates have systematically lower CP limits than the CP values for active sources. In principle, remnant sources must have CP = 0 considering the absence of radio core, however, flux limited observations can only allow us to place an upper limit. Deep observations can put more stringent limits on CP. It is evident that the upper limits on CP derived from the JVLA observations are nearly one order of magnitude deeper than those from the VLASS or FIRST survey (see Figure 3.5).

We find that the CP limits of our remnant candidates are consistent with those for the remnant candidates reported in the literature (*e.g.*, Mahatma et al., 2018; Quici et al., 2021). Figure 3.5 demonstrates that the CP depends on the source flux density such that brighter sources tend to have lower CP in compared to fainter sources. The flux density dependence of CP suggests that it is difficult to assign a sharp cutoff limit on the CP to segregate active and remnant sources. In fact, powerful lobe−dominated FR II radio galaxies can have low CP values despite being active. Therefore, we conclude that CP cannot be considered a reliable parameter for identifying remnants.

3.4.4 Redshifts

The identification of host galaxies of radio sources is essential to estimate their redshifts and luminosities. We attempt to identify the host galaxies of our 268 extended radio sources by using the HSC−SSP imaging survey. To identify optical counterparts we opted a method similar to that followed by Jurlin et al. (2021). For double−lobed radio sources with clear or tentative detection of a core, optical counterpart closest to the core position within $5''.0$ of radius is considered. Search radius is similar to the synthesized beam−sizes of 1.4 GHz FIRST and JVLA observations. Although, most of the sources are found to show optical counterparts within $2''.0$. For double−lobed sources showing attached lobes with unresolved radio core we use flux density weighted centroid position to search for their optical counterparts. For our remnant sources with no detected radio core and detached radio lobes or amorphous morphology we search optical counterpart around the flux density weighted barycentre position that lies on the intersection of two lobes axes. We caution that the identification of a potential host galaxy of a radio source is tentative, if radio core is not detected.

With the aforementioned exercise we identified the optical counterparts of only 179/268 (66.8%) radio sources that have either spectroscopic or photometric redshift estimates. Only 79/179 sources have spectroscopic redshifts derived from various spectroscopic surveys (*e.g.*, PRIMUS, VIPER, and SDSS), while, remaining 100/179 sources have photometric redshifts from the HSC−SSP PDR2 (see Section 3.2.2). Among our 21 remnant candidates all but two have redshift estimates. For two remnant candidates with no redshift estimate we place an upper limit on the redshift (z) >1.0 by comparing them with the HzRGs of known redshifts in the $S_{1.4\ \mathrm{GHz}}$ versus $S_{3.6\ \mu\mathrm{m}}$ diagnostic plot (see Singh et al., 2017). Our 19 remnant candidates have redshifts in the range of 0.14 to 1.89 with a median value of 0.65±0.09, while 159 active sources having redshifts are distributed over the range of 0.059 to 2.66 with a median value of 0.84±0.05. The two−sample KS test shows that the redshift distributions for our remnant candidates and active sources are somewhat different with p−value = 0.27 (see Table 3.5). Thus, on average, our remnant candidates are found at lower redshifts than the active source population. The systematic difference in redshift distributions can possibly be due to observational bias considering the fact that morphological identification of remnant could preferentially pick nearby large−size sources. Although, we find that the redshifts of our remnant candidates tend to be higher than those reported in some of the previous studies in the literature. For instance, the remnant candidates identified in the Lockman−Hole and Herschel−ATLAS fields have the median redshift values 0.5 and 0.31, respectively (see Jurlin et al., 2021; Mahatma et al., 2018). The higher redshifts of our remnant candidates can be attributed to their relatively low radio flux densities and the deeper optical data used. We note that a large fraction of our sources only have photometric redshifts, and hence, results based on these redshift values should be treated with caution.

3.4.5 Large−Scale Environments

It has been suggested that the remnants residing in cluster environments can be detected over much longer timescales due to slow or even arrested expansion of lobes in dense intra−cluster medium, and hence, one can expect a higher tendency of remnants to reside in cluster environments (see Murgia et al., 2011). We investigate the large−scale environments of our remnant candidates by using existing cluster catalogs built from the optical and X−ray surveys in the XMM−LSS field. We used the HSC−SSP survey cluster catalog that consisted of clusters with richness (N_{gal}) ≥15 considering all galaxies brighter than 24 magnitude in z−band. The clusters detected in the HSC−SSP are found to be distributed over 0.1< z <1.1 redshift range with the photometric redshift accuracy of $\Delta z/(1+z)$ <0.01 (Oguri et al., 2021). Also, we used X−ray cluster catalog based on the deep *XMM−N* survey meant to detect X−ray emitting hot gas in intra−cluster medium with the flux limit of a few times of 10^{15} erg s^{-1} cm^{-2} in 0.5−10 keV band within $1'.0$ aperture (Adami et al., 2018). With the follow up optical spectroscopic observations X−ray detected clusters were found to have redshifts over $0.0 < z < 1.2$ with one cluster at $z =$ 2.0. In addition to the cluster catalogs we also use overdensity-selected cluster candidates catalog provided by Krefting et al. (2020) who identified 339 cluster candidates based on the photometric redshifts derived from multi-band (u-band to 4.5 μm) photometry in the 4.8 deg^2 of the XMM-LSS field. The cluster candidates are associated with dark matter halos with masses $\log(M_{halo}/M_{\odot}) > 13.7$ in the range $0.1 < z < 1.6$. In their sample Krefting et al. (2020) recovered 43 of the 70 known spectroscopically confirmed X-ray clusters (Adami et al., 2018), while the unrecovered ones are predominantly below $z =$ 0.4, where the X-ray clusters tend to have lower masses than the threshold value.

We matched our remnant candidates with all three catalogs. Within the redshift interval $\Delta z = 0.1$ (a typical photometric redshift error for our remnant candidates), and a radius corresponding to 1 Mpc, we find that only one (J022305-041232) of our remnant candidates is associated with the cluster which is detected in the optical photometric, spectroscopic and X−ray observations. Another remnant candidate J021659-0044918 (z = 1.3247±0.0011) is found to be associated with the cluster candidate present at redshift (z) = 1.069 − 1.372. The large range of redshift for the cluster candidate is attributed to large uncertainties of photometric redshifts (Krefting et al., 2020). Notably, none of these two remnant candidates reside in the centers of the respective clusters. The J022305-041232 host having $z = 0.6314$ is found to be at the projected distance of 187 kpc ($28''$) from the X−ray assigned cluster center. While, J021659-0044918 host is at the projected distance of 537.8 kpc ($63''.6$) from the center of respective cluster candidate. Considering the redshift upper limit ($z < 1.6$) for the existing clusters and cluster candidates catalogs, we find that, the fraction of our remnant candidates residing in cluster environments is only $2/18 \sim 11.1\%$. Hence, we conclude that, in general, our remnant candidates reside in less dense environments. This result is similar to that found in Jurlin et al. (2021) who reported that only a minority (23%) of remnants in their sample reside in cluster environments.

3.4.6 Radio Power versus Radio Size (P$-$D) Plot

Dynamical evolutionary models predict the growth of radio size as well as radio luminosity during the active phase of radio galaxies (An & Baan, 2012). In the remnant phase, radio luminosity decreases, while radio size can increase, if lobes are over$-$pressured. Therefore, radio power versus radio size diagnostic plot commonly known as the P$-$D plot in the literature, allows us to infer the evolutionary stage of radio galaxies. To examine the nature of our remnant candidates we check their positions in the P$-$D plot. Figure 3.6 shows 1.4 GHz luminosity versus radio size plot. We note that the projected linear size is measured as the end-to-end distance along the direction of maximum elongation in the 325 MHz image. To account for the presence of diffuse extended emission we consider emission upto 3σ level. The physical radio size is obtained from the linear angular size by using angular diameter distance at the corresponding redshift.

We find that, in comparison to active sources, our remnant candidates have systematically larger radio size lying in the range of 241.6 kpc to 1301 kpc with a median value of 469.1$\pm$70.6 kpc. While, active sources have radio sizes in the range of 75.2 kpc to 1651.1 kpc with a median value of 314.3$\pm$22.8 kpc (see Table 3.5). The two$-$sample KS test suggests that the radio size distributions of our remnant candidates and active sources are different with insignificant probability (1×10^{-3}) for null hypothesis, that the two sample come from the same distribution, to be true. We note that despite different radio size distributions for our remnant candidates and active sources, there is no sharp segregating value that can be used to differentiate remnant and active sources.

The P$-$D plot also demonstrates the comparison of radio luminosities for our rem-

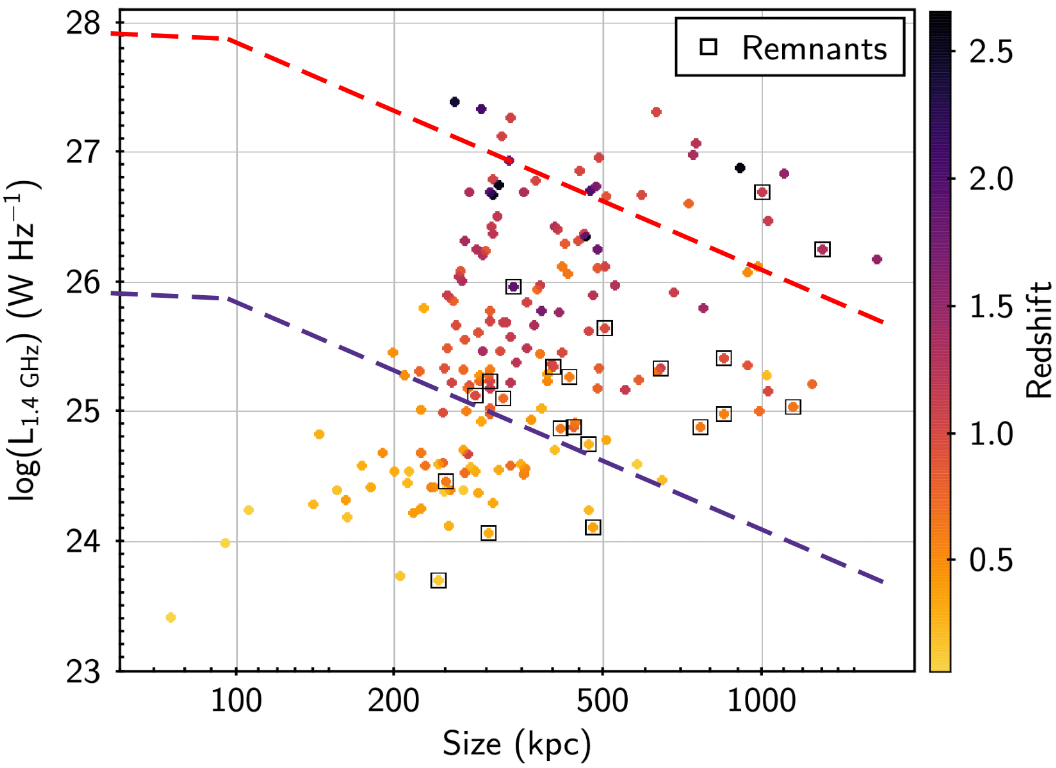

Figure 3.6: The plot of radio size versus 1.4 GHz radio luminosity. Our remnant candidates are marked with square boxes. The points without boxes around them represent active radio sources in our original sample from which remnant candidates are derived. The vertical color bar depicts redshift variation in our sample. The Red and Blue dashed lines represent the evolutionary tracks, as reported in An & Baan (2012), for high-power and low-power radio galaxies, respectively.

nant candidates and active sources. We estimate the total radio luminosity at rest frame where k−correction is applied by using the spectral index measured between 150 MHz and 1.4 GHz ($L_{1.4\ GHz} = 4\pi S_{1.4\ GHz}\, D_L^2\, (1+z)^{-(\alpha+1)}$, where $S_{1.4\ GHz}$ is flux density at 1.4 GHz and D_L is luminosity distance). There is no remarkable difference between 1.4 GHz radio luminosities of active sources and our remnant candidates (see Figure 3.6). We find that our 17 remnant candidates, with 1.4 GHz flux density and redshift estimates, have 1.4 GHz luminosities distributed in the range of 5.0 $\times$ 10^{23} W Hz^{-1} to 4.95 $\times$ 10^{26} W Hz^{-1} with a median value of 1.27$\pm$2.7 $\times$ 10^{25} W Hz^{-1}. While, 154 active sources show 1.4 GHz luminosities in the range of 2.58 $\times$ 10^{23} W Hz^{-1} to 2.47 $\times$ 10^{27} W Hz^{-1} with a median value of 2.84$\pm$0.30 $\times$ 10^{25} W Hz^{-1}. Thus, we find that 1.4 GHz radio luminosities of our remnant candidates tend to be systematically little lower than that for active sources.

The two−sample KS test shows that 1.4 GHz radio luminosity distributions of remnant candidates and active sources are drawn to from the same distribution with a probability of only 0.12. Although, we caution that the small number of remnant candidates must be taken into consideration while interpreting the statistical results.

Further, we also compare 150 MHz luminosities of remnant candidates and active sources noting the fact that the low−frequency radio observations are more effective in capturing diffuse emission of low−surface−brightness often seen in the evolved and remnant sources. The two−sample KS test suggests similarity in the radio luminosity distributions of remnant candidates and active sources with 77% probability for them to be drawn from same distribution (see Table 3.5). Notably, despite having somewhat different radio size distributions, the 150 MHz radio luminosity distributions of remnant candidates and active sources are similar. This result can be understood, if most of our remnant candidates continue to remain as luminous as active sources at 150 MHz even after the cessation of AGN activity. The high 150 MHz luminosities of our remnant candidates can only be expected, if majority of these are not too old, and have spectral break frequency at >150 MHz. Indeed, we find that many of our remnant candidates show strong spectral curvature with an apparent break at >325 MHz (see Section 3.4.1.2).

In the P−D plot we draw evolutionary tracks for radio galaxies reported in An & Baan (2012) (see Figure 3.6). It is clear that most of our sample sources are large-size radio galaxies similar to FR I and FR II type sources representing the late phase of evolution. We note that our P−D plot shows lack of small-size ($<$ 100 kpc) young radio sources due to the effect of radio size cutoff limit ($\geq 30''$) introduced in our sample. Further, owing to the use of deep radio and optical observations, our sample sources are found at relatively higher redshifts in the range of 0.059 to 2.66 with a median value of 0.82$\pm$0.04. The angular size cutoff limit of $30''$ corresponds to 35 kpc even at the lowest redshift of $z =$ 0.059. In fact, the source with the smallest angular size of $30''$ in our sample has redshift 0.77 and corresponding projected linear size of 222 kpc. Hence, lack of young radio sources representing early and intermediate evolutionary phases in our sample can be explained by the combined effect of angular size cutoff limit and the redshift distribution.

We also point out that our P−D plot shows a wide diversity in radio sizes of our remnant candidates in the range of 241.6 kpc to 1301 kpc. We note that the radio size of a remnant can depend on various factors such as the jet kinetic power during the active phase, longevity of active phase, and the large−scale cluster environment (Turner & Shabala, 2015). In general, small size remnant candidates have relatively low radio luminosities (see Figure 3.6). Thus, small size remnant candidates could have possessed jets of low kinetic power during their active phase, if radio luminosity is considered as the proxy for the jet power. Since, our small size remnant candidates mostly reside in non−cluster environments (see Section 3.4.5), then a low jet kinetic power and/or a relatively shorter active phase can be the plausible reasons for a relatively small radio size of our remnant candidates.

3.5 Fraction of Remnant Candidates

Determining the fraction of remnants ($f_{\rm rem}$) among the population of radio galaxies can help us to constrain the AGN duty cycle and evolutionary models. Using our search for remnant candidates we place an upper limit on $f_{\rm rem}$. Since we cannot rule out the possibility that some of our remnant candidates may still be active with the presence of a faint radio core falling below the detection limit we get only an upper limit on the number and fraction of remnants. Our 21 remnant candidates in a sample of 263 extended radio sources above a flux density cutoff limit $S_{325\ \rm MHz} > 6.0$ mJy (the completeness limit, see Section 3.5.2), yield an upper limit on $f_{\rm rem}$ to be only 21/263 < 8.0%. In Table 3.6, we list the fraction of remnants found in our study as well as in other previous searches in different deep fields. At first glance, the upper limit on $f_{\rm rem}$ < 8.0% found in our study appears consistent with that reported in some of the previous studies (*e.g.*, Mahatma et al., 2018; Quici et al., 2021). Moreover, while comparing $f_{\rm rem}$ reported in different studies one needs to account for the differences in sensitivity, resolution, and cutoff limits applied on flux density and angular size. In the following subsections, we discuss the effects of sensitivity, completeness and the flux density cutoff limit.

Table 3.6: Fraction of remnant sources in different deep fields.

Field	Sky Area (deg^2)	ν_{base} (MHz)	rms, ν_{base} (mJy b^{-1})	ν_{high} (GHz)	rms, ν_{high} (mJy b^{-1})	Search Criteria	Flux Limit (mJy)	Size Limit	Fraction of Remnants	Density (deg^{-2})	Ref.
(1)	(2)	(3)	(4)	(5)	(6)	(7)	(8)	(9)	(10)	(11)	(12)
XMM−LSS−JVLA	5.0	325	0.15	1.4	0.016	M, S, U	6.0	30″	5/103 <5%	1.0	1
XMM−LSS−Out	7.5	325	0.15	3.0	0.12	M, S, U	6.0	30″	16/160 <10.0%	2.1	1
XMM−LSS	12.5	325	0.15	1.4−3.0	0.016−0.12	M, S, U	6.0	30″	21/263 <8.0%	1.7	1
GAMA−23	8.3	216	0.9	5.5	0.024	M	10	25″	10/104 <10%	1.2	2
Herschel−ATLAS	140	150	0.1−2.0	6.0	0.020	M	80	40″	11/127 <9%	0.08	3
Lockman−Hole	35	150	0.15−0.9	6.0	0.050	M, S, U	40	40″	13/158 <8%	0.37	4
ATLBS−ESS	7.5	1400	0.072	1.4	0.072	M	1.0	30″	4/119 <4%	0.53	5

Note − Column 1 : Name of the deep field; column 2: Sky area used for remnant search; column 3: low−frequency at which remnant search is based (ν_{base}); column 4: noise−rms at the base frequency observations (rms, ν_{base}); column 5: high−frequency observations used to detect core and compact features (ν_{high}); column 6: noise−rms of high−frequency observations (rms, ν_{high}); column 7: Criteria used to search for remnant candidates (M: morphological criterion, S: spectral curvature criterion, U: USS criterion); column 8: Flux cutoff limit used in the sample; column 9: Linear angular size cutoff applied in the sample; column 10: Upper limit on the fraction of remnants; column 11: surface number density of remnant candidates; column 12: References − (1) This work, (2) Quici et al. (2021), (3) Mahatma et al. (2018), (4) Jurlin et al. (2021), (5) Saripalli (2012). The flux density cutoff is applied at the corresponding base frequency.

3.5.1 Effect of Sensitivity and Resolution

For our remnant candidates, we checked for the absence of radio core by using deep 1.4 GHz JVLA observations in the XMM−LSS−JVLA region and 3 GHz VLASS observations in the XMM−LSS−Out region. The comparison of remnant fraction in the XMM−LSS−JVLA region and in the XMM−LSS−Out region can easily demonstrate the effect of sensitivity. In the XMM−LSS−JVLA region we find only 5 remnant candidates among 103 radio sources, giving an upper limit on $f_{\rm rem}$ < 5% (see Table 3.6). In the XMM−LSS−Out region, where 3 GHz VLASS images are used for the core detection, we find a much higher $f_{\rm rem}$ to be 16/165 < 9.7%. The lower remnant fraction in the XMM−LSS−JVLA region can be explained as the absence of radio core is examined at a much fainter level. Thus, we demonstrate that deep JVLA observations allow us to place a much tighter constraint on the remnant fraction. We note that, in comparison to the previous searches based on the low−frequency radio observations, we obtain the lowest $f_{\rm rem}$ < 5% (see Table 3.6). The lowest fraction obtained in our study may be attributed to the lowest flux density cutoff limit ($S_{\rm 325\ MHz} \geq 6.0$ mJy) that causes rapid increase in the number of active sources at the fainter level. We note that, in the ATLBS−ESS field Saripalli (2012) searched for remnants to the flux limit of 1.0 mJy at 1.4 GHz and found remnant fraction < 4%. Although, unlike low−frequency observations, 1.4 GHz observations are likely to miss the detection of sources having low−surface−brightness emission, which in turn can lead to a lower remnant fraction.

3.5.2 Completeness

The completeness of a sample above a flux density limit is an important factor in determining the fraction. An incomplete sample lacking the detection of all sources at the fainter end can over−estimate the remnant fraction. To assess the flux density completeness in our sample, we check the distribution of 325 MHz integrated flux density and find a limit of 6.0 mJy above which our sample can be treated as complete. The completeness flux limit corresponds to 10.3 mJy at 150 MHz, assuming a typical spectral index of

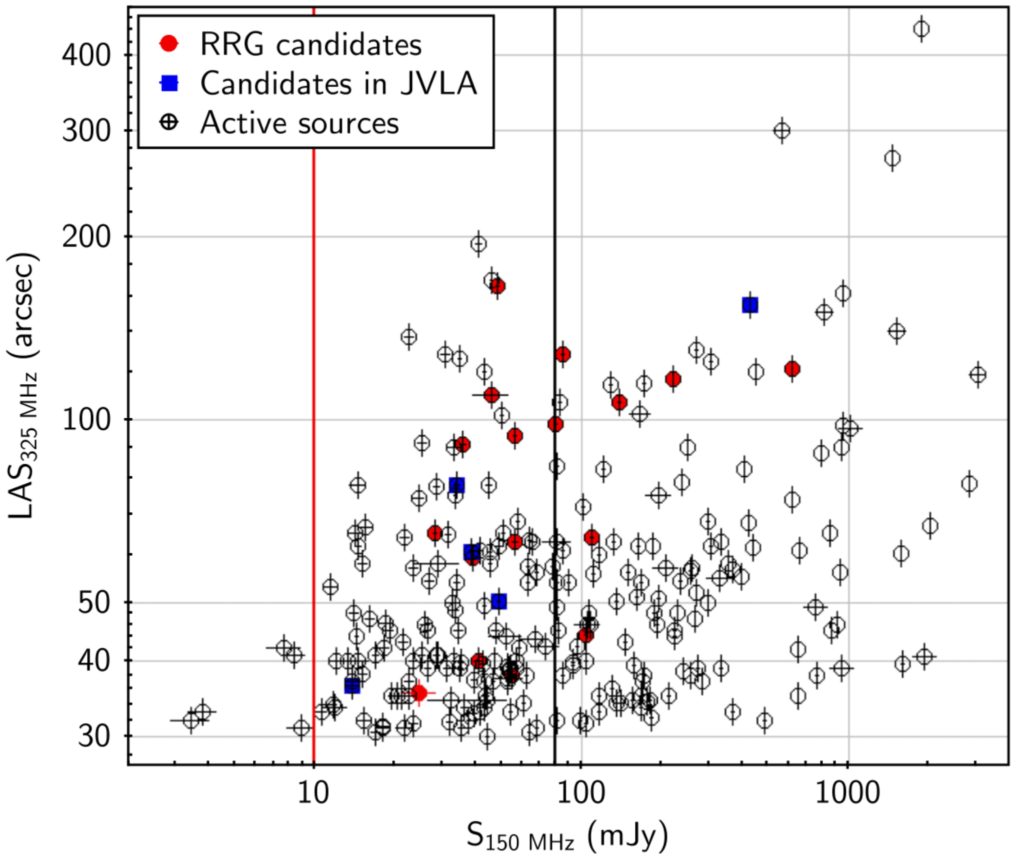

Figure 3.7: 150 MHz flux density versus linear angular size measured at 325 MHz. Fiducial 5 per cent error bars are placed in the LAS. The vertical red line at 10.3 mJy represents the completeness limit, while the vertical black line represents 80 mJy flux cutoff limit used by Mahatma et al. (2018).

-0.7. We find 263 out of 268 sources falling above the flux density limit ($S_{325\ \mathrm{MHz}} \geq 6.0$ mJy). Thus, with the use of flux limit cutoff we ensure not to over−estimate the remnant fraction.

3.5.3 Remnant Candidates at the Fainter Regime

In this subsection we attempt to highlight the importance of searching for remnant candidates at lower flux densities. From Figure 3.7 showing a plot of 150 MHz flux density versus LAS, it is evident that the remnant fraction depends on the flux density at which they are searched. We note that our 21 remnant candidates have 150 MHz flux density in the range of 13.8 mJy to 617.3 mJy with a median value of 55.1±39.3 mJy. A higher flux density cutoff limit, for instance 80 mJy as used by Mahatma et al. (2018), would limit us to detect only 7/21 of our remnant candidates. Thus, a significant fraction of remnant candidates (14/21 $\sim$ 67%) would be missed by applying a high flux density cutoff limit of 80 mJy. Brienza et al. (2017) also placed a flux density cutoff limit at $S_{150\ \rm MHz}$ = 40 mJy. Hence, our study presents the search for remnant candidates in one of the faintest flux regime reaching down to 10 mJy at 150 MHz.

From Figure 3.7 it is evident that the remnant fraction is low at higher flux densities. By dividing our sample at $S_{150\ \rm MHz}$ = 80 mJy we find a lower remnant fraction of (7/119) $<$ 5.9% at $S_{150\ \rm MHz}$ $>$ 80 mJy, and a higher remnant fraction of (14/150) $<$ 9.7% at $S_{150\ \rm MHz}$ $<$ 80 mJy. The comparison of remnant fraction above and below 80 mJy is much starker in the XMM$-$LSS$-$JVLA region *i.e.*, one remnant candidate above 80 mJy limit and four remnant candidates below 80 mJy. In brief, we conclude that the remnant fraction depends on the flux density regime at which remnants are probed, and a high flux cutoff limit would be hindrance in unveiling the full population of remnants. It is also worth pointing out that the remnant candidates of relatively large angular sizes are present at higher flux densities. While, remnant candidates of small sizes (LAS $<$ 50$''$) are found at relatively lower flux densities *i.e.*, $S_{150\ \rm MHz}$ $<$100 mJy (see Figure 3.7).

The comparison of surface number density of remnant candidates in different flux limited observations can further demonstrate the importance of searching them at lower flux densities. For instance, in the XMM$-$LSS$-$JVLA region we find only five remnant candidates over an area of 5.0 deg^2 yielding surface number density of 1.0 source deg^{-2}. In the XMM$-$LSS$-$Out region, the surface number density of remnant candidates is 16/7.5 $\sim$ 2.1 deg^{-2}. The higher number density in the XMM$-$LSS$-$Out region is owing to the use of the relatively shallow VLASS and FIRST observations for the core detection. The remnant number density in the Herschel$-$ATLAS field in only 11/140 $\sim$ 0.08 deg^{-2} that can mainly be attributed to the high flux cutoff limit of $S_{150\ \rm MHz}$ = 80 mJy. Albeit, deep observations used for the core detection would also bring down the remnant fraction and the number density. Interestingly, in the XMM$-$LSS$-$JVLA region we examined the detection of core at similar depth and obtain a higher surface number density than that found in the Herschel$-$ATLAS field (see Table 3.6). We point out that the surface number density of remnant candidates in the XMM$-$LSS$-$JVLA region is similar to that found in the GAMA−23 field in which the flux density cutoff limit is comparable to that for our sample.

3.5.4 Implications of Remnant Fraction

In the literature, there have been attempts to design models that can explain the evolution of radio galaxies and can predict the remnant fraction (Brienza et al., 2017). Recent, evolutionary models predict that the remnant fraction depends inversely to the duration of the active phase ($t_{\rm on}$) (see Shabala et al., 2020). Radio galaxies with longer active phase would result into large−size remnants that would fade rapidly and yield a lower remnant fraction. While, radio galaxies with relatively shorter active phase would result in small−size remnants that can be detected for a relatively longer time−scale in the remnant phase, and hence, can show a higher remnant fraction. In fact, a high remnant fraction (>30%) has been obtained with the models assuming a relatively shorter (30−40 Myr) average life−time of the active phase (see Brienza et al., 2017). To model active, remnant and restarted source population Shabala et al. (2020) considered $t_{\rm on}$ and jet kinetic power ($Q_{\rm jet}$) as the key parameters for the growth of a radio galaxy and found that a model assuming constant age $t_{\rm on}$ = 300 Myr, and power law distribution of log($Q_{\rm jet}$) with an index of -0.8 to -1.2 predicts the fraction of remnant plus restarted sources to be only 2−5%. While, a somewhat higher fraction (10%) of remnant plus restarted sources can be modelled, if power law distributions with an index in the range of -0.8 to -1.2 are assumed for both $t_{\rm on}$ and $Q_{\rm jet}$. A low fraction of only remnant sources (<5%) obtained in our study seems consistent with the model proposed by Shabala et al. (2020).

3.6 Results and Conclusions

In this chapter, we attempt to search and characterize remnant candidates in the XMM−LSS field using deep 150 MHz LOFAR, 325 MHz GMRT, 1.4 GHz JVLA and 3 GHz VLASS observations. These are some of the deepest observations available at the respective frequencies till date. We used both morphological as well as spectral criteria to identify the full population of remnant candidates. Salient features of our study are outlined as below.

- We identified 21 remnant candidates in a sample of 263 extended radio sources (SNR$\geq$10, size$\geq$30$''$, and $S_{325\ \mathrm{MHz}} \geq 6.0$ mJy) derived from the 325 MHz GMRT observations over 12.5 deg^2 in the XMM$-$LSS field.

- Majority (15/21 = 71%) of our remnant candidates can be identified by using the morphological criterion ***i.e.***, absent core. We find that the spectral curvature criterion is useful in identifying remnant candidates of small angular sizes (<60$''$) which pose difficulty in deblending core from lobes using images of 2$''$.5$-$5$''$.0 resolution.

- Unlike previous studies (***e.g.***, Brienza et al., 2017; Mahatma et al., 2018) our study attempts to search for remnants at the faint regime reaching down to 6.0 mJy at 325 MHz that corresponds to 10.3 mJy at 150 MHz assuming a typical spectral index of -0.7. Our remnant candidates have 150 MHz flux densities distributed in the range of 13.8 mJy to 617.3 mJy with a median value of 55.1$\pm$39.3 mJy.

- Our remnant candidates show a wide range of characteristics in terms of spectral index, linear radio size, radio luminosity, and surface$-$brightness. In comparison to active sources our remnant candidates exhibit steeper spectra ($\alpha_{150\ \mathrm{MHz}}^{1.4\ \mathrm{GHz}}$ spans over -1.71 $-$ -0.75 with a median value of -1.10$\pm$0.05), larger radio sizes (in the range of 242 kpc to 1301 kpc with a median value of 469.1$\pm$70.6 kpc), lower surface$-$brightness (in the range of 22.2 to 264 mJy arcmin^{-2} with a median value of 63.4$\pm$14.5 mJy arcmin^{-2}). Although, distributions of various parameters show no sharp division between remnant candidates and active sources.

- Using P$-$D plot we find that our sample sources represent mostly evolved radio galaxies and follow evolutionary tracks reported in An & Baan (2012). As expected, the radio sizes of our remnant candidates tend to be systematically larger than that for active sources, while 1.4 GHz radio luminosities of remnant candidates are little lower than that for active sources. Moreover, 150 MHz radio luminosity distribution of our remnant candidates is similar to that for active sources, suggesting that most of our remnant candidates continue to remain as luminous as active sources at 150 MHz even after the cessation of AGN activity.

- Using cluster catalogs based on the deep HSC−SSP optical and *XMM−N* X−ray surveys we find that only one of our remnant candidates is associated with the cluster environment. Therefore, we conclude that, in general, remnants reside in non−cluster environments which is consistent with the result reported in Jurlin et al. (2021).

- Deep JVLA observations allow us to place a stringent constraint on the remnant fraction to be (5/103) <5% in the XMM−LSS−JVLA region. The remnant fraction (<5%) found in our study is the lowest, compared to previous studies (*e.g.*, Mahatma et al., 2018; Jurlin et al., 2021).

- The low fraction of remnants (<5%) obtained in our study seems to be consistent with the model proposed by Shabala et al. (2020) who assumed power law distributions for the active phase life−time and jet kinetic power with index -0.8 to -1.2 to explain the observed 10% or a higher fraction of remnant plus restarted sources. Further, it predicts a larger population of small−size remnants, which is evident from our study.

- Our study shows that the remnant fraction depends on the flux density at which remnants are searched. A high flux density cutoff limit would miss a substantial fraction of remnants, and in turn, would change the remnant fraction. Thus, our study demonstrates the importance of searching for remnants at the fainter level to detect an unexplored population of remnants.

3.7 Appendix - Notes on Individual Remnant Candidates

In this section, we provide a brief description about each of our remnant candidate.

3.7.1 J021130-033608

This is a relatively faint source detected at 325 MHz with $S_{325\ \mathrm{MHz}}$ = 13.7±0.7 mJy. Non-detection in the NVSS places an upper limit on the spectral index ($\alpha_{325\ \mathrm{MHz}}^{1.4\ \mathrm{GHz}}$) < -1.16.

This source falls outside the LOFAR survey region and hence only an upper limit on $\alpha_{150\ \mathrm{MHz}}^{325\ \mathrm{MHz}}$ < -0.76 is obtained by using TGSS flux limit of 24.5 mJy. The steep spectrum and an apparently relaxed lobe morphology are indicative of remnant status. There is no detection of potential host galaxy in the optical as well as in the WISE W1 3.6 μm images. Using an upper limit on [3.6] magnitude < 0.08 mJy and $S_{1.4\mathrm{GHz}}$ versus $S_{3.6\ \mu\mathrm{m}}$ diagnostic plot we place an upper limit on the redshift $z > 1$.

3.7.2 J021246-033553

This source is classified as a remnant candidate based on the morphological criterion with no detection of a radio core in the FIRST as well as VLASS images. Both radio lobes are edge-brightened suggesting for a recently switched off AGN. The radio spectrum is steep ($\alpha_{150\ \mathrm{MHz}}^{1.4\ \mathrm{GHz}}$ = -1.01±0.01) but with a little curvature ($q = -0.1$). A probable host galaxy is detected in the HCS-SSP *i* band image with a photometric redshift of 1.16±0.11. Its high radio luminosity ($\log L_{150\ \mathrm{MHz}}$ = 27.68) and large radio size of nearly 1.0 Mpc suggest the progenitor to be a powerful FR II radio galaxy.

3.7.3 J021652-060410

This remnant candidate is identified from the morphology with no detection of a radio core in the FIRST as well as VLASS images. The radio spectrum shows a strong curvature with $\Delta\alpha = \alpha_{150\ \mathrm{MHz}}^{325\ \mathrm{MHz}}$ - $\alpha_{325\ \mathrm{MHz}}^{1.4\ \mathrm{GHz}}$ = 0.75. Notably, morphology of radio lobes indicates for the back flow of plasma.

3.7.4 J021655-025703

This source is identified as a remnant candidate based on the morphological criteria. The radio lobes of low-surface-brightness emission ($SB_{325\ \mathrm{MHz}} \sim 22$ mJy arcmin^{-2}) devoid of any compact features strengthen its remnant status. The radio SED can be fitted with a simple power law of index $\alpha_{150\ \mathrm{MHz}}^{1.4\ \mathrm{GHz}}$ = -0.92±0.04. The projected linear radio size of 1149 kpc makes it a giant radio galaxy. The HSC-SSP i band optical image shows a potential host galaxy at redshift (z_{phot}) 0.65±0.04.

3.7.5 J021659-044918

This source is identified as a remnant candidate based on all three criteria ***i.e.***, absence of a radio core, strong spectral curvature ($\Delta\alpha$ = $\alpha_{150\ \mathrm{MHz}}^{325\ \mathrm{MHz}}$ - $\alpha_{325\ \mathrm{MHz}}^{1.4\ \mathrm{GHz}}$ = 0.63) and ultra-steep spectral index ($\alpha_{150\ \mathrm{MHz}}^{1.4\ \mathrm{GHz}}$ = -1.72±0.02). The potential host galaxy is found at z_{spec} = 1.32±0.01. The end-to-end physical size of 1301 kpc makes this source a giant radio galaxy. This sources was also discovered serendipitously by Tamhane et al. (2015).

3.7.6 J021812-064334

This source shows diffuse relaxed lobes devoid of any compact features (see Figure 3.4). The surface-brightness of this source is very low ***i.e.***, $\mathrm{SB}_{325\ \mathrm{MHz}}$ = 39 mJy arcmin^{-2}. Notably, radio SED of this source is unusually concave showing a higher 150 MHz flux density than that extrapolated from 325 MHz flux density using 325 MHz − 1.4 GHz spectral index. The higher flux density at 150 MHz can be explained if a more diffuse emission is detected at 150 MHz than that at 325 MHz. The total linear radio size is found to be 469 kpc at the redshift (z_{phot} = 0.26±0.05) of potential host galaxy.

3.7.7 J021837-024552

This source shows edge-brightened lobes with no detected core in the FIRST and VLASS images. It also shows a steep spectrum ($\alpha_{150\ \mathrm{MHz}}^{325\ \mathrm{MHz}}$ = -0.94±0.02). There are three elliptical galaxies seen close to the centroid radio position (see Figure 3.4). The HSC-SSP image shows a bright elliptical galaxy (G1) at RA = 02 18 36.81, and DEC = -02 45 57.71, with i = 16.40±0.01 and redshift (z_{spec}) = 0.139± 0.001. Another galaxy (G2) with i

band magnitude 17.50±0.01 seems to have similar redshift ($z_{\rm phot}$) = 0.16±0.01. A third galaxy is somewhat fainter with i mag = 18.36 and $z_{\rm phot}$ = 0.18±0.04. By overlaying radio contours on the optical image we consider G1 as the most probable host galaxy.

3.7.8 J021855-040134

This source is identified as a remnant candidate by using spectral curvature criteria with $\Delta\alpha$ = $\alpha_{\rm 150\ MHz}^{\rm 325\ MHz}$ - $\alpha_{\rm 325\ MHz}^{\rm 1.4\ GHz}$ = 0.53. It lies within the XMM-LSS-JVLA region and shows no radio core in the deep JVLA image. The surface-brightness is also low (SB$_{\rm 325\ MHz}$ = 29 mJy arcmin^{-2}). This source has a linear radio size of 414 kpc at the redshift ($z_{\rm phot}$ = 0.63±0.18) of potential host galaxy.

3.7.9 J022045-030735

This source is identified as a remnant based on its diffuse relaxed morphology and ultra-steep spectrum. It shows low surface-brightness *i.e.*, SB$_{\rm 325\ MHz}$ = 64 mJy arcmin^{-2}. The 325 MHz radio emission shows elongation along north-west to south-east direction with a total linear size of 437 kpc at the redshift (z = 0.7590±0.0734) of the potential host galaxy (see Figure 3.4). This sources is detected in the 150 MHz LOFAR observations and 325 MHz GMRT observations but remained undetected at 1.4 GHz NVSS which gives an upper limit on $\alpha_{\rm 150\ MHz}^{\rm 1.4\ GHz}$ < -1.23.

3.7.10 J022218-032137

The 325 MHz image of this source shows diffuse relaxed lobes of low surface-brightness (28 mJy arcmin^{-2}). The radio spectrum shows a strong curvature with $\Delta\alpha$ = $\alpha_{\rm 150\ MHz}^{\rm 325\ MHz}$ - $\alpha_{\rm 325\ MHz}^{\rm 1.4\ GHz}$ = 0.43, and steep spectrum ($\alpha_{\rm 150\ MHz}^{\rm 1.4\ GHz}$ = -1.17±0.04). Thus, both morphological and spectral characteristics suggest its remnant nature. Notably, this source shows an unusual concave spectrum with 150 MHz flux density much higher than that extrapolated from 325 MHz. The concave spectrum can be explained if additional flux density is observed only at 150 MHz from a very low surface brightness relic emission. Also, concave spectrum can arise from a recent particle acceleration or a recent AGN-jet activity but currently available radio morphological features do not support it. The source has a linear radio size of 845 kpc at the redshift ($z_{\rm phot}$ = 0.58±0.05) of potential host galaxy.

3.7.11 J022231-042757

This remnant candidate is identified using spectral curvature criterion ($\Delta\alpha$ = -0.7) and ultra-steep spectral index criterion ($\alpha_{325\ \rm MHz}^{1.4\ \rm GHz}$ = -1.37±0.09). Its radio morphology shows north-south elongation with no compact components (see Figure 3.4). A potential host galaxy is not detected in the optical HSC-SSP *i* band image. We place a lower limit on the linear radio size >401 kpc using z >1.0 limit.

3.7.12 J022252-060937

This remnant candidate is identified based on the USS criterion *i.e.*, $\alpha_{150\ \rm MHz}^{1.4\ \rm Hz}$ = -1.44±0.04. The 325 MHz image shows a double-lobe radio morphology surrounded by a diffuse radio emission. The total linear radio size is 338 kpc at the redshift ($z_{\rm phot}$) = 0.84±0.23 of potential host galaxy.

3.7.13 J022305-041232

The remnant candidate is identified by using spectral curvature criterion *i.e.*, $\Delta\alpha$ = $\alpha_{150\ \rm MHz}^{325\ \rm MHz}$ - $\alpha_{325\ \rm MHz}^{1.4\ \rm GHz}$ = 0.57. It is one of the faintest ($S_{325\ \rm MHz}$ = 9.1±0.6 mJy) and smallest (LAS ∼ 36″) sources in our sample. It shows the importance of SPC criterion that can be enable us to identify remnants of small angular sizes. The total linear radio size is ∼ 250 kpc at the redshift ($z_{\rm spec}$ = 0.6314±0.0001) of the potential host galaxy.

3.7.14 J022318-044526

This remnant candidate is identified by using SPC criterion. The radio core is undetected in the FIRST as well as VLASS images. It shows edge-brightened double-lobe radio morphology in the 325 MHz image (see Figure 3.4). The presence of hotspots suggests it to be a young remnant. The total linear radio size is 642 kpc at the redshift of ($z_{\rm phot}$ = 1.15$\pm$0.17) of the potential host galaxy.

3.7.15 J022435-062004

This remnant candidate is identified by using SPC criterion *i.e.*, $\Delta\alpha = \alpha_{\rm 150\ MHz}^{\rm 325\ MHz}$ - $\alpha_{\rm 325\ MHz}^{\rm 1.4\ GHz}$ = 0.52. The 325 MHz image shows a double-lobe radio morphology (see Figure 3.4). This source remained undetected in 1.4 GHz FIRST image suggesting the presence of dominant diffuse emission detected only at the low frequencies. The linear radio size corresponds to 337 kpc at the redshift ($z_{\rm phot}$ = 1.89$\pm$0.16) of potential host galaxy.

3.7.16 J022500-032102

This remnant candidate is identified by using morphological criteria with no radio core detected in the FIRST as well as VLASS images. The FIRST image shows only a feeble detection of a peak emission at the south-west lobe (see Figure 3.4). It also shows a steep spectral index *i.e.*, $\alpha_{\rm 150\ MHz}^{\rm 1.4\ GHz}$) = -0.97$\pm$0.04. The total linear radio size scales to 430 kpc at the redshift of ($z_{\rm phot}$ = 0.61$\pm$0.06) potential host galaxy.

3.7.17 J022511-055641

This remnant candidates is identified by using morphological criteria. The 325 MHz GMRT image shows a diffuse emission with no apparent individual lobes (see Figure 3.4).

The radio SED is steep ($\alpha_{150\ \mathrm{MHz}}^{1.4\ \mathrm{GHz}}$ = -0.92±0.04) with a mild curvature ($\Delta\alpha$ = $\alpha_{150\ \mathrm{MHz}}^{325\ \mathrm{MHz}}$ - $\alpha_{325\ \mathrm{MHz}}^{1.4\ \mathrm{GHz}}$ = 0.29). The total linear radio size corresponds to 302 kpc at the redshift of (z_{spec} = 0.3193±0.0001) potential host galaxy.

3.7.18 J022545-031650

This remnant candidate is identified by using both morphological and spectral criteria. The 325 MHz GMRT image shows a diffuse emission devoid of any compact features. The average surface-brightness is fairly low *i.e.*, $\mathrm{SB}_{325\ \mathrm{MHz}}$ = 37 mJy arcmin^{-2}. The enhanced surface-brightness at the north-west lobe is due to the contamination from a foreground galaxy located at RA = 02$^{\mathrm{h}}$ 25$^{\mathrm{m}}$ 44$^{\mathrm{s}}$.00, DEC = -03° 16′ 34″.90 with redshift ($\mathrm{z_{phot}}$) 0.186±0.0336 (see Figure 3.4). Its radio spectrum shows a strong curvature ($\alpha_{150\ \mathrm{MHz}}^{325\ \mathrm{MHz}}$ - $\alpha_{325\ \mathrm{MHz}}^{1.4\ \mathrm{GHz}}$ > 1.1) and ultra-steep spectrum ($\alpha_{325\ \mathrm{MHz}}^{1.4\ \mathrm{GHz}}$ < -1.78). The total linear radio size corresponds to 478 kpc at the redshift (z_{phot} = 0.36±0.07) of potential host galaxy.

3.7.19 J022620-061515

This remnant candidate is identified by using morphological as well as USS criteria. The 325 MHz GMRT image shows a relaxed double-lobe radio morphology. The northern lobe appears to show a hint of edge-brightening, while southern lobe lacks any such feature (see Figure 3.4). Its radio SED can be represented with an ultra-steep power law ($\alpha_{150\ \mathrm{MHz}}^{1.4\ \mathrm{GHz}}$ = -1.61±0.07). Its average surface-brightness at 325 MHz is found to be low (56 mJy arcmin^{-2}). The total linear radio size corresponds to 731 kpc at the redshift (z_{phot} = 0.63±0.082) of potential host galaxy.

3.7.20 J022655-054242

This remnant candidate is identified by using both SPC ($\Delta\alpha$ = -0.78) and USS ($\alpha_{150\ \mathrm{MHz}}^{1.4\ \mathrm{GHz}}$ = -1.42±0.10) criteria. The 325 MHz GMRT image shows an elongated morphology with and a total linear size of 304 kpc at the redshift ($z_{\rm spec}$ = 1.0256±0.0002) of potential host galaxy.

3.7.21 J023107-053327

This remnant candidate is identified by using both morphological as well as spectral criteria. The 325 MHz GMRT image shows diffuse radio lobes of low-surface-brightness ($\rm SB_{325\ MHz}$ = 55 mJy arcmin^{-2}) suggesting it to be an old remnant (see Figure 3.4). The radio SED shows a strong curvature ($\Delta\alpha$ = 0.82) and steep spectrum ($\alpha_{\rm 150\ MHz}^{\rm 1.4\ GHz}$ < -1.10). The total linear radio size corresponds to 764 kpc at the redshift ($z_{\rm phot}$) = 0.65±0.09 of potential host galaxy.

Chapter 4

Remnant Radio Galaxy Candidates of Small Angular Sizes

4.1 Introduction

Understanding the evolution of radio galaxies is one of the important aspects of galaxy evolution as AGN jet activity influences host galaxy and surrounding inter-galactic-medium (IGM) via feedback processes (McNamara & Nulsen, 2007). Large-area multi-frequency sensitive radio continuum surveys have played a vital role in advancing our understanding on the radio galaxies evolution by detecting a large number of sources representing different phases of the radio galaxy's life cycle. According to the evolutionary models infancy phase of a radio galaxy can be depicted by compact sources with linear-angular-size (LAS) less than a kpc. Based on their spectral characteristics these sources are known as High-Frequency-Peakers (HFP) and Gigahertz-Peak-Spectrum (GPS) sources, that evolves into Compact-Steep-Spectrum (CSS) sources with LAS of a few to tens of kpc (O'Dea & Saikia, 2021). The CSS radio sources can evolve into large-size radio galaxies of a few hundreds of kpc via sustained supply of plasma through jets that can remain active for tens of millions of years (see An & Baan, 2012; Turner & Shabala, 2015). Remnant phase begins after the cessation of AGN activity during which jets are no longer sustained and lobes start to fade away. In the remnant phase, radio core and jets disappear but the radio lobes can still be detected for a time-scale of a few times of 10^7 years before they disappear due to radiative and adiabatic losses (Murgia et al., 2011). The time-scale over which remnant lobes can be detected is arguably much shorter than the active phase, and hence, remnant phase represents a short-lived final phase of radio galaxy evolution (Brienza et al., 2017). The short-lived remnant phase makes remnant radio galaxies (remnants) rare objects to be detected. Also, it is clear that at what stage in the life-cycle of radio galaxies, AGN activity ceases and remnant phase begins. Are there radio galaxies in which AGN-jet activity stop when their total size is just few tens or a few hundred kpc? With an objective to address these questions we search and characterise the nature remnant radio galaxies which have angular size smaller than $30''$.

In recent times, deep low-frequency radio surveys have been exploited to search for the population of remnants with an expectation to find a large number of remnant sources exhibiting diffuse low-surface-brightness emission of steep spectrum. However, contrary to the predictions of evolutionary models based on radiative cooling of lobes plasma, the fraction of remnants is found to be as low as 5% to 10%. For instance, using deep 150 LOFAR survey ($5\sigma = 0.1 - 2.0$ mJy beam^{-1}) and deep 6 GHz ($5\sigma = 0.02$ mJy beam^{-1}) observations Mahatma et al. (2018) identified only $11/127 < 9\%$ potential remnants with absent-core criterion in the Herschel-ATLAS field. In a similar study Jurlin et al. (2021) found only $11/158 < 8\%$ remnants in the Lockman Hole field. In Chapter 3, we presented a search for remnants in the XMM-LSS field using deep 325 MHz GMRT radio observations, 150 MHz LOFAR radio observations and 1.4 GHz JVLA radio observations, and found that the remnants fraction is even lower upto $< 5\%$ if fainter population ($S_{325\ \mathrm{MHz}} \geq 6.0$ mJy) is considered (Dutta et al. 2022, *under review*, D22 hereafter). Unlike D22 both Jurlin et al. (2021) and Mahatma et al. (2018) have introduced a high flux density cutoff limits *i.e.*, $S_{150\ \mathrm{MHz}} \geq 40$ mJy and $S_{150\ \mathrm{MHz}} \geq 80$ mJy in their samples, respectively. In addition to relatively high flux density cut-off limit, all the previous studies have also introduced a cut-off limit of $30'' - 60''$ on LAS (see Saripalli, 2012; Brienza et al., 2017; Quici et al., 2021). For instance, Brienza et al. (2017) identified remnants using a sample of extended source with LAS $\geq 60''$, while Mahatma et al. (2018) limited their search to the radio sources with LAS $\geq 40''$ in the 150 MHz LOFAR images. In the XMM-LSS field, D22 attempted to identify remnants in a sample of extended sources with LAS $\geq 30''$ in the 325 MHz GMRT images. We note that the requirement of placing a cut-off limit on the LAS arises due the use of morphological criteria *i.e.*, absence of radio core, hotspots, in the radio images of few arcsec resolution. Moreover, the cut-off limit placed on the angular size introduces a bias towards large and powerful radio galaxies. In their sample of remnants with LAS $\geq 60''$ Jurlin et al. (2021) found that all remnants show double-lobe morphology with high radio luminosity ($L_{150\ \mathrm{MHz}} > 10^{25}$ W Hz^{-1}) suggesting their progenitors to be powerful FR II radio galaxies.

We point out that the bias towards the remnants of large powerful radio galaxies continues to exist even in case of individual remnants reported in the literature. In fact, individual remnants were discovered primarily owing to their peculiar radio morphology that appeared extended, amorphous, and lacked compact features (*e.g.*, Tamhane et al., 2015; Brienza et al., 2016; Shulevski et al., 2017; Duchesne & Johnston-Hollitt, 2019). Individual remnants such as blob1 (Brienza et al., 2016), NGC 1534 (Duchesne & Johnston-Hollitt, 2019), J021659-044920 (Tamhane et al., 2015), B2 0924+30 (Cordey, 1987; Jamrozy et al., 2004; Shulevski et al., 2017) were identified based on their unusual amorphous-shaped large-scale radio morphology of low-surface-brightness emission at low-frequencies ($\leq$ 325 MHz). Considering the biases and limitations introduced by the angular size cut-off we attempt to search and characterize the nature of remnants of small angular sizes (LAS $< 30''$) that have remained unexplored, hitherto. We note that small angular size poses difficulty in deciphering radio morphology, and hence, morphological criteria cannot be applied to search for small size remnants detected with the radio images of several arcsec resolution. Although, remnant characteristics are manifested in the radio spectra in the form of strong spectral curvature resulted from the frequency-dependent radiative losses. Therefore, we exploit spectral curvature criterion to identify remnants of small angular sizes.

This chapter is structured as follows. In Section 4.2 we briefly mention about the available radio and optical data in the XMM-LSS field. Section 4.3 describes the selection criteria and the sample of identified remnant candidates. In Section 4.4 we report the characteristic properties of our remnant candidates and compare them with active sources. In Section 4.5 we attempt to identify plausible reasons for existence of small-size remnants. Section 4.6 is devoted on the discussion for biases that can influence the remnant fraction. Section 4.7 lists the conclusions of our study.

4.2 Radio and Optical Surveys in the XMM-LSS Field

To identify remnant candidates and their host galaxies we use deep multi-frequency radio and optical data available in the XMM-LSS field. In our study we mainly utilize 150 MHz LOFAR survey, 325 MHz GMRT survey, 1.4 GHz JVLA survey and the Hyper Suprime-Cam Subaru Strategic Program (HSC-SSP) optical survey. The detail of these observations are already presented in the section 3.2 of chapter 3. So, we refer reader to the previous chapter. We note that 1.4 GHz JVLA survey overlaps partially with the 325 MHz GMRT survey. Therefore, we divide 325 MHz survey region into two parts − (i) 5.0 deg^2 area covered with the deep 1.4 GHz JVLA survey named as the XMM-LSS-JVLA, and (ii) 325 MHz GMRT survey region not covered with the 1.4 GHz JVLA survey named as the XMM-LSS-Out (see Figure 3.1). We use relatively less sensitive 1.4 GHz FIRST survey in the XMM-LSS-Out region.

4.3 Identification of Remnant Candidates of Small Angular Sizes

In the literature, remnants are identified mostly by using morphological criteria *viz.*, absence of radio core and presence of diffuse amorphous shaped low-surface-brightness emission (Mahatma et al., 2018; Quici et al., 2021; Jurlin et al., 2021). For sources of small angular sizes (LAS $< 30''$) morphological details cannot be deciphered from the images with a typical resolution of $5'' - 10''$. Notably, spectral curvature criterion can allow us to identify remnant candidates even among unresolved sources. One of the key examples of such remnants is J1615+5452 which is identified mainly using the spectral curvature criterion and does not reveal much morphological details in the images of $5'' - 10''$ angular resolution (see Randriamanakoto et al., 2020). Also, the absence of core supporting the remnant status of J1615+5452 was inferred from its non-detection in the moderately deep ($5\sigma = 0.45$ mJy) 1.4 GHz VLA observations of $5''$ resolution. We note that the core detection particularly in small sources ($< 30''$) poses requirement for deep (noise-rms less than a few μJy), high-resolution (of sub-arcsec level or even better) observations at higher frequencies (>1.4 GHz). Also, we cannot rule out the possibility of existence of a faint core falling below the detection limit even in the deep high-frequency observations. Keeping these limitations in mind, we exploit the spectral curvature criterion to identify candidates of remnant sources of small angular sizes.

4.3.1 Spectral Curvature Selection Criterion

Relativistic electrons present in radio lobes lose their energy via synchrotron emission as well as Inverse Compton (IC) scattering with the Cosmic Microwave Background (CMB) photons (Komissarov & Gubanov, 1994). Since electrons of higher-energy lose their energy faster than the low-energy electrons, a spectral break in the power law radio spectrum develops such that the spectrum becomes steeper at higher frequency above the break frequency (ν_b), while spectrum continues to exhibit original spectral index below ν_b. As explained in Section 3.3.2, in case of a remnant source with no supply of relativistic electrons, a new break appears at higher frequencies ($\nu_{\rm b,\ high}$) beyond which spectrum falls of exponentially. The ratio of $\nu_{\rm b,\ low}$ and $\nu_{\rm b,\ high}$ depends on the duration of remnant phase *w.r.t.* the total source age (Komissarov & Gubanov, 1994). Thus, radio spectrum of an active source can be represented by a broken power law that exhibits spectral index same to that of injected plasma $\alpha_{\rm inj}$, typically in the range -0.5 to -1.0 below $\nu_{\rm b}$ and a steeper spectral index $\alpha_{\rm inj}$ - 0.5 above $\nu_{\rm b}$ (Blandford & Ostriker, 1978). However, in a remnant source radio spectrum would appear curved with two break frequencies *i.e.*, $\nu_{\rm b,\ low}$ above which spectrum steepens with index $\alpha_{\rm inj}$ - 0.5, and $\nu_{\rm b,\ low}$ above which spectrum falls exponentially. Thus, a remnant source is expected show strong curvature with $\alpha_{\rm low}$ - $\alpha_{\rm high}$ > 0.5 (Murgia et al., 2011). To identify remnant sources showing curved radio spectrum we examine the difference between low-frequency and high-frequency spectral indices *i.e.*, $\Delta\alpha = \alpha_{\rm low}$ - $\alpha_{\rm high}$. In our study, we define $\Delta\alpha = \alpha_{\rm 150\ MHz}^{\rm 325\ MHz}$ - $\alpha_{\rm 325\ MHz}^{\rm 1.4\ GHz}$, and consider $\Delta\alpha \geq 0.5$ as a characteristic signature of remnant. We note that the spectral curvature criterion selects only a fraction of remnants that show strong curvature ($\geq$ 0.5) within the considered frequency window, 150 MHz $-$ 1.4 GHz in our case. The remnants with spectral break ($\nu_{\rm b}$) falling outside the frequency window of 150 MHz $-$ 1.4 GHz and even below 325 MHz would be missed in our study. In the following subsection, we describe the identification of remnant candidates.

4.3.2 The Sample Selection

Our initial sample is consisted of 2513 radio sources detected in the 325 MHz GMRT survey with the signal-to-noise ratio (SNR) $\geq$ 7 and LAS < 30$''$. The SNR cutoff is chosen to avoid any contamination from spurious sources. While, cutoff on the LAS is applied owing to the fact that the sample of extended radio sources with LAS $\geq$ 30$''$ is already probed to search for remnants reported in Chapter 3. To use spectral curvature criterion we obtain low-frequency ($\alpha_{\rm 150\ MHz}^{\rm 325\ MHz}$) and high-frequency ($\alpha_{\rm 325\ MHz}^{\rm 1.4\ GHz}$) spectral indices of 325 MHz GMRT sources by finding their counterparts at 150 MHz and 1.4 GHz. Table 4.1 lists the number of 325 MHz sources with counterparts at 150 MHz and 1.4 GHz.

4.3.2.1 Counterparts at 150 MHz and 1.4 GHz

We search 150 MHz counterparts of 325 MHz GMRT sources using 150 MHz LOFAR survey, whenever available, otherwise a relatively shallow 150 MHz TIFR GMRT Sky Survey (TGSS; Intema et al., 2017) is used. We find that 2179 out of 2513 (86.7%) sources fall within the LOFAR survey region owing to a substantially large overlap between 325 MHz GMRT survey and 150 MHz LOFAR survey (see Figure 3.1 in chapter 3). The cross-matching of 325 MHz GMRT sources to 150 MHz source catalogue with a search radius of 15$''$ gives only 1480 sources. We note that a larger search radius of 15$''$ is considered due to large positional uncertainties (a few arcsec) associated with faint diffuse sources detected at both frequencies. In fact, majority of sources are found to be matched within 5$''$ radius. The number of cross-matched sources by chance is only 1.6%, if source density of 300 deg^{-2} in the 325 GMRT survey is considered. The non-detection of 699/2179 (32%) of 325 MHz GMRT sources in the LOFAR survey can be understood due to their low flux densities *i.e.*, fainter source population. We find that the 325 MHz flux density distribution for the non-detected sources peaks around 1.0 mJy and most of the sources are fainter than 2.0 mJy.

For 334 radio sources falling outside the LOFAR survey region we searched 150 MHz counterparts using TGSS source catalogue having flux density limit of 24.5 mJy at 7σ. We find that only 36 relatively bright sources ($S_{325\ \rm MHz} \geq 11$ mJy) show counterparts in the TGSS. Thus, we have a total of 1516 sources detected at both 325 MHz and 150 MHz frequencies, providing the estimates of spectral index between 150 MHz − 325 MHz ($\alpha_{150\ \rm MHz}^{325\ \rm MHz}$). We do not consider sources for which low-frequency spectral indices are unconstrained *i.e.*, no detected counterparts at 150 MHz. Hence, our study is limited to the sample of 1516 radio sources detected at the both 325 MHz and 150 MHz frequencies.

To estimate high-frequency (325 MHz − 1.4 GHz) spectral index we attempt to find 1.4 GHz counterparts for 1516 sources by using the NVSS, whenever available, otherwise JVLA and FIRST surveys are used. We prefer to use the NVSS survey due to its large beam-size (45$''$) that is more effective in capturing low-surface-brightness-emission often associated with remnant sources. We find that only 599/1516 sources show 1.4 GHz counterparts in the NVSS catalogue within a search radius of 15$''$. Low detection rate

Table 4.1: Selection steps for small-size remnant candidates.

Sample	Criteria	Size
Detected at 325 MHz GMRT	SNR $\geq$ 7 and size < 30″	2513
Detected at 150 MHz		1516
LOFAR		1480/2179
TGSS (outside LOFAR region)		36/334
Detected at 325 MHz and 150 MHz	$\alpha_{150\ \mathrm{MHz}}^{325\mathrm{MHz}}$ constrained	1516
Detected at 1.4 GHz		1160
NVSS		599/1516
JVLA		430/434
FIRST (outside JVLA region)		131/483
150 MHz, 325 MHz and 1.4 GHz	$\alpha_{150\ \mathrm{MHz}}^{325\mathrm{MHz}}$ and $\alpha_{325\ \mathrm{MHz}}^{1.4\ \mathrm{GHz}}$	1160
150 MHz, 325 MHz but no 1.4 GHz	$\alpha_{150\ \mathrm{MHz}}^{325\mathrm{MHz}}$ but $\alpha_{325\ \mathrm{MHz}}^{1.4\ \mathrm{GHz}}$ upper limits	356
Remnant candidates	$\Delta\alpha \geq 0.5$ and $\alpha_{150\ \mathrm{MHz}}^{325\ \mathrm{MHz}} \leq$ -0.5	48/1516 (3.2%)
	spec-z	353
Redshift estimates	photo-z	505
	no redshift	658

in the NVSS is due to its higher detection limit of 2.5 mJy at 5σ, that corresponds to nearly 7.0 mJy at 325 MHz, if a typical spectral index of -0.7 is assumed. We caution that the large beam-size of NVSS (45$''$) can occasionally suffer contamination from the neighboring sources which can result spectral index flatter than the true value. For 917 sources with no counterparts in the NVSS we search for the 1.4 GHz counterparts using JVLA survey, if available, otherwise the FIRST survey. We find that only 434 sources fall within the JVLA survey region, and 430/434 sources show counterparts in the 1.4 GHz JVLA survey. High detection rate in the JVLA survey is due to its high sensitivity (0.08 mJy at 5σ). Among remaining 483 sources we find 1.4 GHz counterparts of only 131 sources in the FIRST survey. We note that, for 356 sources with no detected counterparts at 1.4 GHz, we place an upper limit of 2.5 mJy based the NVSS detection limit, if source is resolved, otherwise a more stringent upper limit of 1.0 mJy is placed based the FIRST survey.

4.3.2.2 Remnant Candidates Identified from $\alpha_{\rm low}$ versus $\alpha_{\rm high}$ Diagnostic Plot

We use $\alpha_{\rm low}$ versus $\alpha_{\rm high}$ diagnostic plot to identify remnant candidates exhibiting strong spectral curvature. With our spectral coverage limited to only three frequencies *i.e.*, 150 MHz, 325 MHz and 1.4 GHz, we consider $\alpha_{\rm low}$ = $\alpha_{\rm 150\ MHz}^{\rm 325\ MHz}$ and $\alpha_{\rm high}$ = $\alpha_{\rm 325\ MHz}^{\rm 1.4\ GHz}$. Figure 4.1 shows $\alpha_{\rm 150\ MHz}^{\rm 325\ MHz}$ versus $\alpha_{\rm 325\ MHz}^{\rm 1.4\ GHz}$ plot for our sample of 1516 sources that include upper limits on $\alpha_{\rm 325\ MHz}^{\rm 1.4\ GHz}$ for 356 sources. We find that our sources exhibit concentration at $\alpha_{\rm 150\ MHz}^{\rm 325\ MHz}$ = -0.36, and $\alpha_{\rm 325\ MHz}^{\rm 1.4\ GHz}$ = -0.79 that are the median values of respective spectral index distributions. The substantial difference between the median spectral indices at lower and higher frequencies suggests spectral aging even in active sources. This fact is also evident from a systematic shift for a majority of sources from the line representing $\alpha_{\rm 150\ MHz}^{\rm 325\ MHz}$ = $\alpha_{\rm 325\ MHz}^{\rm 1.4\ GHz}$ (black diagonal line) towards $\alpha_{\rm 150\ MHz}^{\rm 325\ MHz}$ = $\alpha_{\rm 325\ MHz}^{\rm 1.4\ GHz}$ + 0.5 (red diagonal line) in Figure 4.1 . Sources showing strong spectral curvature of $\Delta\alpha$ (= $\alpha_{\rm 150\ MHz}^{\rm 325\ MHz}$ - $\alpha_{\rm 325\ MHz}^{\rm 1.4\ GHz}$) $\geq$ 0.5 fall beyond the $\alpha_{\rm 150\ MHz}^{\rm 325\ MHz}$ = $\alpha_{\rm 325\ MHz}^{\rm 1.4\ GHz}$ + 0.5 line. We note that while identifying remnant candidates of strong spectral curvature we avoid radio sources showing flat and inverted spectral index at lower frequency *i.e.*, $\alpha_{\rm 150\ MHz}^{\rm 325\ MHz}$ > -0.5, that is understood to arise from self-synchrotron absorption (SSA) caused by an active core. Thus, we identify sources showing spectral curvature ($\Delta\alpha$) $\geq$ 0.5, and low-frequency

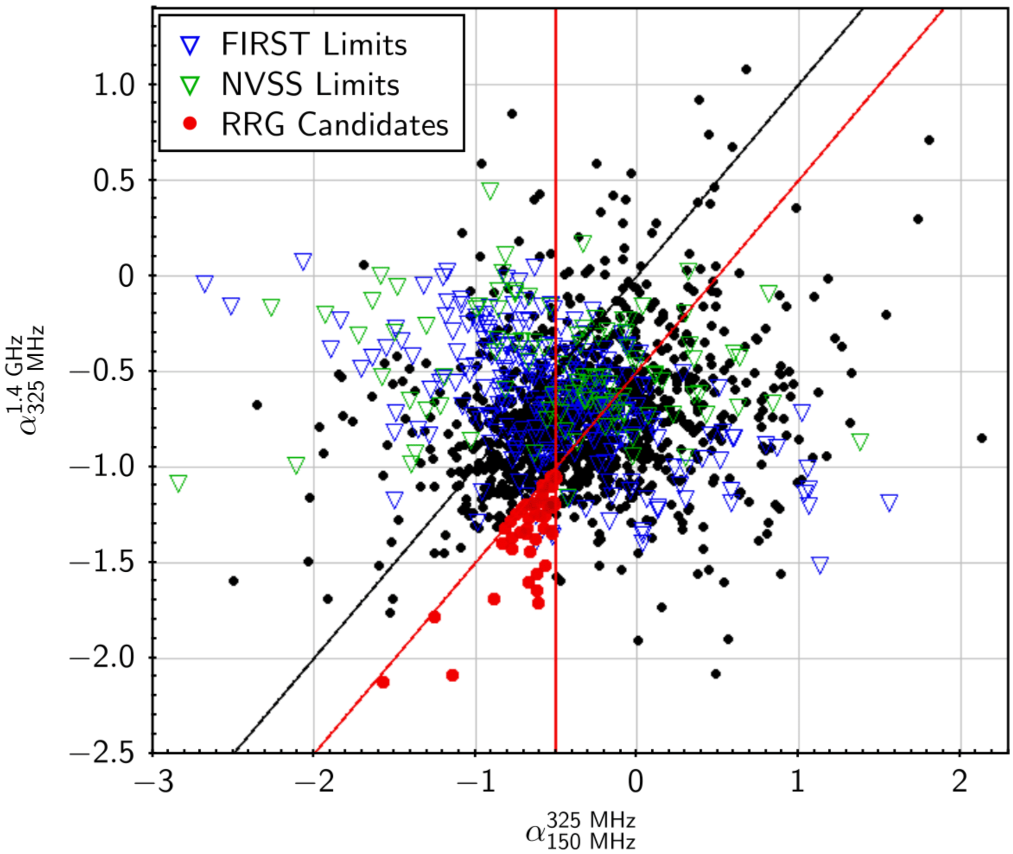

Figure 4.1: Diagnostic plot of $\alpha_{150\ \mathrm{MHz}}^{325\ \mathrm{MHz}}$ versus $\alpha_{325\ \mathrm{MHz}}^{1.4\ \mathrm{GHz}}$. Vertical red line represents $\alpha_{150\ \mathrm{MHz}}^{325\ \mathrm{MHz}}$ = -0.5, while diagonal black and red lines depict $\alpha_{150\ \mathrm{MHz}}^{325\ \mathrm{MHz}} = \alpha_{325\ \mathrm{MHz}}^{1.4\ \mathrm{GHz}}$ and $\alpha_{150\ \mathrm{MHz}}^{325\ \mathrm{MHz}} = \alpha_{325\ \mathrm{MHz}}^{1.4\ \mathrm{GHz}} + 0.5$, respectively.

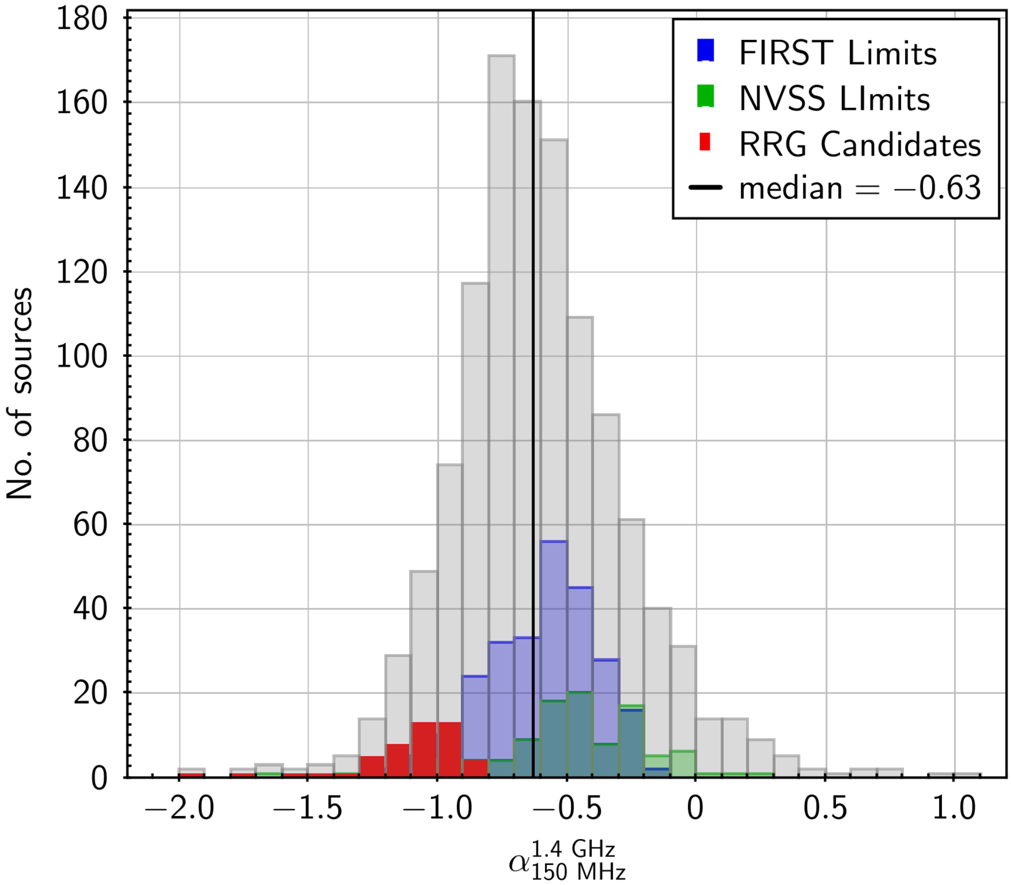

Figure 4.2: Histogram of spectral index between 150 MHz and 1.4 GHz.

spectral index steeper than -0.5 (sources falling within the region bounded by $\alpha_{150\ \mathrm{MHz}}^{325\ \mathrm{MHz}}$ = $\alpha_{325\ \mathrm{MHz}}^{1.4\ \mathrm{GHz}}$ + 0.5 line and $\alpha_{150\ \mathrm{MHz}}^{325\ \mathrm{MHz}}$ = -0.5 line in Figure 4.1, as the potential candidates of remnants. We find only 48 remnant candidates with 06 sources having only upper limit on the 1.4 GHz flux density. Table 5.1 shows the list of our 48 remnant candidates. We caution that strong spectral curvature seen for our remnant candidates can be affected by the resolution bias *i.e.*, unlike 150 MHz and 325 MHz, 1.4 GHz observations especially from the JVLA and FIRST can underestimate the flux density by missing the detection of diffuse low-surface-brightness emission.

4.4 Characteristics of Remnants of Small Angular Sizes

In this section we describe characteristics properties of our remnant candidates and compare them with active sources.

4.4.1 Broad-band Spectral Index ($\alpha_{150\ \mathrm{MHz}}^{1.4\ \mathrm{GHz}}$)

Active sources are generally expected to show power law radio spectrum with a spectral index in the range of -0.5 to -1.0. Spectral turn over caused by SSA is often seen in active sources with a peak (ν_{p}) $\leq$ 1.0 GHz, that shifts towards lower frequencies as a radio source evolves and becomes lobe-dominated (An & Baan, 2012). In contrast, remnant sources exhibit power law spectrum with a spectral break that progressively shifts towards lower frequency as the remnant source evolves with time (Murgia et al., 2011). Therefore, spectral index measured over a broad range can give us a clue about the evolutionary stage of a radio source. We estimate spectral index between 150 MHz and 1.4 GHz ($\alpha_{150\ \mathrm{MHz}}^{1.4\ \mathrm{GHz}}$), the widest spectral coverage available, for our sample sources. Figure 4.2 shows the spectral index ($\alpha_{150\ \mathrm{MHz}}^{1.4\ \mathrm{GHz}}$) distributions of our remnant candidates and active sources. Spectral index ($\alpha_{150\ \mathrm{MHz}}^{1.4\ \mathrm{GHz}}$) for our remnant candidates is found to be distributed in the range of -1.94 to -0.86 with a median value of -1.04. While, active sources have $\alpha_{150\ \mathrm{MHz}}^{1.4\ \mathrm{GHz}}$ is the range of -1.91 to 1.09 with a median value of -0.61. Thus, it is evident that our remnant candidates show systematically steeper spectral index than that for the active sources. The two-sample KS test shows that the distributions of $\alpha_{150\ \mathrm{MHz}}^{1.4\ \mathrm{GHz}}$ for our remnant candidates and active sources are different (see Table 4.3). We caution that the systematically steeper spectral index of our remnant candidates can be the result of selection criteria bias *i.e.*, strong spectral curvature ($\Delta\alpha \geq 0.5$) and $\alpha_{150\ \mathrm{MHz}}^{325\ \mathrm{MHz}} <$ -0.5. In Figure 4.3−4.6, we show four examples of the radio spectra of our remnant candidates. We find that the radio spectra of our remnant candidates are better fitted by a curved power law that is defined as $\mathrm{S}_{\nu} = \mathrm{S}_0\ (\nu/\nu_0)^{\alpha}\ \mathrm{e}^{q(ln\nu)^2}$, where q parameterises the curvature of spectrum such that $q < 0$ represents a convex spectrum (see Quici et al., 2021). For optically-thin synchrotron emission arising from radio lobes, typical value of q ranges over $-0.2 \leq q \leq 0$. We find that values of q parameter of our remnant candidates is generally < -0.2 consistent with an optically-thin emission from the relic lobes.

We point out that the two point spectral index $\alpha_{150\ \mathrm{MHz}}^{325\ \mathrm{MHz}}$ of our remnant candidates is similar to that found for the large-size remnants. For instance, large-size remnant candidates reported in the chapter 3 show $\alpha_{150\ \mathrm{MHz}}^{1.4\ \mathrm{GHz}}$ distributed in the range of -1.71 to -0.74 with a median value of -1.02. It is worth to note that the majority (15/21) of remnant candidates reported in the chapter 3 are identified by using mainly morphological criteria. Also, using only morphological criterion, (Mahatma et al., 2018) found that the spectral index ($\alpha_{150\ \mathrm{MHz}}^{1.4\ \mathrm{GHz}}$) of their remnant candidates is distributed in the range of -1.5 to -0.5 with a median value of -0.97. Thus, we find that the spectral index distribution for our small-size remnant candidates is similar to that for the large-size remnant candidates despite being selected using different criteria. The similar spectral index distributions for our small-size remnant candidates and the large-size remnants identified by using morphological criteria strengthens the remnant status of our candidates.

4.4.2 Radio Morphology

Our remnant candidates are selected to be of small-sizes (LAS $\leq 30''$), and hence, they are not well suited for revealing the morphological details. Despite the limitations imposed by small size we examine radio morphologies of our remnant candidates by inspecting 325 MHz GMRT and 1.4 GHz radio images. We use 1.4 GHz images either from the JVLA survey, whenever available, or from the FIRST survey due to their relatively higher

Table 4.2: The sample of small-size remnant candidates.

Source Name	$S_{150\ \mathrm{MHz}}$ (mJy)	$S_{325\ \mathrm{MHz}}$ (mJy)	$S_{1.4\ \mathrm{GHz}}$ (mJy)	$S_{3.0\ \mathrm{GHz}}$ (mJy)	$\alpha_{150\ \mathrm{MHz}}^{325\ \mathrm{MHz}}$	$\alpha_{325\ \mathrm{MHz}}^{1.4\ \mathrm{GHz}}$	$\Delta\alpha$	$\alpha_{150\ \mathrm{MHz}}^{1.4\ \mathrm{GHz}}$	$\alpha_{1.4\ \mathrm{GHz}}^{3.0\ \mathrm{GHz}}$	LAS $''$ (kpc)	z	$\log L_{150\ \mathrm{MHz}}$ (W Hz^{-1})
J020750-030455	189.6±19.5	106.4±0.6	17.1±0.7	4.39±0.57	-0.75±0.13	-1.25±0.03	0.51	-1.08±0.05	-1.78±0.18	24.9 (201.2)	1.041±0.105	27.06
J021109-033244	31.0±5.5	17.1±0.2	2.29±0.4	2.03±0.33	-0.77±0.23	-1.37±0.12	0.60	-1.16±0.11	-0.16±0.31	<10 (<80.1)	>1.0	>26.26
J021146-041402	34.3±0.8	20.6±0.35	2.5±0.5		-0.66±0.04	-1.44±0.14	0.78	-1.17±0.09		21.1 (168.9)	>1.0	>26.31
J021408-053456	10.6±0.5	7.0±0.6	<1.0		-0.53±0.13	<-1.33	>0.80	<-1.06		<10 (<57)	0.442±0.036	24.89
J021446-053941	29.5±0.8	19.6±0.56	3.9±0.4		-0.53±0.05	-1.11±0.07	0.58	-0.91±0.05		<10 (<83.8)	1.30±0.102	26.43
J021504-030420	31.0±0.6	16.3±0.18	2.1±0.4	1.50±0.29	-0.83±0.03	-1.40±0.13	0.57	-1.20±0.09	-0.44±0.35	<10 (<76.1)	0.834±0.065	26.07
J021528-044045	29.9±1.0	20.3±0.30	4.4±0.02		-0.51±0.05	-1.05±0.01	0.54	-0.86±0.01		24 (119)	0.353±0.023	25.08
J021536-045220	3.1±0.5	2.01±0.18	0.34±0.01		-0.55±0.25	-1.21±0.06	0.67	-0.98±0.08		<10 (<80.1)	>1.0	>25.19
J021548-035934	20.8±0.9	8.61±0.45	0.41±0.01		-1.14±0.09	-2.09±0.04	0.95	-1.76±0.02		17.7 (124.8)	0.677±0.042	25.79
J021555-041245	4.1±0.5	2.56±0.26	0.26±0.01		-0.62±0.19	-1.56±0.06	0.95	-1.24±0.05		<10 (<84.4)	1.413±0.132	25.79
J021603-025647	20.8±0.6	11.1±0.20	1.60±0.15		-0.81±0.04	-1.32±0.07	0.51	-1.15±0.04		<10 (<83.1)	1.221±0.154	26.30
J021646-051004	2.9±0.5	1.93±0.12	0.38±0.01		-0.54±0.23	-1.10±0.04	0.57	-0.91±0.07		<10 (<80.1)	>1.0	>25.16
J021702-060327	350.3±4.0	132.8±0.4	9.8±0.5	4.73±0.54	-1.25±0.02	-1.78±0.03	0.53	-1.60±0.02	-0.96±0.16	25.4 (203.4)	>1.0	>27.44
J021706-031513	36.7±0.7	23.3±0.43	4.70±0.5		-0.58±0.04	-1.09±0.07	0.51	-0.92±0.05		<10 (<80.1)	>1.0	>26.26
J021759-061642	19.5±0.4	13.2±0.62	2.8±0.6		-0.50±0.07	-1.06±0.15	0.56	-0.87±0.10		29 (232.3)	>1.0	>25.97
J021836-035711	25.9±0.5	17.41±0.13	3.10±0.5	2.46±0.36	-0.52±0.03	-1.18±0.11	0.67	-0.95±0.07	-0.30±0.29	<10.0 (<84.1)	1.362±0.145	26.44
J021904-063436	48.1±0.8	28.3±0.3	3.94±0.16		-0.69±0.02	-1.35±0.03	0.66	-1.12±0.02		17.3 (132.6)	0.853±0.0652	26.26
J021907-061611	36.5±0.8	21.69±0.20	3.40±0.5	2.26±0.25	-0.67±0.03	-1.27±0.10	0.59	-1.06±0.07	-0.53±0.24	<10 (<80.1)	>1.0	>26.29
J021917-042654	9.7±0.5	2.87±0.16	0.12±0.01		-1.58±0.09	-2.13±0.09	0.55	-1.94±0.03		<10 (<80.1)	>1.0	>25.99
J021926-051535	20.4±0.7	13.3±0.37	2.3±0.5		-0.55±0.06	-1.20±0.15	0.64	-0.98±0.10		20.1 (160.9)	>1.0	>26.02
J022024-040240	6.4±0.5	3.9±0.18	0.68±0.01		-0.63±0.11	-1.20±0.03	0.56	-0.99±0.03		<10 (<84.2)	1.377±0.136	25.87
J022106-043925	3.6±0.4	2.3±0.16	0.40±0.01		-0.54±0.17	-1.21±0.05	0.68	-0.98±0.05		<10 (<79.9)	0.993±0.0862	25.25
J022127-063808	29.4±0.6	18.6±0.35	3.40±0.4	1.95±0.24	-0.59±0.04	-1.16±0.08	0.57	-0.96±0.05	-0.73±0.22	<10 (<84.5)	1.446±0.144	26.57

J022145-032930	34.8±0.6	19.0±0.19	2.90±0.5	2.68±0.53	-0.78±0.02	-1.29±0.12	0.51	-1.11±0.08	-0.10±0.34	18 (144.2)	>1.0	>26.29
J022152-053619	9.7±0.5	6.2±0.20	0.67±0.01		-0.57±0.08	-1.52±0.03	0.95	-1.19±0.02		<10 (<76.4)	0.843±0.0765	25.57
J022207-040055	4.1±0.5	2.75±0.21	0.48±0.01		-0.51±0.18	-1.20±0.05	0.69	-0.96±0.05		<10 (<80.1)	>1.0	>25.32
J022211-054906	182.9±2.1	121.4±0.26	21.4±0.8	8.31±0.23	-0.53±0.01	-1.19±0.03	0.66	-0.96±0.02	-1.24±0.06	<10 (<80.1)	>1.0	>26.97
J022227-040719	18.4±0.5	10.6±0.24	1.79±0.01		-0.71±0.05	-1.22±0.02	0.50	-1.04±0.01		16.6 (135.4)	1.087±0.104	26.09
J022250-031152	39.2±1.0	23.5±0.36	4.10±0.50		-0.66±0.04	-1.19±0.08	0.54	-1.01±0.06		<10 (<80.1)	>1.0	>26.31
J022301-060627	137.3±1.5	88.6±0.35	14.2±0.60	4.88±0.32	-0.57±0.01	-1.25±0.03	0.68	-1.01±0.02	-1.40±0.10	27.3 (218.6)	>1.0	>26.86
J022302-024656	10.8±1.1	7.2±0.35	<1.0		-0.53±0.15	<-1.35	>0.83	<-1.07		<10 (<76.1)	3.117±0.318	27.01
J022302-042850	12.3±0.6	7.2±0.13	1.26±0.01		-0.69±0.06	-1.19±0.01	0.50	-1.02±0.02		<10 (<82.7)	1.176±0.112	25.99
J022338-045418	7.04±0.3	4.42±0.47	0.70±0.01		-0.60±0.15	-1.25±0.07	0.65	-1.03±0.02		15.3 (122.5)	>1.0	>25.57
J022413-044643	7.97±0.7	4.02±0.15	0.34±0.01		-0.89±0.14	-1.69±0.03	0.80	-1.41±0.04		<10 (<80.1)	>1.0	>25.74
J022433-043709	4.1±0.5	2.47±0.11	0.43±0.01		-0.65±0.17	-1.19±0.03	0.54	-1.00±0.06		<10 (<80.1)	>1.0	>25.33
J022455-032906	20.7±0.6	12.9±0.17	0.85±0.15		-0.61±0.04	-1.71±0.10	1.10	-1.33±0.06		16 (<128.1)	>1.0	>26.13
J022611-050508	18.8±0.7	11.2±0.16	1.08±0.01		-0.67±0.05	-1.60±0.01	0.93	-1.28±0.02		<10 (<80.1)	>1.0	>26.08
J022627-033301	18.4±0.7	11.37±0.21	0.62±0.15		-0.62±0.05	-1.65±0.10	1.37	-1.29±0.07		<10 (<83.4)	1.253±0.126	26.37
J022631-043926	14.2±0.4	9.11±0.38	1.32±0.01		-0.57±0.06	-1.32±0.03	0.75	-1.06±0.01		18.4 (27.1)	0.0778±0.006	23.33
J022654-025821	7.1±0.7	4.67±0.35	<1.00		-0.53±0.16	<-1.05	>0.52	<-0.87		<10 (<80.1)	>1.0	>25.53
J022713-031247	7.9±0.8	5.02±0.27	<1.00		-0.58±0.14	<-1.10	>0.52	<-0.92		<10 (<79.7)	0.979±0.0848	25.57
J022717-061832	9.9±0.8	6.16±0.42	<1.00		-0.63±0.14	<-1.25	>0.62	<-1.03		<10 (<46.3)	0.317±0.029	24.52
J022720-033039	28.7±1.0	16.4±0.27	2.30±0.5		-0.72±0.05	-1.35±0.15	0.62	-1.13±0.10		21.0 (168.2)	>1.0	>26.22
J022723-051242	47.1±0.8	25.9±0.63	3.20±0.5		-0.77±0.04	-1.43±0.11	0.66	-1.20±0.07		27 (216.3)	>1.0	>26.45
J022737-052139	6.3±0.8	3.99±0.20	0.75±0.01		-0.58±0.17	-1.14±0.04	0.56	-0.94±0.05		19.5 (156.2)	>1.0	>25.49
J022750-024524	12.1±0.9	7.46±0.65	<1.0		-0.63±0.15	<-1.38	>0.79	<-1.12		<10 (<82.8)	1.185	26.02
J022759-051354	4.1±0.8	2.73±0.16	0.58±0.01		-0.52±0.25	-1.05±0.04	0.53	-0.86±0.08		<10 (<80.1)	>1.0	>25.29
J022802-041417	37.3±0.9	22.06±0.7	3.20±0.5		-0.68±0.05	-1.32±0.11	0.64	-1.09±0.07		19.1 (112.3)	0.467±0.0344	25.49

Notes – An upper limit of $10''$ is kept for the size of unresolved sources.

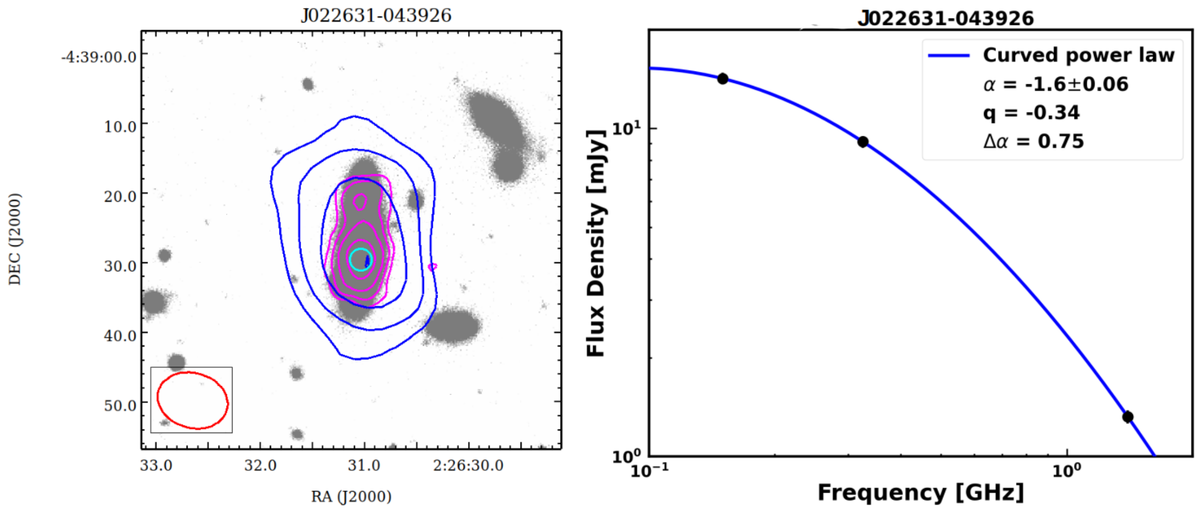

Figure 4.3: *Left Panel*: Image of a resolved remnant candidate showing extended radio emission. The 325 MHz GMRT radio contours (in Blue) and 1.4 GHz JVLA radio contours (in Magenta) are overlaid on the corresponding *i*-band HSC-SSP optical images. Radio contours are at $3\sigma \times$ (1, 2, 4, 8, 16, ...) levels and the corresponding optical image is logarithmically scaled. Potential host galaxy is marked with a small circle (in Cyan) around it. The 325 MHz GMRT synthesized beam of $10''.7 \times 7''.9$ is shown by an ellipse (in Red) in the bottom left corner in each plot. *Right Panel*: Radio SED, modelled with curved power law.

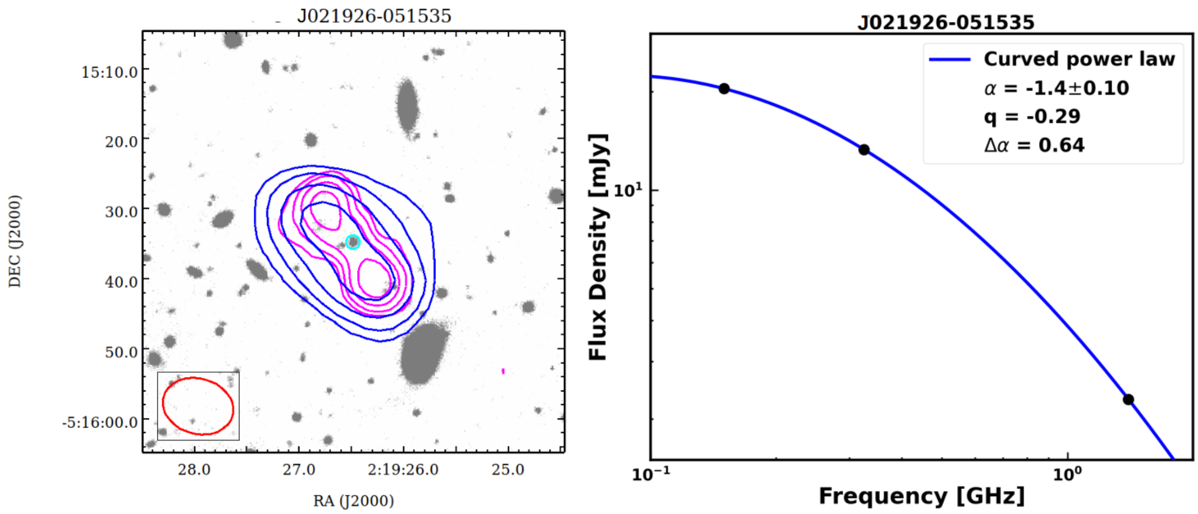

Figure 4.4: *Left Panel*: Image of a resolved remnant candidate showing extended radio emission with $S_{325\ \mathrm{MHz}} = 13.3 \pm 0.37$ mJy. *Right Panel*: Radio SED, modelled with curved power law, is shown and the modelled values are given in the legend.

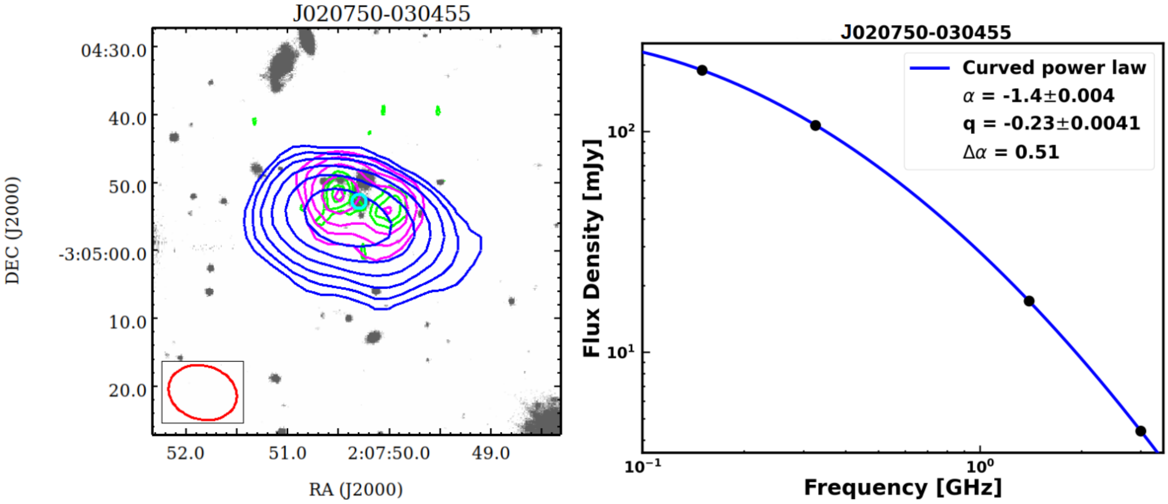

Figure 4.5: *Left Panel*: Image of a slightly resolved remnant candidate at 325 MHz is shown with $S_{325\ \mathrm{MHz}}$ = 106.4±0.6 mJy. Green contours are 3.0 GHz VLASS. *Right Panel*: Corresponding radio SED, modelled with curved power law, is shown. Here '$\Delta\alpha$' is the SPC = $\alpha^{1.4\ \mathrm{GHz}}_{325\ \mathrm{MHz}}$ - $\alpha^{325\ \mathrm{MHz}}_{150\ \mathrm{MHz}}$.

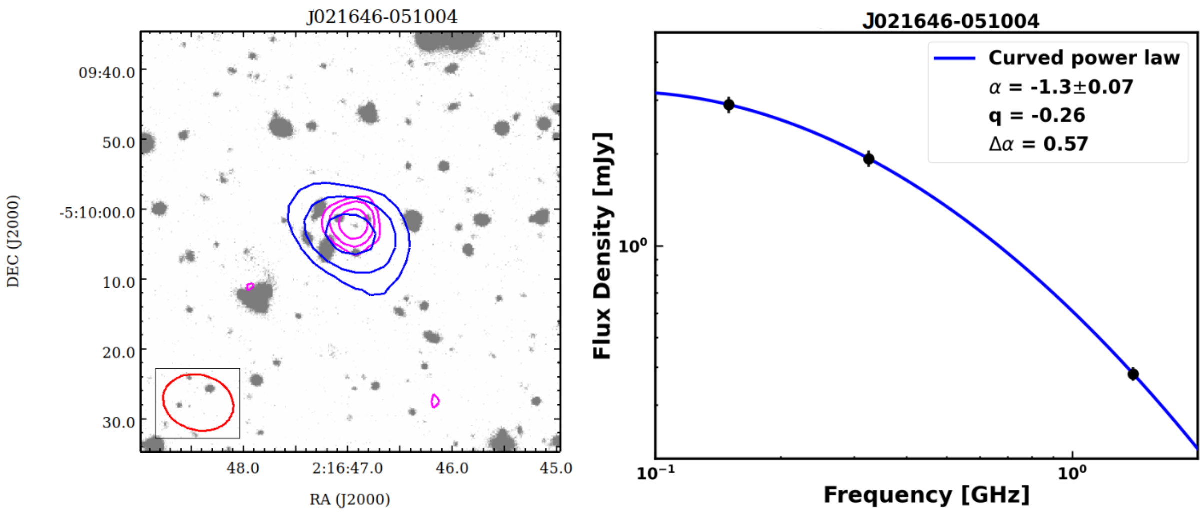

Figure 4.6: *Left Panel*: An example of unresolved and faint remnant candidate with $S_{325\ \mathrm{MHz}}$ = 1.93±0.12 mJy. *Right Panel*: Radio SED of the same source is shown.

resolution of 5$''$.0. We classify a source as resolved if extended emission is seen either in the 1.4 GHz image or in the 325 MHz image. We find that only 15/48 (31%) of our remnant candidates show resolved emission ***i.e.***, emission at scales larger than the synthesized beam. As expected morphological features are often seen only in the 1.4 GHz images due to its higher resolution. In Figure 4.3−4.6, we show radio contours (325 MHz (in blue) and 1.4 GHz (in magenta)) over-plotted onto the ***i***-band HSC-SSP optical images for four remnant candidates and their integrated radio spectra. In several sources, 1.4 GHz radio contours clearly show a double-lobe radio morphology, for example, J021926-051535 (see Figure 4.4). In case of J022631-043926, radio morphology appears to match with the optical host, similar to a star forming galaxy. Since strong spectral curvature suggests it to be a remnant candidate high-resolution radio images and spectral index maps are needed to confirm its true nature. In a few cases (J022338-045418 and J021759-061642), 325 MHz radio emission appears much extended than that at 1.4 GHz, suggesting the presence of diffuse relic emission detected only at the low-frequency. We note that the majority (33/48) of our remnant sources appear unresolved at both frequencies. We find that both resolved and unresolved sources are present at the wide range of flux densities with $S_{325\ \rm MHz}$ spanning from 1.93 mJy to 132.8 mJy with a median value of 11.2 mJy.

Also, we inspected 3 GHz VLASS quick look image cutouts for all our remnant candidates. The VLASS provides wide-band ($2-4$ GHz) images with median noise-rms of 0.145 mJy and angular resolution of 2$''$.5 (Gordon et al., 2020). We find that only 10/48 of our remnant candidates show detection in the VLASS. One of our sample source J020750-030455 exhibits a clear double lobe morphology with a total end-to-end projected size of 13$''$.6 ($\sim$ 112 kpc at z = 1.04) in the VLASS image (see Figure 4.5). Table 4.2 lists 3.0 GHz total flux densities derived from the VLASS epoch 1 quick look catalogue and the spectral index measured between 1.4 GHz and 3.0 GHz. We used only catalogue source components with `duplicate_flag` < 2 and `quality_flag` $= 0$, and corrected for 10% systematic underestimation of flux density. The non-detection of a large fraction (38/48 = 79%) of our remnant candidates, in particular for relatively bright sources at low-frequency ($S_{150\ \rm MHz} > 20$ mJy), in the VLASS can be understood if they posses relic emission of low-surface-brightness characterised with steep spectral index. The non-detection of relatively fainter remnant candidates can also be attributed to the shallow sensitivity of the VLASS. We note that, as expected, our remnant candidates continue to exhibit steep spectral index at higher frequency (1.4 GHz − 3.0 GHz) regime. While, 05/10 of our remnant candidates detected in the VLASS show flatter spectral index ($\alpha >$ -0.5) in the higher frequency regime, despite exhibiting steeper spectrum at low-frequency regime (< 1.4 GHz). The changing spectral characteristics of these remnant candidates can be understood if these candidate sources depict recurrent AGN activity such that a new phase of AGN activity showing flat or inverted radio spectrum at higher frequencies co-exists along with the relic emission from the previous episode of AGN activity showing steep spectrum at lower frequencies (see Murgia et al., 2011). Therefore, we note that a fraction of our remnant candidates can possibly show the existence of active core, if deep high-frequency observations are performed.

4.4.3 Redshifts

We find that only 858/1516 (56.6%) of our sample sources have optical counterparts with redshift estimates in the HSC-SSP catalogues. Spectroscopic redshifts are available for 353 sources and remaining 505 sources have photometric redshifts. Among the 48 remnant candidates only 23 sources have redshift estimates that include spectroscopic redshifts for four sources and photometric redshifts for remaining 19 sources (see Figure 4.7).

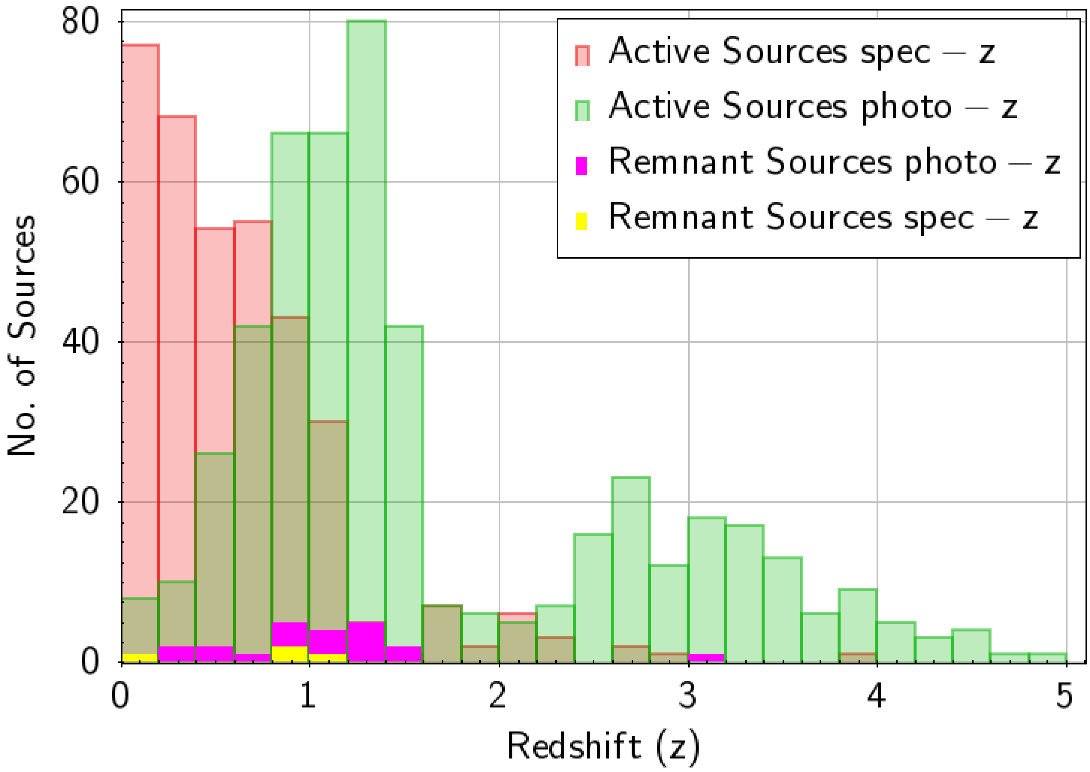

Figure 4.7: Histogram showing the redshift distribution of active and remnant sources in our sample.

We find that 23 remnant candidates have redshifts in the range of 0.077 to 3.12 with a median value of 1.04. While, 835 active radio sources have a wide redshift distribution ranging from 0.026 to 5.29 with a median value of 0.81. Thus, in compared to active sources, our remnant candidates are relatively at higher redshifts. The two-sample KS test shows that the redshift distributions of our remnant candidates and active sources are somewhat different with p-value = 0.13 (see Table 4.3). Our 25 remnant candidates with no available redshift estimates have either undetected or too faint optical counterparts. We attempt to place a lower limit on the redshifts of these remnant candidates by using a diagnostic plot based on the ratio of 325 MHz flux density to 3.6 μm flux density ($S_{325\ \mathrm{MHz}}/S_{3.6\ \mu m}$). In Figure 4.8, we plot $S_{325\ \mathrm{MHz}}/S_{3.6\ \mu m}$ versus redshift plot for our remnant candidates. We obtain 3.6 μm flux density from the Spitzer Wide-area Infrared Extragalactic Survey (SWIRE; Lonsdale et al. (2003)), whenever available. For sources falling outside the SWIRE coverage we check their detection in 3.4 μm band of the WISE all-sky imaging survey (Wright et al., 2010). We convert 3.4 μm flux density to 3.6 μm by assuming a power law spectrum with index of -2 in the near-IR regime. For sources

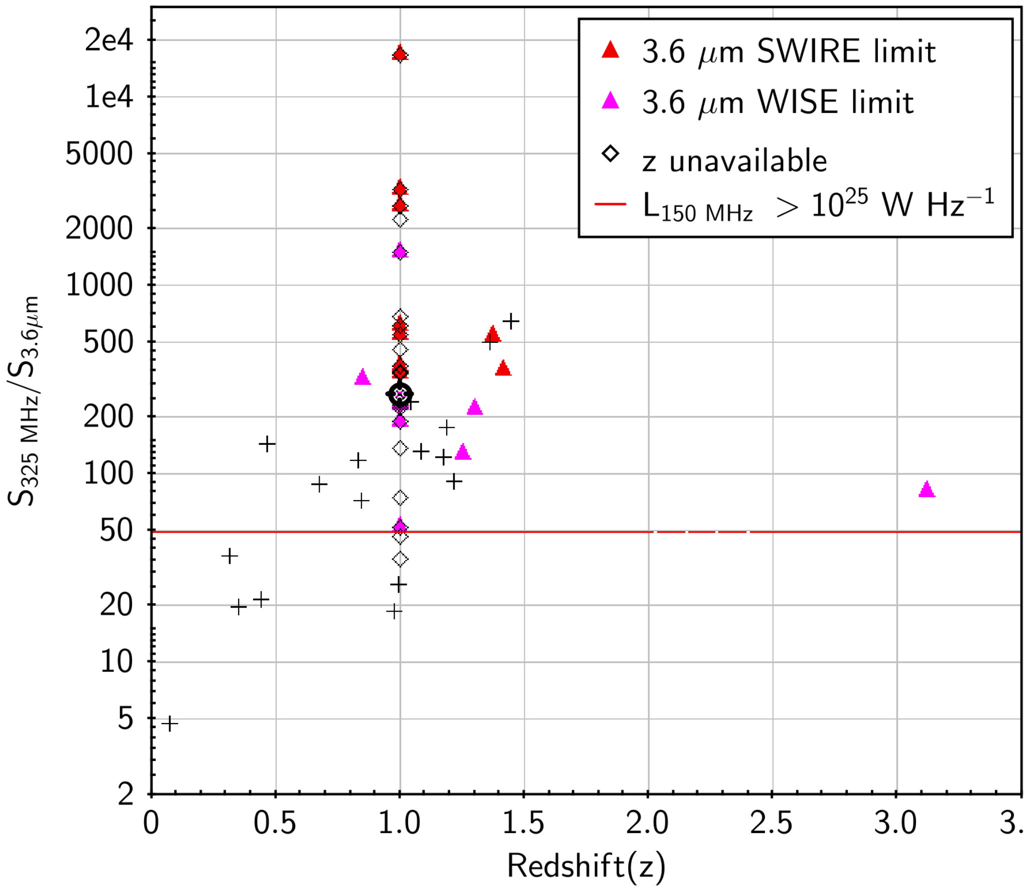

Figure 4.8: Ratio of 325 MHz radio flux density to 3.6 μm flux density plotted against the redshift. Sources with no redshift estimates are assigned an upper limit of $z > 1.0$ based the ratio of 325 MHz to 3.6μm flux densities similar to the high-z radio sources.

Table 4.3: The comparison between small-size remnant candidates and active sources.

Parameter	Remnant Candidates			Active Sources			KS Test	
	N_{source}	Range	Median	N_{source}	Range	Median	D	p-value
$S_{150\ MHz}$ (mJy)	48	2.9 − 350.3	19.5	1468	1.15 − 2543.3	5.8	0.32	2×10^{-4}
$S_{325\ MHz}$ (mJy)	48	1.93 − 132.8	11.2	1468	0.78 − 1511.2	4.8	0.21	0.03
$\alpha_{150\ MHz}^{1.4\ GHz}$	48	-1.94 − -0.86	-1.04	1118	-1.91 − 1.09	-0.61	0.81	1.6×10^{-6}
$\Delta\alpha$	48	0.50 − 1.10	0.62	1118	-3.81 − 2.98	0.38	0.58	2.1×10^{-4}
z	23	0.077 − 3.12	1.04	835	0.026 − 5.29	0.81	0.25	0.13
Linear size (kpc)	7	27.1 − 201.2	124	266	11.5 − 245.1	157.4	0.52	0.032
$\log L_{150\ MHz}$ (W Hz^{-1})	23	23.33 − 27.06	25.99	835	21.56 − 28.29	25.17	0.46	2×10^{-4}

Notes - The two sample Kolmogorov−Smirnov (KS) test is non-parametric statistical test that examines the hypothesis that two samples come from same distribution. D represents the maximum difference between the cumulative distributions of two samples and p-value is the probability that the null hypothesis, i.e., two samples comes from same distribution, is true.

with no detection in the SWIRE and WISE images we placed an upper limit on 3.6 μm flux density based on the 5σ detection limits.

From Figure 4.8, it is evident that the ratio $S_{325\ MHz}/S_{3.6\ \mu m}$ increases with the increase in redshift, which is analogous to the well known correlation between K band magnitude and redshift (K−z relation) for radio galaxies (Willott et al., 2003). We note that all but one of our remnant candidates at z > 1.0 have ratio $S_{325\ MHz}/S_{3.6\ \mu m}$ > 100. Hence, high ratio of $S_{325\ MHz}/S_{3.6\ \mu m}$ can be considered as an indicator for high redshift. Our remnant candidates with no detected 3.6 μm counterparts have high upper limits on $S_{1.4\ GHz}/S_{3.6\ \mu m}$ in the range of 52 to 16632 with a median value 338, similar to HzRGs. In fact, six of the 20 remnant candidates with no detected 3.6 μm counterparts have photometric redshift estimates in the range of 0.85 to 3.11 with a median value of 1.33. Hence, considering the fact that all of our remnant candidates with no redshift estimates show high values or limits of $S_{325\ MHz}/S_{3.6\ \mu m}$, similar to H$z$RGs or radio-loud AGN at z > 2 (Singh et al., 2017), we place an upper limit of z > 1.0 for all our remnant candidates with no available redshifts.

4.4.4 Radio Power versus Radio Size (P$-$D) Plot

According to the dynamical evolutionary models radio size and radio luminosity of a radio galaxy continues to increase till it becomes fully evolved with total end-to end radio size in the range of a few hundreds of kpc to even a few Mpc (An & Baan, 2012). Once AGN activity switches off radio luminosity begins to decrease due to radiative cooling. Therefore, in compared to active sources, remnants are expected to show lower radio luminosities but larger radio sizes similar to that for fully evolved radio galaxies. We use radio luminosity versus radio size plot, commonly known as P$-$D plot, to infer the evolutionary stage of our remnant candidates and compare them with active sources. We derive 150 MHz luminosity for all our sources with available redshift estimates and apply K-correction using spectral index measured between 150 MHz and 1.4 GHz ($L_{150\ \mathrm{MHz}} = 4\pi S_{150\ \mathrm{MHz}}\ D_{L}^{2}/(1+z)^{1+\alpha}$, where D_L is luminosity distance and $\alpha = \alpha_{150\ \mathrm{MHz}}^{1.4\ \mathrm{GHz}}$). Figure 4.9 shows the 150 MHz radio luminosity versus radio size plot for our sample sources. We note that the radio size estimates are available for only 395/1516 (26%) of our sample sources that show emission on scales larger than the synthesized beam of $10''$ in the 325 MHz GMRT survey. For remaining (1121/1516 = 74%) unresolved sources we place an upper limit of $10''$. It is worth mentioning that 1.4 GHz JVLA and FIRST images of higher resolution ($5''.0$) can place a tighter constraint on the radio size of apparently unresolved sources, but it would result a bias towards sources of higher surface-brightness. Also, a substantial fraction (356/1516 $\sim$ 23%; see Table 4.2) of our sample sources remained undetected at 1.4 GHz. Therefore, we prefer to use radio size obtained with the 325 MHz GMRT survey.

We compare linear radio sizes of our remnant candidates and active sources by considering only sources that have angular size estimates and redshifts. Sources with angular size estimates but no redshift estimates have only upper limits on their linear radio sizes. Also, unresolved sources with no redshift estimates do not allow us to place any limit on their radio sizes, hence, these sources are discarded from our analysis. We note that the redshift estimates are available for only 226/395 sources that include seven remnant candidates. We find that seven remnant candidates have linear radio size in the range of 27.1 kpc to 201.2 kpc with a median value of 124 kpc. The linear radio sizes of 219

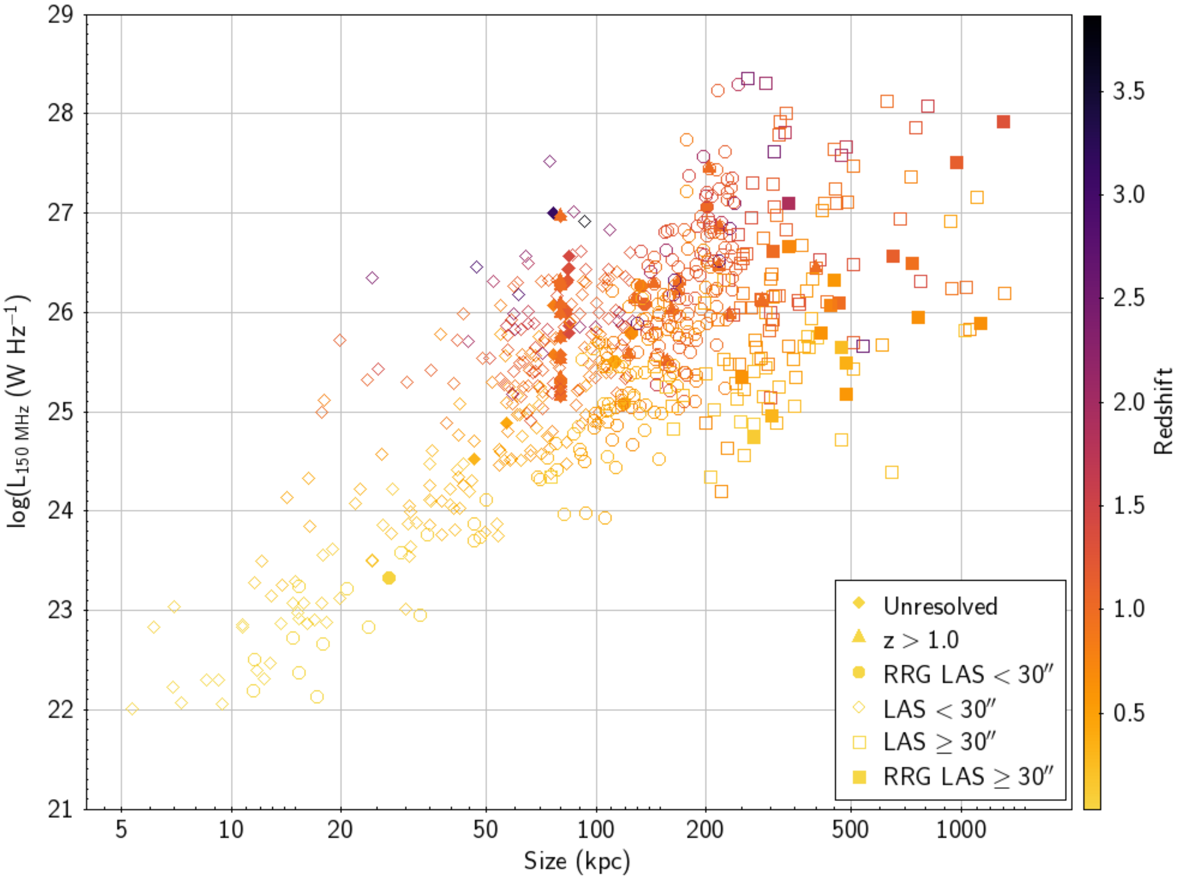

Figure 4.9: 150 MHz rest-frame radio luminosity versus radio size plot. For unresolved sources an upper limit of 10″ on the radio size is considered.

active radio sources are distributed in the range of 11.5 kpc to 245.1 kpc with a median value of 155.4 kpc. Thus, we find that the linear radio sizes of our remnant candidates and active sources are similar. The two-sample KS test suggests that the distributions of radio sizes of active and remnant candidates not very different with D = 0.52 and p-value = 0.03 (see Table 4.3), even when the sample size of remnant candidates is too small. Also, our remnant candidates with upper limit z >1.0 corresponds to the upper limit of 200 kpc for the radio sizes (see Figure 4.9). Thus, we find that our remnant candidates of small angular sizes are small (< 200 kpc) in their physical sizes too. We point out that the remnant candidates of large sizes reported in chapter 3 have radio sizes distributed in the range of 241.6 kpc to 1301 kpc with a median value of 478.3 kpc (see Figure 4.9). Therefore, we conclude that the SPC criterion applied on the small angular size sources (LAS < 30″) allows us to identify remnant candidates of small sizes (≤200 kpc).

To understand the nature of small-size remnant candidates we examine their radio luminosities. We find that our 23/48 remnant candidates have 150 MHz radio luminosities in the range of 2.14 $\times$ 10^{23} W Hz^{-1} to 1.15 $\times$ 10^{27} W Hz^{-1} with a median value of 6.17 $\times$ 10^{25} W Hz^{-1}. While, active sources have 150 MHz luminosities distributed in the range of 3.6 $\times$ 10^{21} W Hz^{-1} to 1.94 $\times$ 10^{28} W Hz^{-1} with a median value of 1.48 $\times$ 10^{25} W Hz^{-1}. The two-sample KS test shows that the 150 MHz luminosity distributions of remnant candidates and active sources are different *i.e.*, probability that the two distributions come from same distribution is only 2 $\times$ 10^{-4}. We note that the active radio sources are on average less luminous and contain a substantial fraction of sources at lower luminosities down to 3.6 $\times$ 10^{21} W Hz^{-1}. Sources of low radio luminosities can be possibly be radio-quiet AGN and star-forming galaxies. We find that, unlike active radio sources, both extended as well as unresolved remnant candidates are luminous *i.e.*, all but one remnant candidates have $L_{150\ \rm MHz} \geq 10^{24}$ W Hz^{-1}. Our 25/48 remnant candidates with upper limit on their redshifts (z) $>$ 1.0 have high 150 MHz luminosities ($L_{150\ \rm MHz}$ $>$ 10^{25} W Hz^{-1}; Figure 4.10). Also, we point out that 150 MHz radio luminosities of our remnant candidates are similar to those of large-size remnant candidates reported in chapter 3. Thus, we find that our remnant candidates represent a population of small-size ($\leq$ 200 kpc) luminous radio sources. High 150 MHz radio luminosity of our remnant candidates can be understood if they are at high redshifts, and/or appear bright at low-frequency due to their steep radio spectra. In Section 4.5 we discuss the plausible reasons for their small size.

4.5 Evolutionary Scenario for Small Size Remnants

From the P-D plot it is evident that, in general, our remnant candidates have small radio size ($<$ 200 kpc) but high radio luminosity ($L_{150\ \rm MHz} \geq 10^{25}$ W Hz^{-1}). The trend shown by our remnant candidates in the P-D plot is rather unusual as remnants are expected to show relatively large radio size and low radio luminosity. We note that the evolution of both luminosity and physical size depends on the jet kinetic power, longevity of active phase, and large-scale environment of a radio source (Hardcastle et al., 2019). Assuming radio luminosity as the proxy for jet power, the progenitors of our remnant candidates are expected to possess high jet power. Thus, small radio-size can be

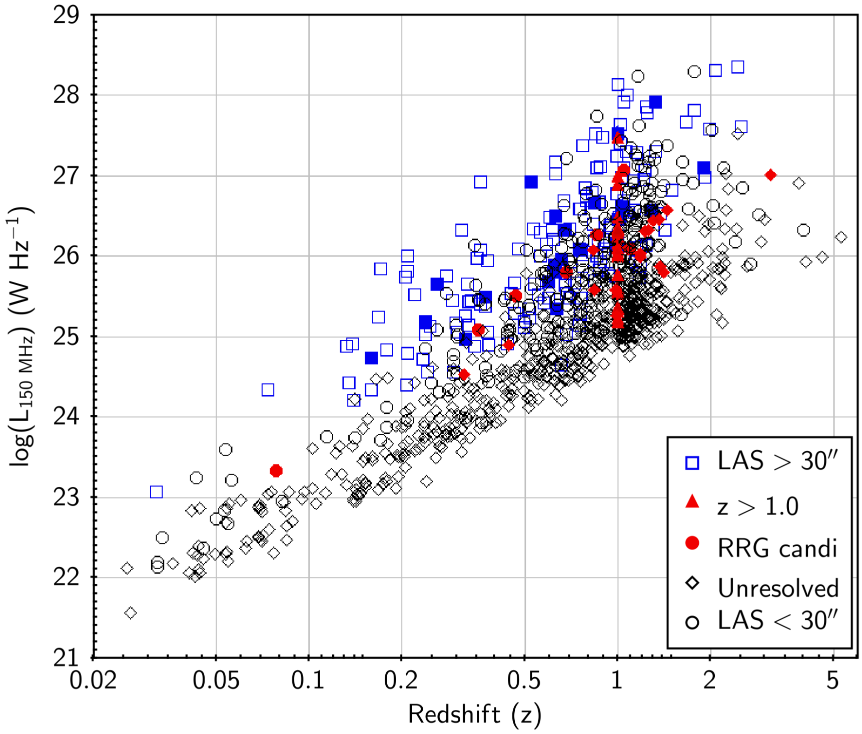

Figure 4.10: Redshift versus 150 MHz rest-frame radio luminosity.

expected if our remnant candidates reside in the centers of cluster environments wherein dense surrounding medium confines the growth of radio source (Murgia et al., 2011). We investigated the large-scale environments of our remnant candidates by checking their association with the clusters detected in the XMM-LSS region. We used optically-selected cluster catalogue derived from the HSC-SSP survey (Oguri et al., 2021) and X-ray selected cluster catalogue based on the deep *XMM-N* survey (Adami et al., 2018). The deep multi-band images of the HSC-SSP survey detect clusters over a wide range of redshifts $0.1 < z < 1.1$ with photometric redshift accuracy of $\Delta z/\ (1+z) < 0.01$ and richness $(N_{gal}) \geq 15$ considering galaxies brighter than 24 magnitude in $z-$band (Oguri et al., 2021). The *XMM-N* survey detects hot X-ray emitting gas present in the Intra-Cluster Medium (ICM) with the flux limit of a few times of 10^{-15} erg s^{-1} cm^{-2} in the $0.5 - 10$ keV band within $1'.0$ aperture (Adami et al., 2018). The follow-up optical spectroscopic observations found X-ray detected clusters to be distributed over $0.0 < z < 1.2$ with one cluster at $z = 2.0$. We find that only two of our remnant candidates J021408-053456 and J021528-044045 are associated with clusters at $z = 0.445$ and $z = 0.348$, respectively, within a matching radius of $1'.0$ and the redshift uncertainty of $\Delta z/(1+z) < 0.01$. Remnant candidates J021408-053456 and J021528-044045 lie at the projected distance of nearly $2''.2$ (12.7 kpc) and

$5''.4$ (26.8 kpc) away from the optically assigned cluster centers, respectively. Since only 15 remnant candidates fall within the clusters redshift cutoff limit $z < 1.2$, the fraction of remnant candidates associated with clusters is merely 13% (02/15) in our sample. Our result is consistent with Jurlin et al. (2021) who found that only a small fraction (23%) of their remnants reside in the cluster environments. Hence, we conclude that our small size remnant candidates generally reside in a less dense environments.

The small size of our remnant candidates showing high radio luminosity and residing in non-cluster environments can be plausible if the active phase of these radio sources is unusually short ($< 50 \times 10^6$ years). Also, we caution that the high monochromatic radio luminosity may not necessarily imply high jet kinetic power due to degeneracy caused by variable parameters such as magnetic field strength in lobes and spectral curvature (Turner et al., 2018). Thus, it is possible that progenitors of our remnant candidates can possess low power jets resulting into smaller radio size. Further, projection effect can also play a role *i.e.*, a remnant in which jet axis were closely aligned to the line-of-sight would appear smaller in size.

4.6 Remnant Fraction

The fraction of remnant sources in a sample of radio galaxies can allow us to constrain the AGN duty cycle and remnant evolutionary models. We attempt to determine the remnant fraction ($f_{\rm rem}$) in our sample of small size (LAS $< 30''$) radio sources. The small size of our sources does not allow us to characterise their radio morphologies in detail, and hence, we cannot rule out the possibility of some of them being active with the presence of a faint core. Also, the identification of remnants based on the spectral curvature can be erroneous due to the resolution bias *i.e.*, when 1.4 GHz flux density from the FIRST or JVLA observations of relatively higher resolution is used. Thus, remnant sources identified in our study are only candidates and allow us to place only an upper limit on $f_{\rm rem}$. With the identification of 48 remnant candidates in a sample of 1516 radio sources we obtain $f_{\rm rem} \leq 3.2\%$. The upper limit on the remnant fraction would reduce to 2.8% if we exclude five remnant candidates with possible recurrent AGN activity. We note that $f_{\rm rem}$ found in our sample of small-size sources is much lower than that reported for the large-size radio sources. For instance, using absent-core criterion Mahatma et al. (2018) found $f_{\rm rem} \leq$ 9% in a sample of 127 bright ($S_{150\ \rm MHz} \geq$ 80 mJy) and large (LAS $\geq 40''$) radio sources detected in the 150 MHz LOFAR survey. In the Lockman Hole field (Jurlin et al., 2021) reported $f_{\rm rem} \leq 8.0\%$ in a sample of 158 sources with $S_{150\ \rm MHz} \geq$ 40 mJy and size $\geq 40''$. In the chapter 3, we obtained $f_{\rm rem} \leq 9\%$ in a sample of 268 sources with flux density limit cutoff of 6.0 mJy at 325 MHz that corresponds to 10 mJy at 150 MHz, and a size cutoff limit of $30''$. With the availability of deep 1.4 GHz JVLA survey in the XMM-LSS-JVLA region we placed a tighter constraint on $f_{\rm rem}$ to be $\leq 5\%$. A significantly lower value of $f_{\rm rem}$ $\leq$3.2% found in our sample consists of small-size sources ($< 30''$) can be attributed to various factors such as – (i) a single criterion based on the spectral curvature fails to identify all remnants and selects only those remnants for which spectral break falls within the frequency window of 150 MHz to 1.4 GHz, (ii) remnants depicting the last evolutionary phase of radio galaxies are generally of larger size, and only a low fraction of remnants appear small as they fail to grow large, (iii) sources at fainter flux densities have substantial contamination from radio-quiet AGN and star-forming galaxies. In the following subsection we discuss the effects of various biases.

4.6.1 Selection Criteria Bias

Radio spectrum of a remnant source can be characterized with a broken or curved power law wherein break frequency ($\nu_{\rm b}$) depends on the time elapsed since the cessation of AGN activity (see Section 4.3.1). As the relic plasma ages $\nu_{\rm b}$ shifts progressively towards the lower frequency. Our spectral curvature criterion used in the frequency range of 150 MHz to 1.4 GHz would miss old remnants with $\nu_{\rm b}$ < 150 MHz as well as young remnants with $\nu_{\rm b}$ > 1.4 GHz. Limitations of the spectral curvature criterion are evident from the fact that we identified only 09/24 of their remnant candidates using spectral curvature criterion in chapter 3. Thus, spectral curvature criterion allows us to identify only a fraction of remnant candidates and not the full population. Hence, a low fraction of remnant (3.2%) found in our study can partly be attributed to the use of only one criterion.

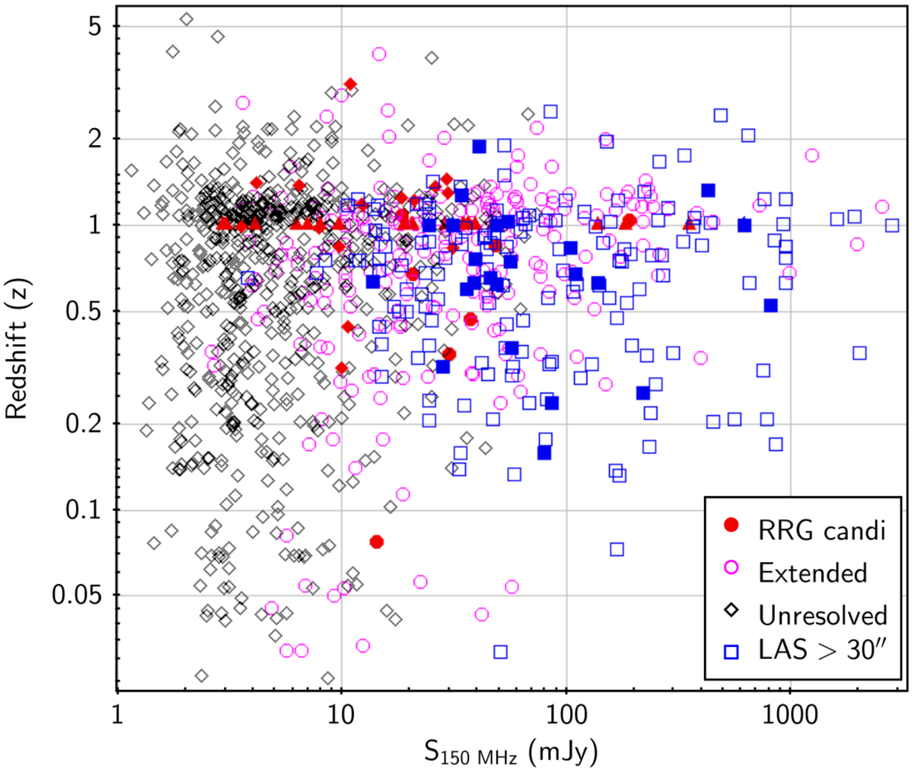

Figure 4.11: 150 MHz flux density versus redshift plot.

4.6.2 Flux Density and Luminosity Bias

Our 1516 sample sources have 325 MHz flux densities in the range of 0.78 mJy to 1511 mJy with a median value of 4.8 mJy, while 48 remnant candidates are distributed across 1.93 mJy to 132.0 mJy with a median of 11.2 mJy (see Table 4.3). From Figure 4.11 it is evident that our sample contains increasingly a large fraction of sources at the fainter end reaching down to 1.0 mJy. If we place a flux density limit of $S_{325\ \mathrm{MHz}} \geq 6.0$ mJy or $S_{150\ \mathrm{MHz}} \geq 10$ mJy, similar to that we used in chapter 3, we obtain only 34 remnant candidates among 655 radio sources, yielding f_{rem} to be $\leq 5.2\%$. Thus, one of the reasons for the low remnant candidates fraction (f_{rem} $\leq$3.2%) in our sample is flux density bias. This can be understood as the faint source population is likely to be dominated by non radio-loud AGN, while remnant candidates belong to the radio-loud AGN population. The flux density bias also translates into luminosity bias. If we place a luminosity cutoff limit of $L_{150\ \mathrm{MHz}} \geq 10^{24}$ W Hz^{-1} we recover a high fraction 22/23 (95.7%) of our remnant candidates but a relatively lower fraction 680/835 (81%) of active sources, where only sources with available redshifts are considered. The different recovery rates for remnant and active sources can be explained if remnant candidates are of higher luminosities and active sources contain a large fraction of low-luminosity sources from non radio-loud sources.

To examine the presence of non-radio-loud AGN at fainter flux densities we exploit well-known radio-FIR correlation that relates radio emission and FIR emission in star-forming galaxies (Helou et al., 1985; Garrett, 2002). The tight correlation observed between radio and FIR emission in star-forming galaxies is explained as the emission at both wavebands arise from stellar processes, *i.e.*, the non-thermal synchrotron radio emission is produced via relativistic particles (cosmic rays) accelerated by supernovae explosions, and FIR emission is due to thermal emission from the ISM dust heated by UV photons from young massive stars. Due to the presence addition radio emission from AGN, the galaxies hosting radio-loud AGN show clear deviation in the radio-FIR correlation. We consider ratio of 24 μm FIR to 325 MHz radio flux densities ($q_{24} = S_{24\ \mu\mathrm{m}}/S_{325\ \mathrm{MHz}}$) for our sample sources. The 24 μm FIR flux densities are derived from the *Spitzer* Wide−area InfraRed Extragalactic survey (SWIRE; Lonsdale et al., 2003). The SWIRE survey centered at RA = 02$^{\mathrm{h}}$ 21$^{\mathrm{m}}$ 00$^{\mathrm{s}}$ and DEC = -04° 30′ 00″ (J2000) and covers a total area of nearly 9.0 deg^2 with 5-sigma sensitivity at 24 μm reaching down to 0.45 mJy beam^{-1}. There are only 1004/1516 radio sources lie in the SWIRE regime among which only 299/1004 (29.8 per cent) show detection at 24 μm using a positional cross-matching within the search radius of 5″.0. For remaining 705/1004 radio sources we place a 5σ upper limit of 0.45 mJy for 24 μm flux density. In Figure 4.12 we plot $S_{24\ \mu\mathrm{m}}/S_{325\ \mathrm{MHz}}$ versus redshift. Since our sample sources are predominantly radio-loud AGN, in particular, for bright and high-redshift radio sources, we find a large scatter in the radio-FIR correlation rather than a tight correlation known for star-forming galaxies (see Ibar et al., 2008). We also mark the positions of our remnant candidates (falling within the SWIRE region) in the $S_{24\ \mu\mathrm{m}}/S_{325\ \mathrm{MHz}}$ versus redshift plot where flux densities are depicted by colour and radio-loud radio-quiet division is marked (see Figure 4.12). It is evident that all but one remnant sources fall in the radio-loud region and only relatively faint radio sources are radio-quiet. Therefore, we demonstrate that a substantial contamination by non radio-loud population, in particular towards fainter flux densities, is one of the reasons for the low remnant fraction (f_{rem} $\leq$3.2%) in our sample. As argued above, both small-size ($<$ 30″) and large-size ($\geq$ 30″)

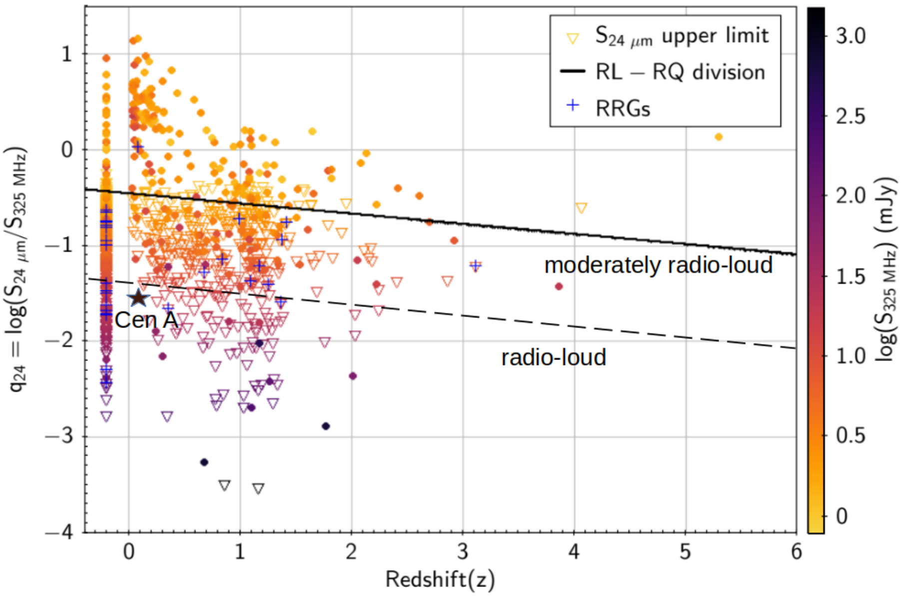

Figure 4.12: Radio to IR flux ratio versus redshift plot. The radio-loud and radio-quiet division is based on the composite spectrum for radio-loud AGN given by Elvis et al. (1994).

radio sources show similar remnant fraction, once flux density bias is accounted for.

4.6.3 Redshift Bias

In our sample only 23/48 remnant candidates have redshift estimates distributed in the range of 0.077 to 3.12 with a median value of 1.04. For remaining 25/48 remnant candidates we place an upper limit of $z > 1.0$ based on the ratio of 325 MHz flux density to 3.6 μm flux density. Thus, we find that our remnant candidates tend to lie at higher redshift with 37/48 (77%) sources at $z > 1.0$. It is worth pointing out that using the same data in chapter 3 we found that large-size (LAS $\geq 30''$) remnants lie systematically at lower redshifts in the range of 0.139 to 1.895 with a median value of 0.65. Therefore, unlike large-size remnants, majority of our remnant candidates appear small due to their higher redshifts. From Figure 4.11 it is clear that many of our small-size remnants tend to lie at higher redshifts and fainter flux densities. Hence, our study probes a somewhat different phase space in the flux density versus redshift plot. Therefore, it is possible that the sample containing high$-z$ radio sources may have different remnant fraction.

4.6.4 Fraction in the XMM-LSS-JVLA Region

There are a total of 637 radio sources falling within the 5.0 deg^2 of the XMM-LSS-JVLA region, while only 25 remnant candidates are identified within this region. We obtain $f_{\rm rem}$ < 3.9% in the XMM-LSS region which is little higher than that found for the full sample ($f_{\rm rem}$ < 3.2%). A slightly higher remnant fraction in the JVLA survey region can be due to the availability of deeper 1.4 GHz data (5σ = 0.08 mJy). We note that all but four of 356 sources with no detected 1.4 GHz counterparts fall outside the XMM-LSS-JVLA region, and upper limits on 1.4 GHz flux density is based on the FIRST (5σ = 1.0 mJy) and NVSS (5σ = 2.5 mJy). It is fairly possible that several sources with no detected 1.4 GHz counterparts can have 1.4 GHz flux densities much lower than their upper limits, and hence, these sources can show strong spectral curvature $\geq$ 0.5, if 1.4 GHz flux density estimates are available. Therefore, a fraction of active sources having only 1.4 GHz flux density upper limits can possibly turn out to be remnant candidates. These sources remained unidentified in our study due to the unavailability of 1.4 GHz flux densities. Therefore, the remnant fraction ($f_{\rm rem}$ < 3.9%) obtained in the XMM-LSS-JVLA region provides a better constraint. If we place 6.0 mJy flux density cutoff limit, same as used in chapter 3, we obtain only 13 remnant candidates yielding $f_{\rm rem}$ < 5.4% (13/240) that is similar to the one ($f_{\rm rem}$ < 5%) obtained in chapter 3 for the extended sources (LAS $\geq 30''$) in the XMM-LSS region. Therefore, we find similar remnant fractions for both small-size (LAS < $30''$) as well as for large-size (LAS $\geq 30''$) sources once the bias introduced by the flux density limit is taken into account.

4.7 Results and Conclusions

We carried out a search for remnant candidates of small angular sizes (LAS < $30''$) using deep multi-frequency radio surveys (150 MHz LOFAR, 325 MHz GMRT and 1.4 GHz JVLA, NVSS and FIRST) in the XMM-LSS field. Our study is the first attempt to perform a systematic search for remnants of small sizes. Owing to the small angular sizes of sources we exploit spectral curvature criterion and discover 48 remnant candidates exhibiting strong spectral curvature *i.e.*, $\alpha_{\rm low}$ - $\alpha_{\rm high} \geq 0.5$; where $\alpha_{\rm low} = \alpha_{150\ \rm MHz}^{325\ \rm MHz}$ and $\alpha_{\rm high} = \alpha_{325\ \rm MHz}^{1.4\ \rm GHz}$. The main conclusions of our study are outlined as below.

- Unlike most of the previous studies limited to large and bright remnant sources our study identified remnant candidates of small angular sizes (LAS $< 30''$) that include faint sources with flux density reaching down to 1.0 mJy at 150 MHz. Thus, our study unveils remnant candidates at the faintest flux density regime than that reported earlier.

- Using 1.4 GHz images of higher resolution mainly from the JVLA survey we find that a fraction (15/48 = 31%) of our remnant candidates have extended double-lobe like radio morphology, while majority of remnant candidates appear unresolved or slightly resolved in the 325 MHz GMRT images of $10''$ resolution. Our remnant candidates show steep radio spectral index with $\alpha_{150\ \rm MHz}^{1.4\ \rm GHz}$ distributed in the range of -1.94 to -0.86 with a median value of -1.04, which is similar to that found for large-size remnants identified mainly using morphological criteria.

- The 3 GHz VLASS quick look image cutouts show the detection of only 10/48 remnant candidates. Some of our remnant candidates continue to show steep spectral index at higher frequency (1.4 GHz $-$ 3.0 GHz). While, five remnant candidates show a flatter spectral index at higher frequency regime inferring the possibility of recurrent AGN activity. Deep high-frequency imaging of our remnant candidates would be useful in deciphering their nature. Thus, remnant candidates identified in our study can be used for follow-up observations.

- Unlike large-size remnant candidates, our small-size remnant candidates are found at relatively higher redshifts. There are 23/48 remnant candidates with redshift estimates in the range of 0.077 to 3.12 with a median value of 1.04, while remaining 25 remnant candidates have an upper limit of $z > 1.0$.

- Radio luminosity versus radio size plot shows that our remnant candidates are of smaller sizes ($\leq$ 200 kpc) but have high 150 MHz luminosities similar to that found for the large-size remnant candidates. 150 MHz luminosities of our 23 remnant candidates with redshift measurements are distributed in the range of 2.12×10^{23} W Hz^{-1} to 1.15×10^{27} W Hz^{-1} with a median value of 9.77×10^{25} W Hz^{-1}. Remaining 25 remnant candidates with $z > 1.0$ have $L_{150\ \mathrm{MHz}} > 10^{25}$ W Hz^{-1}.

- We find that only a small fraction (02/15 $\sim$ 13%) of our remnant candidates reside in clusters, and hence, small radio size is unlikely to be caused by dense large-scale environment. We speculate that a relatively short active phase ($< 50 \times 10^{6}$ years) can plausibly limit the growth of radio source to the size of $<$ 200 kpc, although projection effect can also make apparent size smaller.

- Our study allows us to place an upper limit on the remnant fraction (f_{rem}) to be 3.2%. In the XMM-LSS-JVLA region, f_{rem} is slightly higher (3.9%) due to the availability of deep 1.4 GHz JVLA survey. Therefore, it is fairly possible that a fraction of sources having only upper limits on 1.4 GHz flux density may turn out to be remnant candidates, if actual 1.4 GHz flux density is much lower than the upper limit. Further, we find that the a low value of f_{rem} can arise due to various factors such as the usage of single selection criterion, contamination from non radio-loud AGN at fainter flux densities, and redshifts bias. Notably, using a flux density cutoff of 6.0 mJy at 325 MHz we find $f_{\mathrm{rem}} < 5.4\%$ in the XMM-LSS-JVLA region, which is similar to that for large-size remnant candidates in the same region. Therefore, f_{rem} is nearly same for both small-size and large-size remnant candidates once bias introduced by the flux density limit is accounted for.

Chapter 5

Spectral Ages of Remnant Radio Galaxies

5.1 Introduction

The serendipitous discovery of individual remnants ***e.g.***, B2 0924+30 (Cordey, 1987; Shulevski et al., 2017), J021659-044920 (Tamhane et al., 2015), blob1 (Brienza et al., 2016) and NGC 1534 (Duchesne & Johnston-Hollitt, 2019), WISEA J152228.01+274141.3 (Lal, 2021) etc., as well as small samples found in the deep field surveys (Mahatma et al., 2018; Jurlin et al., 2021) led the notion of remnants being rare sources. The rarity of remnants has conventionally been attributed to the rapid energy losses at work in relic lobes. Albeit, the timescale over which a remnant can be detected varies from source to source and depends on various factors such as the source size, magnetic field in the lobes and the large-scale environment (Turner, 2018). In fact, the evolution of radio galaxies in their remnant phase is not well understood, due to their paucity.

There have been attempts to perform systematic searches for remnants to constrain AGN duty cycle and evolutionary models (see Godfrey et al., 2017; Brienza et al., 2017; Mahatma et al., 2018). However, such studies often face limitations imposed by the selection criteria and the flux density limits of radio observations. For instance, in their sample of 127 sources with $S_{150\ \mathrm{MHz}} \geq 80$ mJy and radio size $\geq 40''$ Mahatma et al. (2018) found only 11 remnants with no detected radio core in deep (noise-rms $\sim$ 0.02 mJy beam^{-1}) 6 GHz JVLA observations. More recently, Jurlin et al. (2021) noted that a feeble radio core representing a dying AGN activity can still be present in a remnant and identified only 13 remnants in their sample of 158 sources. Notably, despite the concerted efforts the studies based on the sensitive low-frequency radio observations in deep fields have yielded only small samples with remnant fraction limited to 5%$-$10% (see Mahatma et al., 2018; Quici et al., 2021; Jurlin et al., 2021).

It is important to note that the remnants identified by using morphological criteria are of large angular sizes ($\geq 30''$), where a limit on the minimum size is placed for deciphering the morphological details. Hence, morphologically selected remnants are inherently biased towards the remnants of more powerful large-size radio galaxies. In Chapter 4, we identified remnants of small angular sizes ($<30''$) using spectral curvature criterion and found them to be more abundant, which is consistent with the theoretical models. For instance, using 'Radio AGNs in Semi-Analytic Environments' (RAiSE) dynamical model Shabala et al. (2020) showed that the models assuming a power-law distribution of jet kinetic powers and source ages can explain the observed fraction of remnants and their distributions of flux density, angular size and redshift. In fact, the power law distribution of jet kinetic powers predicts a more number of small-size remnants. Thus, the remnant population can be more diverse than that envisaged from the small samples of large-size remnants discovered earlier. Hence, it becomes important to study individual remnant sources and estimate various source parameters such as magnetic field, remnant age, AGN duty cycle and their large-scale environments. The detailed study of individual remnant sources can help us to understand the evolutionary scenario at work in different sources. In this chapter, we present spectral ageing analysis for a sample of five remnant sources using multi-frequency radio observations.

This chapter is organized as follows. In Section 5.2 we provide the details of radio observations. The sample selection criteria and source characteristics are described in Section 5.3. In Section 5.4 we describe the radio SED modelling, spectral age determination of our sample remnants, and their comparison with the remnants reported in the literature. In Section 5.5 we discuss the potential of deep and wide radio continuum radio surveys planned with the Square Kilometer Array (SKA) and its pathfinders. The results and conclusions of our study are presented in Section 5.6.

5.2 Radio Observations

For our study we use band-3 observations from the upgraded Giant Meterwave Radio Telescope (uGMRT; Gupta et al., 2017), along with the auxiliary radio observations available at 325 MHz from the legacy GMRT (Swarup, 1991)), 150 MHz observations from the LOFAR and 1.5 GHz JVLA observations. All our remnant sources are located within a small region of 2.3 deg^2 of the *XMM*−LSS field. We give a brief description of these observations in the following subsections.

5.2.1 Band-3 uGMRT Radio Observations

Our band-3 (250 MHz − 550 MHz) uGMRT observations were performed on 11 September 2017 (proposal code 32_066) in full synthesis mode with nearly 10 hours of total observing time. With an aim to obtain the deepest possible image, these observations were limited only to one pointing centered at RA = $02^{\rm h}\ 26^{\rm m}\ 45^{\rm s}$ and DEC = $-04^{\circ}\ 41'\ 30''$ in the *XMM*−LSS field. The observations were acquired in a standard manner by observing the flux calibrators 3C48 and 3C147 for 15−20 minutes at the beginning and end of the observing session, respectively. The phase calibrators 0116-0208 and 0323+055 were observed for nearly 5 minutes with scans inter-leaved with 30 minutes scans of the targeted field. The uGMRT radio data were reduced using a pipeline based on the Common Astronomy Software Applications (CASA[1]) routines. We followed the standard data reduction procedure that involved flagging of bad data, calibrating visibilities, imaging of calibrated visibilities, and several iterations of self calibration. The final primary beam corrected image achieves a median noise-rms of 30 μJy beam^{-1}. As expected, the noise-rms is lowest ($\sim$20 μJy beam^{-1}) in the central region, while a higher noise-rms ($\sim$40 μJy beam^{-1}) is seen around bright sources and in the peripheral regions. The synthesized beam-size is $6''.7 \times 5''.3$. Using the Python Blob Detector and Source Finder (PyBDSF[2]; Mohan & Rafferty (2015)) algorithm we detected a total number of 2332 sources at $\geq 5\sigma$ over the full sky-area of 2.3 deg^2. More details on the data reduction and creation of the source catalogue can be found in Kayal et al. (2022).

5.2.2 Auxiliary Radio Observations at 150 MHz, 325 MHz and 1.5 GHz

To build radio spectral energy distributions (SEDs) of our remnants, we utilized radio observations available at other frequencies over the widest range. We used 150 MHz LOFAR observations available in the *XMM*−LSS field (Hale et al., 2019). The region of our band-3 uGMRT observations is also covered with the 325 MHz observations performed with the legacy GMRT equipped with software correlator giving 32 MHz instantaneous

[1]https://casa.nrao.edu/

[2]https://github.com/lofar-astron/PyBDSF

bandwidth (Proposal: 20_006). We also utilised 1.5 GHz JVLA observations reported by Heywood et al. (2020). The 1.5 GHz observations performed with the VLA in B-configuration. The details of these radio observations can be found in the Section 3.2 of Chapter 3.

The JVLA observations with better resolution are efficient in revealing structural details. Although, while building radio SEDs we ensure that the JVLA observations do not suffer with the missing flux issue wherein diffuse emission of low-surface-brightness can be missed due its higher resolution. We compare JVLA flux densities with those from the 1.4 GHz NVSS, whenever available, and we use NVSS flux densities, in case of missing flux issue. With its large beam-size of $45''$ NVSS observations can efficiently detect the diffuse emission of low-surface-brightness emission.

We note that the sky region of our band-3 uGMRT observations is also covered with the 240 MHz, 610 MHz GMRT observations (Tasse et al., 2007) and 74 MHz VLA observations (Tasse et al., 2006). In principle, these observations can be useful in building radio SEDs, however, we found that, unexpectedly, 240 MHz and 610 MHz flux densities are systematically underestimated (see Singh et al., 2021). Hence, we prefer not use 240 MHz and 610 MHz GMRT observations. Also, 74 MHz VLA observations yielding noise-rms of 32 mJy beam^{-1} are too shallow to detect our relatively faint sources. Therefore, in our study we used radio observations mainly from the LOFAR at 150 MHz, the GMRT at 325 MHz, the uGMRT at 400 MHz, and the JVLA at 1.5 GHz.

5.3 The Remnant Sample and band-3 uGMRT Observations

In this subsection, we describe the sample selection criteria and the characteristics of our remnant sources.

5.3.1 Remnant Sample and Selection Criteria

Our one pointing uGMRT radio observations detected 10 remnant candidates from the samples reported in chapter 3 and chapter 4. We note that redshift and radio size measurements are available for only five remnant candidates. Therefore, our spectral ageing analysis is limited only to five sources with available redshift and radio size estimates. We list basic parameters ***i.e.***, flux densities, surface brightness, radio sizes, redshifts, and 400 MHz radio luminosities of our sample sources in Table 5.1. All the five remnant sources are selected by using spectral curvature criterion ***i.e.***, $\alpha_{150\ \mathrm{MHz}}^{325\ \mathrm{MHz}}$ - $\alpha_{325\ \mathrm{MHz}}^{1.5\ \mathrm{GHz}} \geq 0.5$. Using 150 MHz LOFAR, 325 MHz GMRT and 1.4 GHz JVLA observations, we demonstrated in Chapter 4 that the remnant sources of small angular sizes ($<30''$) often lacking morphological details in the radio images of $5'' - 10''$ angular resolution, can be identified by using spectral curvature criterion (see Singh et al., 2021). We note that our five remnant sources also satisfy morphological criteria ***i.e.***, diffuse emission of low-surface-brightness ($36-201$ mJy arcmin^{-2} at 400 MHz, see Table 5.1) detected at low-frequencies and absence of core in the high frequency 3.0 GHz VLASS images. Therefore, our sources satisfying both morphological and spectral criteria can be regarded as the confirmed remnants. Further, we note that unlike most of the remnant sources reported in the literature, our sample sources are relatively faint (150 MHz flux density in the range of 6.3 mJy to 37.3 mJy) and reside at relatively higher redshifts ($z \geq 0.44$) (see Table 5.1). It is worth mentioning that most of the individually studied remnant sources (***e.g.***, Brienza et al., 2016; Shulevski et al., 2017; Duchesne & Johnston-Hollitt, 2019) as well as the remnant samples derived from the LOFAR observations are relatively bright ***i.e.***, $S_{150\ \mathrm{MHz}}$ >80 mJy and extended (size $\geq 40''$) (see Mahatma et al., 2018; Jurlin et al., 2021). Therefore, our sample of relatively faint and small-size remnant sources allow us to probe a different phase space for remnant sources.

5.3.2 Characteristics of Our Remnants

In the following subsections, we describe radio morphologies and characteristics of our sample sources in the context of new uGMRT observations. Notably, our new 400 MHz uGMRT observations discover a wing-shaped radio morphology in J022338-045418 (see Figure 5.2). To compare the radio morphological details at different frequencies, we plot radio contours of 400 MHz uGMRT, 325 MHz GMRT and 1.5 GHz JVLA emission onto the corresponding optical i band images from the HSC-SSP (see Figure 5.3).

5.3.2.1 J022318-044526:

This source shows a clear double-lobed radio morphology with a total end-to-end projected size of 78$''$ that corresponds to the physical size of 643 kpc at the redshift of the potential host (see section 3.7). The deep 1.5 GHz JVLA observations detect no core but only two lobes that appear edge-brightened similar to the FR II radio galaxies. Our new 400 MHz uGMRT observations revealed nearly the same structures that were seen in the previous 325 MHz observations (see Figure 5.1). Based on the radio contours overlaid on the HSC-SSP i band image, a galaxy J022318.1-044520.7 matching close to the centroid of the low-frequency radio emission, is identified as the potential host with i band magnitude (m_i) 24.09±0.08 and photometric redshift ($z_{\rm phot}$) 1.15±0.17.

5.3.2.2 J022338-045418:

The band-3 uGMRT image of J022338-045418 shows a wing-shaped radio morphology (see Figure 5.2), wherein the northern (upper) component resembles a back-flow like feature, while the southern (lower) component shows a double-peaked emission. This source has very low surface-brightness emission (36 mJy arcmin^{-2} at 400 MHz) such that the southern component is completely undetected in the 1.5 GHz JVLA image, while 325 MHz GMRT image of relatively low resolution ($10''.2 \times 7''.9$) shows only north-south elongation with no apparent structures (see Figure 5.3, *upper panel*). Interestingly, the northern component which resembles with a backflow tail in the 400 MHz uGMRT image clearly shows two peaks in the 1.5 GHz JVLA image. Thus, we find that both northern

Table 5.1: The remnant sample for ageing analysis.

Source Name	$S^{int}_{150\ MHz}$ (mJy)	$S^{int}_{325\ MHz}$ (mJy)	$S^{int}_{400\ MHz}$ (mJy)	$S^{int}_{1.5\ GHz}$ (mJy)	$\alpha^{325\ MHz}_{150\ MHz}$	$\alpha^{1.5\ GHz}_{400\ MHz}$	$SB_{400\ MHz}$ (mJy arcmin^{-2})	z	Size (kpc($''$))	$\log L_{400\ MHz}$
J022318-044526	33.9±1.0	20.2±2.2	12.1±1.4	1.70±0.10	-0.67±0.15	-1.48±0.10	106	1.15±0.17	643 (78)	25.99
J022338-045418	7.04±0.3	3.7±0.7	3.1±0.7	0.6±0.09	-0.83±0.25	-1.24±0.21	36	0.81±0.01	200 (26.5)	25.29
J022723-051242	45.7±0.8	21.1±1.1	15.8±0.5	2.20±0.30	-0.98±0.07	-1.49±0.11	201	0.87±0.07	255 (33)	26.06
J022737-052139	6.3±0.8	3.7±0.60	3.3±0.3	0.6±0.07	-0.69±0.27	-1.29±0.11	56	0.62±0.13	190 (28)	25.25
J022802-041417	37.3±0.9	19.5±1.0	16.2±0.5	2.4±0.2	-0.84±0.07	-1.44±0.07	127	0.44±0.05	216 (38)	25.19

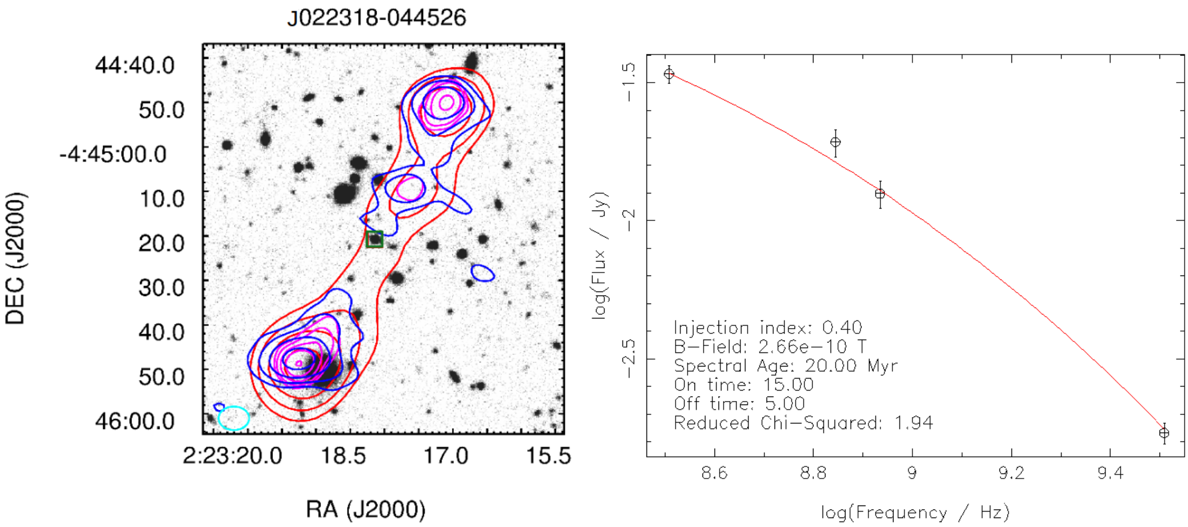

Figure 5.1: *Left panel*: The radio contours of band-3 uGMRT (in Blue), 325 MHz (in Red) and 1.5 GHz JVLA (in Magenta) are overplotted on the corresponding HSC *i*-band optical image for remnant candidate J022318-044526. The radio contours are at $3\sigma \times$ (1, 2, 4, 8, 16, ...) levels and the optical image is logarithmically scaled. The uGMRT band-3 synthesized beam of $6''.7 \times 5''.3$ is shown in the bottom left corner. The potential host galaxy of remnant is marked with a green box around it. *Right panel*: The best fit radio SEDs of J022318-044526. The red solid curve represents model fitted to the data points.

and southern components have two-peak emission, which is commonly seen in the winged radio galaxies classified as the Z-shaped and X-shaped radio sources, wherein diagonally opposite bright peaks correspond to primary lobes, and fainter peaks correspond to secondary lobes, possibly from the previous episode of AGN jet activity (Lal et al., 2019; Bera et al., 2022).

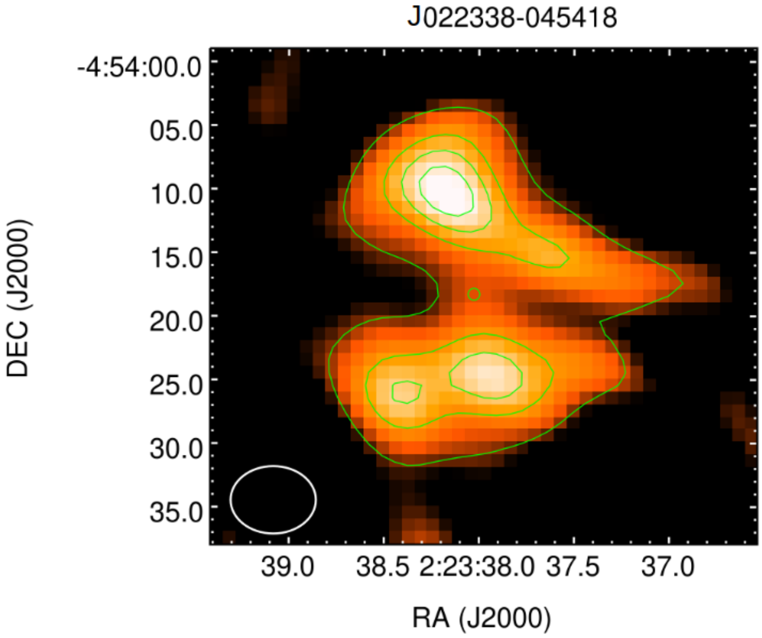

Figure 5.2: The band-3 uGMRT image of remnant source J022338-045418. For the better representation of intensity distribution radio contours (in Green colour) are overplotted onto the corresponding false colour radio image. The radio contours are shown at σ(3, 6, 10, 15, ...) levels. The centroid position is marked with a small Green circle. The uGMRT beam-size of $6''.7\times5''.3$ is shown in the bottom left corner.

We note that the discovery of a wing-shaped radio morphology in J022338-045418 is credited to the sensitivity and resolution of band-3 uGMRT observations that are adequate to detect faint diffuse radio emission. The total flux density at 400 MHz of this source is only 3.1±0.5 mJy, while northern and southern components have a flux density of 1.62±0.3 mJy and 1.48±0.3 mJy, respectively. The lack of its complete detection in all but band-3 observations poses a challenge in characterising this source. For instance, spectral index map requires images at more than one widely separated frequencies with similar angular resolutions. Also, with the present set of radio observations we cannot rule out if wing-shaped radio morphology is the result of two individual double−lobe radio sources located close to each other. Deeper radio observations of higher resolution are needed to examine if this source consists of two individual radio sources. Although, given the lack of optical counterparts matching with individual lobes and a backflow-like feature seen in the band-3 image (see Figure 5.1) suggest that the wing-shaped morphology is unlikely to be the result of two individual double−lobed radio sources coincidentally placed adjacent to each other. We note that there is no detected optical counterpart close to the centroid of the band-3 radio morphology (see Figure 5.1). However, within a radius of 10″ there are two optical sources, *i.e.*, a relatively bright source J022337.7-045414.8 towards the north-west with $m_{\rm i}$ = 22.29±0.01 and photometric redshift ($z_{\rm phot}$) 0.81±0.01, and a faint source J022338.2-045418.6 towards east with $m_{\rm i}$ = 24.99±0.05 and photometric redshift ($z_{\rm phot}$) 2.75±0.56. Because radio galaxies are generally hosted in bright ellipticals we assumed the brighter optical counterpart J022337.7-045414.8 as the potential host.

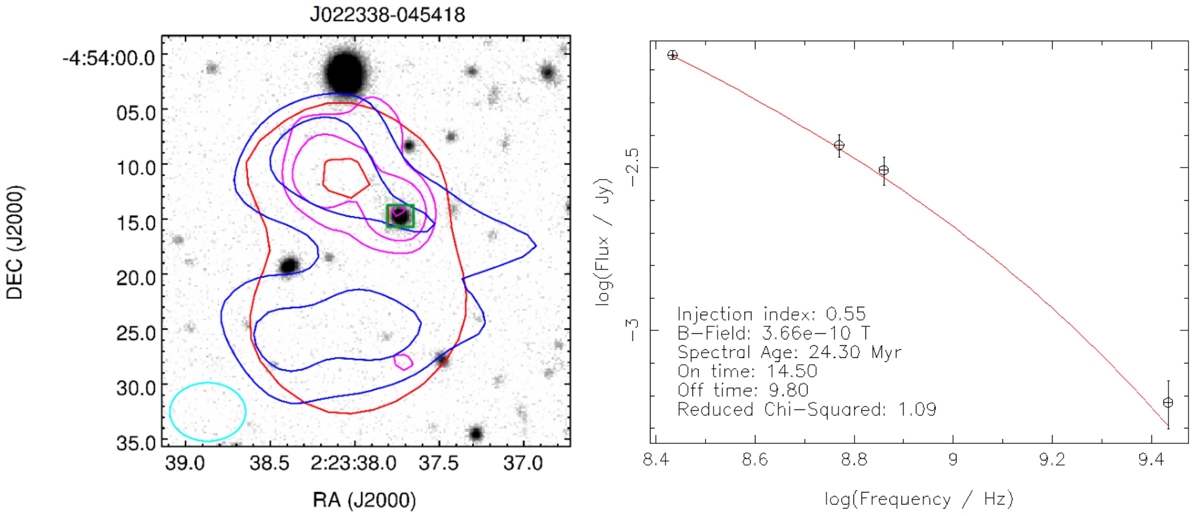

Figure 5.3: *Left panel*: The radio contours of band-3 uGMRT (in Blue), 325 MHz (in Red) and 1.5 GHz JVLA (in Magenta) are overplotted on the corresponding HSC *i*-band optical image for remnant candidate J022338-045418. The position of potential host marked with a green box differs from the centroid position. *Right panel*: The best fit radio SEDs of J022338-045418. The plotting convention is the same as for Figure 5.1.

We point out that the 1.5 GHz JVLA image is showing a peak around the assumed host at J022337.7-045414.8. This peak has been interpreted as the peak of in western lobe of upper wing. However, we cannot rule out the possibility that this peak can be a radio core coinciding with the potential host. Thus, remnant candidate J022338-045418 can have an active radio core, however, deep high resolution radio observations are required to confirm this possibility. If an active core exists, then this source is likely to be a restarted radio galaxy in which extended diffuse radio emission seen in the band-3 uGMRT arise from the previous episode of AGN activity.

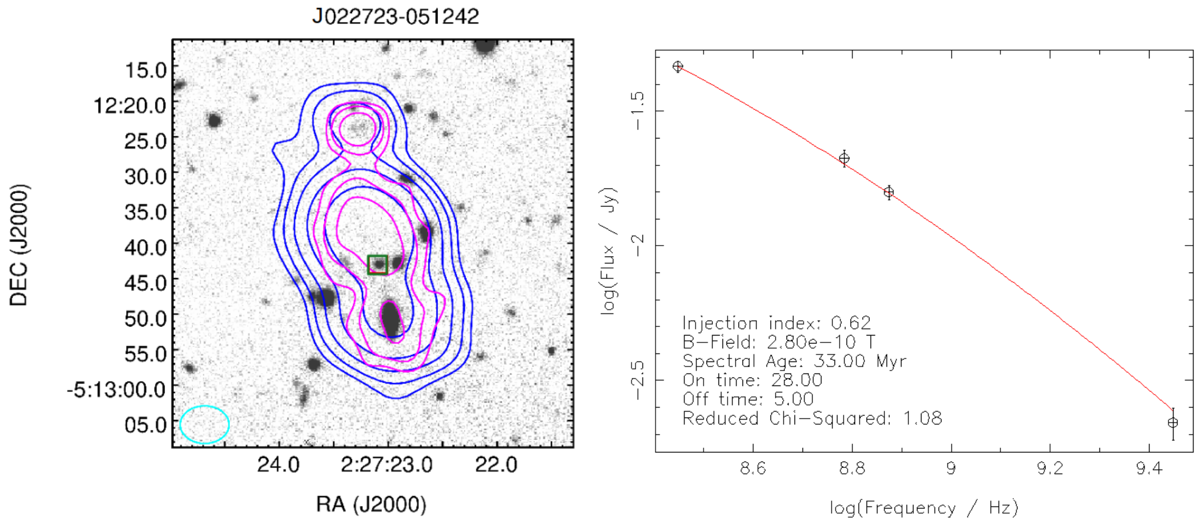

Figure 5.4: *Left panel*: The radio contours of band-3 uGMRT (in Blue), 325 MHz (in Red) and 1.5 GHz JVLA (in Magenta) are overplotted on the corresponding HSC *i*-band optical image for remnant candidate J022723-051242. *Right panel*: The best fit radio SEDs of J022723-051242. The plotting convention is the same as for Figure 5.1.

5.3.2.3 J022723-051242:

The radio morphology of this source resembles a double-lobed source, but the two lobes are not well resolved due to its small angular size of nearly 33″. We note that a separate point radio source J022723.2-051223.8 is located close to its northern side (see Figure 5.4). Due to its proximity, the point radio source contaminates the emission of the remnant source at 150 MHz, 325 MHz and 400 MHz as the spatial resolution is somewhat coarser at these frequencies. To accurately determine the flux density of our remnant source, we removed the contamination of the point radio source by considering its 1.5 GHz flux density from the JVLA image and extrapolating it to the lower frequencies by assuming a spectral index of -0.7. The 1.5 GHz JVLA radio contours of our remnant show two emission peaks each apparently corresponding to the northern and southern lobes, respectively. It is worth noting that the southern peak coincides with a foreground galaxy (J022722.9-051250.6) having $m_i = 19.90 \pm 0.05$ and $z_{\rm phot} = 0.26 \pm 0.10$. From the current observations, it is unclear if the foreground galaxy also contaminates and up to what extent. Although, considering

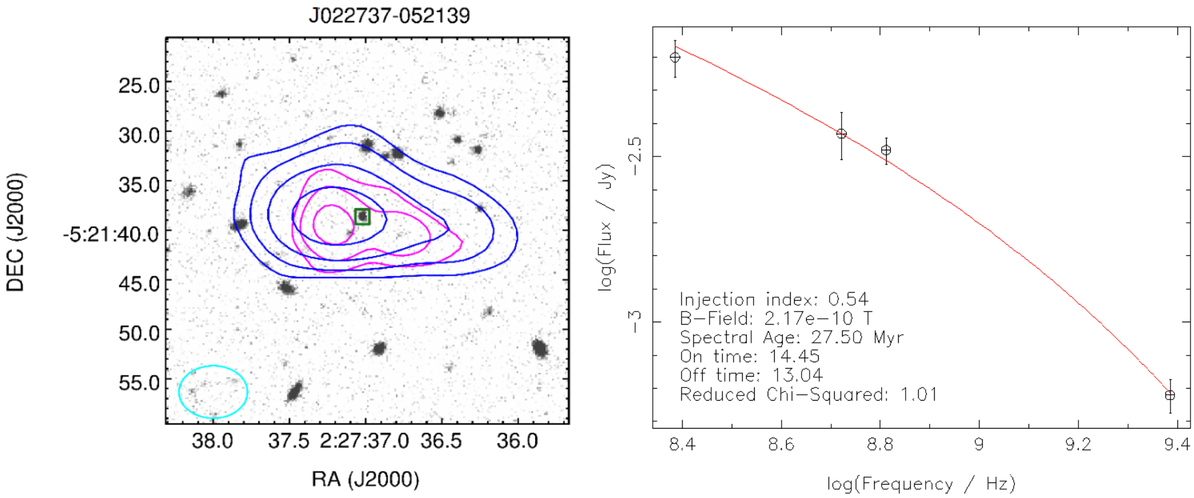

Figure 5.5: *Left panel*: The radio contours of band-3 uGMRT (in Blue), 325 MHz (in Red) and 1.5 GHz JVLA (in Magenta) are overplotted on the corresponding HSC *i*-band optical image for remnant candidate J022737-052139. *Right panel*: The best fit radio SEDs of J022737-052139. The plotting convention is the same as for Figure 5.1.

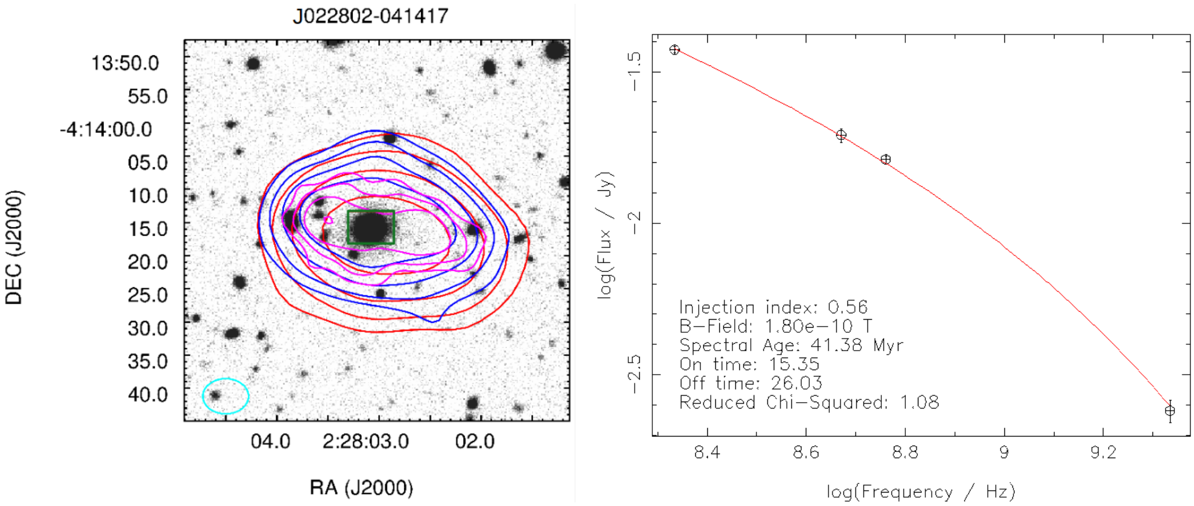

Figure 5.6: *Left panel*: The radio contours of band-3 uGMRT (in Blue), 325 MHz (in Red) and 1.5 GHz JVLA (in Magenta) are overplotted on the corresponding HSC *i*-band optical image for remnant candidate J022802-041417. *Right panel*: The best fit radio SEDs of J022802-041417. The plotting convention is the same as for Figure 5.1.

the relaxed radio morphology of our remnant with an evident diffusion of emission along the direction perpendicular to the jet-axis, the foreground galaxy is unlikely to give rise any significant contamination.

Also, the ultra-steep radio spectrum towards high-frequencies ($\alpha_{400\ \mathrm{MHz}}^{1.5\ \mathrm{GHz}}$ = -1.49±0.11) suggests only minimal contamination from the foreground galaxy, if it exists. Based on the radio contours, in particular from the 1.5 GHz JVLA overlaid on the i band optical image, we consider J022723.1-051242.9 as a potential host with m_i = 23.02±0.01 and z_{phot} = 0.87±0.07. However, another galaxy J022722.9-051242.8 located close to its centroid cannot be ruled out from being a plausible host. Our new uGMRT radio observations show radio morphology similar to that seen with the 325 MHz GMRT and 1.5 GHz JVLA observations.

5.3.2.4 J022737-052139:

The radio morphology of this source shows east-west elongation. The high resolution 1.5 GHz JVLA image indicates the double-lobe-like structure (see Figure 5.5). The two lobes are not well resolved due to the small angular size (28$''$) of this source. Our new uGMRT observations show emission consistent with the 325 MHz GMRT observations. With radio contours overlaid on the i band optical image we identify J022737-052139 as a potential host with m_i = 24.17±0.03 with z_{phot} = 0.62±0.13. With a total size of 190 kpc this source is the smallest in our sample. The strong spectral curvature and low surface brightness of 56 mJy arcsec^{-2} at 400 MHz suggest it to be a remnant source.

5.3.2.5 J022802-041417:

This source is hosted in a nearby bright (m_i = 19.45±0.01) elliptical galaxy with a photometric redshift of 0.44±0.05. The angular size (38$''$) of this source corresponds to the total projected linear size of 216 kpc. Due to its relatively small angular size, 325 MHz and 400 MHz observations do not reveal clear structures. However, 1.5 GHz JVLA image showing east-west elongation and two tentative peaks infer it to be a double-lobed source (see Figure 5.6).

5.4 The Spectral Ages of Remnant Sources

In this section, we estimate the spectral ages of our remnants and compare them with the remnants already studied in the literature.

5.4.1 Modelling of Radio SEDs

We derive the spectral ages of our remnants via modeling their SEDs with physically motivated models. We note that the radio spectrum of an active radio galaxy can be characterised by the continuous injection model (CI model, Kardashev (1962); Jaffe & Perola (1973)) that assumes continuous replenishment of radio lobes at a constant rate for the duration of $t_{\rm ON}$. The relativistic particles emitting radio emission have power law energy distribution ($N(E) \propto E^{-p}$) which results a power law radio spectrum with an index of $\alpha_{\rm inj}$ = (p - 1)/2. Due to the energy dependent cooling rate of relativistic particles the radio spectrum develops a break, during the active phase itself, such that the spectral index above $\nu_{\rm b}$ steepens to the value of $\alpha_{\rm inj}$ - 0.5, where $\alpha_{\rm inj}$ is typically found in the range of -0.5 to -0.8. As radio source evolves, the break frequency ($\nu_{\rm b}$) shifts progressively towards lower frequencies. As mentioned in equation 3.2, the relation between source age ($t_{\rm s}$) and break frequency $\nu_{\rm b}$ can be expressed as below (see Komissarov & Gubanov, 1994; Slee et al., 2001; Parma et al., 2007).

$$t_{\rm s} = 1590 \left[\frac{B_{\rm eq}^{0.5}}{(B_{\rm eq}^2 + B_{\rm CMB}^2)\sqrt{\nu_{\rm b}(1+z)}} \right] \text{Myr}$$

where $t_{\rm s}$ is the total source age, $B_{\rm eq}$ and $B_{\rm CMB}$ =3.25(1+z)^2 are equipartition magnetic field and inverse Compton equivalent magnetic field, respectively, in the unit of μG, and $\nu_{\rm b}$ is the break frequency in GHz above which spectrum steepens from the initial injection spectral index. We note that the spectral age calculation assumes a uniform magnetic field strength across all the emitting regions, and it also assumes that the magnetic field

Table 5.2: The spectral ages and source parameters.

Source Name	$\alpha_{\rm inj}$	d (kpc)	I_0 (mJy arcsec^{-2})	$\xi(\alpha,\nu_1,\nu_2)$	u_{min} (erg cm^{-3})	B$_{\rm eq}$ (μG)	$\nu_{\rm b,\ low}$ (GHz)	$\nu_{\rm b,\ high}$ (GHz)	$t_{\rm s}$ (Myr)	$t_{\rm ON}$ (Myr)	$t_{\rm OFF}$ (Myr)	$\frac{t_{\rm OFF}}{t_{\rm s}}$	$\chi^2_{\rm red}$
J022318-044526	-0.40	188	0.029	3.79×10^{-12}	6.61×10^{-13}	2.66	0.255	3.60	$20.3^{+2.5}_{-2.8}$	$15.2^{+1.9}_{-1.7}$	$5.1^{+1.0}_{-1.2}$	0.25	1.94
J022338-045418	-0.54	187	0.010	2.50×10^{-12}	1.24×10^{-12}	3.66	0.702	4.32	$24.3^{+2.7}_{-2.6}$	$14.5^{+1.7}_{-1.5}$	$9.8^{+1.9}_{-1.6}$	0.40	1.09
J022723-051242	-0.62	197	0.056	1.72×10^{-12}	7.35×10^{-13}	2.80	0.251	10.9	$33.2^{+3.8}_{-3.6}$	$28.0^{+3.4}_{-3.1}$	$5.2^{+1.5}_{-2.8}$	0.16	1.08
J022737-052139	-0.54	94	0.016	2.50×10^{-12}	4.37×10^{-13}	2.17	0.875	3.89	$27.5^{+4.3}_{-3.6}$	$14.5^{+4.2}_{-3.3}$	$13.0^{+1.1}_{-1.6}$	0.47	1.01
J022802-041417	-0.56	157	0.035	1.72×10^{-12}	3.03×10^{-13}	1.80	0.812	2.05	$41.4^{+2.8}_{-2.2}$	$15.4^{+2.5}_{-1.9}$	$26.0^{+1.1}_{-1.0}$	0.63	1.08

remains constant during the radiative cooling process. Further, the model considers only radiative losses without accounting for the losses due to expansion.

To estimate the age of remnants we use continuous injection off ($\mathrm{CI_{OFF}}$) model (Komissarov & Gubanov, 1994) that considers remnant phase after switching off the continuous injection phase lasting for the duration of t_{ON}. In the remnant phase, a new break appears at higher frequencies ($\nu_{\mathrm{b,\ high}}$) beyond which spectrum drops exponentially. As the remnant phase progresses $\nu_{\mathrm{b,\ high}}$ shifts towards lower frequencies. The ratio of $\nu_{\mathrm{b,\ low}}$ and $\nu_{\mathrm{b,\ high}}$ depends on the duration of remnant phase (t_{OFF}) *w.r.t.* the total source age as given by the following formula.

$$\frac{t_{\mathrm{OFF}}}{t_{\mathrm{s}}} = \left(\frac{\nu_{\mathrm{b,\ low}}}{\nu_{\mathrm{b,\ high}}}\right)^{0.5} \tag{5.1}$$

Where t_{s} is the total source age and can be expressed as $t_{\mathrm{s}} = t_{\mathrm{ON}} + t_{\mathrm{OFF}}$. It is obvious that $\nu_{\mathrm{b,\ low}}$ would be lower than $\nu_{\mathrm{b,\ high}}$ as $t_{\mathrm{OFF}} < t_{\mathrm{s}}$. However, for a very old remnant $\nu_{\mathrm{b,\ high}}$ would appear sufficiently close to $\nu_{\mathrm{b,\ low}}$. We note that the computation of spectral age requires knowledge of magnetic field strength (see eqn 3.2). We estimate magnetic field strength by assuming equipartition of minimum energy between particles and magnetic field and use the following equation.

$$B_{\mathrm{eq}}[G] = \left(\frac{24\pi}{7}u_{min}\right)^{1/2} \tag{5.2}$$

Where minimum particle energy (u_{min}) can be calculated using Equation 5.3 with an approximation of isotropic particle distribution (see Govoni & Feretti, 2004).

$$\begin{aligned} u_{min}\left[\frac{\mathrm{erg}}{\mathrm{cm}^3}\right] = {} & \xi(\alpha,\nu_1,\nu_2)(1+k)^{4/7}(\nu_0[\mathrm{MHz}])^{-4\alpha/7}\times \\ & (1+z)^{(12-4\alpha)/7}\left(I_0[\mathrm{mJy\ arcsec^{-2}}]\right)^{4/7}(d[\mathrm{kpc}])^{-4/7} \end{aligned} \tag{5.3}$$

where parameter ξ depends on the spectral index ($\alpha < 0$ is considered for the observed spectrum) and spectrum is integrated over frequencies ν_1 and ν_2 that correspond to 10 MHz and 100 GHz, respectively, which in turn correspond to a minimum Lorentz factor ($\gamma_{\rm min}$) 10 and maximum Lorentz factor ($\gamma_{\rm max}$) 10^5. We use ξ values from the Table 1 of Govoni & Feretti (2004). The parameter k represents the energy ratio of relativistic protons to electrons and is assumed to be 1 for our calculations, I_0 is surface brightness at measuring frequency which is 400 MHz in our case, and d is the source depth. The geometry of our sources is assumed to be cylindrical and the cross-sectional diameter is taken as the source depth.

The estimated values of minimum particle energy ($u_{\rm min}$), equipartition magnetic field strength $B_{\rm eq}$ of our remnant sources are given in Table 5.2. We note that the $B_{\rm eq}$ values for our remnants are found in the range of 1.8 μG to 3.66 μG which are similar to that reported for the remnants studied in the literature *e.g.*, 1.0 μG for BLOB1 (Brienza et al., 2016), 0.89−1.6 μG for B2 0924+30 (Jamrozy et al., 2004; Shulevski et al., 2017), 2.7 μG for NGC 1534 (Duchesne & Johnston-Hollitt, 2019) and 4.1 μG for J1615+5452 (Randriamanakoto et al., 2020). The remnants in DDRGs also show the magnetic field strength of a few μG (see Konar et al., 2012). To estimate the break frequencies ($\nu_{\rm b,\ low}$ and $\nu_{\rm b,\ high}$) and spectral ages of our remnants, we model their radio spectra by using the Broad-band Radio Astronomy ToolS (BRATS[3]; Harwood et al. (2013)) package. Given the remnant nature of our sources, we use $\rm CI_{OFF}$ model, also known as KGJP model (Komissarov & Gubanov, 1994), which is a modified form of the continuous injection model (CI; Jaffe & Perola (1973)) with the inclusion of energy losses via synchrotron and inverse Compton emission, after the cessation of AGN activity. While fitting the radio spectra in the BRATS we provide input parameters $B_{\rm eq}$ and $\alpha_{\rm inj}$, and obtain output parameters such as the break frequencies ($\nu_{\rm low}$ and $\nu_{\rm high}$), time-scales of active ($t_{\rm ON}$) and remnant ($t_{\rm OFF}$) phases, total source age ($t_{\rm s}$), and the goodness of fit parameter reduced χ^2. We point out that the accurate value of $\alpha_{\rm inj}$ is not known a priori, and hence, we begin with a value similar to $\alpha_{\rm 150\ MHz}^{\rm 1.5\ GHz}$ which is the low frequency spectral index available for our sample sources. The best fit values of $\alpha_{\rm inj}$ for our sources are in the range -0.5 − -0.6 which are similar to the typical values measured in remnant and active radio galaxies (Murgia et al., 2011). Although, for one of our sample sources J022318-044526,

[3]http://www.askanastronomer.co.uk/brats/

the radio SED is best fitted with a somewhat lower value of $\alpha_{\rm inj}$ = -0.4 (see Table 5.2). The modelled radio spectra of our sources are shown in Figure 5.1 (*lower panel*) and the best fit parameters are listed in Table 5.2. We note that our remnants show $\nu_{\rm b,\ low}$ in the range of 250 MHz to 875 MHz above which their spectra steepen. The values of $\nu_{\rm b,\ low}$ are consistent with the fact that our sources exhibit strong spectral curvature between 150 MHz and 1.5 GHz *i.e.*, $\alpha_{\rm 150\ MHz}^{\rm 325\ MHz}$ - $\alpha_{\rm 400\ MHz}^{\rm 1.5\ GHz}$ $\geq$0.5. Although, in all sources, the $\nu_{\rm b,\ high}$ above which spectrum falls off exponentially lies outside the frequency coverage (>1.5 GHz) (see Table 5.2), and it is determined from the SED modelling. The knowledge of break frequencies allows us to obtain spectral age estimates. Based on the best spectral fits, we find the total spectral ages ($t_{\rm s}$) of our remnants in the range of 20.3 Myrs to 41.4 Myrs. The duration of the active phase ($t_{\rm ON}$) is in the range 14.5 Myr to 28.0 Myr, while sources have spent nearly 5.0 Myr to 26.0 Myr in the remnant phase (see Table 5.2). We note that the typical errors associated with the spectral ages ($t_{\rm s}$, $t_{\rm ON}$ and $t_{\rm OFF}$) are of nearly 10 per cent. Although, the quoted errors are rendered by the model fittings and true uncertainties can be much larger owing to the several assumptions made in computing spectral ages (Harwood, 2017). Hence, we caution that the spectral age estimates should only be treated as the characteristic time-scales.

Further, we compute the average speed of lobes along the jet axis by dividing the average distance between centre and the outer edge of lobes with the time-scale of active phase $t_{\rm ON}$. We assume that our sources are lying in the plane of sky *i.e.*, the angle between the jet axis and the line-of-sight is 90°. For our remnants, we find that, the average speeds of lobes are in the range of 0.01c to 0.07c, which are similar to those found for powerful radio galaxies (see O'Dea et al., 2009). In other words, dynamical ages if derived by using a typical average speed of lobes would be consistent with the spectral ages. We also examine the ratio of remnant age to total source age ($t_{\rm OFF}/t_{\rm s}$) which describes the fraction of total life a source spent in the remnant phase. For our remnant, sources we find $t_{\rm OFF}/t_{\rm s}$ in the range of 0.16 to 0.63 (see Table 5.2). The wide range of $t_{\rm OFF}/t_{\rm s}$ infers that our sources are in different phases of their evolution. One of the noteworthy examples in our sample is J022802-041417 which has spent nearly 63 per cent of its total life in the remnant phase. The active phase duration of this source is only 15.4 Myr, while it has spent nearly 26.0 Myr in the remnant phase. Thus, we emphasize that despite the limited frequency coverage (150 MHz − 1.5 GHz) our observations are capable of detecting remnants in the different phases.

5.4.2 Comparison with Other Remnants

To understand the nature of our remnants, we compare their spectral ages with the previously studied remnant sources. The comparison sources include BLOB1 (Brienza et al., 2016), B2 0924+30 (Shulevski et al., 2017), J1615+5452 (Randriamanakoto et al., 2020), NGC 1534 (Duchesne & Johnston-Hollitt, 2019), four sources from Murgia et al. (2011) and nine sources from Parma et al. (2007). In Figure 5.7, we show a plot of total source age ($t_{\rm s}$) versus fractional remnant duration ($t_{\rm OFF}/t_{\rm s}$). It is evident that our sample remnants have systematically lower spectral ages than that for most of the remnant sources. There are only three sources, in addition to our five sample sources, that have spectral ages <50 Myr. However, we note that a simple comparison of the spectral ages in a heterogeneous sample of remnants may not yield meaningful insights considering the fact that source age depends on various factors such as physical radio size, magnetic field, large-scale environment and redshift (Turner, 2018). Therefore, we consider the effects of these parameters in our further discussion.

We note that Murgia et al. (2011) found a longer duration of source ages ($t_{\rm s}$ >50 Myr) for their remnant sources residing in cluster environments. The longer source age for sources residing in clusters can be attributed to the slow or arrested expansion of lobes due to the high pressure of the dense intra-cluster medium. Hence, fading lobes of a remnant can last longer if energy losses due to dynamical effects are insignificant or absent (Murgia et al., 2011). We point out that most of the remnant sources presented in Parma et al. (2007) also reside in cluster environments, and hence, they show high spectral ages. There are only three sources in the sample of Parma et al. (2007) with t_s <50 Myr. Two of these sources with small values of $t_{\rm OFF}/t_{\rm s}$ are recently switched-off sources and show unusually small radio sizes (<10 kpc). The relatively short source ages can be understood as jets and lobes taking less time to grow to the smaller size. The radio sizes of our remnants, in the range of 190 kpc to 643 kpc, are similar to other remnants that show higher spectral ages. We point out that all our remnants with lower ages reside in non-cluster environments, while sources of similar radio sizes but of higher spectral ages reside

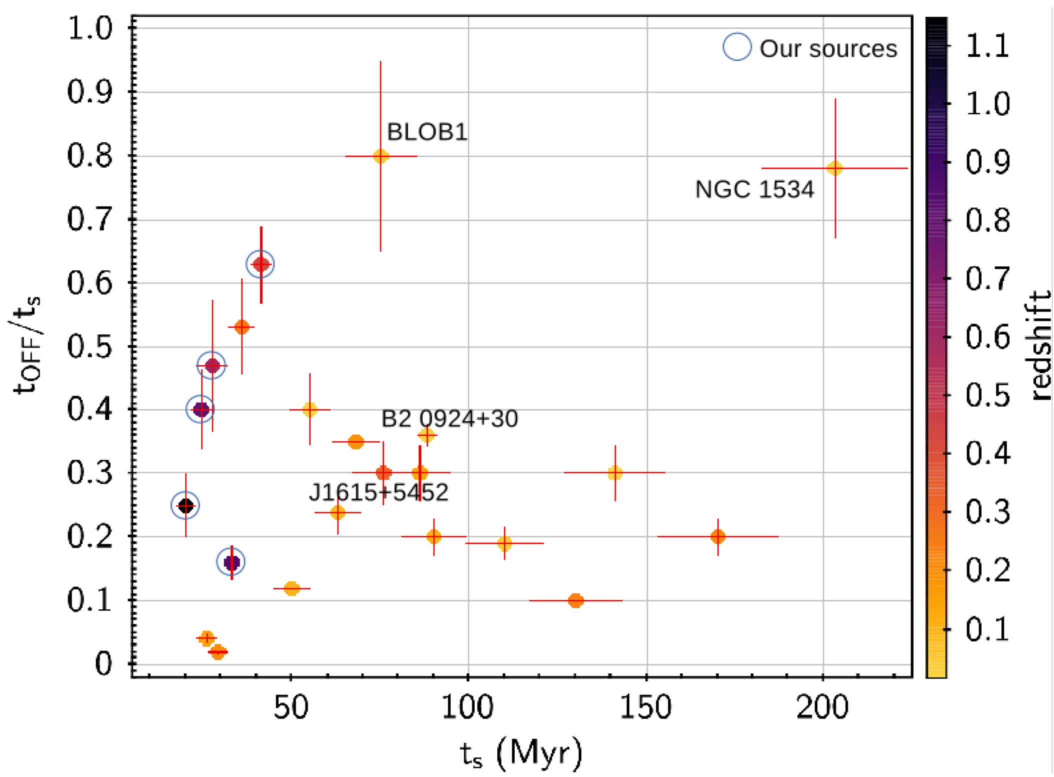

Figure 5.7: The plot of total source age t_s versus fractional remnant time-scale (t_{OFF}/t_s). The vertical colour bar indicates the redshifts of remnant hosts. The individually studied remnant sources are marked by their popular names. Our sample sources are marked by large blue circles.

mostly in cluster environments. Hence, as expected, our sample sources residing in less dense environments fade away more rapidly due to the faster expansion of lobes. Thus, relatively low spectral ages of our remnants when compared to the remnants residing in cluster environments can be partly attributed to the less dense large-scale environment.

Further, remnants with large radio sizes are expected to show high spectral ages owing to the fact that jets and lobes take a longer time to traverse longer distances and to fill up large volumes. Both BLOB1 and NGC 1534 are the examples of old large-size remnants with their radio sizes spanning upto nearly 700 kpc and 600 kpc, respectively (see Brienza et al., 2016; Duchesne & Johnston-Hollitt, 2019). The spectral ages of BLOB1 and NGC 1534 are 75 Myr and 203 Myr, respectively. The high value $t_{\rm OFF}/t_{\rm s} \sim 0.8$ confirms them to be old remnants that have spent nearly 80 per cent of their life in the remnant phase. Therefore, high spectral ages of BLOB1 and NGC 1534 remnants can be attributed to the combined effects of large radio size and long duration of the remnant phase. We note that one of our sample sources J022318-044526 has the radio size of 643 kpc but it has source ages ($t_{\rm s}$) of only 20.3 Myr. The low value of $t_{\rm OFF}/t_{\rm s} = 0.25$ suggests it to be a a relatively younger remnant. Notably, J022318-044526 reside at a much higher redshift (z) = 1.15 (see Table 5.1). In fact, we would like to emphasize that all our sample sources are at relatively higher redshifts ($z \sim 0.44-1.15$) which is evident from Figure 5.7. At high redshifts, inverse Compton losses dominate owing to the high density of Cosmic Microwave Background (CMB) photons. The inverse Compton equivalent magnetic field ($B_{\rm CMB}$) scales with $(1+z)^2$ (see equation 3.1). Thus, due to increased inverse Compton losses, remnant sources at higher redshifts are expected to fade away much faster than their counterparts at lower redshifts. Hence, relatively lower spectral ages of our remnants can be largely attributed to their high redshifts.

We note that, to nullify the effects of the environment, radio size, redshift, one should compare remnants matched in these parameters. However, due to the paucity of remnant sources we do not have such a comparison sample. It is worth mentioning that one remnant source WNB1127.5+4927 in the sample of Parma et al. (2007) is reported to reside in non-cluster environment at redshift $z = 0.25$ with its radio size of 211 kpc. The WNB1127.5+4927 shows similarity with our sample sources in terms of environment, size, redshift, and hence, as expected, it has t_s = 36 Myr and $t_{\rm OFF}$ = 19 Myr, similar to our remnants. The remnant source J1615+5452 residing in non-cluster environments at $z = 0.33$ and radio size of 100 kpc, is also similar to our remnants, but it is reported to have apparently higher spectral age with $t_s = 76$ Myr and $t_{\rm OFF} = 22$ Myr (see Randriamanakoto et al., 2020). A careful inspection of the spectral fitting of this source reveals that a statistically better fit with reduced $\chi^2 = 1.42$ yields $t_s = 35.9$ Myr and $t_{\rm OFF} = 21.5$ Myr, although, it requires unusually flat $\alpha_{\rm inj} = 0.4$ and high value of $B_{\rm eq} = 12\ \mu$G. We emphasize that more robust spectral modelling using flux densities measured across a wide range of frequencies, is required. In this context, the role of deep multi-frequency radio surveys is discussed in the next Section.

5.5 Potential of Deeper Radio Continuum Surveys

Our full synthesis band-3 uGMRT observations have provided sensitive images with noise-rms down to 30 μJy beam^{-1} and angular resolution of $6''.7 \times 5''.3$. Owing to its depth and angular resolution we discovered wing-shaped radio morphology in one of our sample sources J022338-045418. The diffuse emission of low-surface-brightness related to the southern component of this source is completely missed in the 1.5 GHz JVLA observations. Previous less sensitive 325 MHz GMRT observations with somewhat coarser resolution ($10''.2 \times 7''.9$) could not decipher radio structures in J022338-045418 (see Figure 5.3). Therefore, in the context of ongoing and planned deep radio continuum surveys, our band-3 uGMRT observations can be considered as a test-bed for discovering remnants possessing diffuse low-surface-brightness emission. For instance, the Evolutionary Map of the Universe (EMU) survey conducted with the ASKAP at 944 MHz provides deep continuum images with noise-rms of 25$-$30 μJy beam^{-1} and resolution of $11'' - 18''$ over a large area of 270 deg^2 (Norris et al., 2021). Despite being at relatively higher frequency EMU is capable of discovering large-scale diffuse emission owing to the short baselines up to 22m available in the ASKAP.

Recently, in a small area of 8.3 deg^2 of GAMA-23 field Quici et al. (2021) identified ten remnant candidates by using 119$-$216 MHz Murchison Wide-field Array (MWA) observations, 400 MHz uGMRT observations, 944 MHz EMU survey, and 5.5 GHz Australian Telescope of Compact Array (ATCA) observations. The multi-frequency observations were used to build broad-band SEDs and confirm the remnant status of radio galaxies. We emphasize that recent studies indicate remnant sources to be more abundant than that thought earlier. For instance, we used the spectral curvature criterion and identified a large sample of 48 small-size ($<30''$) remnant candidates in 12.5 deg^2 area in the *XMM*−LSS field (see chapter 4). The majority of small-size remnants are found at higher redshift (z >1.0). In the *XMM*−LSS field, we also identified 21 large-size ($>30''$) remnant candidates which show distinct double-lobe morphology with absent core and tend to be more powerful ($L_{150\ \rm MHz} > 10^{25}$ W Hz^{-1}) radio sources (see chapter 3). Thus, remnant searches performed in the deep fields have demonstrated the existence of a variety of remnant sources residing across a wide range of redshifts. Although, most of the searches in the deep field are limited only to small sky-area of a few deg^2 and rendered only small samples. The large-area deep surveys have the potential to discover a large population of remnants that would offer better insights into the evolution of radio galaxies in the remnant phase.

In Section 5.4, we pointed out that the radio observations over a wide range of frequencies are needed for robust determination of spectral ages of remnants. The upcoming radio continuum surveys from the Square Kilometer Array (SKA) telescope covering a wide range of frequencies *i.e.*, 50 MHz − 350 MHz with SKA1−low, and 350 MHz − 15.3 GHz with SKA1-mid would be ideal for spectral modelling. As per the baseline design performance, SKA1-mid is expected to provide noise-rms of 4.4 μJy beam^{-1} in one hour observing time in the 0.35−1.05 GHz band centered at 770 MHz (see SKA factsheet[4]). Thus, the large-area multi-frequency deep radio surveys from the SKA and its pathfinder are expected to unveil a large population of remnants distributed over different evolutionary phases.

[4]https://www.skatelescope.org/wpcontent/uploads/2018/08/16231-factsheet-telescopes-v71.pdf

5.6 Results and Conclusions

In this chapter, we presented the new band-3 uGMRT observations of five remnant sources selected based on the strong spectral curvature, emission of low-surface-brightness from lobes, and absent radio core in the 3.0 GHz VLASS images. We performed modelling of radio SEDs using observations from the LOFAR at 150 MHz, GMRT at 325 MHz, uGMRT at 400 MHz (band-3) and JVLA at 1.5 GHz. The salient results of our study are outlined as below.

- With our deep full synthesis band-3 uGMRT observations (median noise-rms $\sim$ 30 mJy beam^{-2}), we confirm the presence of low-surface-brightness emission in all our five remnant sources. The surface brightness at 400 MHz is found in the range of 36 mJy arcmin^{-2} to 201 mJy arcmin^{-2} which is similar to those found in remnants studied in the literature (Brienza et al., 2017).

- With our band-3 uGMRT observations, we discovered a wing-shaped radio morphology in one of our sample sources J022338-045418. Previous 325 MHz GMRT observations were unable to reveal structures due to its coarser resolution, while 1.5 GHz JVLA observations did not detect diffuse emission from the southern component. Both northern as well as southern components show two peaks that are similar to the primary and secondary lobes commonly seen in the Z-shaped and X-shaped radio sources. Despite its extended morphology this source is faint with the total flux density of only 3.1$\pm$0.5 mJy at 400 MHz, which in turn yields low surface-brightness of 36 mJy arcmin^{-2}.

- We fitted the radio SEDs with CI$_{\rm OFF}$ model that assumes a continuous injection phase for the duration of $t_{\rm ON}$, and thereafter, a remnant phase for the duration of $t_{\rm OFF}$ with total source age $t_{\rm s}$ = $t_{\rm ON}$ + $t_{\rm OFF}$. For our remnant sources, the best fit models yield source ages ($t_{\rm s}$) in the range of 20.3 Myr to 41.4 Myr.

- We find that our small sample of remnants shows a wide distribution of $t_{\rm OFF}/t_{\rm s}$ in the range of 0.16 to 0.63. In other words, our sample sources have spent 16 per cent to 63 per cent of their total life in the remnant phase. Hence, our sources belong to the different phases of evolution.

- The estimated spectral ages of our remnants are, in general, lower than those found for several remnants previously studied in the literature. We caution that spectral age depends on various factors such as the radio size, magnetic field, redshift, and the large-scale environment, so we need to account for these parameters while comparing spectral ages. Notably, remnants residing in cluster environments show higher spectral ages due to less or insignificant dynamical energy losses from the reduced or absent expansion of lobes embedded within the dense intra-cluster medium. Further, we found that our remnant sources have systematically higher redshifts than most of the sources reported in the literature. Therefore, inverse Compton energy losses are more dominant for our high redshift sources, which in turn reduces their source ages.

- We note that the total source ages of our remnants are similar to one of the sample sources WNB1127.5+4927 of Parma et al. (2007), which has similar radio size, redshift, and environment.

- Our study, limited to a small sample lying within a small area of 2.3 deg^2 covered with one pointing of band-3 uGMRT observations, demonstrates the potential of deep large-area surveys from the SKA and its pathfinders. Based on our study we expect a large population of remnants to be detected with the ongoing and planned deep radio continuum radio surveys.

Chapter 6

Summary and Future Work

6.1 Summary

This thesis presents the search and characterization of remnants using multi-frequency radio observations in the XMM-LSS field. Using morphological and spectral criteria we discovered the largest sample of remnants, hitherto, known to us. Our sample of remnants contains a large fraction of faint sources residing at higher redshifts ($z > 1.0$). This thesis also highlights the bias towards large-size remnants identified by using mainly morphological criteria, and presents a sample of 48 small-size ($\leq 30''$) remnant candidates. Here, we summarise the work reported in the thesis.

6.1.1 Large-Size Remnants and Their Properties

In chapter 3, we presented the search and characterization of remnant candidates in 12.5 deg^2 of the XMM−LSS field by using deep radio observations at 325 MHz from the GMRT, at 150 MHz from the LOFAR, at 1.4 GHz from the JVLA, and at 3 GHz from the VLASS. By using both morphological criteria *viz.*, undetected radio core as well as spectral criteria *viz.*, high spectral curvature, and ultra−steep spectrum, we identify 21 large-size ($\geq 30''$) remnant candidates. The cutoff limit on the radio size is introduced for applying the morphological criteria which require clear detection of lobes and core components. We find that our remnant candidates reside mostly in non−cluster environments, and exhibit diverse properties in terms of morphology, spectral index ($\alpha_{150\mathrm{MHz}}^{1.4\ \mathrm{GHz}}$ in the range of -1.71 to -0.75 with a median of -1.10), and linear radio size (ranging from 242 kpc to 1.3 Mpc with a median of 469 kpc). Most of the previous studies have been limited to relatively bright radio sources (e.g. $\mathrm{S}_{150\ \mathrm{MHz}} > 80$ mJy). In our study, we attempted to search remnant candidates down to the flux density limit of 6.0 mJy at 325 MHz, and obtained a stringent upper limit on the remnant fraction (f_{rem}) to be 5%, a value lower than those reported previously. The observed f_{rem} seems consistent with the predictions of an evolutionary model assuming power law distributions of the duration of active phase and jet kinetic power with index -0.8 to -1.2. This work would appear in Dutta et al. (2022), ApJ, (*under review*).

6.1.2 Small-Size Remnants and Their Properties

In chapter 4, we attempted to highlight that the searches for remnants mainly based on the morphological criteria have identified exclusively remnants of large angular size sources, resulting into a bias towards the remnants of powerful FR II radio galaxies. In this study we made the first attempt to perform a systematic search for remnants of small angular sizes (<30″) in the XMM-LSS field. By using spectral curvature criterion we discover 48 remnant candidates exhibiting strong spectral curvature *i.e.*, $\alpha_{150\ \rm MHz}^{325\ \rm MHz}$ - $\alpha_{325\ \rm MHz}^{1.4\ \rm GHz} \geq 0.5$. The majority (38/48) of our remnant sources lack any detection in the VLASS images, which in turn suggests the absence of a core. The remaining ten sources with 3.0 GHz detection include sources depicting steep as well as flat spectra in the 1.4 GHz − 3.0 GHz regime. The flat spectral index in the 1.4 GHz − 3.0 GHz regime and strongly curvature spectrum in 150 MHz − 1.4 GHz regime can be explained, if these sources exhibit recurrent AGN activity with presence of an active core as well as diffuse emission from the previous episode of AGN activity. In fact, much deeper and higher resolution observations are required to decipher their true nature. We place an upper limit on the remnant fraction ($f_{\rm rem}$) to be 3.9%, which increases to 5.4% if flux cut-off limit of $S_{150\ \rm MHz} \geq 10$ mJy is considered. Our study unveils, hitherto unexplored, a new population of small-size (<200 kpc) remnant candidates that are often found to reside in less dense environments and at higher redshifts (z) >1.0. We speculate that a relatively shorter active phase and/or low jet power can be plausible reasons for the small size of remnant candidates. This work has been reported in Singh et al. (2021).

6.1.3 Spectral Ageing Analysis of Remnant Sources

In chapter 5, we emphasized that the time-scale of remnant phase and AGN duty cycle are vital to understanding the evolution of radio galaxies. We performed radio spectral ageing analysis for five remnant radio galaxies using new band-3 uGMRT observations and ancillary radio data. Our uGMRT observations reveal emission of low-surface-brightness in all five remnants with 400 MHz surface brightness in the range of 36−201 mJy arcmin^{-2}.

With band-3 uGMRT observations, we discover the wing-shaped radio morphology in one of our sample sources. Using radio observations at 150 MHz, 325 MHz, 400 MHz, and 1.5 GHz we model the radio spectral energy distributions (SEDs) of our sample sources with the continuous injection off model ($\mathrm{CI_{OFF}}$), that assumes an active phase with continuous injection followed by a remnant phase. We obtain total source ages ($t_{\rm s}$) in the range of 20.3 Myr to 41.4 Myr with $t_{\rm OFF}/t_{\rm s}$ distributed in the range of 0.16 to 0.63, which in turn suggests them to belong to different evolutionary phases. We note that, in comparison to the remnants reported in the literature, our sample sources tend to show lower spectral ages that can be explained by the combined effects of more dominant inverse Compton losses for our sources present at the relatively higher redshifts, and the possible rapid expansion of lobes in their less dense environments. This work has been reported in Dutta et al. (2022).

6.2 Future Work

To understand the nature of remnants, we require robust determination of their ages, which in turn need multi-frequency observations across a wide range of frequencies. Importantly, radio observations at different frequencies are ought to be matched in the resolution and sensitivity to ensure that extended diffuse emission is detected across all frequencies. The observations presented in the thesis have been mainly limited to 325 MHz from GMRT and 1.4 GHz from the JVLA, FIRST, NVSS and 150 MHz from the LOFAR. The JVLA and FIRST observations of higher resolution ($5''.0$) preferentially detect emission of high surface-brightness and have been primarily used to detect the radio core. The NVSS observations with a large synthesized beam of $45''$ detect lobe emission of low-surface-brightness but often fail to resolve structures due to coarser resolution. Also, 150 MHz LOFAR images are not yet publicly available to create spatially resolved spectral index and spectral age maps. Hence, we plan to use multi-frequency observations from uGMRT and MeerKAT telescopes. The deep band-3 (250 MHz $-$ 500 MHz), band-4 (550 MHz $-$ 900 MHz) and band-5 (1000 MHz $-$ 1450 MHz) observations from uGMRT and MeerKAT *L*-band (856 MHz $-$ 1712 MHz) observations would allow us to accurately model SED and determine spectral ages more robustly. The sensitivity at the level of a few tens of μJy and resolution of $8''.0 - 10''.0$ would be sufficient enough to detect diffuse emission from relic lobes. Therefore, using these observations, we plan to perform spectral ageing analysis for remnant sources. This exercise would provide us better insights to the evolution of remnant sources.

References

Abdo A. A., et al., 2009, ApJS, 183, 46

Adami C., et al., 2018, A&A , 620, A5

Ahumada R., et al., 2020, ApJS, 249, 3

Aihara H., et al., 2018, PASJ, 70, S4

Aihara H., et al., 2019, PASJ, 71, 114

Alexander D. M., et al., 2003, AJ, 126, 539

An T., Baan W. A., 2012, ApJ, 760, 77

Antonucci R., 1993, ARA&A, 31, 473

Baldi R. D., Capetti A., Giovannini G., 2015, A&A , 576, A38

Baldry I. K., Glazebrook K., Brinkmann J., Ivezić Ž., Lupton R. H., Nichol R. C., Szalay A. S., 2004, ApJ, 600, 681

Barthel P. D., Tytler D. R., Thomson B., 1990, A&AS , 82, 339

Basu A., Wadadekar Y., Beelen A., Singh V., Archana K. N., Sirothia S., Ishwara-Chandra C. H., 2015, ApJ, 803, 51

Becker R. H., White R. L., Helfand D. J., 1995, ApJ, 450, 559

Benson A. J., Bower R. G., Frenk C. S., Lacey C. G., Baugh C. M., Cole S., 2003, ApJ, 599, 38

Bera S., Sasmal T. K., Patra D., Mondal S., 2022, ApJS, 260, 7

Blandford R. D., Ostriker J. P., 1978, ApJ , 221, L29

Blandford R. D., Payne D. G., 1982, MNRAS , 199, 883

Blandford R. D., Znajek R. L., 1977, MNRAS , 179, 433

Blanton E. L., 2000, PhD thesis, Columbia University, New York

Blundell K. M., Rawlings S., 2000, AJ, 119, 1111

Bonzini M., Padovani P., Mainieri V., Kellermann K. I., Miller N., Rosati P., Tozzi P., Vattakunnel S., 2013, MNRAS , 436, 3759

Bower R. G., Benson A. J., Crain R. A., 2012, MNRAS , 422, 2816

Brienza M., Morganti R., Shulevski A., Godfrey L., Vilchez N., 2016, Astronomische Nachrichten, 337, 31

Brienza M., et al., 2017, A&A , 606, A98

Callingham J. R., et al., 2017, ApJ, 836, 174

Carilli C. L., Perley R. A., Dreher J. W., Leahy J. P., 1991, ApJ, 383, 554

Chen C. T. J., et al., 2018, MNRAS , 478, 2132

Cho H., James Jee M., Smith R., Finner K., Lee W., 2022, ApJ, 925, 68

Condon J. J., 1992, ARA&A, 30, 575

Condon J. J., Cotton W. D., Greisen E. W., Yin Q. F., Perley R. A., Taylor G. B., Broderick J. J., 1998, AJ, 115, 1693

Cool R. J., et al., 2013, ApJ, 767, 118

Cordey R. A., 1987, MNRAS , 227, 695

Cornwell T. J., Evans K. F., 1985, A&A , 143, 77

Croston J. H., Kraft R. P., Hardcastle M. J., 2007, ApJ, 660, 191

Dabhade P., et al., 2020, A&A , 642, A153

Davies L. J. M., et al., 2018, MNRAS , 480, 768

Di Matteo T., Springel V., Hernquist L., 2005, Nature, 433, 604

Doeleman S. S., et al., 2012, Science, 338, 355

Duchesne S. W., Johnston-Hollitt M., 2019, PASA, 36, e016

Duffy P., Blundell K. M., 2012, MNRAS , 421, 108

Dunlop J. S., McLure R. J., Kukula M. J., Baum S. A., O'Dea C. P., Hughes D. H., 2003, MNRAS , 340, 1095

Dutta S., Singh V., Ishwara Chandra C. H., Wadadekar Y., Kayal A., 2022, arXiv e-prints, p. arXiv:2207.07871

Dwarakanath K. S., Kale R., 2009, ApJ , 698, L163

Elvis M., et al., 1994, ApJS, 95, 1

Erben T., et al., 2013, MNRAS , 433, 2545

Fabian A. C., 2012, ARA&A, 50, 455

Falcke H., Sherwood W., Patnaik A. R., 1996, ApJ, 471, 106

Fanaroff B. L., Riley J. M., 1974, MNRAS , 167, 31P

Fomalont E. B., Perley R. A., 1999, in Taylor G. B., Carilli C. L., Perley R. A., eds, Astronomical Society of the Pacific Conference Series Vol. 180, Synthesis Imaging in Radio Astronomy II. p. 79

Gabuzda D. C., Knuettel S., Reardon B., 2015, MNRAS , 450, 2441

Gabuzda D. C., Roche N., Kirwan A., Knuettel S., Nagle M., Houston C., 2017, MNRAS , 472, 1792

Garilli B., et al., 2014, A&A , 562, A23

Garrett M. A., 2002, A&A , 384, L19

Gendre M. A., Best P. N., Wall J. V., Ker L. M., 2013, MNRAS , 430, 3086

Gendron-Marsolais M., et al., 2017, MNRAS , 469, 3872

Ghisellini G., Celotti A., 2001, A&A , 379, L1

Giommi P., Padovani P., Polenta G., 2013, MNRAS , 431, 1914

Godfrey L. E. H., Morganti R., Brienza M., 2017, MNRAS , 471, 891

Gordon Y. A., et al., 2020, Research Notes of the American Astronomical Society, 4, 175

Govoni F., Feretti L., 2004, International Journal of Modern Physics D, 13, 1549

Gupta Y., et al., 2017, Current Science, 113, 707

Hale C. L., et al., 2019, A&A , 622, A4

Hale C. L., et al., 2021, PASA, 38, e058

Hardcastle M. J., Looney L. W., 2008, MNRAS , 388, 176

Hardcastle M. J., et al., 2019, A&A , 622, A12

Harwood J. J., 2017, MNRAS , 466, 2888

Harwood J. J., Hardcastle M. J., Croston J. H., Goodger J. L., 2013, MNRAS , 435, 3353

Harwood J. J., Hardcastle M. J., Croston J. H., 2015, MNRAS , 454, 3403

Helou G., Soifer B. T., Rowan-Robinson M., 1985, ApJ , 298, L7

Heywood I., Hale C. L., Jarvis M. J., Makhathini S., Peters J. A., Sebokolodi M. L. L., Smirnov O. M., 2020, MNRAS , 496, 3469

Heywood I., et al., 2022, MNRAS , 509, 2150

Högbom J. A., 1974, A&AS , 15, 417

Horiuchi S., Meier D. L., Preston R. A., Tingay S. J., 2006, PASJ, 58, 211

Hotan A. W., et al., 2021, PASA, 38, e009

Hovatta T., Lister M. L., Aller M. F., Aller H. D., Homan D. C., Kovalev Y. Y., Pushkarev A. B., Savolainen T., 2012, AJ, 144, 105

Hughes D. H., et al., 1998, Nature, 394, 241

Hurley-Walker N., et al., 2017, MNRAS , 464, 1146

Ibar E., et al., 2008, MNRAS , 386, 953

Ibar E., Ivison R. J., Biggs A. D., Lal D. V., Best P. N., Green D. A., 2009, MNRAS , 397, 281

Ilbert O., et al., 2006, A&A , 457, 841

Inoue S., Takahara F., 1996, ApJ, 463, 555

Intema H. T., Jagannathan P., Mooley K. P., Frail D. A., 2017, A&A , 598, A78

Irwin C. M., Tang X., Piran T., Nakar E., 2019, MNRAS , 488, 4926

Ishwara-Chandra C. H., Taylor A. R., Green D. A., Stil J. M., Vaccari M., Ocran E. F., 2020, MNRAS , 497, 5383

Isobe N., Tashiro M., Makishima K., Iyomoto N., Suzuki M., Murakami M. M., Mori M., Abe K., 2002, ApJ , 580, L111

Isobe N., Makishima K., Tashiro M., Hong S., 2005, ApJ, 632, 781

Isobe N., Koyama S., Kino M., Wada T., Nakagawa T., Matsuhara H., Niinuma K., Tashiro M., 2017, ApJ, 850, 193

Jaffe W. J., Perola G. C., 1973, A&A , 26, 423

Jamrozy M., Klein U., Mack K. H., Gregorini L., Parma P., 2004, A&A , 427, 79

Järvelä E., Dahale R., Crepaldi L., Berton M., Congiu E., Antonucci R., 2022, A&A , 658, A12

Jarvis M. J., et al., 2013, MNRAS , 428, 1281

Jonas J., MeerKAT Team 2016, in MeerKAT Science: On the Pathway to the SKA. p. 1

Jurlin N., Brienza M., Morganti R., Wadadekar Y., Ishwara-Chandra C. H., Maddox N., Mahatma V., 2021, arXiv e-prints, p. arXiv:2106.13161

Kaiser C. R., Alexander P., 1997, MNRAS , 286, 215

Kardashev N. S., 1962, Soviet Ast., 6, 317

Kataoka J., Leahy J. P., Edwards P. G., Kino M., Takahara F., Serino Y., Kawai N., Martel A. R., 2003, A&A , 410, 833

Kayal A., Singh V., Ishwara Chandra C. H., Wadadekar Y., Dutta S., 2022, arXiv e-prints, p. arXiv:2207.06938

Kellermann K. I., Sramek R., Schmidt M., Shaffer D. B., Green R., 1989, AJ, 98, 1195

Kellermann K. I., Sramek R. A., Schmidt M., Green R. F., Shaffer D. B., 1994, AJ, 108, 1163

Kharb P., Shastri P., 2004, A&A , 425, 825

Kim J., et al., 2018, ApJ, 861, 129

Komissarov S. S., Gubanov A. G., 1994, A&A , 285, 27

Konar C., Hardcastle M. J., Jamrozy M., Croston J. H., Nandi S., 2012, MNRAS , 424, 1061

Kraft R. P., Vázquez S. E., Forman W. R., Jones C., Murray S. S., Hardcastle M. J., Worrall D. M., Churazov E., 2003, ApJ, 592, 129

Krefting N., et al., 2020, ApJ, 889, 185

Kuźmicz A., Jamrozy M., Bronarska K., Janda-Boczar K., Saikia D. J., 2018, ApJS, 238, 9

Lacy M., et al., 2020, PASP, 132, 035001

Laing R. A., Bridle A. H., 2002, MNRAS , 336, 1161

Lal D. V., 2021, ApJ, 915, 126

Lal D. V., Sebastian B., Cheung C. C., Pramesh Rao A., 2019, AJ, 157, 195

Lane W. M., Cotton W. D., van Velzen S., Clarke T. E., Kassim N. E., Helmboldt J. F., Lazio T. J. W., Cohen A. S., 2014, MNRAS , 440, 327

Laor A., 2000, ApJ , 543, L111

Laurent-Muehleisen S. A., Kollgaard R. I., Feigelson E. D., Brinkmann W., Siebert J., 1999, ApJ, 525, 127

Le Fèvre O., et al., 2013, A&A , 559, A14

Le Fèvre O., et al., 2015, A&A , 576, A79

Lister M. L., et al., 2013, AJ, 146, 120

Longair M. S., Ryle M., Scheuer P. A. G., 1973, MNRAS , 164, 243

Lonsdale C. J., et al., 2003, PASP, 115, 897

Machalski J., Kozieł-Wierzbowska D., Jamrozy M., Saikia D. J., 2008, ApJ, 679, 149

Mack K. H., Prieto M. A., Brunetti G., Orienti M., 2009, MNRAS , 392, 705

Mahatma V. H., et al., 2018, MNRAS , 475, 4557

Mahatma V. H., et al., 2019, A&A , 622, A13

Marecki A., Jamrozy M., Machalski J., Pajdosz-Śmierciak U., 2021, MNRAS , 501, 853

Marscher A. P., et al., 2008, Nature, 452, 966

Massaro F., Ajello M., 2011, ApJ , 729, L12

Matthews A. P., Scheuer P. A. G., 1990, MNRAS , 242, 616

Mauduit J. C., et al., 2012, PASP, 124, 714

McConnell D., et al., 2020, PASA, 37, e048

McLure R. J., Jarvis M. J., 2004, MNRAS , 353, L45

McNamara B. R., Nulsen P. E. J., 2007, ARA&A, 45, 117

McNamara B. R., Nulsen P. E. J., 2012, New Journal of Physics, 14, 055023

Mertens F., Lobanov A. P., Walker R. C., Hardee P. E., 2016, A&A , 595, A54

Mingo B., et al., 2019, MNRAS , 488, 2701

Mohan N., Rafferty D., 2015, PyBDSF: Python Blob Detection and Source Finder (ascl:1502.007)

Morganti R., 2017, Nature Astronomy, 1, 596

Mullin L. M., Riley J. M., Hardcastle M. J., 2008, MNRAS , 390, 595

Murgia M., Fanti C., Fanti R., Gregorini L., Klein U., Mack K. H., Vigotti M., 1999, A&A , 345, 769

Murgia M., et al., 2011, A&A , 526, A148

Nandi S., Saikia D. J., 2012, Bulletin of the Astronomical Society of India, 40, 121

Nandi S., et al., 2019, MNRAS , 486, 5158

Narayan R., Nityananda R., 1986, ARA&A, 24, 127

Norris R. P., et al., 2021, PASA, 38, e046

Nyland K., et al., 2020, ApJ, 905, 74

O'Dea C. P., 1998, PASP, 110, 493

O'Dea C. P., Saikia D. J., 2021, A&A Rev., 29, 3

O'Dea C. P., Daly R. A., Kharb P., Freeman K. A., Baum S. A., 2009, A&A , 494, 471

Oguri M., et al., 2021, VizieR Online Data Catalog, p. J/PASJ/70/S20

Oke J. B., Gunn J. E., 1983, ApJ, 266, 713

Oliver S. J., et al., 2012, MNRAS , 424, 1614

Orienti M., 2016, Astronomische Nachrichten, 337, 9

Orienti M., Dallacasa D., 2021, Astronomische Nachrichten, 342, 1151

Orienti M., Brunetti G., Nagai H., Paladino R., Mack K. H., Prieto M. A., 2017, MNRAS , 469, L123

Osmer P. S., Smith M. G., 1976, ApJ, 210, 267

Owsianik I., Conway J. E., 1998, A&A , 337, 69

Padovani P., et al., 2017, A&A Rev., 25, 2

Pâris I., et al., 2018, A&A , 613, A51

Park J., Hada K., Kino M., Nakamura M., Ro H., Trippe S., 2019, ApJ, 871, 257

Parma P., Murgia M., Morganti R., Capetti A., de Ruiter H. R., Fanti R., 1999, A&A , 344, 7

Parma P., Murgia M., de Ruiter H. R., Fanti R., Mack K. H., Govoni F., 2007, A&A , 470, 875

Pasetto A., et al., 2021, ApJ , 923, L5

Peck A. B., Taylor G. B., 2000, ApJ, 534, 90

Perley R. A., Chandler C. J., Butler B. J., Wrobel J. M., 2011, ApJ , 739, L1

Peterson B. M., 1997, An Introduction to Active Galactic Nuclei

Peterson J. R., Kahn S. M., Paerels F. B. S., Kaastra J. S., Tamura T., Bleeker J. A. M., Ferrigno C., Jernigan J. G., 2003, ApJ, 590, 207

Pierre M., et al., 2004, J. Cosmology Astropart. Phys., 2004, 011

Quici B., et al., 2021, PASA, 38, e008

Rafter S. E., Crenshaw D. M., Wiita P. J., 2011, AJ, 141, 85

Randall S. W., et al., 2015, ApJ, 805, 112

Randriamanakoto Z., Ishwara-Chandra C. H., Taylor A. R., 2020, MNRAS , 496, 3381

Readhead A. C. S., et al., 2021, Astronomische Nachrichten, 342, 1185

Retana-Montenegro E., Röttgering H. J. A., 2017, A&A , 600, A97

Sabater J., et al., 2019, A&A , 622, A17

Saikia D. J., Jamrozy M., 2009, Bulletin of the Astronomical Society of India, 37, 63

Saripalli L., 2012, AJ, 144, 85

Schmidt M., 1963, Nature, 197, 1040

Schmidt M., 1965, ApJ, 141, 1

Schoenmakers A. P., Mack K. H., de Bruyn A. G., Röttgering H. J. A., Klein U., van der Laan H., 2000, A&AS , 146, 293

Schuldt S., Suyu S. H., Cañameras R., Taubenberger S., Meinhardt T., Leal-Taixé L., Hsieh B. C., 2021, A&A , 651, A55

Scodeggio M., et al., 2018, A&A , 609, A84

Seyfert C. K., 1943, ApJ, 97, 28

Shabala S. S., Jurlin N., Morganti R., Brienza M., Hardcastle M. J., Godfrey L. E. H., Krause M. G. H., Turner R. J., 2020, MNRAS , 496, 1706

Shimwell T. W., et al., 2017, A&A , 598, A104

Shulevski A., et al., 2017, A&A , 600, A65

Sikora M., Stawarz Ł., Lasota J.-P., 2007, ApJ, 658, 815

Silk J., Rees M. J., 1998, A&A , 331, L1

Singh V., et al., 2014, A&A , 569, A52

Singh V., Ishwara-Chandra C. H., Wadadekar Y., Beelen A., Kharb P., 2015, MNRAS , 446, 599

Singh V., Wadadekar Y., Ishwara-Chandra C. H., Sirothia S., Sievers J., Beelen A., Omont A., 2017, MNRAS , 470, 4956

Singh V., Dutta S., Wadadekar Y., Ishwara-Chandra C. H., 2021, Galaxies, 9, 121

Slee O. B., Roy A. L., Murgia M., Andernach H., Ehle M., 2001, AJ, 122, 1172

Smolčić V., et al., 2018, A&A , 620, A14

Stocke J. T., Rector T. A., 1997, ApJ , 489, L17

Strateva I., et al., 2001, AJ, 122, 1861

Swarup G., 1991, in Cornwell T. J., Perley R. A., eds, Astronomical Society of the Pacific Conference Series Vol. 19, IAU Colloq. 131: Radio Interferometry. Theory, Techniques, and Applications. pp 376–380

Tamhane P., Wadadekar Y., Basu A., Singh V., Ishwara-Chandra C. H., Beelen A., Sirothia S., 2015, MNRAS , 453, 2438

Tasse C., et al., 2006, A&A , 456, 791

Tasse C., Röttgering H. J. A., Best P. N., Cohen A. S., Pierre M., Wilman R., 2007, A&A , 471, 1105

Tchekhovskoy A., Bromberg O., 2016, MNRAS , 461, L46

Thompson A. R., Clark B. G., Wade C. M., Napier P. J., 1980, ApJS, 44, 151

Thompson A. R., Moran J. M., Swenson George W. J., 2017, Interferometry and Synthesis in Radio Astronomy, 3rd Edition, doi:10.1007/978-3-319-44431-4.

Turner R. J., 2018, MNRAS , 476, 2522

Turner R. J., Shabala S. S., 2015, ApJ, 806, 59

Turner R. J., Shabala S. S., Krause M. G. H., 2018, MNRAS , 474, 3361

Urry C. M., Padovani P., 1995, PASP, 107, 803

Venturi T., Bardelli S., Morganti R., Hunstead R. W., 1998, MNRAS , 298, 1113

Verdoes Kleijn G. A., Baum S. A., de Zeeuw P. T., O'Dea C. P., 2002, AJ, 123, 1334

Véron-Cetty M. P., Véron P., 2010, A&A , 518, A10

Visnovsky K. L., Impey C. D., Foltz C. B., Hewett P. C., Weymann R. J., Morris S. L., 1992, ApJ, 391, 560

Vlahakis N., Königl A., 2004, ApJ, 605, 656

Wang Y., Kaiser C. R., 2008, MNRAS , 388, 677

Werner M. W., Murphy D. W., Livingston J. H., Gorjian V., Jones D. L., Meier D. L., Lawrence C. R., 2012, ApJ, 759, 86

Wilkinson P. N., Polatidis A. G., Readhead A. C. S., Xu W., Pearson T. J., 1994, ApJ , 432, L87

Williams W. L., et al., 2016, MNRAS , 460, 2385

Willott C. J., Rawlings S., Jarvis M. J., Blundell K. M., 2003, MNRAS , 339, 173

Worrall D. M., Birkinshaw M., 1994, ApJ, 427, 134

Wright E. L., et al., 2010, AJ, 140, 1868

van Breugel W., Miley G., Heckman T., 1984, AJ, 89, 5

van Haarlem M. P., et al., 2013, A&A , 556, A2

van Weeren R. J., Röttgering H. J. A., Brüggen M., Cohen A., 2009, A&A , 508, 75

van Weeren R. J., Brüggen M., Röttgering H. J. A., Hoeft M., Nuza S. E., Intema H. T., 2011, A&A , 533, A35

van Weeren R. J., de Gasperin F., Akamatsu H., Brüggen M., Feretti L., Kang H., Stroe A., Zandanel F., 2019, Space Sci. Rev., 215, 16